Walter Schottky Institut
Zentralinstitut für physikalische Grundlagen der Halbleiterelektronik
Fakultät für Physik der Technischen Universität München

Spin-spin interactions of localized electronic states in semiconductors

Tobias Graf

Vollständiger Abdruck der von der Fakultät für Physik der Technischen Universität München zur Erlangung des akademischen Grades eines

Doktors der Naturwissenschaften
(Dr. rer. nat.)

genehmigten Dissertation.

Vorsitzender:		Univ.-Prof. Dr. Axel Groß
Prüfer der Dissertation:	1.	Univ.-Prof. Dr. Martin Stutzmann
	2.	Univ.-Prof. Dr. Rudolf Gross

Die Dissertation wurde am 22.09.2003 bei der Technischen Universität München eingereicht und durch die Fakultät für Physik am 09.12.2003 angenommen.

Zusammenfassung

Lokalisierte elektronische Zustände treten in Halbleitern an Punktdefekten wie Fremdatomen oder intrinsischen Störstellen des Kristallgitters auf. Zusätzlich zu ihrer Ladung besitzen solche Zustände durch ungepaarte Spins in vielen Fällen ein magnetisches Moment. Die Vermeidung der häufig schädlichen Defekte und das gezielte Einbringen von Dotieratomen ermöglicht in Halbleitern die Realisierung einer Vielzahl von elektronischen Bauelementen. Eine vergleichbar präzise Kontrolle der Spineigenschaften wird im Fall von Metallen seit langem angewendet, während die Realisierung von spinbasierten Halbleiterbauelementen noch immer Gegenstand intensiver Forschung ist. Paramagnetische Defektzustände lassen sich experimentell mittels Elektronenspinresonanz (ESR) identifizieren und auf ihre mikroskopischen Eigenschaften wie Symmetrie und Lokalisierung hin untersuchen. Besonders empfindlich ist eine indirekte Detektion der ESR mittels elektrisch detektierter Elektronenspinresonanz (EDMR). Beide Methoden beruhen auf der Messung des Zeeman-Effektes des lokalisierten Elektrons, d.h. der Aufspaltung seiner Spinzustände unter Einwirkung eines äußeren magnetischen Feldes. Gleichzeitig lassen sich auch Feinstrukturwechselwirkungen innerhalb des Elektronenspinsystems und Hyperfeinwechselwirkungen des Elektronenspins mit in der Nähe befindlichen Kernspins beobachten.

In dieser Arbeit wurden lokalisierte Zustände in drei verschiedenen Materialsystemen untersucht: Ungesättigte Bindungen oder "dangling bonds" (dbs), die typischen intrinsische Defekte in amorphem Germanium (a-Ge), Phosphor-Donatoren, die neuerdings die n-Dotierung von Diamantkristallen ermöglichen, und Manganatome, die als Kandidaten für eine "magnetische Dotierung" von Gruppe-III Nitriden gelten. Die gewonnenen Ergebnisse werden jeweils mit den in der Literatur eingehend untersuchten Referenzsystemen von dbs in amorphem Silizium, Phosphor-Donatoren in kristallinem Silizium und Manganatomen in ferromagnetischem Galliummanganarsenid verglichen.

Die elektronischen Eigenschaften von a-Ge werden insbesondere durch hohe Konzentrationen an dbs beeinträchtigt. Aus der beobachteten Verbreiterung der EDMR-Signale in einer Serie von a-Ge Filmen mit maßgeschneiderten ^{73}Ge-Isotopenkonzentrationen im Bereich von 0.1% bis 95.6% und bei Mikrowellenfrequenzen ν von 0.434 GHz bis 9.35 GHz konnte in dieser Arbeit die Hyperfeinwechselwirkung des elektronischen Spins von dbs mit einer großen Zahl an ^{73}Ge-Kernspins bestimmt werden und daraus der Lokalisationsradius der dbs in a-Ge abgeschätzt werden. In einer kernspinfreien Probe bei 0.434 GHz wurde

eine minimale Linienbreite von nur 2.6 G beobachtet. Es wurde gezeigt, dass die frequenzabhängige Verbreiterung von 4.4 $\nu \times$ G/GHz bei niedrigen Kernspinkonzentrationen durch g-Faktoranisotropie und -unordnung bestimmt wird, und dass bei den untersuchten Defektkonzentrationen eine frequenzunabhängige dipolare Verbreiterung mit ungefähr 1 G zur ESR-Linienbreite beiträgt. In einem weiten Bereich von Kernspinkonzentrationen wird die ESR-Linienbreite durch die statistisch verteilten ^{73}Ge-Kernspins in der Umgebung des Defektatoms bestimmt. Die maximal beobachtete EDMR-Linienbreite von 300 G für eine Probe mit [^{73}Ge] = 95.6% lässt sich auf eine zentrale Fermi-Kontaktwechselwirkung von 29 G $\times$ $g\mu_B$ zurückführen. Das zeigt, dass die 4s-Wellenfunktion des Zentralatoms mit einem Anteil von 3.4% zur Defektwellenfunktion beiträgt. Mit Hilfe eines numerischen Modells konnte der Spin-Lokalisierungsradius der restlichen Spinwellenfunktion auf ca. 3.5 Å festgelegt werden. Folglich ist die Wellenfunktion der Spindichte der dbs in a-Ge deutlich stärker lokalisiert als die Ladungsdichte, deren Lokalisierungsradius durch Transportexperimente in der Literatur zu 11 Å bestimmt wurde.

Diamant läßt sich mit Phosphordonatoren seit einigen Jahren reproduzierbar n-Typ dotieren. Allerdings ist die Ionisierungsenergie dieses Donators unerwartet hoch, was auf mikroskopische Besonderheiten der Spinwellenfunktion des Donatorelektrons in der Nähe der Phosphoratome hindeutet. Zur Charakterisierung der Donatorwellenfunktion wurde ein n-leitfähiger Phosphor-dotierter Diamantfilm mittels EDMR untersucht und die Signale mehrerer elektrisch aktiver Zentren vom Untergrund der Stickstoffzentren im Substrat und der dbs im Bereich der elektrischen Kontakte isoliert. Ähnlich wie Defekte in nicht n-leitfähigen P-dotierten Diamantproben, deren ESR-Signatur zuvor in der Literatur berichtet wurde, zeigte das erste der hier beobachteten Zentren mit $A_{\text{iso}} = 17.6$ G und $A_{\text{aniso}} = 1.8$ G eine viel geringere Spindichte am Phosphoratom, als es für wasserstoffähnliche Donatoren in Diamant zu erwarten wäre. Statt auf einen Effektiv-Masse-Donator deuten diese Hyperfeinparameter eher auf einen phosphorhaltigen Defektkomplex als Ursprung des EDMR-Signals hin. Ein zweites EDMR Signal mit $A_{\text{iso}} = 380$ G und $A_{\text{aniso}} = 15$ G, das vorübergehend unter nicht klar definierten Bedingungen in der gleichen Probe beobachtet wurde, lässt sich dagegen eher mit den Vorhersagen der Effektiv-Masse-Theorie in Einklang bringen. Allerdings zeigt auch dieses Zentrum einen nennenswerten anisotropen Beitrag der Hyperfeinwechselwirkung, der wiederum auf eine signifikante Gitterverzerrung hindeutet. Zum Bau von bipolaren Bauelementen aus Halbleitermaterialien mit großer Bandlücke bieten sich neben rein diamantbasierten Strukturen auch Heterostrukturen aus Diamant und anderen Materialien an. Besonders kritisch für die Funktion eines solchen Bauelements sind Grenzflächendefekte, wie sie im Rahmen dieser Arbeit exemplarisch an einer AlN/Diamant-Heterostruktur untersucht wurden.

Halbleitern mit geeigneten magnetischen Eigenschaften wird ein großes Potential für neuartige "spintronische" Anwendungen prognostiziert. Insbesondere für GaN:Mn wurde aufgrund von Austauschwechselwirkungen der Mn^{2+}-Spins mit Löchern im Valenz-

band Ferromagnetismus bei Raumtemperatur vorhergesagt. Spin-Spin-Wechselwirkungen in GaN:Mn und AlN:Mn mit Mn-Konzentrationen um 10^{20} cm^{-3} wurden in der vorliegenden Arbeit mittels konventioneller ESR untersucht. Die Vorhersage von ferromagnetischen Wechselwirkungen zwischen den Mn^{2+}-Spins ist allerdings auf Grundlage dieser experimentellen Ergebnisse nicht aufrechtzuerhalten. Die beobachtete paramagnetischen Resonanz zeigt eindeutig die zu erwartende Hyperfeinwechselwirkung $A_{\rm iso} = -69\ {\rm G} \times g\mu_B$ der kompensierten substitionellen, d.h. vierfach stickstoffkoordinierten Mn^{2+}-Akzeptoren in GaN:Mn und AlN:Mn. Je nach biaxialer Verspannung der epitaxischen Filme wurden Feinstrukturwechselwirkungen zwischen $-218\ {\rm G}\times g\mu_B$ und $-236\ {\rm G}\times g\mu_B$ in GaN:Mn bzw. $-648\ {\rm G} \times g\mu_B$ in AlN:Mn beobachtet. Diese Werte lassen sich im Rahmen des Superpositionsmodells von Kristallfeldern quantitativ durch kleine Verschiebungen der Mn-Atome um $\delta_{\rm GaN} = 0.085$ Å bzw. $\delta_{\rm AlN} = 0.13$ Å von den idealen Gitterplätzen der Wurtzitstruktur von GaN bzw. AlN erklären. Bei Verkippungen der Kristallachse c gegenüber dem Magnetfeld wurden durch das Wechselspiel von Zeeman- und Feinstrukturwechselwirkung zahlreiche verbotene ESR-Übergänge mit $\Delta m_I > 0$ beobachtet und durch numerische Diagonalisierung der vollständigen Spin-Hamiltonfunktion erklärt. Aus der Intensität der ESR-Signale zeigte sich, dass die Mn-Konzentration in den Schichten die der kompensierten Mn^{2+}-Akteptoren bei weitem übertrifft, solange nicht durch Kodotierung zusätzlich Elektronen in vergleichbarer Menge zur Verfügung gestellt wurden. Diese Beobachtung schließt die gleichzeitige Existenz von Mn^{2+} und Löchern im Valenzband aus und zeigt, dass Mn in nicht kodotiertem GaN hauptsächlich im neutralen Ladungszustand vorliegt. Mit Hilfe optischer Messungen konnte dieser neutrale Zustand mit Absorptionsbanden um 1.5 eV und 1.8 eV korreliert werden. Spektral aufgelöste Photoleitungsmessungen zeigten, dass es sich bei dem Absorptionsprozess oberhalb von 1.8 eV um die direkte optische Ionisation des Mn-Akzeptors handelt. Die entsprechende Ionisationsenergie in AlN:Mn beträgt 2.6 eV. Andererseits ist der Absorptionsprozess bei 1.5 eV einem inneren ${}^5T_2 \rightarrow {}^5E$ Übergang von Mn^{3+} zuzuordnen. Qualitativ können die Unterschiede zwischen den neutralen Mn-Akzeptorzuständen in GaN und GaAs anhand eines einfachen Defektmolekülbildes erklärt werden, in Übereinstimmung mit den Ergebnissen neuerer *ab initio* Rechnungen aus der Literatur. Da sich nach den Ergebnissen dieser optischen Untersuchungen das Akzeptorniveau von Mangan in Gruppe-III Nitriden weit oberhalb der Valenzbandkante befindet, sind im Gegensatz zu GaAs:Mn^{2+} bei Dotierkonzentrationen über 0.1% daher für GaN:Mn^{2+} keine elektrostatischen und magnetischen Kopplungen zwischen Mn-Zuständen und Löchern im Valenzband zu erwarten, und die Vermittlung von Ferromagnetismus über freie Ladungsträger ist in GaN:Mn als sehr unwahrscheinlich anzusehen.

Contents

1 Introduction **1**

2 Localized electronic states **5**

2.1 Bases for orbital wave functions 5

2.1.1 Effective-mass states 6

2.1.2 Molecular wave functions 8

2.2 The spin Hamiltonian 10

2.2.1 Matrix representation 11

2.2.2 Diagonalization procedures 12

2.2.3 Transition intensities 15

3 Spin-spin interactions **17**

3.1 Spin-orbit interaction 17

3.1.1 Effective g-factor 17

3.1.2 Axial anisotropy 18

3.2 Electron-electron interaction 21

3.2.1 Dipolar interaction 22

3.2.2 Exchange interaction 24

3.2.3 Spin polarization 25

3.3 Hyperfine interaction 26

3.3.1 Dipolar interaction 28

3.3.2 Fermi contact interaction 28

3.3.3 Ligand hyperfine interaction 29

4 Detection of electron spin resonance **33**

4.1 Spectrometer components 33

4.2 Resonance Lineshape 35

4.3 Indirect detection methods 37

5 Dangling bonds in amorphous germanium **41**

5.1 Experimental details 42

5.2 EDMR results 45

5.2.1 Isotopically pure a-^{70}Ge . . . 45
5.2.2 a-Ge and a-Ge:H with natural isotope composition . . . 49
5.2.3 ^{73}Ge-enriched samples . . . 51
5.3 Hyperfine interactions with ^{73}Ge . . . 54
5.3.1 Spin Hamiltonian . . . 54
5.3.2 Convolution of multiple hyperfine interactions . . . 58
5.3.3 Analytical lineshape calculations . . . 61
5.3.4 Numerical lineshape simulation . . . 64
5.4 Discussion . . . 71
5.4.1 Line broadening mechanisms . . . 71
5.4.2 Spin polarization . . . 72
5.4.3 Charge localization . . . 74
5.5 Conclusions and outlook . . . 76

6 Shallow donors in diamond 79
6.1 ESR of phosphorus in diamond . . . 80
6.2 EDMR of n-type diamond . . . 82
6.2.1 Bias dependence . . . 83
6.2.2 Anisotropy at high bias voltage . . . 84
6.2.3 Additional signal after illumination . . . 87
6.3 Discussion of the EDMR signals . . . 88
6.3.1 Effective-mass donors in diamond . . . 88
6.3.2 Hyperfine values from the literature . . . 89
6.4 Conclusions . . . 91
6.5 Outlook: Alternatives to n-type diamond . . . 91
6.5.1 Spin-dependent recombination . . . 92
6.5.2 Anisotropy of the EDMR signal . . . 92

7 The $Mn^{3+/2+}$ acceptor level in group III nitrides 97
7.1 Transition-metal states in semiconductors . . . 99
7.2 Growth of GaN:Mn films . . . 107
7.2.1 Elastic recoil detection . . . 109
7.2.2 SQUID measurements . . . 111
7.3 ESR of GaN:Mn^{2+} and AlN:Mn^{2+} . . . 113
7.3.1 Crystal field spin Hamiltonian . . . 115
7.3.2 Spin Hamiltonian analysis with $\vec{B} \parallel c$ . . . 120
7.3.3 Arbitrary orientations . . . 127
7.3.4 Discussion of the ESR parameters . . . 135
7.3.5 Mn^{2+} spin density . . . 142
7.4 Identification of the Mn^{3+} state . . . 144

7.4.1 Optical absorption measurements . . . 146
7.4.2 Tight-binding picture . . . 153
7.5 Outlook: Ferromagnetism in GaN . . . 157
7.5.1 Charge-transfer levels of Cr, Mn, and Fe . . . 158
7.5.2 Prospects for carrier-mediated ferromagnetism . . . 162
7.5.3 Other exchange mechanisms . . . 163
7.6 Conclusions . . . 167

8 Summary **169**

List of publications **173**

Acknowledgements **177**

Chapter 1

Introduction

The manipulation of the electrical properties of bulk semiconductors and semiconductor heterostructures is the basis for most electronic devices. Sophisticated lithography techniques and material purity have been optimized to a degree, which allows precisely controlled electronic landscapes to be constructed, whose functionality is based on doping control and external programming, e.g. via metallic gate electrodes. However, compared to metallic or insulating materials, the wide tunability of semiconductor electrical properties also makes them very sensitive to unintentional impurities and to intrinsic defects. Electron spin resonance (ESR) is a well established technique for the identification and characterization of the localized electronic states formed in the presence of such "point defects" in an otherwise perfectly regular crystal.

Microscopically, the symmetry and extent of a defect wave function is far from being point-like, and its shape and size are directly linked to its electronic and magnetic properties in the host crystal. Theoretical predictions of these properties are still a challenge in many cases. Spin-spin interactions can provide an ideal tool for the experimental investigation of the shape and size of a defect wave function. Particularly useful for this purpose are the hyperfine interactions between an electronic spin and the surrounding nuclear spins. Because of the weakness of these interactions, nuclear spins can hereby be considered as non-perturbing and extremely local probes. Also the much stronger exchange interactions between neighboring electronic spins are known to depend critically on the shape and size of the involved spin wave functions. On the other hand, such spin-spin interactions can be strong enough to dominate material properties even at technologically relevant temperatures. This makes the investigation of spin-spin interactions interesting not only from a fundamental point of view, but also with respect to possible technological applications.

Spin-spin interactions at a variety of point defects are described in this work: intrinsic defects in amorphous germanium, phosphorus for the n-type doping of diamond, and manganese impurities as candidates for magnetic "dopants" in group III nitrides. The symmetry and extent of the investigated defect wave functions in these materials are then

compared to the well-known analogue defects in amorphous silicon, in n-type crystalline silicon, and in dilute magnetic gallium manganese arsenide. The results are critical for the anticipated technological applications in the new material systems.

The dominant point defects in amorphous germanium are “dangling bonds” formed at under-coordinated germanium atoms. These were identified years ago, and can be made electrically inactive to a great extent by hydrogenation. However, little is known microscopically about the shape and size of the electronic wave function of dangling bonds in a-Ge. The first part of this work shows how the hyperfine interaction of dangling bond spins with the large number of surrounding nuclear spins can be extracted from electrically detected magnetic resonance (EDMR) spectra of isotopically engineered amorphous germanium films, even in the presence of spin-orbit and spin-spin interactions. Following this, the hybridization and localization of the dangling bond wave function will be discussed, based on the observed interaction strength and the number of interacting nuclei.

The material properties of silicon are sufficient for the fabrication of most electronic devices. However, other properties are required for devices operating at high temperatures or in particular chemical environments, e.g. within the human body. Electrical doping is still a challenge in many of these materials. In diamond, which is a wide band gap semiconductor with a considerable potential for sensor, UV-LED, and display applications, n-type doping via phosphorus has been achieved only recently. The identification and characterization of the active donor states in diamond is a current challenge for research. The second part of this thesis deals with the localization of the phosphorus bound donor states in diamond, which can be obtained from hyperfine interactions between the electronic and nuclear spins. Particular attention is paid again to the EDMR detection technique, which makes it possible to monitor the hyperfine interactions in epitaxial diamond films.

Today the antiferromagnetic, ferromagnetic, and non-magnetic properties of materials are of similar technological interest as the electronic properties of semiconducting, conducting and insulating materials. In modern data storage devices, external magnetic fields are used to control the magnetization of thin films with otherwise fixed magnetic properties. New materials with tunable magnetic properties have been predicted to offer a breakthrough in the field of “spintronic” devices, similar to the tunability of semiconductor “electronic” devices via doping and gates. Novel applications are anticipated from the combination of both electric and magnetic tunability. The interplay of electronic and magnetic properties has been predicted as being particularly strong in manganese-doped gallium nitride. Detailed structural information is obtained in this thesis from the spin-spin interactions at the negatively charged acceptor state of this impurity. Its neutral acceptor state is found to be invisible to electron spin resonance experiments, and will therefore be discussed based on optical absorption measurements. The observations for both defect states show that the anticipated very strong spin-spin interaction will be im-

possible to achieve in GaN:Mn, as the Mn impurity states are much more localized in gallium nitride than in gallium arsenide.

In the following, the basic concepts in the description of orbital and spin states of defects in semiconductors will be introduced in Chap. 2. The evaluation and interpretation of electron spin resonance spectra will then be discussed in some detail in Sec. 2.2. Typical interaction mechanisms between the spins of several electrons or nuclei, and the influence of the orbital momentum on the observable spin parameters will be introduced in Chap. 3, followed by a summary of the experimental spin resonance techniques used in Chap. 4.

The investigations of dangling bond defects in amorphous germanium will be presented in Chap. 5, those of phosphorus donors in n-type diamond films in Chap. 6, and those on Mn^{2+} and Mn^{3+} gap states in group III nitrides in Chap. 7. Detailed descriptions of the respective materials and the types of point defect wave functions studied will be given in the respective chapters of this work. All results are summarized in Chap. 8.

Chapter 2

Localized electronic states

The experimental observations available from electron spin resonance experiments are mostly related to the spin properties of electronic states, which, however, are directly connected with the orbital properties, e.g. the shape and localization of the electronic wave function. In many cases, these orbital properties are impossible to determine otherwise. The theoretical interpretation of both spin and orbital properties depends on the bases employed for the description of the orbital wave function as well as for the spin. In the following sections, some basic concepts for orbital and spin states of defects in semiconductors will be introduced. The analysis of a spin Hamiltonian will be explained in some detail, which will be important for the interpretation of the experimental data presented later.

2.1 Bases for orbital wave functions

One of the most characteristic properties of defects in a crystalline matrix is their ionization energy with respect to the valence or conduction bands of the host material. The wave functions of "shallow defects" with ionization energies below 100 meV typically extend over many unit cells. These wave functions are clearly distinct from the wave functions of "deep defects" with ionization energies of the order of 1 eV and large parts of their wave function localized in one or two unit cells of the crystalline lattice. The limiting cases of free electrons, i.e. plane waves, which are preferably described in $\vec{k}$-space, and of tightly bound atomic states, which are preferably described in real space, will be discussed briefly in the following sections. Defect states are better approximated from one or the other of these approaches depending on their degree of localization.

Similar to the Bloch formalism for band states, plane waves are used as the favored basis set for the description of shallow defects, as discussed in Sec. 2.1.1. In contrast, deep defects are preferably constructed from atomic or molecular wave functions, which are also used in the tight-binding formalism, as discussed in Sec. 2.1.2. Much more elaborate theoretical models like the pseudopotential method [1] and the local spin density

approximation (LSDA) using the Korringa-Kohn-Rostocker (KKR) method, the Linear Muffin-Tin Orbital (LMTO) method, and the Augmented Plane Wave (APW) method can be used very successfully in modern numerical calculations for defect wave functions.[2]

2.1.1 Effective-mass states

According to Bloch's theorem, a single-particle electron wave function in a crystalline lattice is represented by the product of a plane wave $\exp(i\vec{k}\vec{r})$ with the wave-vector $\vec{k}$ within the first Brillouin zone, and a periodic Bloch function $u_{n,\vec{k}}$ with the band index n

$$\psi_{n,\vec{k}}(\vec{r}) = \exp(i\vec{k}\vec{r}) \cdot u_{n,\vec{k}}(\vec{r}) \quad . \tag{2.1}$$

Insertion of this product function in the Schrödinger equation results in a differential equation for the Bloch functions with an additional term $(\hbar/m_0)\ \vec{k}\cdot\vec{p}$. The solutions for this equation can be expanded in terms of the Bloch functions at high-symmetry points of the Brillouin zone as

$$u_{n,\vec{k}}(\vec{r}) = u_{n,\vec{k}_0}(\vec{r}) + \frac{\hbar}{m_0}\sum_{n'\neq n}\frac{\langle u_{n,\vec{k}_0}|\,\vec{k}\cdot\vec{p}\,|u_{n',\vec{k}_0}\rangle}{E_{n,\vec{k}_0}-E_{n',\vec{k}_0}}\cdot u_{n',\vec{k}_0}(\vec{r}) \quad . \tag{2.2}$$

Typically, the contributions to Eq. (2.2) of those bands with a large energy separation $E_{n,\vec{k}_0} - E_{n',\vec{k}_0}$ can be neglected. Therefore, the dispersion relation of conduction band states of many cubic semiconductors close to $\vec{k}_0 = 0$ is reasonably well described by a 5-band $\vec{k}\cdot\vec{p}$ approximation with

$$E(\vec{k}) = E_{n,\vec{k}_0} + \frac{\hbar^2\vec{k}^2}{2m^*} \quad , \tag{2.3}$$

and the parameters m^* for the effective electron mass and g^* for its effective g-factor

$$\frac{m_0}{m^*} = 1 + \frac{P^2}{E_G} - \frac{P'^2}{E'} \tag{2.4}$$

$$\frac{g^*}{g_0} = 1 - \frac{\Delta_0}{3}\left(\frac{P}{E_G}\right)^2 - \frac{\Delta_0'}{3}\left(\frac{P'}{E'}\right)^2 \quad . \tag{2.5}$$

With the typical value of the matrix element $P^2 = \left|\langle\Gamma_1|\,\vec{k}\cdot\vec{p}\,|\Gamma_4\rangle\right|^2 \times 2/(m_0k^2) \approx 20$ eV between the s-like Γ_1 conduction band, and the p-like Γ_4 valence band, good agreement of the effective parameters predicted from the band gap E_G, the spin-orbit coupling Δ_0, and the corresponding primed parameters P' and Δ_0' of the next higher Γ_4 conduction band with the experimental values for m^* and g^* can be obtained for many materials.[1, 3]

Because the corrections from the valence band are particularly large in narrow band gap semiconductors like Ge, GaAs, or InAs, even influences from the next-higher conduction band are negligible there. In contrast, contributions from these bands are essential for

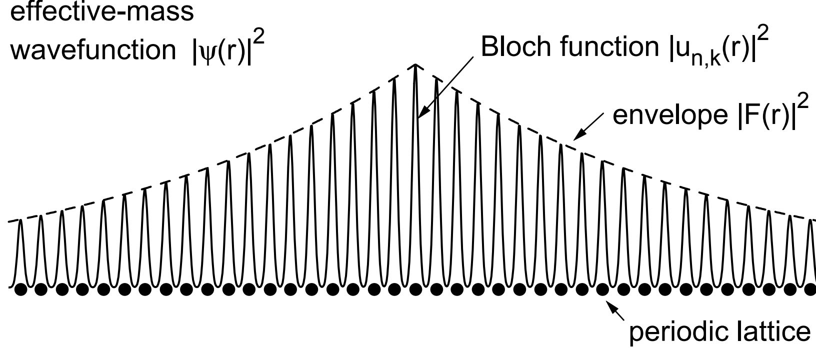

Figure 2.1: A weakly localized state can be described in the effective-mass approximation with the product wave function of a periodic band state $\psi_{n,\vec{k}}$ constructed with the Bloch wave functions $u_{n,\vec{k}}$, and of an hydrogenic envelope function F defined by the screened impurity potential.

a reasonable agreement of $\vec{k}\cdot\vec{p}$ calculations with the experimental parameters in wide band gap semiconductors, e.g. for the g-values of effective-mass donors in wurtzite $Al_{1-x}Ga_xN$ alloys.(4) Typically, the effective-mass approximation for electronic states at the conduction band minimum also holds for shallow donor states, as both types of states undergo very similar spin-orbit interactions (see Sec. 3.1).

The periodic part of the wave function of weakly localized shallow donor or acceptor states can be expressed in conduction and valence band states with few, or even a single orbital momentum $\vec{k}$. In this approximation, a localized wave function

$$\Psi(\vec{r}) = F(\vec{r})\ \exp(i\vec{k}\vec{r}) \cdot u_{n,\vec{k}}(\vec{r}) \tag{2.6}$$

is described by the product of a band state $\psi_{n,\vec{k}}(\vec{r})$ of Eq. (2.1) and a slowly varying envelope function $F(\vec{r})$, as shown in Fig. 2.1. Because of the sixfold conduction band minima, summation over six equivalent $\vec{k}^{(i)}$ and $F^{(i)}(\vec{r})$ is required for the description of effective-mass donors in crystalline silicon.(5, 6) As the periodic crystalline potential of the Schrödinger equation is solved by $\psi_{n,\vec{k}}(\vec{r})$, the remaining differential equation resembles the Schrödinger equation for the hydrogen atom with the electron mass replaced by the effective mass m^*, and the Coulomb potential $V(\vec{r}) = -e^2/(4\pi\varepsilon_0\varepsilon^*|\vec{r}|)$ of the positive core screened by the relative dielectric constant ε^*. Therefore, the wave function $\Psi(\vec{r})$ of Eq. (2.6) and its radius of localization a^* are given approximately by the envelope function

$$F(\vec{r}) = \frac{1}{\sqrt{\pi a^{*3}}} \exp\left(\frac{-|\vec{r}|}{a^*}\right) \qquad \text{with} \tag{2.7}$$

$$a^* = \frac{4\pi\varepsilon_0\varepsilon^*\hbar^2}{m^*e^2} = \varepsilon^*\frac{m_0}{m^*}\cdot a_0 \quad , \tag{2.8}$$

where $a_0 = 0.529$ Å is the Bohr radius of the $1s$ wave function of the hydrogen atom. Accordingly, the ionization energy E^* from the localized state $\Psi(\vec{r})$ to the band $\psi_{n,\vec{k}}(\vec{r})$

is given by

$$E^* = -\frac{e^2}{4\pi\varepsilon_0\varepsilon^* \cdot 2a^*} = -\frac{m*}{m_0}\left(\frac{1}{\varepsilon^*}\right)^2 \cdot E_0 \quad , \tag{2.9}$$

where $E_0 = 13.6$ eV is the ionization energy of the $1s$ ground state of the hydrogen atom. As an example, the ground state of donors in Si is a superposition of plane waves of the six conduction band minima at $\vec{k}_0 \approx 0.85\ \vec{k}_{\max}$ along the $\langle 001 \rangle$ directions.(5, 7) With $m^* = \sqrt[3]{m_l \cdot m_t^2} = \sqrt[3]{0.98 \cdot 0.19^2}\ m_0$ and $\varepsilon^* = 11.9$, one would obtain $E^* = 32$ meV for the effective-mass donors in Si, which is not too far from the observed values between 43-54 meV. However, the wave function amplitudes predicted at the donor site in this approximation(5) are still too small by at least a factor of five compared to the values extracted from the experimental hyperfine constants. Therefore corrections for the non-spherical conduction band minima, the unscreened wave function of the central donor cell, and a complex envelope function sampled throughout the Brillouin zone must be taken into account for a more realistic donor wave function in the case of silicon,(5, 6) as well as for shallow donors in diamond, as discussed in Chap. 6.

2.1.2 Molecular wave functions

As suggested in Ref. 5, a first approximation to a Bloch function can be constructed from the atomic valence states obtained via Hartree-Fock calculations. In orthogonalized form, these quasi-atomic orbitals are known as Löwdin orbitals.(1) Formally, such an effective-mass approach is similar to band-structure calculations based on a tight-binding model. However, the interpretations of both terms in Eq. (2.1) as wave function and envelope function are exchanged. In the tight-binding approach, spatially localized atomic states $\phi(\vec{r})$ are used as the basis for the electronic wave functions instead of the plane-wave basis for free electrons, localized in $\vec{k}$-space. The $\vec{k}$-periodic exponential function now appears in form of coefficients for the atomic wave functions, and the valence and conduction bands of a solid now are formed from the bonding and antibonding $\sigma_{s,p,d}$ orbitals resulting from the overlap of the relevant atomic states. As an example, the wave functions $\psi_k(\vec{r})$ and the energy dispersion relation $E(\vec{k})$ for the hypothetical textbook-example of a periodic linear chain of atoms with spacing a is given by

$$\psi = \sum_n \exp(ikna) \cdot \phi(r - na) \tag{2.10}$$

$$E(k) = E_0 - E_\alpha - 2E_\gamma \cdot \cos(ka) \quad , \tag{2.11}$$

with the parameters $E_\alpha = \int \phi^*(r)\, \Delta U(r)\, \phi(r)\, dV$ and $E_\gamma = \int \phi^*(r + a)\, \Delta U(r)\, \phi(r)\, dV$ defined via the atomic states $\phi(r)$ and the difference potential $\Delta U(r)$ of the atomic and crystalline Hamiltonians.(8) The curvature at $k = 0$ is upward for the s-like states with $E_\gamma > 0$ at the bottom of the conduction band, and downward for the p-like states with $E_\gamma < 0$ at the top of the valence band.

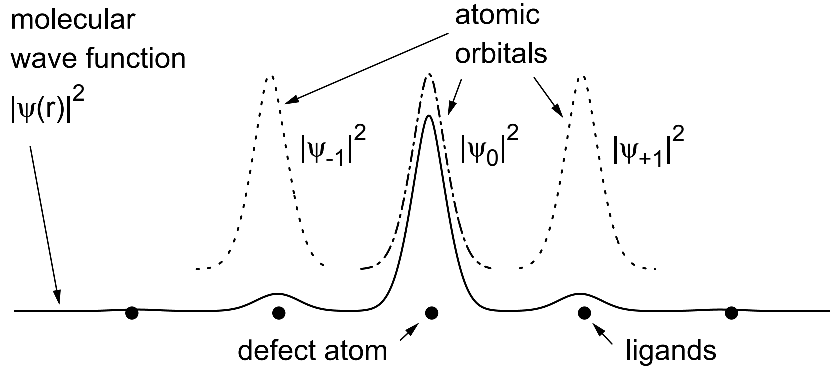

Figure 2.2: A strongly localized defect state can be described as a superposition of few atomic orbitals, similar to a molecular state. Therefore, its properties are mostly determined by the size and symmetry of the involved atomic orbitals instead of the properties of the surrounding lattice. Such a defect state is best characterized by the few non-vanishing wave function amplitudes at the ligand atoms instead of the envelope function shown in Fig. 2.1.

The lattice periodicity has only a minor influence on the shape of a strongly localized defect state, as shown in Fig. 2.2. Thus, Bloch functions from a large number of bands and with a large range of $\vec{k}$-vectors would be required to describe such a defect wave function. It is much more convenient to construct the wave functions directly in real space from atomic wave functions ϕ centered at a small number of atoms around a defect site, similar to the method of linear combinations of atomic orbitals (LCAO) of molecular physics and chemistry. As a first approximation neglecting all wave function overlap terms, the so-called Hückl molecular orbital (HMO) approach is derived from Eq. (2.10) by replacing the periodic coefficient function with a characteristic set of coefficients for the projections of the defect wave function onto the atomic basis states.[9] Assuming that the defect wave function can be separated into the product of this spatial wave function and the spin, these coefficients can be mapped out via hyperfine interactions, as described in Sec. 3.3.3. Examples of strongly localized defect states that have been described successfully as a superpositions of a few atomic orbitals are the P1 center of nitrogen impurities in diamond,[10, 11] discussed in detail in Sec. 3.3.3, and intrinsic defects like the negatively charged vacancy in Si (V_{Si}^-).[12]

The electronic states of a transition metal ion in a solid represent complex many-electron systems. In many cases, it is sufficient to treat the influence of the electronic orbitals at the nearest neighbors via crystal field theory in a point charge approximation. In certain cases, however, covalent effects and hybridization with the neighbor atoms must be taken into account explicitly via ligand field theory. Different single-particle wave functions and energies must be considered in general for each charge state of the same impurity or defect molecule.[13]

2.2 The spin Hamiltonian

The analysis of the complete Hamiltonian of defect states in a semiconductor matrix is very complex. For a description of the spin properties only, this difficulty is circumvented by the concept of a spin Hamiltonian, which explicitly includes only spin states and operators, e.g.

$$\mathcal{H} = \mu_B \vec{B} \hat{g} \vec{\mathcal{S}} + \vec{\mathcal{S}} \hat{D} \vec{\mathcal{S}} + \vec{\mathcal{S}} \hat{A} \vec{\mathcal{I}} \quad , \tag{2.12}$$

with the Bohr magneton $\mu_B = 9.274015 \times 10^{-28}$ J/G, the magnetic field $\vec{B}$, and the electronic and nuclear spin operators $\vec{\mathcal{S}}$ and $\vec{\mathcal{I}}$. The parameters $\hat{g}$, $\hat{D}$, and $\hat{A}$ are in general spatially anisotropic matrices with at least the symmetry properties of the orbital defect wave function. By convention, $\hat{g}$ represents the Zeeman interaction of the electronic spin $\vec{\mathcal{S}}$ with the magnetic field, $\hat{D}$ the fine structure interaction, and $\hat{A}$ the hyperfine interaction between the electronic and a nuclear spin.

To separate the spin and real space operators in such a way, it must be assumed that a defect ground state wave function can be factorized as the product of a spin state and some non-degenerate many-particle orbital wave function. The time-independent Schrödinger-equation

$$\mathcal{H} \left|\psi\right\rangle = E_\psi \left|\psi\right\rangle \quad , \tag{2.13}$$

for the spin states $|\psi\rangle$ and their eigen-energies E_ψ can often be solved analytically. In more complex spin systems, they must be calculated numerically or via perturbation theory. The orbital parts of the wave function, and spatial operators like crystal field and spin-orbit interaction are integrated out and appear only implicitly in the spin Hamiltonian via effective numerical parameters such as the effective g-tensor, whose deviation from the free electron's g-factor $g_0 = 2.002319$ stems from spin-orbit coupling $\mathcal{H}_{so} = \lambda \vec{\mathcal{L}} \vec{\mathcal{S}}$ treated by second order perturbation theory (Sec. 3.1).[9] The form of the spin Hamiltonian is found either ad hoc, i.e. phenomenologically, motivated by symmetry considerations, or by a perturbative expansion of the full Hamiltonian.[14] Not only effective parameters, but even "fictive spins" are sometimes considered in an "effective spin Hamiltonian", in order to reflect the ground state degeneracy correctly.[13, 15] In these cases, it is more appropriate to use the more general term "electron paramagnetic resonance" (EPR) spectroscopy instead of ESR, which implies the presence of "real" spins. The energy scale of those states attributed to the ground state manifold is hereby given by the microwave energy employed in the ESR experiment, which is usually much smaller than the energy separation from excited electronic states.

At this point, it seems as if most of the information about the quantum-mechanical system is lost during the reduction of the full Hamiltonian to the spin properties. However, by parameterizing the observable properties of the spin system, the remaining spin Hamiltonian provides a valuable language for the interpretation of experimental ESR data. Furthermore, the actual form and symmetry of the spin Hamiltonian alone often

gives important clues for the identification and characterization of the spin state under observation. Later, the tabulated parameters might eventually be interpreted via elaborate theoretical models for the complete quantum-mechanical ground state wave functions.(2, 16)

A successful interpretation of ESR data at first requires the knowledge of the relation of the spin Hamiltonian parameters to experimentally observable resonance fields and intensities. After an introduction to the basic steps in defining and solving a spin Hamiltonian in Sec. 2.2.1 to 2.2.3, the most relevant interaction terms of spin Hamiltonians will be discussed separately in Sec. 3.1 to 3.3.

2.2.1 Matrix representation

Spin operators $\vec{S}$, which are used in various combinations to form the spin Hamiltonian $\mathcal{H}$, have the general quantum-mechanical properties of an angular momentum(17)

$$\vec{\mathcal{S}}^2 \left|m\right\rangle = S(S+1)\left|m\right\rangle \tag{2.14}$$

$$\mathcal{S}_z \left|m\right\rangle = m\left|m\right\rangle \tag{2.15}$$

$$\mathcal{S}_\pm \left|m\right\rangle = (\mathcal{S}_x \pm i\mathcal{S}_y)\left|m\right\rangle = \sqrt{S(S+1)-m(m\pm 1)}\left|m\pm 1\right\rangle \quad . \tag{2.16}$$

These equations are valid for spin $S = 1/2$ electrons as well as for many-electron systems with higher values of S. A set of basis vectors for the $2S+1$-dimensional spin space is defined by unit vectors for the orthonormal states $|m\rangle$ with the eigen-values $m = -S, \ldots, S$ of the operator $\mathcal{S}_z$. The spin operators $\mathcal{S}_{x,y,z}$ take the form of matrices with dimension $(2S+1)\times(2S+1)$. For a spin-$\frac{1}{2}$ system, these are the well-known Pauli matrices, which may be combined in a vector notation of operators to $\vec{\mathcal{S}} = (\mathcal{S}_x, \mathcal{S}_y, \mathcal{S}_z)$ to describe the anisotropic properties of spins. The matrix forms of the spin operators for all higher values of S are defined by Eqs. (2.14) to (2.16). In short form, all non-zero matrix elements $\langle n|\,\mathcal{S}_{x,y,z}\,|m\rangle$ of the operators $\mathcal{S}_{x,y,z}$ can be summarized as

$$\langle n|\,\mathcal{S}_x\,|m\rangle = \delta_{n,m\pm1}\ \tfrac{1}{2}\ \sqrt{S(S+1)-m(m\pm1)} \tag{2.17}$$

$$\langle n|\,\mathcal{S}_y\,|m\rangle = \mp\,\delta_{n,m\pm1}\ \tfrac{i}{2}\ \sqrt{S(S+1)-m(m\pm1)} \tag{2.18}$$

$$\langle n|\,\mathcal{S}_z\,|m\rangle = \delta_{m,n}\ \ m \quad . \tag{2.19}$$

With a spin Hamiltonian built from linear combinations of such matrix operators, the Schrödinger equation becomes a simple matrix equation, whose eigen-values can be calculated from the characteristic polynomial $\det(\mathcal{H} - \mathbf{1}E_i) = 0$, where $\mathbf{1}$ is the unity matrix, and $E_i(\vec{B})$ is one of the eigen-values of the matrix equation. The corresponding eigen-vector $|\psi_i\rangle$ defines the spin eigen-state for E_i as a linear combination $|\psi_i\rangle = \sum_m \alpha_{im}\,|m\rangle$ of the pure basis vectors of $\mathcal{S}_z$. These basis vectors $|m\rangle$ of $\mathcal{S}_z$ are usually the eigen-states

of the spin Hamiltonian $\mathcal{H}$ in the limit of very high magnetic fields along the z-axis, where all other perturbations can be neglected.

A system of several spins, e.g. one electronic spin S and one nuclear spin I requires a total of $(2S+1)\otimes(2I+1)$ orthogonal eigen-vectors. The orthonormal basis vectors $|m_s, m_i\rangle$ of the product space may again be organized as unit vectors, now with a combined index (m_s, m_i), which takes all values $(-S,-I), (-S,-I+1), \ldots, (S, I)$. The matrix elements $\langle n_s, n_i|\,\mathcal{S}_{x,y,z}, \mathcal{I}_{x,y,z}\,|m_s, m_i\rangle$ of the electronic and nuclear spin operators are defined according to Eqs. (2.17) to (2.19) also in this product space. The operators $\mathcal{S}_{x,y,z}$ leave the nuclear spin states unaffected and are represented by the unity matrix elements δ_{n_i,m_i} for the nuclear spin, and vice versa $\mathcal{I}_{x,y,z}$ leave the electronic spin states unaffected and are represented by the unity matrix elements δ_{n_s,m_s} for the electronic spin, i.e.

$$\langle n_s, n_i|\,\mathcal{S}_{x,y,z}\,|m_s, m_i\rangle = \delta_{n_i,m_i}\langle n_s|\,\mathcal{S}_{x,y,z}\,|m_s\rangle \quad (2.20)$$

$$\langle n_s, n_i|\,\mathcal{I}_{x,y,z}\,|m_s, m_i\rangle = \delta_{n_s,m_s}\langle n_i|\,\mathcal{I}_{x,y,z}\,|m_i\rangle \quad (2.21)$$

with the operators on the right-hand side as defined in Eqs. (2.17) to (2.19).

2.2.2 Diagonalization procedures

The spin Hamiltonian matrix needs to be diagonalized in order to obtain its eigen-energies E_i and eigen-vectors $|\psi_i\rangle$.[18] In cases where it is not possible to solve the matrix Schrödinger equation Eq. (2.13) analytically, approximate solutions from perturbation theory, or exact numerical solutions for one set of matrix elements at a time must be obtained. These calculations are somewhat simplified, if the magnetic field is oriented along the z-axis of the spin Hamiltonian, as typically the Zeeman term dominates the eigen-energies of the spin. For other orientations of the magnetic field, this can be achieved by a rotation of the coordinate system of the spin operators $\vec{\mathcal{S}}' = \hat{R}\vec{\mathcal{S}}$.[18] In the new coordinate system, the other possible interactions then introduce only small off-diagonal elements to the spin Hamiltonian.

As an example, which can be solved analytically by inspection, consider the spin Hamiltonian

$$\mathcal{H} = \mu_B \vec{B} g \vec{\mathcal{S}} + \vec{\mathcal{S}} A \vec{\mathcal{I}} = \mu_B B g \mathcal{S}_z + A(\mathcal{S}_x\mathcal{I}_x + \mathcal{S}_y\mathcal{I}_y + S_z I_z) \quad (2.22)$$

with the external magnetic field $\vec{B} = (0, 0, B)$ along the z-direction, the isotropic g-factor $\hat{g} = \mathbf{1}\ g$, and the isotropic hyperfine interaction $\hat{A} = \mathbf{1}\ A$ for $S = \frac{1}{2}$ and $I = \frac{1}{2}$. The basis vectors $|m_s, m_i\rangle$ of the 4-dimensional product basis of S_z and I_z in this example are

$$|\tfrac{1}{2}, \tfrac{1}{2}\rangle = \begin{pmatrix}1\\0\\0\\0\end{pmatrix}; \quad |\tfrac{1}{2}, -\tfrac{1}{2}\rangle = \begin{pmatrix}0\\1\\0\\0\end{pmatrix}; \quad |-\tfrac{1}{2}, \tfrac{1}{2}\rangle = \begin{pmatrix}0\\0\\1\\0\end{pmatrix}; \quad |-\tfrac{1}{2}, -\tfrac{1}{2}\rangle = \begin{pmatrix}0\\0\\0\\1\end{pmatrix}. \quad (2.23)$$

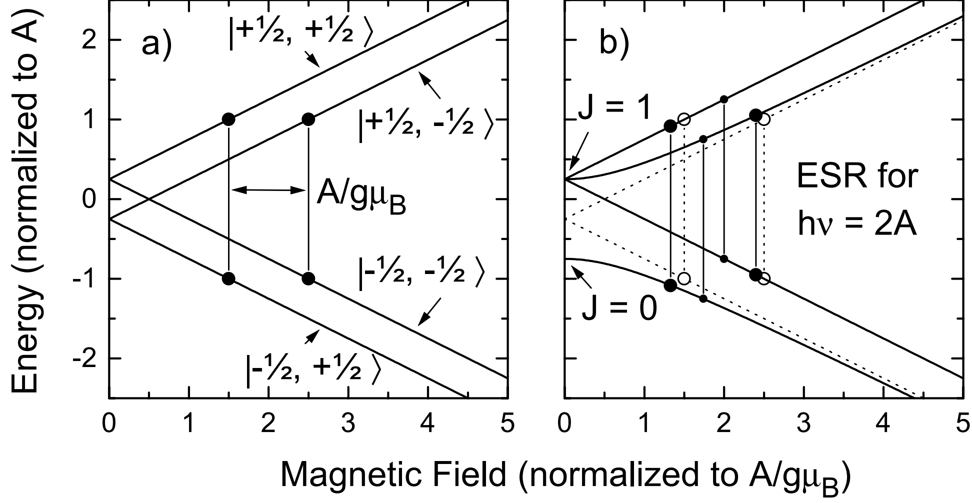

Figure 2.3: Breit-Rabi diagrams (a) of the first-order solutions and (b) of the exact solutions of the spin Hamiltonian of Eq. (2.22) with the electronic spin $S = 1/2$, the nuclear spin $I = 1/2$, and the hyperfine interaction A. For better comparison, the first-order solutions are included in (b) with dashed lines. The energy levels are labelled according to the basis states $|m_s, m_i\rangle$, which are eigen-states of $\mathcal{H}$ at $\mu_B Bg \gg A$. For $\mu_B Bg \ll A$, I tends to be coupled with S to an effective angular momentum $J = S - I, \ldots, S + I$. The vertical lines indicate the two strongly allowed ESR transitions for a microwave energy $h\nu = 2A$. In (b), also the weakly allowed transitions $|\pm\frac{1}{2}, \mp\frac{1}{2}\rangle \leftrightarrow |\mp\frac{1}{2}, \pm\frac{1}{2}\rangle$ are indicated.

The nuclear Zeeman interaction has been neglected in the spin Hamiltonian of Eq. (2.22), but could be easily included analogous to the electronic Zeeman interaction. The matrix form of this spin Hamiltonian is given by

$$\mathcal{H} = \begin{pmatrix} +\frac{\mu_B Bg}{2} + \frac{A}{4} & 0 & 0 & 0 \\ 0 & +\frac{\mu_B Bg}{2} - \frac{A}{4} & \frac{A}{2} & 0 \\ 0 & \frac{A}{2} & -\frac{\mu_B Bg}{2} - \frac{A}{4} & 0 \\ 0 & 0 & 0 & -\frac{\mu_B Bg}{2} + \frac{A}{4} \end{pmatrix} . \qquad (2.24)$$

The off-diagonal elements $\frac{A}{2} \ll \frac{\mu_B Bg}{2}$ can be neglected for small hyperfine couplings compared to the Zeeman interaction. In this case, $\mathcal{H}$ is already approximately diagonal, which means that the diagonal elements of $\mathcal{H}$ and the $|m_s, m_i\rangle$ basis vectors of Eq. (2.23) are a first-order approximation to the eigen-energies and eigen-vectors of the system. This regime, in which both S and I are quantized along the external magnetic field, is called the *Back-Goudsmith* regime.[13] These first-order eigen-energies are shown as a function of B in the energy diagram of Fig. 2.3a.

According to the dipole selection rules, the allowed ESR transitions are those with $|+\frac{1}{2}, \pm\frac{1}{2}\rangle \leftrightarrow |-\frac{1}{2}, \pm\frac{1}{2}\rangle$ with $\Delta m_s = 1$ and $\Delta m_i = 0$. For a given transition energy $\Delta E = h\nu$, these two transitions appear at the magnetic fields $B = (h\nu \pm \frac{A}{2})/\mu g$ in the first-order approximation. With the characteristic polynomial of the inner 2×2 Block

Matrix, the exact energy eigen-values $E_1, \dots E_4$ can be calculated analytically without approximations over the complete magnetic field range

$$E_{1,4} = +\frac{1}{4}A \pm \frac{1}{2}\mu_B B g \quad (2.25)$$

$$E_{2,3} = -\frac{1}{4}A \pm \frac{1}{2}\sqrt{(\mu_B B g)^2 + A^2} \quad . \quad (2.26)$$

The characteristic anti-crossing between the $|\pm\frac{1}{2}, \mp\frac{1}{2}\rangle$ levels for small external fields is shown in Fig. 2.3b. In the low-field regime, the eigen-vectors $|E_{2,3}\rangle$ are symmetric and antisymmetric combinations of the $|\frac{1}{2}, -\frac{1}{2}\rangle$ and $|-\frac{1}{2}, \frac{1}{2}\rangle$ basis vectors. As a consequence, the transitions $|+\frac{1}{2}, \pm\frac{1}{2}\rangle \leftrightarrow |-\frac{1}{2}, \mp\frac{1}{2}\rangle$ are not completely "forbidden" in the low-field regime, as indicated with the smaller dots in Fig. 2.3b. Physically, the system is then best described via a coupled angular momentum $J = S - I, \dots, S + I$ for $\mu_B B g \ll A$. For $A > 0$, the $J = 0$ singlet state with opposite nuclear and electronic spin orientation has lower energy than the "ferromagnetically" coupled $J = 1$ triplet state.

The analytical treatment of a more complex spin Hamiltonian often requires approximations by perturbation theory. For a weakly perturbed spin Hamiltonian $\mathcal{H} = \mathcal{H}_0 + \lambda\mathcal{H}_1$ with non-degenerate and diagonal $\mathcal{H}_0$, the Schrödinger equation can be expanded in terms of the basis vectors $|m\rangle^{(0)}$ of $\mathcal{H}_0$. The unknown spin states $|\psi\rangle$ then take the form[9]

$$|\psi\rangle = |m\rangle^{(0)} + \lambda\,|\psi\rangle^{(1)} + \lambda^2\,|\psi\rangle^{(2)} + \dots \quad (2.27)$$

$$E_\psi = E_m^{(0)} + \lambda E_\psi^{(1)} + \lambda^2 E_\psi^{(2)} + \dots \quad . \quad (2.28)$$

With these expansions, the Schrödinger equation of the perturbed Hamiltonian now can be solved for $|\psi\rangle^{(i)}$ and $E_\psi^{(i)}$ for each order of λ^i separately. The first and second order corrections are[9]

$$E_\psi^{(1)} = {}^{(0)}\langle m|\,\mathcal{H}_1\,|m\rangle^{(0)} \quad (2.29)$$

$$|\psi\rangle^{(1)} = \sum_{n\neq m} \frac{{}^{(0)}\langle m|\,\mathcal{H}_1\,|n\rangle^{(0)}}{E_m^{(0)} - E_n^{(0)}}\,|n\rangle^{(0)} \quad (2.30)$$

$$E_\psi^{(2)} = \sum_{n\neq m} \frac{{}^{(0)}\langle m|\,\mathcal{H}_1\,|n\rangle^{(0)}\ {}^{(0)}\langle n|\,\mathcal{H}_1\,|m\rangle^{(0)}}{E_m^{(0)} - E_n^{(0)}} \quad (2.31)$$

$$|\psi\rangle^{(2)} = \sum_{k\neq m}\left[\sum_{n\neq m} \frac{{}^{(0)}\langle k|\,\mathcal{H}_1\,|n\rangle^{(0)}\ {}^{(0)}\langle n|\,\mathcal{H}_1\,|m\rangle^{(0)}}{(E_m^{(0)} - E_k^{(0)})(E_m^{(0)} - E_n^{(0)})} - \quad (2.32)\right.$$

$$\left.\frac{{}^{(0)}\langle m|\,\mathcal{H}_1\,|m\rangle^{(0)}\ {}^{(0)}\langle k|\,\mathcal{H}_1\,|m\rangle^{(0)}}{(E_m^{(0)} - E_k^{(0)})^2}\right]|k\rangle^{(0)} - \quad (2.33)$$

$$\frac{1}{2}\sum_{k\neq m} \frac{{}^{(0)}\langle k|\,\mathcal{H}_1\,|m\rangle^{(0)}\ {}^{(0)}\langle m|\,\mathcal{H}_1\,|k\rangle^{(0)}}{(E_m^{(0)} - E_k^{(0)})^2}\,|m\rangle^{(0)} \quad . \quad (2.34)$$

As the matrix elements ${}^{(0)}\langle m|\,\mathcal{H}_1\,|n\rangle^{(0)}$ of the perturbing spin Hamiltonian are simple linear combinations of the spin operator matrix elements of Eq. (2.14)-(2.16), no integration is required to evaluate these energies.

For the spin Hamiltonian of Eq. (2.22), the first- and second-order corrections to the eigen-energies, and the corresponding corrections to the eigen-vectors are by inspection

$$\begin{array}{ll} E^{(1)}_{\pm\frac{1}{2},\mp\frac{1}{2}} = 0, & |\pm\tfrac{1}{2},\mp\tfrac{1}{2}\rangle^{(1)} = \pm\,\frac{A}{2g\mu_B B}\;|\mp\tfrac{1}{2},\pm\tfrac{1}{2}\rangle^{(0)} \\ E^{(2)}_{\pm\frac{1}{2},\mp\frac{1}{2}} = \pm\frac{A^2}{4g\mu_B B}, & |\pm\tfrac{1}{2},\mp\tfrac{1}{2}\rangle^{(2)} = -\tfrac{1}{2}(\frac{A}{2g\mu_B B})^2\;|\pm\tfrac{1}{2},\mp\tfrac{1}{2}\rangle^{(0)} \quad . \end{array} \tag{2.35}$$

2.2.3 Transition intensities

Without doubt, such a mixing of levels will also affect the transition probabilities between two spin states $|\psi_1\rangle$ and $|\psi_2\rangle$. Usually ESR is induced by linearly polarized electromagnetic waves, oriented perpendicular to the static magnetic field. These enter the time-dependent Schrödinger equation via an oscillating magnetic field B_1, in the following assumed to be oriented along the y-direction

$$i\hbar\frac{\partial}{\partial t}\;|\psi\rangle = [\mathcal{H} + 2g\mu_B B_1 \mathcal{S}_y \sin(\omega t)]\;|\psi\rangle \quad . \tag{2.36}$$

According to Fermi's golden rule, the first-order transition rate $r_{i\leftrightarrow j}$ under these conditions is[13, 18, 19]

$$r_{i\leftrightarrow j} = \frac{y(\omega)}{4\hbar^2} g^2 \mu_B^2 B_1^2 |\langle E_i|\,\mathcal{S}_y\,|E_j\rangle|^2 \tag{2.37}$$

with the normalized lineshape function $y(\omega)$. Considering $\mathcal{S}_y = -i(\mathcal{S}_+ + \mathcal{S}_-)$ from Eq. (2.18), this equation contains the well-known dipole selection rules $\Delta m = 1$ for the pure spin states $|m\rangle$. The non-zero transition matrix elements

$$|\langle m|\,\mathcal{S}_y\,|m\pm 1\rangle|^2 = S(S+1) - m(m\pm 1) \tag{2.38}$$

are e.g. $|\langle\frac{1}{2}|\,\mathcal{S}_y\,|-\frac{1}{2}\rangle|^2 = 1$ for $S = \frac{1}{2}$, and $|\langle m|\,\mathcal{S}_y\,|m\pm 1\rangle|^2 = 5$, 8, 9, 8, and 5 for the five allowed transitions of a system with $S = \frac{5}{2}$.

The lineshape function $y(\omega)$ for a spin system with $S = 1/2$ can be obtained conveniently from the Bloch equations describing the dynamics of a classical magnetization vector $\vec{M} = \frac{1}{V}\sum_i \langle\psi_i|\,g\mu_B\vec{\mathcal{S}}\,|\psi_i\rangle$ with the sample volume V due to an ensemble of spins

$$\frac{dM_x}{dt} = \frac{g\mu_B}{\hbar}\,(M_y B_0 - 2M_z B_1 \sin\omega t) - \frac{M_x}{T_2} \tag{2.39}$$

$$\frac{dM_y}{dt} = -\frac{g\mu_B}{\hbar}\,M_x B_0 - \frac{M_y}{T_2} \tag{2.40}$$

$$\frac{dM_z}{dt} = \frac{g\mu_B}{\hbar}\,2M_x B_1 \sin\omega t - \frac{M_z - M_0}{T_1} \quad . \tag{2.41}$$

The longitudinal and transverse relaxation times T_1 and T_2 are usually named spin-lattice relaxation time and spin-spin relaxation time, respectively, without further specification of the microscopic relaxation process. The magnetization at thermal equilibrium is

$$M_0 = \frac{g\mu_B}{2}(N_\uparrow - N_\uparrow) = \tfrac{1}{2}Ng\mu_B \cdot \tanh\left(\frac{g\mu_B B}{2k_B T}\right) \approx N\frac{g^2\mu_B^2 B}{4k_B T} \tag{2.42}$$

for an ensemble of spins with a total spin density N and the spin densities $N_\uparrow$ and $N_\downarrow$ in the upper and lower Zeeman levels separated by the energy distance $g\mu_B B$. This magnetization is tilted by the circularly polarized component of the microwave magnetic field B_1, which is constant in a coordinate frame rotating at the incident microwave frequency. The other circularly polarized component is oscillating rapidly in the coordinate frame of the magnetization vector, and therefore averages to zero. In this coordinate system, the steady-state solutions of the Bloch equations are

$$M'_\perp = M_0 \frac{-(g\mu_B B_1/\hbar)\ (\omega_{\mathrm{res}} - \omega)\ T_2^2}{1 + (\omega_{\mathrm{res}} - \omega)^2\ T_2^2 + (g\mu_B B_1/\hbar)^2\ T_1 T_2} \tag{2.43}$$

$$M''_\perp = M_0 \frac{(g\mu_B B_1/\hbar)\ T_2}{1 + (\omega_{\mathrm{res}} - \omega)^2\ T_2^2 + (g\mu_B B_1/\hbar)^2\ T_1 T_2} \tag{2.44}$$

$$M_z = M_0 \frac{1 + (\omega_{\mathrm{res}} - \omega)^2\ T_2^2}{1 + (\omega_{\mathrm{res}} - \omega)^2\ T_2^2 + (g\mu_B B_1/\hbar)^2\ T_1 T_2}\quad , \tag{2.45}$$

with the dynamic in-phase and out-of phase magnetization $M'_\perp, M''_\perp$ representing the dispersion and absorption components of the magnetic radiation. Usually, the out-of-phase absorption is recorded in ESR measurements under "slow adiabatic passage" conditions, i.e. with B_0 going in and out of resonance slowly compared to T_1 and T_2. The lineshape function $y(\omega) \propto M''_\perp$ is then a Lorentzian function with the homogeneous full width at half maximum $\Delta\omega = 2/T_2$ and the ESR amplitude $y(\omega_{\mathrm{res}}) \propto M''_{\perp\mathrm{res}} \propto M_0 B_1$, as long as $(g\mu_B B_1/\hbar)^2 T_1 T_2 \ll 1$ is fulfilled. At higher microwave fields B_1, the population difference $(N_\uparrow - N_\downarrow)$ is eventually reduced proportional to $|\vec{M}| \propto B_1^{-2}$, and the ESR signal saturates and decreases with $y(\omega_{\mathrm{res}}) \propto M''_{\perp\mathrm{res}} \propto M_0/B_1$.

Chapter 3

Spin-spin interactions

In the following sections, the spin interaction mechanisms at point defects in semiconductors relevant for this thesis are introduced. After a short review of spin-orbit interactions, the form and interpretation of the isotropic and anisotropic interactions between several electronic spins, and the interactions between an electronic spin with several nuclear spins are discussed in detail, with special focus on the use of the spin Hamiltonian parameters to describe the wave functions of point defects in semiconductors.

3.1 Spin-orbit interaction

The spin Hamiltonian includes orbital momentum effects only in parameterized form. For a known non-degenerate orbital ground state, these parameters can be calculated via second and higher order perturbation theory. Obviously, a state without degeneracy is also free of orbital degeneracy and of orbital momentum L. This turns out to be the case for almost all localized states in solids, where the orbitally degenerate wave functions of isolated atoms are split into multiple states because of the interaction with the crystal field, or because of Jahn-Teller distortion.[13, 15] Such a splitting results in a non-degenerate crystalline wave function $\psi(\vec{r})$ without a good quantum number L and the expectation value $\langle\psi(\vec{r})| \vec{\mathcal{L}} |\psi(\vec{r})\rangle = 0$. This consequence of the crystal field is referred to in the literature as the *quenching* of orbital momentum.[9, 20]

Because of time-reversal symmetry, pairs of spin states of any odd-electron system must form undistorted doublets in the absence of magnetic fields. These are called Kramers doublets,[19] and can be considered as having an effective spin $S' = \frac{1}{2}$.

3.1.1 Effective g-factor

Although the orbital angular momentum and the influences of excited states are suppressed as first order perturbations, they affect the ground state spin via spin-orbit inter-

action in second order perturbation theory

$$\tilde{\mathcal{H}}_{so} = \lambda \vec{\mathcal{L}} \vec{\mathcal{S}} \quad . \tag{3.1}$$

The spin-orbit coupling constant λ increases approximately as the second power of the atomic charge Z for neutral atoms (or as Z^4 for hydrogenic states[9]), so that e.g. $\lambda_{\text{Ge}} \approx 7 \times \lambda_{\text{Si}}$. Treating spin-orbit coupling and the Zeeman interaction

$$\tilde{\mathcal{H}}_z = -\vec{B}\vec{\mu} = \mu_B \vec{B}(\vec{\mathcal{L}} + g_0 \vec{\mathcal{S}}) \tag{3.2}$$

as small perturbations of the full Hamiltonian with the unperturbed eigen-states $|\psi_n\rangle^{(0)}$, the matrix elements of the spin Hamiltonian can be obtained by integrating out only the orbital components of the ground state energy $E_0^{(2)}$ in second order perturbation theory. The matrix elements of the spin operators are not integrated, but rearranged and summarized in short form with the help of the $\hat{\Lambda}$-matrix[9]

$$\hat{\Lambda}_{ij} = -\sum_{n \neq 0} \frac{\langle \psi_0 | \mathcal{L}_i | \psi_n \rangle \langle \psi_n | \mathcal{L}_j | \psi_0 \rangle}{E_n - E_0} \quad , \tag{3.3}$$

to obtain the spin-Hamiltonian

$$\mathcal{H}_z = \mu_B^2 \vec{B} \hat{\Lambda} \vec{B} + \mu_B \vec{B} \underbrace{(g_0 \mathbf{1} + 2\lambda \hat{\Lambda})}_{\hat{g}_{\text{eff}}} \vec{\mathcal{S}} + \vec{\mathcal{S}} \underbrace{\lambda^2 \hat{\Lambda}}_{\hat{D}} \vec{\mathcal{S}} \quad . \tag{3.4}$$

The first term contributes only a constant energy to all spin states and can be neglected in the spin Hamiltonian. It represents the temperature-independent Van-Vleck paramagnetism. The second term defines the effective g-factor $g_{\text{eff}} \approx g_0 - 2\lambda/\Delta E$ with a typical energy separation ΔE to higher electronic states.[9] The components of the three-dimensional tensor $\hat{g}_{\text{eff}}$ can be calculated, if the transition matrix elements $\langle \psi_0 | \mathcal{L}_i | \psi_n \rangle$ are known. They can often be estimated from experimental data, e.g. from $\vec{k} \cdot \vec{p}$ theory for the conduction band wave functions,[4, 21] or from optical data for transition metal centers.[22, 23]

The third term scales with the second power of the spin-orbit coupling constant λ, and can be treated formally like a spin-spin interaction. For $S > \frac{1}{2}$, this becomes the dominant contribution to the zero-field splitting of spin states in the absence of external magnetic fields. Similar to $\hat{g}_{\text{eff}}$, the symmetry of $\hat{D}$ reflects the symmetry of the ground state wave function, and is therefore very useful for identification purposes.

3.1.2 Axial anisotropy

It is plausible even without the explicit knowledge of the spatial wave functions of Eq. (3.4), that for magnetic ions with an axially symmetric environment also the g-matrix must have axial symmetry. This happens e.g. for dangling bond centers,[24] or

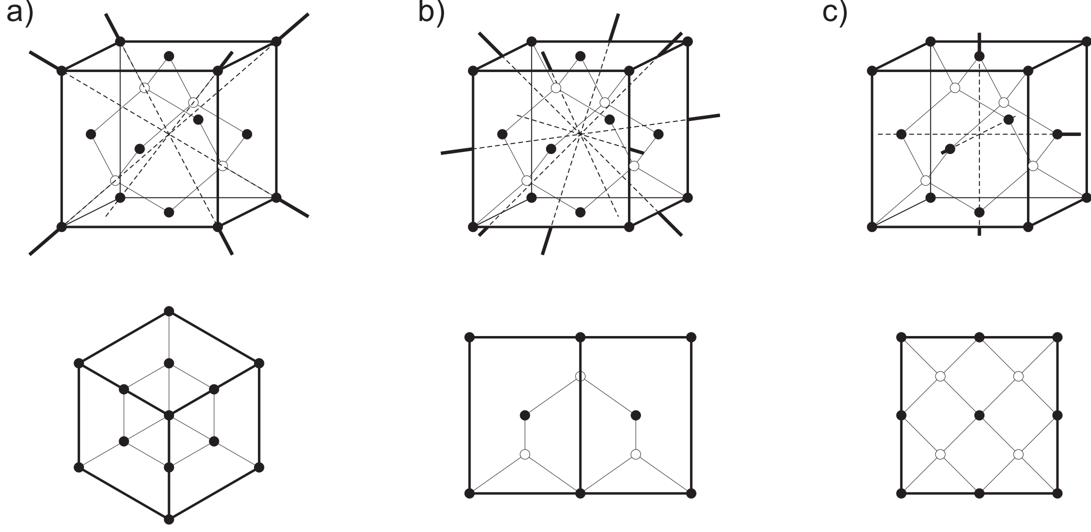

Figure 3.1: Zinkblende structure with (a) the four equivalent $\langle 111 \rangle$ directions along the C_3 rotation axis, (b) the six equivalent $\langle 110 \rangle$ directions perpendicular to the σ reflection planes, and (c) the three equivalent $\langle 100 \rangle$ directions along the S_2 and C_2 rotation axes. The same axes are found in other cubic lattices, e.g. the diamond lattice with only a single type of atoms. The lower row shows the unit cell of the Zinkblende lattice, as seen along the respective directions.

for conduction-band like states in group-III nitrides.[4] In the coordinate system with the principle axes x, y, and z, the Zeeman interaction is given by an effective g-matrix

$$\mathcal{H}_z = \mu_B \vec{B} \hat{g}_{\text{eff}} \vec{\mathcal{S}} = \mu_B \vec{B} \begin{pmatrix} g_\perp & 0 & 0 \\ 0 & g_\perp & 0 \\ 0 & 0 & g_{||} \end{pmatrix} \vec{\mathcal{S}} \quad . \tag{3.5}$$

Typical values for the two parameters $g_\perp$ and $g_{||}$ are e.g. $g_\perp = 2.0084$, $g_{||} = 2.0016$ for the P_b-center on a Si(100) surface, and $g_\perp = 2.022$, $g_{||} = 2.005$ for dangling bonds in amorphous germanium. The corresponding eigen-energies form an ellipsoid with the Zeeman energy $g_{||}\,\mu_B|\vec{B}|$ along the z axis of Eq. (3.5), and the energy $g_\perp\,\mu_B|\vec{B}|$ in the x-y plane. If the magnetic field $\vec{B} = (\sin\theta, 0, \cos\theta)B_0$ is tilted by an angle θ with respect to the symmetry axis z of the defect, the effective g-factor is given by

$$g(\theta) = \sqrt{g_\perp^2 \sin^2\theta + g_{||}^2 \cos^2\theta} \approx \tfrac{2}{3}g_\perp + \tfrac{1}{3}g_{||} - \tfrac{1}{3}(g_\perp - g_{||})\,(3\cos^2\theta - 1) \quad . \tag{3.6}$$

This useful first-order approximation is valid for $|g_\perp - g_{||}| \ll |2g_\perp + g_{||}|$.

In cubic crystals, there are four equivalent C_3 axes[25] along the directions [111], $[\bar{1}\bar{1}1]$, $[\bar{1}1\bar{1}]$, and $[1\bar{1}\bar{1}]$, as shown in Fig. 3.1a. The paramagnetic states are distributed equally among these axis, unless there is a preferential direction, e.g. of P_b-centers pointing out of the Si(111) surface. For arbitrary orientations of the sample with respect to a fixed magnetic field, each of the C_3 axes has a different tilt angle θ with respect to the magnetic

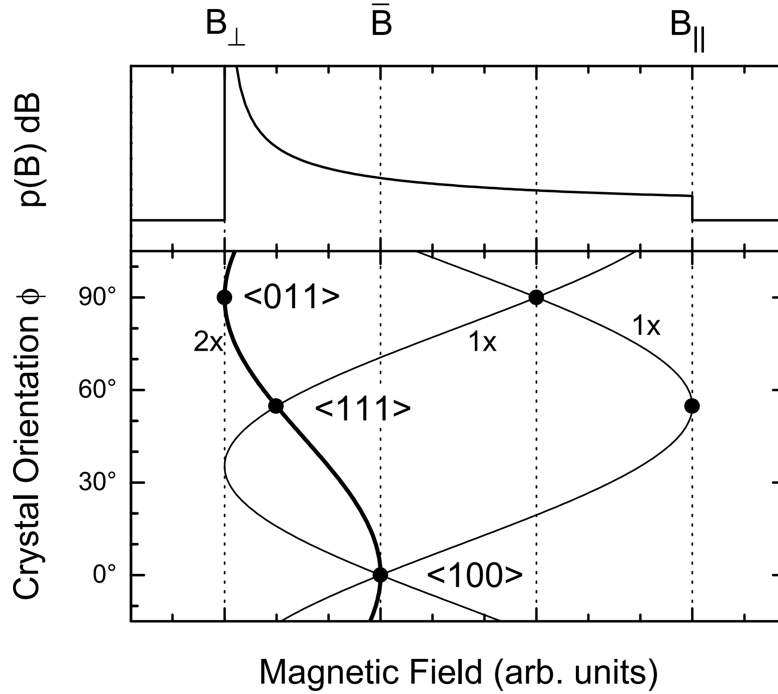

Figure 3.2: Resonance fields $B = h\nu/\mu_B g$ of ESR centers with a C_3 symmetry axis along the $\langle 111 \rangle$ axes of a cubic crystal (lower panel). Two of the four equivalent sites coincide for this rotation axis. The upper panel shows the probability $p(B)dB$ of finding a resonance at the magnetic field position B for such an axial center in an amorphous environment with equal probability for all defect orientations.(9)

field axis. However, all orientations are met at least once for experiments, in which the sample is e.g. rotated in a $(0\bar{1}1)$-plane. In such an experiment, the rotation angle ϕ is usually defined in a way that $\phi = 0°$ corresponds to a [100] axis (vertical direction in the lower part of Fig. 3.1b), $\phi = 54.74°$ to a [111] axis, and $\phi = 90°$ to a [011] axis (horizontal direction in the lower part of Fig. 3.1b). Characteristic resonance patterns are observed between these orientations, as shown in Fig. 3.2.

- For $\phi = 0°$ with $\langle 100 \rangle || \vec{B}$, all four C_3 axes have the same angle $\theta = 54.74°$ with respect to the external magnetic field. Therefore, one finds only one resonance with the average g-factor $\bar{g} = \frac{1}{3}(2g_\perp + g_{||})$.

- For $\phi = 54.74°$ with $\langle 111 \rangle || \vec{B}$, three of the C_3 axes are tilted by $\theta = 70.53°$ towards the magnetic field, and the forth is at $\theta = 0°$. Therefore, one finds two thirds of the intensity at a resonance with $\frac{1}{9}(8g_\perp + g_{||})$, and one third at $g_{||}$.

- For $\phi = 90°$ with $\langle 011 \rangle || \vec{B}$, two of the C_3 axes are at $\theta = 90°$, and the others are at $\theta = 35.26°$. Therefore, one finds half of the intensity at a resonance with $g_\perp$, and half at $\frac{1}{3}(g_\perp + 2g_{||})$.

In amorphous materials, all possible orientations of the defect axes are equally distributed, so that the probability of finding an axis with orientation θ is proportional to $p(\theta)d\theta \propto \sin(\theta)d\theta$, and the probability $p(B)dB$ for resonant transitions at the magnetic

field B is [9]

$$p(B)dB \propto \sin\theta \left(\frac{dB(\theta)}{d\theta}\right)^{-1} dB = \frac{(h\nu/\mu_B)^2\ dB}{B^3\sqrt{(g_\perp^2 - g_{||}^2)[g_\perp^2 - (h\nu/\mu_B B)^2]}} \tag{3.7}$$

for $g_{||} < h\nu/\mu_B B < g_\perp$. This distribution, which is known as *powder pattern* in the literature, has been included in Fig. 3.2. Its average field position $\bar{B}$ is the same as that observed for $B||\langle 100\rangle$ in a crystalline sample.

3.2 Electron-electron interaction

The electronic ground and excited states are often well approximated by atomic or molecular wave functions (see Sec. 2.1.2). In such systems, the presence of one electron can strongly affect all other electronic states, as is well known e.g. for the He atom.

In principle, all spins of the ground state electrons can be included in the spin Hamiltonian in a similar way to the nuclear spin in Eq. (2.22) in a large product space. This *uncoupled representation*[9] with the independent spin operators $\vec{\mathcal{S}}_1, \vec{\mathcal{S}}_2, \ldots$ is used for the analysis of experimental spectra only in the limit of very weak coupling, where the resonant spin is almost unaffected by all other spins in the system. Then, e.g. the eigen-values of $\vec{\mathcal{S}}_1$ can be corrected in first order perturbation theory for the possible orientations of the other spins.

In the case of stronger coupling, the *coupled representation* $S = S_1 - S_2 \ldots S_1 + S_2$ provides the most efficient description of the ground state degeneracy. As shown in Fig. 3.3, the ground states of two spins $S_1 = S_2 = \frac{1}{2}$ with four uncoupled product states $|\uparrow\uparrow\rangle$, $|\uparrow\downarrow\rangle$, $|\downarrow\uparrow\rangle$, and $|\downarrow\downarrow\rangle$ can either be a symmetric triplet

$$S = 1: \qquad \begin{aligned} |{+1}\rangle &= |\uparrow\uparrow\rangle \\ |0\rangle &= \tfrac{1}{\sqrt{2}}\,(\,|\uparrow\downarrow\rangle + |\downarrow\uparrow\rangle\,) \\ |{-1}\rangle &= |\downarrow\downarrow\rangle \end{aligned} \tag{3.8}$$

or an antisymmetric singlet

$$S = 0: \qquad |0\rangle = \tfrac{1}{\sqrt{2}}\,(\,|\uparrow\downarrow\rangle - |\downarrow\uparrow\rangle\,) \quad . \tag{3.9}$$

According to the Pauli principle, composed wave functions must be antisymmetric under electron interchange. Therefore, only the singlet state is allowed for both electrons with the individual spins S_1 and S_2 occupying the same orbital. As discussed in Sec. 3.2.2, similar considerations also apply for partially overlapping spatial orbitals, and enter the spin Hamiltonian via exchange interactions.

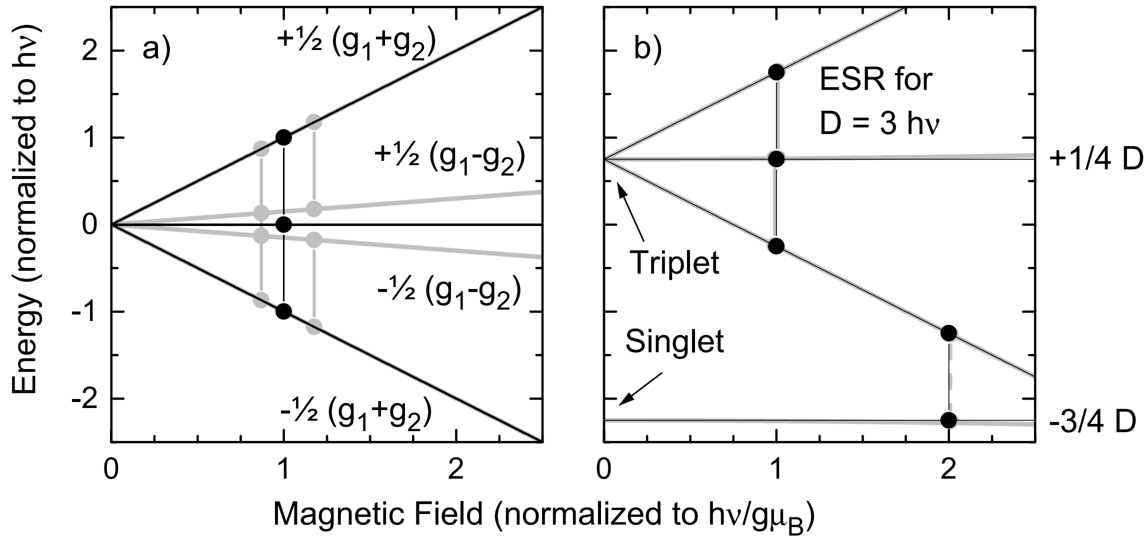

Figure 3.3: Eigen-energies for a system of two isotropically coupled spins with $S = 1/2$. (a) In the limit of weak coupling (black lines for equal g-factors, gray lines for different g-factors), the total energy of the system is given by the sum and difference of the energies of both single spins. (b) For strong coupling $D \gg h\nu$, the system is better described by a singlet state with $J = 0$, and a triplet state with $J = 1$ and the average g-factor $\frac{1}{2}(g_1 + g_2)$. The difference in resonance positions because of the different g-factors of the individual spins is suppressed in first order. Note, that the underlying spin Hamiltonian is the same as in Eq. (2.22), however with an additional term for the Zeeman interaction of the second spin. The half-field transitions $|\uparrow\uparrow\rangle \leftrightarrow |\downarrow\downarrow\rangle$ with $\Delta m = 2$ (not shown) become allowed if the magnetic field axis is tilted with respect to the symmetry axis of $\hat{D}$.

3.2.1 Dipolar interaction

The dipolar energy between two spins is defined analogously to the classical expression for two magnetic dipole moments $p = \mu_B g m$ with a spatial extent negligible compared to their separation $\vec{r}$. For simplicity, we consider only the parallel orientation of both, as shown in Fig. 3.4,[9] where θ is defined as the angle between $\vec{r}$ and the direction of both moments imposed by a strong external magnetic field.

$$E_{\text{dip}} = -\frac{\mu_0}{4\pi}\frac{(\mu_B g m)^2}{r^3}(3\cos^2\theta - 1) \quad . \tag{3.10}$$

For $g = 2$, a separation of $r = 1$ nm, and $\theta = 0°$, this dipolar energy would be 0.1 μeV only, which corresponds to a magnetic field offset of $E_{\text{dip}}/g\mu_B \approx 10$ G in ESR experiments.

Therefore, up to a concentration of $(1 \text{ nm})^{-3} = 10^{21}$ cm^{-3}, the dipolar interaction between two individual spins can be treated as small perturbation to the Zeeman energy of 38 μeV$/g\mu_B = 3300$ G in X-band ESR experiments, and it is appropriate to include the other spins as perturbations in the uncoupled representation of a single-spin Hamiltonian. The dipolar broadening due to a large number of spins on a regular lattice has been

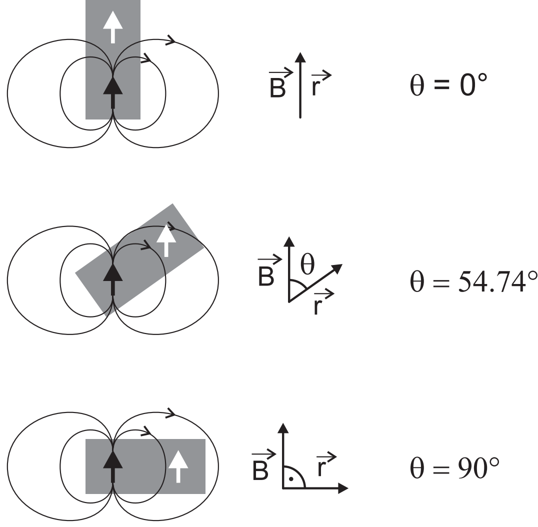

Figure 3.4: The energy of two classical point-dipoles aligned in a strong external field depends on their relative orientation. Its minimum is found at the orientation $\theta = 0°$ of their relative axis along the external field, and its maximum for the orientation $\theta = 90°$ with the relative axis perpendicular to the external field. At the intermediate orientation with $\theta = 54.74°$, the dipolar energy is zero.

calculated by the method of moments in Ref. 26. Other dipolar effects of a large number of spins will be discussed in more detail in Sec. 5.3.3.

For more strongly coupled states like a defect complex with its total spin being extended over the nearest lattice sites, the dipole-dipole and the anisotropic exchange interactions are better expressed by a traceless matrix $\hat{D}$ in the coupled representation for the total spin $S = S_1 + S_2$. Formally, such spin-spin coupling is equivalent to the indirect spin-orbit-spin coupling summarized in $\hat{D}$ of Eq. (3.4).

$$\mathcal{H}_{\mathrm{dip}} = \vec{\mathcal{S}}\hat{D}\vec{\mathcal{S}} = \vec{\mathcal{S}}\ \frac{1}{3}\begin{pmatrix} -D & 0 & 0 \\ 0 & -D & 0 \\ 0 & 0 & 2D \end{pmatrix}\vec{\mathcal{S}} = D\left(\mathcal{S}_z^2 - \tfrac{1}{3}S(S+1)\mathbf{1}\right) \quad . \tag{3.11}$$

The reason for including the constant energy offset $\frac{1}{3}S(S{+}1)$ in $\mathcal{H}_{\mathrm{dip}}$ is to make $\hat{D}$ traceless, i.e. to avoid shifts of the average energy of all spin states. Like the symmetry information obtained from the effective g-factor (Sec. 3.1.2), the multiplicity and orientation of the principal axes of $\hat{D}$ often provides a valuable information about the symmetry of the observed defect state.

The dipolar energy in an external magnetic field $\vec{B} = (B\sin\theta, 0, B\cos\theta)$ is obtained according to first order perturbation theory as

$$E_{\mathrm{dip}}^{(1)} = D\left[m^2 - \tfrac{1}{3}S(S+1)\right]\ \frac{3\cos^2\theta - 1}{2} \quad , \tag{3.12}$$

from the diagonal elements of $\mathcal{H}_{\mathrm{dip}}$ in the rotated coordinate system with $\mathcal{S}_z = \mathcal{S}_z'\cos\theta + \mathcal{S}_x'\sin\theta = \mathcal{S}_z'\cos\theta + \frac{1}{2}(\mathcal{S}_+' + \mathcal{S}_-')\sin\theta$. For systems with $S > \frac{1}{2}$, the magnetic resonance fields are shifted by

$$\Delta B_{|m\rangle\leftrightarrow|m-1\rangle} = \frac{D(m-\frac{1}{2})}{\mu_B g}(3\cos^2\theta - 1) \quad . \tag{3.13}$$

Therefore D, or the corresponding parameter P for nuclear spins are called "magnetic quadrupole splitting". Alternatively D is often called "zero-field splitting", as its determines the separation of states with different m^2 at zero magnetic field according to Eq. (3.11). This name is more general than the term "axial crystal field splitting", which implies the presence of crystal fields.[14]

Comparison of the classical dipolar energy of Eq. (3.10) for the magnetic moments of two point-like spins $S = 1/2$ in the uncoupled representation and of Eq. (3.12) for the quantum-mechanical energy in the coupled representation with $S = 1$ allows the identification of the spin Hamiltonian parameter D with an effective dipolar distance r via

$$D = \frac{3\mu_0}{8\pi}(g\mu_B)^2\frac{1}{r^3} \quad . \tag{3.14}$$

However, identical terms in the spin Hamiltonian and in the ESR spectra are also expected from the parameter D, as defined from spin-orbit interaction in Eq. (3.4). Therefore, both effects cannot be separated without further knowledge about the defect wave function.

3.2.2 Exchange interaction

The point dipole approximation is insufficient to describe quantum-mechanical systems with a large number of indistinguishable electrons, for which exchange interactions become important. The most dramatic exchange effect is summarized in Hund's rules for the electronic states of atoms, where a high probability density of several electrons at the same place is energetically unfavorable because of Coulomb repulsion. This ensures a spatially antisymmetric ground state, which according to Pauli's principle must be a high-spin state, as requested by Hund's rules.[9, 27, 28]

Intermediate exchange interactions of several eV or less also occur for molecular states, e.g. for the bonding and antibonding states $(\,|\psi_a\psi_b\rangle \pm |\psi_b\psi_a\rangle\,)/\sqrt{2}$ of the hydrogen molecule constructed from the single-electron atomic states ψ_a and ψ_b.[17] Pauli's principle requires the spatially antisymmetric state, i.e. the antibonding state of the hydrogen molecule, to be a spin triplet. In contrast, the spatially symmetric bonding state is a spin singlet. Thus, considering spin-spin interactions only, the orbital binding energy appears indirectly as an antiferromagnetic exchange interaction in the spin Hamiltonian. Therefore, the isotropic exchange constant $\hat{J} = \mathbf{1} \cdot J$ in the Heisenberg spin Hamiltonian is given by the exchange overlap integral

$$\mathcal{H}_{\text{ex}} = -2\vec{S}_1\hat{J}\vec{S}_2 = -2\langle\psi_a\psi_b|\,\tfrac{e^2}{4\pi\varepsilon_0 r}\,|\psi_b\psi_a\rangle\;\vec{S}_1\cdot\vec{S}_2 \quad . \tag{3.15}$$

with the inter-electron distance r. As the bonding electrons can be thought of interchanging their sites rapidly, the energy gain can be understood as a direct consequence of delocalization. Besides this so-called *direct kinetic exchange*, also *indirect exchange* of two magnetic ions with negligible direct overlap, but with a sufficient overlap with

intermediate diamagnetic states can enable a magnetic coupling over longer distances. Both antiferromagnetic coupling with $J < 0$ (see Fig. 2.3), as well as ferromagnetic coupling with $J > 0$ can result from these mechanisms, depending on the net phase of the overlapping wave functions.

For the interpretation of ESR spectra, exchange becomes particularly important if other spin interactions are active for one of the exchange-coupled spins only. Such interactions could e.g. be a local hyperfine interaction, which becomes averaged out for sufficiently fast exchange rates. This time-averaging process during exchange or a motional averaging process are the origin of the vanishing hyperfine satellites in SiC at high donor concentrations(29) and of the *exchange narrowing*(19, 30) of the inhomogeneously broadened ESR of effective-mass donors in AlN.(4) The coupled Bloch equations for two spins with exchange are analyzed in Ref. 9 (10.5) as an instructive example.

3.2.3 Spin polarization

According to the models introduced in Secs. 2.1.1 and 2.1.2, the electronic wave functions of shallow and deep defects can be constructed from a few band-like or atomic valence states. The doubly occupied states from filled energy bands at lower energies, i.e., from the core shells, are neglected in this approximation. In reality, there are significant interactions between the core and valence electrons, so that even for isolated ions, corrections to the core and valence states are required in order to obtain a reliable model of the respective valence state wave function. These corrections are taken into account in Hartree-Fock calculations for the isolated ions.

In the case of a paramagnetic valence state, the interactions with the core states, and therefore also the spatial redistribution of the electronic wave functions are different for both spin orientations. Therefore, although the net spin of the diamagnetic state is zero, locally unbalanced spin densities with both positive and negative sign might exist compared to the unpaired electron's spin.(2, 13, 16, 19) Consequently, spin-unrestricted Hartree-Fock calculations are required to calculate the correct charge and spin densities for paramagnetic ions. Qualitatively speaking, it is favorable to redistribute the majority spin components of the diamagnetic states towards places with maximum unpaired spin density.(2) This is illustrated schematically in Fig. 3.5 for the case of an unpaired electron $\psi_{\uparrow}$(shaded curve) with majority spin orientation and zero charge and spin density at the nucleus (at the origin of the distance axis). The diamagnetic core states with non-zero probability density at the nucleus are indicated schematically by ψ_{dia} (straight line). Because the exchange interaction with the unpaired electron is most attractive for the majority spin component $\psi_{\mathrm{dia}\,\uparrow}$, this component is dragged towards the position of the unpaired electron, leaving behind some oppositely oriented spin polarization. Consequently, the unpaired electron causes a net spin polarization at the nuclear position. The sign of the net spin polarization depends on the center of gravity of the diamagnetic core

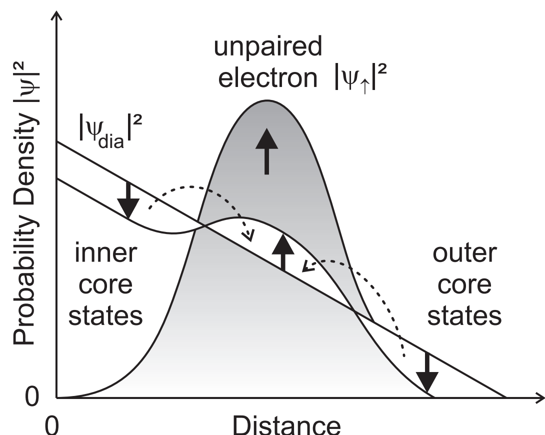

Figure 3.5: In many-electron systems, the presence of unpaired spin density $|\psi_\uparrow|^2$ induces non-zero spin density of the net diamagnetic states $|\psi_{\text{dia}}|^2$ even at places with vanishing density of the unpaired electron, e.g. at the nucleus for p and d unpaired electrons. Due to the spin polarization of core states and bonds, charge and spin density wave functions can differ significantly, which adds some ambiguity to the interpretation of small hyperfine constants.

states. As an example, the majority spin 1s and 2s orbitals are dragged outwards at neutral interstitial iron in silicon Si:Fe^0, whereas the 3s orbital is pushed inwards, resulting in a negative net spin polarization at the nucleus.[2]

The spin-dependent deformation of the diamagnetic states can be described by "configuration interaction" or spin dependent admixture of excited states. Analogously to the need for spin-unrestricted Hartree-Fock calculations in atoms, the description of spin polarization in solids requires the Local Spin Density Approximation (LSDA) instead of the Local Density Approximation (LDA) for the calculation of realistic defect wave functions.[2, 16, 31] Besides the polarization of core states, in solids one must additionally take into account that unpaired spin density at a defect atom can cause opposite spin density in the bonding orbitals of the neighboring atoms. This effect is the dominant contribution to the total spin wave function in conjugated radicals.[9] Similarly, the "hyperconjugation" mechanism is employed to explain qualitatively the spin polarization on remote atoms via geometric arguments.[9, 32]

Spin polarization effects complicate the interpretation of experimentally determined hyperfine parameters in most cases. For p- and d-like states, which otherwise would not show any Fermi contact interaction, this effect can be used to study the polarization of the bonds and valence band states.

3.3 Hyperfine interaction

One of the most rewarding features of ESR data is the analysis of hyperfine interactions, i.e. the interactions between electronic and nuclear spins. Because of the weak and almost point-like nuclear magnetic moment $\mu_n = \mu_B \frac{m_e}{m_n} = \mu_B/1836$, hyperfine interactions are restricted to an even shorter range than electron-electron interactions. Therefore, the nuclear spins are ideal local probes for the electronic spin density, if the nuclear positions in the crystal lattice are known, or can be approximated like for the dangling bonds in amorphous semiconductors (Chap. 5).

nuclide	natural abundance	I	g_n	A_s ($\mathrm{G}\times g\mu_B$)	A_p ($\mathrm{G}\times g\mu_B$)
^{1}H	99.9 %	1/2	5.59	0.51×10^3	0
^{13}C	1.11 %	1/2	1.40	1.3×10^3	38
^{14}N	99.6 %	1	0.40	0.65×10^3	20
^{17}O	0.04 %	5/2	-0.76	-1.9×10^3	-60
^{29}Si	4.67 %	1/2	-1.11	-1.6×10^3	-41
^{31}P	100 %	1/2	2.26	4.7×10^3	131
^{55}Mn	100 %	5/2	1.38	1.8×10^3	-89
^{73}Ge	7.8 %	9/2	-0.20	-0.84×10^3	-17

Table 3.1: Natural abundances, nuclear spins I, and g-factors g_n of isotopes relevant to this thesis (from Ref. 9). The atomic hyperfine constants A_s and A_p were determined via unrestricted Hartree-Fock calculations.

According to Sec. 2.1.2, linear combinations of atomic orbitals often provide a reasonable first approximation to a molecular defect wave function. Ideally, the coefficients of this wave function can be mapped out from its atomic components by comparison of the measured hyperfine data with the theoretical data for atomic wave functions, as summarized in Tab. 3.1.[9] A successful example for such a reconstruction of an impurity wave function in diamond is discussed in Sec. 3.3.3.

Hyperfine interactions $\mathcal{H}_{\mathrm{hf}} = \vec{S}\hat{A}\vec{I}$ can be understood in terms of local magnetic fields that shift the ESR transitions by $\Delta B = -m_i A/\mu_B g$ according to the $2I+1$ possible settings of the nuclear spin. As discussed earlier for the spin Hamiltonian (2.22), this approximation holds in first order perturbation theory for $A \ll \mu_B B g$. The first clue about the interacting nucleus comes from the number of equidistant satellites. Furthermore, different nuclei might be recognized by the relative intensity of the satellites with respect to the central resonance, as this is related to the concentration of this isotope in the sample, which is usually given by the natural abundance.

The experimentally observed hyperfine tensor $\hat{A}$ may be decomposed in its isotropic and anisotropic components along the principle axes of an axially symmetric center, similar to the g-factor in Eq. (3.5)[9, 19]

$$A = \begin{pmatrix} A_\perp & 0 & 0 \\ 0 & A_\perp & 0 \\ 0 & 0 & A_{||} \end{pmatrix} = A_{\mathrm{iso}} \cdot \mathbf{1} + A_{\mathrm{aniso}} \begin{pmatrix} -1 & 0 & 0 \\ 0 & -1 & 0 \\ 0 & 0 & 2 \end{pmatrix} \quad . \tag{3.16}$$

The microscopic interpretations for the experimental parameters A_{iso} and A_{aniso} for defect wave functions in semiconductors are discussed in the following sections.

3.3.1 Dipolar interaction

Replacing one of the Bohr magnetons μ_B in Eq. (3.10) with the nuclear magneton μ_n, the classical point-dipole approximation of Fig. 3.4 also applies for the interaction between electronic and nuclear spins. Here, the point-dipole approximation is much more justified, because of the strongly localized nature of the nuclear spin. Similar to the traceless tensor $\hat{D}$ of electronic dipolar interactions (see Eq. (3.11)), only the anisotropic component A_{aniso} of $\hat{A}$ in Eq. (3.16) is related to dipolar hyperfine interactions. Often, the crystalline orientation and multiplicity of hyperfine interactions with several equivalent defect sites provides helpful symmetry information for the identification of the ESR center studied.

The spatial extent of the electronic spin density requires the definition of an effective dipolar distance between the electronic and nuclear spin via the spatial expectation value of the dipolar interaction energy [9] $E_{\text{dip}} \propto (3\cos^2\theta - 1)\, r^{-3}$ (see Sec. 3.2.1)

$$A_{\text{aniso}} = \frac{2}{5}\frac{\mu_0}{4\pi}\; g\mu_B\; g_n\mu_n \langle\psi|\, \tfrac{3\cos^2\theta - 1}{r^3}\, |\psi\rangle \quad . \tag{3.17}$$

This expectation value is zero for s wave functions with spherical symmetry around the nuclear position, however, is nonzero for a p (or d) wave function. The dipolar interactions of s-wave functions at neighboring atoms with the nucleus at the defect atom are negligibly small, as the bond lengths typically are of the order of several Å, and the magnetic moment of the nucleus is much smaller than that of the electron. Therefore, the dipolar hyperfine interaction A_{aniso} is associated with the unpaired electron density in an atomic p (or d) orbital centered on the interacting nucleus.

3.3.2 Fermi contact interaction

The classical description of point-like electronic and nuclear spins breaks down for non-zero electronic spin density at the nuclear position. In a simplified picture, one can imagine this nucleus as a sphere with the magnetization $M = g_n\mu_n/V$ and a demagnetization field $\mu_0 M/3$. The orientation of this magnetization in the magnetic field $B_\psi = g\mu_B|\psi(0)^2|\; V$ due to an electronic spin density $\psi(0)$ at the nuclear position would require the energy $E = M \cdot B_\psi$.[19, 27] This result happens to coincide with the isotropic hyperfine energy that comes out of the full relativistic quantum-mechanical calculation as the isotropic Fermi contact interaction[33, 34, 35]

$$A_{\text{iso}} = \frac{2}{3}\mu_0\; g\mu_B\; g_n\mu_n|\psi(0)|^2 \quad . \tag{3.18}$$

This interaction takes place only for s orbitals, which have a non-zero spin density at the nuclear position. Therefore, isotropic hyperfine interactions with the spins of p or d electronic states must arise from spin polarization (Sec. 3.2.3) of diamagnetic inner shells or of the bonds. For the 1s ground state of the free hydrogen atom

$$\psi_{1s}(r)^2 = \frac{1}{\pi a_0^3}\; \exp\left(-\frac{2r}{a_0}\right) \quad , \tag{3.19}$$

with the Bohr radius $a_0 = 0.529$ Å, the hyperfine interaction $A_{\mathrm{iso}} = 1.42$ GHz $\times h =$ 508 G $\times g\mu_B$ is predicted from Eq. (3.18), which is in very good agreement with the literature value of Tab. 3.1.

In a many-electron systems, there are possibly several diamagnetic core shells and bonds contributing to the Fermi contact interaction (Sec. 3.2.3), which in general will have different nuclear spin orientations with respect to the electronic spin. These contributions have to be balanced, so that the signs of the net spin polarization $|\psi_\uparrow(0)|^2 - |\psi_\downarrow(0)|^2$ and of A_{iso} depend on their relative magnitude. In the spin Hamiltonian, the sign of A_{iso} indicates whether the magnetic moments of electron and nucleus tend to align either parallel or antiparallel.[9]

3.3.3 Ligand hyperfine interaction

Usually, the wave functions of localized states are extended at least to the nearest neighbor atoms. Extended states like P donors in Si even cover as many as 10^4 nuclei within their radius of localization. All these nuclear spins are included in the uncoupled representation of the spin Hamiltonian

$$\mathcal{H} = \mu_B \vec{\mathcal{S}} \hat{g} \vec{B} + \sum_n \vec{\mathcal{S}} \hat{A}_n \vec{\mathcal{I}}_n \quad . \tag{3.20}$$

It is convenient to write an extended wave function $\Psi(\vec{r})$ as a linear combination of s and p valence orbitals of the respective host atoms according to Sec. 2.1.2. Examples for such composed wave functions are discussed in more detail in Sec. 5.3.1. Like for Fermi contact interactions with isolated atoms (Sec. 3.3.2), the multiple isotropic hyperfine parameters $A_{n,\mathrm{iso}}$ are then interpreted as local Fermi contact interactions of the s-like component of the wave function at the n-th host atom. The multiple anisotropic hyperfine parameters $A_{n,\mathrm{aniso}}$ are in analogue interpreted as dipolar hyperfine interactions of the respective atoms (Sec. 3.3.3). Sometimes, the assignment of several hyperfine interactions A_n to the various atoms is not unique, and requires additional input from theoretical calculations.[2]

The value of a simple set of hyperfine data will be illustrated now at the P1 center of nitrogen in diamond.[10] The observed hyperfine constants are summarized in Tab. 3.2. P1 occurs on 4 equivalent sites with axial symmetry along $\langle 111 \rangle$. The ESR signal of each site consists of an isotropic central signal with two satellites of equal intensity due to hyperfine interaction with ^{14}N. Additionally, all lines show two weak hyperfine satellites due to one nucleus of the rare isotope ^{13}C. The fractions of the s and p wave functions on both nuclei are listed in Tab. 3.2. Most noticeably, about 70% of the wave function is transferred from the N impurity to one neighboring C atom, and the p/s-ratio of the paramagnetic electron is $\beta^2/\alpha^2 > 3$ on both atoms. This suggests that P1 occupies an antibonding C-N orbital with high p content, and almost sp^2 hybridization for the other bonds. The bond angles concluded from the p/s ratios of Tab. 3.2 suggest the structural

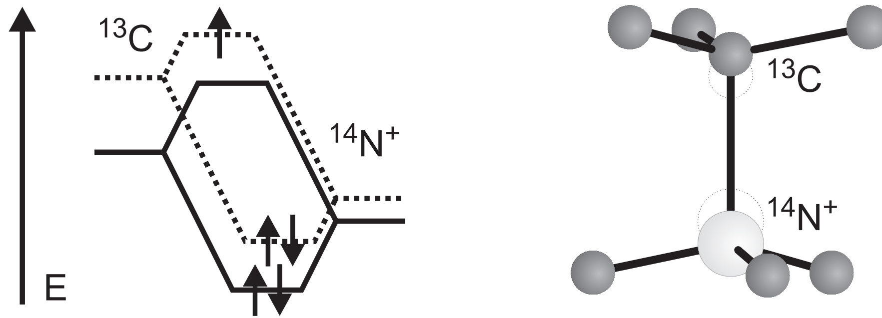

Figure 3.6: Based on hyperfine data for the P1 center in diamond,(10) a detailed structural model of its molecular wave function was developed.(11) The solid lines represent the sp^3-coordinated pseudo-molecule CN^+ with $\beta^2/\alpha^2 = 3$. As indicated by dashed lines in the hybridization diagram, the additional electron in a molecular C-N defect wave function occupies an antibonding orbital with much larger p-content $\beta^2/\alpha^2 = 11.2$ at the ^{13}C atom and $\beta^2/\alpha^2 = 3.8$ at the ^{14}N atom due to the structural relaxation along $\langle 111 \rangle$ shown on the right.

atom	A_{iso} ($g\mu_B$G)	α^2 (%)	A_{aniso} ($g\mu_B$G)	β^2 (%)	$\alpha^2+\beta^2$ (%)	β^2/α^2
^{14}N	33.1	5.12	3.85	19.4	24.6	3.8
^{13}C	74.3	5.51	23.6	61.6	67.1	11.2

Table 3.2: Hyperfine data of the P1 nitrogen center in diamond. The largest fraction of its wave function is found on a p orbital at one of the neighboring C atoms. The total wave function $\alpha^2 + \beta^2$ at one nucleus and the hybridization ratio β^2/α^2 are essential for the structural model shown in Fig. 3.6.

model shown in Fig. 3.6,(11) which has been confirmed by elaborate *ab initio* calculations later.(36)

For more extended wave functions, a shell of n ligand nuclei might have the same hyperfine constant. Each nuclear spin then splits all other resonances into $2I + 1$ equally spaced satellites, so that the complete satellite pattern consists of $2nI + 1$ equally spaced lines.(19) At the natural abundance c, the probability of finding an atom with the nuclear spin is increased to nc. Therefore, for example the inner hyperfine satellites due to 6 equivalent ^{29}Si nuclei have the approximate intensities $\frac{6}{2} \times 4.67\% = 11\%$ relatively to the central line, and the satellites due to 6 equivalent ^{13}C nuclei would have the intensity 3.3%.

Hyperfine interactions at the central defect atom are presented for most ESR signals reported in this thesis. Unfortunately, the observed linewidths are too large to resolve any hyperfine satellites from the ligand atoms for the amorphous germanium films discussed in Chap. 5. At sufficiently small nuclear spin concentrations, the probability of finding a nuclear spin at large distances from the defect site is relatively high compared to the

probability at the central atom, because the number of ligand atoms increases rapidly with increasing distance. Therefore, the number of participating nuclei and the localization length of the spin wave function can be estimated from the line broadening in isotope-engineered samples, as described in Sec. 5.3.2.

Chapter 4

Detection of electron spin resonance

The basic components of a conventional ESR spectrometer are discussed in the following sections. Access to the detailed microscopic information about paramagnetic centers is in many cases restricted experimentally by the limited sensitivity of the detection system because of the small microwave transition energies and the small occupation differences listed in Tab. 4.1. Today, state-of-the-art spectrometers still require typically a minimum of 10^{10} spins per G linewidth for the detection of ESR. For the investigation of a small number of defects with broad ESR resonance lines, another detection method with much greater sensitivity than conventional ESR has been used in this thesis. This method, called electrically detected magnetic resonance (EDMR), will be introduced in Sec. 4.3.

4.1 Spectrometer components

In a conventional continuous wave (CW)-ESR spectrometer (see Fig. 4.1), the magnetic field is varied at a fixed microwave frequency. This makes it possible to enhance the microwave amplitude with the help of a resonant cavity. However, it requires a separate

Resonator type	Frequency ν Band	(GHz)	ΔE (μeV)	$\lambda/2$ (cm)	$\Delta N/N$ [300 K]	B (T) [$g=2$]
LRC circuit	L	0.434	1.8	35	3.5×10^{-5}	0.015
split ring	S	2.00	8.3	7.5	1.6×10^{-4}	0.071
rectangular TE_{102}	X	9.35	39	1.6	7.5×10^{-4}	0.33
cylindrical TE_{011}	Q	34.0	141	0.44	2.7×10^{-3}	1.21

Table 4.1: Resonance frequencies ν, transition energies $\Delta E = h\nu$, and half-wavelengths $\lambda/2 = c/(2\nu)$ of the microwave cavities used in this work. The spectrometers are named after the respective microwave frequency bands. Also listed are the corresponding occupation differences $\Delta N/N \approx h\nu/(2kT)$ at $T = 300$ K, and the magnetic fields at which the ESR transitions occur for defects with $g = 2$.

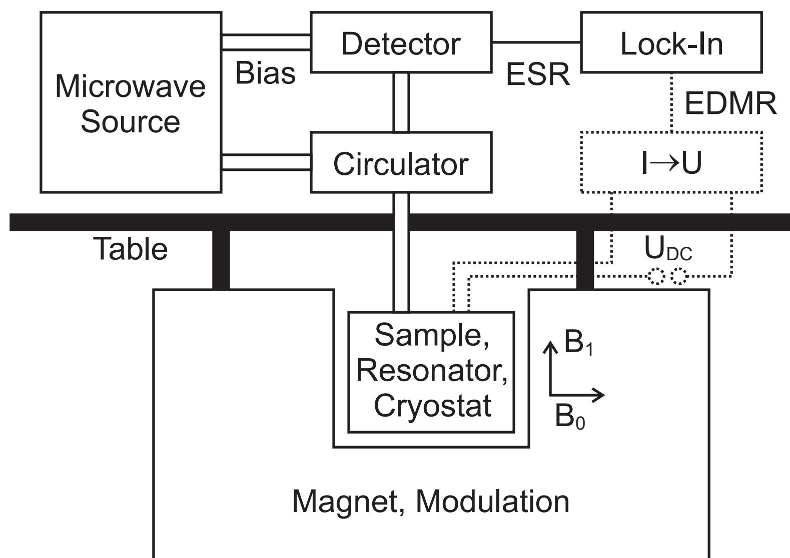

Figure 4.1: The basic components of an ESR spectrometer. No microwave bias arm, but the electrical circuit for conductivity measurements is required for EDMR measurements.

resonator for each measurement frequency. The frequencies and typical dimensions of several resonators are listed in Tab. 4.1. All ESR spectra in this work have been recorded with the TE_{102} resonator of a commercial X-band spectrometer (Bruker ESP 300). The other resonators have been used for EDMR measurements, as discussed in Sec. 4.3. The X-band spectrometer is equipped with a klystron operating at about 9.3 GHz. The microwave power can be amplified up to 2 W with an optional solid-state amplifier. Details about the other components of the microwave bridge can be found in Ref. 37. The klystron is locked to the resonance frequency of the cavity with an automatic frequency control (AFC) circuit and its frequency is measured accurately with a microwave frequency counter (HP 5350B). Critical coupling of the waveguide to the resonator is achieved with an adjustable iris. For optimum sensitivity, the detection diode is biased with a microwave bias arm. The amplitude and phase of this bias can be adjusted independently from the microwave amplitude at the sample.

Microwave radiation for the Bruker resonators at 2.00 GHz and 34 GHz is generated by an HP 83640A microwave source based on Gunn-diodes with maximum power up to 10 mW. Higher microwave powers of 1 W or 250 mW can be achieved with optional solid state amplifiers, as in the case of the 9.3 GHz system. In these resonators, critical coupling to the resonator is achieved via mechanical positioning of the coaxial or waveguide antenna in the resonator. At both frequencies, the detection diodes can be biased, which makes ESR measurements possible. However, the sensitivity of these basic ESR spectrometers is about 2-3 orders of magnitude lower compared to the optimized X-band system.

It would be impossible to fit a cavity of a resonator at 0.43 GHz with dimensions of 35 cm into a normal electromagnet. Therefore, the alternating magnetic field is generated in the coil of a resonant LRC circuit for the home-build spectrometer at 0.43 GHz. For the samples studied here, conventional ESR cannot be observed in this system, probably

because of the low quality factor of this resonator. Radio frequency for this spectrometer is generated by a YAESU UHF ham radio transceiver and can be amplified up to a power level of 100 W. The coupling to the resonator is monitored with a standing wave ratio meter instead of the circulator shown in Fig. 4.1. Temperatures from room temperature down to liquid He temperatures can be adjusted either in a helium flow cryostat within the microwave resonator (0.43 GHz, 9.3 GHz), or in a helium bath cryostat, in which the resonator assembly (2.0 GHz, 34 GHz) is embedded. The temperature is measured with AuFe-Chromel thermoelements.

Highly uniform magnetic fields up to $B = 1.4$ T are applied with a pole-face electromagnet perpendicular to the direction of polarization of the alternating microwave field, as indicated in Fig. 4.1. The static magnetic field is additionally modulated at frequencies up to 100 kHz, and with modulation amplitudes up to 32 G with two Helmholtz coils mounted on the resonator walls. Phase-sensitive detection with a Lock-In amplifier of signal components only at this frequency makes it then possible to distinguish true ESR or EDMR components from statistically fluctuating noise.

If ESR is possible, i.e. at 2.0, 9.3, and 34 GHz, small offsets of the magnetic field or the microwave frequency can be corrected with the known g-factor $g = 2.0036$ of diphenylpicrylhydrazyl (DPPH) recorded under identical conditions. At 0.43 GHz, the g-factor resolution is so low, that the magnetic field corrections were calculated from the g-factors measured for the same sample at 9.3 GHz.

4.2 Resonance Lineshape

Low frequency noise is suppressed in conventional ESR spectrometers by magnetic field modulation. As shown in Fig. 4.2, such modulation together with a slope of the microwave absorption signal $y(B_0)$ versus the magnetic field B_0 results in an oscillating signal $y'(B_0)$ at the microwave detector, which can be amplified independently from noise at frequencies other than the modulation frequency with a lock-in amplifier. This signal $y'(B_0)$ is proportional to the derivative of the original absorption line with respect to the magnetic field and will be called the ESR signal in the following.

According to the solution Eq. (2.43) of the Bloch equations, the lineshape function $y(\omega)$ for the resonant microwave absorption of electron spins has a Lorentzian shape, which is the lineshape of any harmonic system at resonance. The experimental features of the corresponding derivative curve $y'(B) = dy(B)/dB$ observed in ESR are the magnetic field B_{res} of the zero-crossing of the ESR signal, which fulfills the resonance condition $h\nu = \Delta E$, the peak-to-peak linewidth ΔB_{pp}, not to be confused with the full width at half maximum (FWHM) of the absorption curve, and the peak-to-peak amplitude A_{pp}. With the area $A = \int y(B)dB$ of the integrated Lorentzian curve, the homogenous ESR

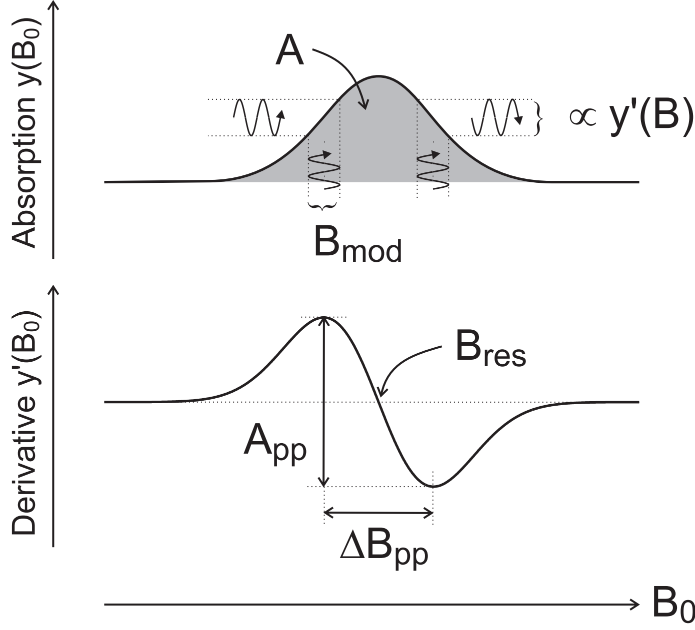

Figure 4.2: Resonant microwave absorption and the corresponding derivative ESR signal detected with a lock-in amplifier using magnetic field modulation. Also indicated are the resonant field B_{res}, the peak-to-peak amplitude A_{pp}, and the peak-to-peak linewidth ΔB_{pp}. The area A of the absorption signal is proportional to the number of spins in the sample.

lineshape is given by

$$y'_{\text{Lorentz}}(B) = -A \, \frac{\sqrt{3}}{\pi} \left(\frac{B - B_{\text{res}}}{\Delta B_{pp}^3} \right) \left[\frac{3}{4} + \left(\frac{B - B_{\text{res}}}{\Delta B_{pp}} \right)^2 \right]^{-2} \tag{4.1}$$

with a peak-to-peak amplitude

$$A_{pp,\text{Lorentz}} = y'(B_{\text{res}} + \tfrac{1}{2}\Delta B_{pp}) - y'(B_{\text{res}} + \tfrac{1}{2}\Delta B_{pp}) = \frac{\sqrt{3}\ A}{\pi\ \Delta B_{pp}^2} \quad . \tag{4.2}$$

Arbitrary derivative lineshapes $y'(B)$ can be characterized conveniently by the lineshape factor

$$l_{\text{Lorentz}} = \frac{\iint y'(B) dB^2}{\frac{1}{2} A_{pp,\text{Lorentz}} \Delta B_{pp}^2} = 3.628 \quad . \tag{4.3}$$

The inhomogeneous ESR lineshape of a large number of spin packets displaced by random perturbations of the resonance field B_{res} is given by the derivative of a Gaussian curve

$$y'_{\text{Gauss}}(B) = -A \, \sqrt{\frac{32}{\pi}} \left(\frac{B - B_{\text{res}}}{\Delta B_{pp}^3} \right) \ \exp \left[-2 \left(\frac{B - B_{\text{res}}}{\Delta B_{pp}} \right)^2 \right] \tag{4.4}$$

with

$$A_{pp,\text{Gauss}} = \sqrt{\frac{32}{\pi e}} \, \frac{A}{\Delta B_{pp}^2} \qquad \text{and} \qquad l_{\text{Gauss}} = 1.033 \quad . \tag{4.5}$$

The ratio of the Lorentzian and Gaussian derivative amplitudes and lineshape factors shows that the number spins is about 4 times larger for a Lorentzian curve with the same observed parameters B_{pp} and A_{pp} .

The ESR amplitude for a Gaussian curve in the X-band spectrometer and $S = 1/2$ has been calibrated by comparing the signal intensity to a Si:P sample with known doping concentration N_S. The calibration is

$$N_S = \frac{A_{pp}\ T\ \Delta B_{pp}^2}{V\ B_{\text{mod}}\sqrt{\text{P}}} \times 5.1 \times 10^7\ \frac{\sqrt{\text{mW}}}{(\text{mV/sweep})\ \text{K G}} \quad , \tag{4.6}$$

where V denotes the sample volume, A_{pp} the peak-to-peak amplitude at the lock-in amplifier per sweep, T the temperature, and P the incident microwave power in front of the resonator. For other lineshapes, double integration of the ESR signal is required. The main uncertainty of the concentration measurements comes from the reproducibility of the sample position in the resonator. For the calculation of N_S, care must be taken to keep the microwave power below saturation and the modulation amplitude below ΔB_{pp}. It is important to note that the ESR amplitude $A_{pp} \propto N_S/\Delta B_{pp}^2$ depends strongly on the linewidth, which makes the same number of spins much harder to detect for broad resonances. Narrow lines, on the other hand, often require a lower microwave power level to avoid saturation, and allow only small modulation amplitudes B_{mod}, which limits the maximum possible signal amplitude A_{pp} .

4.3 Indirect detection methods

The ESR sensitivity for a fixed sample volume increases approximately proportionally to ν^2.[9] However, other exponents ν^0–$\nu^{9/2}$ of the frequency are obtained, depending on the actual sample size, the filling factor, the dielectric losses, and the microwave saturation level.[9] Practically, the choice of frequency is limited by the requirements on the magnet and microwave compounds. The sensitivity limit of conventional ESR spectrometers is particularly problematic in studies of high quality samples with small defect densities, or with small volumes of interest, like thin films and microelectronic devices. Under the right circumstances, such studies can still be done via indirect detection methods like optically detected magnetic resonance (ODMR), and electrically detected magnetic resonance (EDMR). Recent improvements in both methods have enabled the detection of single spins in ODMR,[38] and of a few hundred spins in EDMR.[39, 40] Both detection methods can be optimized for the electrical or optical process of choice, respectively, and therefore can be made insensitive to spins in the substrate material, and elsewhere in the microwave cavity. Unwanted background absorption, eventually masking the conventional ESR signal, can therefore be suppressed in ODMR and EDMR. The occupation difference between the Zeeman levels, which is most relevant for the sensitivity of conventional ESR, is in these detection methods connected to the transition rates in a spin-dependent process via the Pauli principle, as illustrated in Fig. 4.3.

For a random distribution of both spin orientations, the populations of all four states $|\uparrow\uparrow\rangle$, $|\uparrow\downarrow\rangle$, $|\downarrow\uparrow\rangle$, and $|\downarrow\downarrow\rangle$ of a pair of spins are distributed equally. For small interaction,

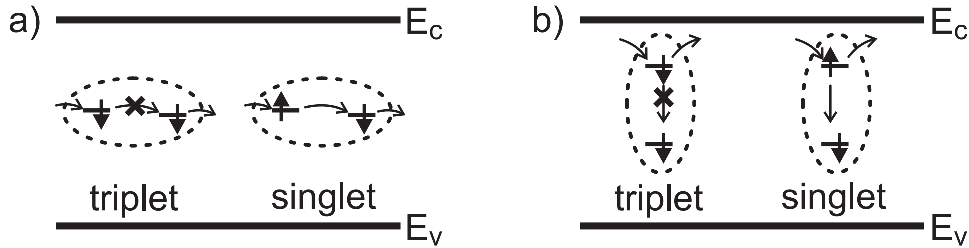

Figure 4.3: The Pauli principle determines the mechanisms for (a) spin-dependent hopping transport and (b) spin-dependent recombination at defects in semiconductors. As spin is typically conserved during these transition processes, hopping transport and spin-dependent recombination are allowed only for singlet states with antiparallel spin orientation. Under resonance conditions, both processes are are enhanced, as at spin resonance more triplet states are converted into singlet states than vice versa.

this uncoupled representation is appropriate to describe the resonance of the individual spins. The spin selection rules of Fig. 4.3 are described naturally in the coupled representation. Of course, also the populations of the singlet $(\,|\uparrow\downarrow\rangle - |\downarrow\uparrow\rangle\,)/\sqrt{2}$, and the three triplet states $|\uparrow\uparrow\rangle$, $(\,|\uparrow\downarrow\rangle + |\downarrow\uparrow\rangle\,)/\sqrt{2}$, and $|\downarrow\downarrow\rangle$ of Eqns. (3.8) and (3.9) are equally distributed.

According to Pauli's principle, two electrons in the same spatial orbital must have opposite spin orientation. Thus, the hopping and recombination process shown in Fig. 4.3 is possible only for singlets, but not for triplets. In the case of the *occupation* not being random after thermalization, the overall *transition rate* is also to be expected to be different from the transition rate at equal population. Under spin resonance conditions, any such difference would be reduced and destroyed completely at saturation of resonance, which would again equalize the occupation. The maximum influence of ESR on transport or recombination is therefore limited by the initial occupation difference between the singlet and triplet states.

Two basic mechanisms for this difference have been discussed in the literature: According to Lepine's model,[41] the thermal Boltzmann population $N_\uparrow/N_\downarrow = \exp(-h\nu/k_BT)$ between the Zeeman levels of each spin results in a depopulation of the singlet states, as

$$\frac{N_{\uparrow\downarrow}}{N} = \frac{N_{\uparrow\downarrow}}{N_{\uparrow\uparrow} + N_{\uparrow\downarrow} + N_{\downarrow\uparrow} + N_{\downarrow\downarrow}} = [\, 1 - \left(\frac{h\nu}{2k_BT}\right)^2 + \,\ldots]/4 \quad . \tag{4.7}$$

Therefore, the conductivity change $\Delta\sigma/\sigma$ at spin resonance is limited to $(h\nu/2k_BT)^2$, which is of the order of 10^{-6} at $T = 300$ K and $\nu = 9.35$ GHz according to Tab. 4.1. This mechanism depends strongly on temperature, and allows only small EDMR signals at room temperature. However, as conductivity measurements and optical detectors in the eV range can be made sensitive enough for single-electron and single-photon detection, it nevertheless provides an attractive detection scheme, e.g. via the enhancement of hopping

conduction, the enhancement of photoluminescence, or the quenching of photoconductivity under spin resonance conditions.

Much larger conductivity changes than predicted by Lepine's model, and sometimes independent of ν and T have been observed experimentally.[37, 41, 42] According to a mechanism proposed by Kaplan, Solomon and Mott,[42] a deficiency of singlets may also occur, if the thermalization rate of each spin orientation is slow compared to the singlet recombination rate. The thermalization happens by capture and dissociation of the correlated spin pair, as indicated by the arrows to the outside reservoirs in Fig. 4.3. For very slow thermalization, EDMR and ODMR signals could reach the order of one in this model, and they could become very small, if the exchange and the thermalization rates are much faster than the rate of microwave depopulation. Because the effective thermalization rate is not known *a priori*, the relative importance of either mechanism is speculative in most cases. Therefore, there is no universal calibration of the spin density for EDMR as for conventional ESR in Eq. (4.6), unless care is taken to establish the identical transition rates in different samples, as for example for the P_b centers at differently prepared Si/SiO_2 surfaces in Ref. 43.

Furthermore, spin-independent transport channels like recombination at diamagnetic defect states, thermally activated transport parallel to hopping conduction, or transport through grain boundaries cannot be excluded completely in most systems. Such transport channels are expected to shunt the spin-dependent transport processes and hence to reduce the intensity of the EDMR signal. An additional decrease of the EDMR intensity must be expected for spin-dependent hopping, if the correlation energy of the final state is large compared to the thermal energy. In this case, the energy cost for the hopping transition from two singly occupied initial states to a doubly occupied final state as shown in Fig. 4.3a would be significantly higher than the cost for a comparable transition into an unoccupied final state. As unoccupied states are usually available not far above the Fermi level, large correlation energies are expected to suppress the EDMR intensity in this kind of system.[44] Nevertheless, the measurement of B_{res} and therefore of all other spin Hamiltonian parameters like the g-factor and the hyperfine tensor is still possible from the EDMR resonance positions. This makes EDMR the method of choice for the investigation of broad lines at different microwave frequencies (Chap. 5), and for the detection of spin resonance in thin, conducting samples on isolating substrates with strong ESR background (Chap. 6).

Not much additional experimental effort is required for EDMR measurements in an ESR spectrometer. As indicated in Fig. 4.1, the sample conductivity is, for example, measured by application of a voltage (source-measure unit Keithley 237) and a current measurement. The current-to-voltage conversion can either be done by a resistor or by a current amplifier, which is particularly beneficial at a sample impedance above 1 MΩ. Contact resistance could be avoided by four-point measurements. For highly

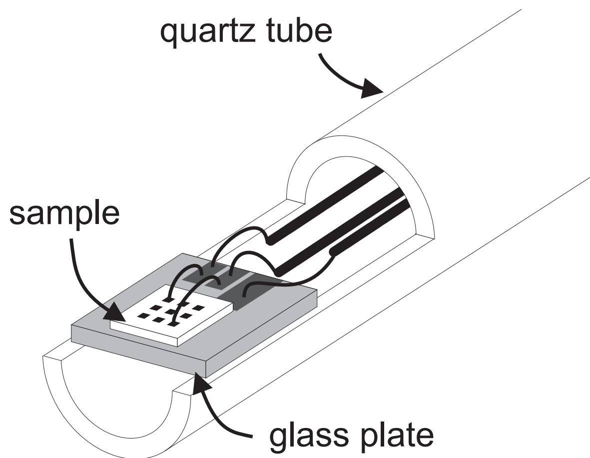

Figure 4.4: Samples are mounted on the cut end of a 4 mm ESR quartz tube for EDMR measurements and contacted with gold wires. A glass plate with large contact pads is only required for the study of small samples, or when back contacts are needed, while large samples, as a-Ge films on glass substrates can be mounted on the quartz glass tubes directly.

resistive samples, however, interdigitated contacts are necessary, which makes four-point measurements impossible. The sample is mounted on a cut quartz glass tube (Suprasil), as shown in Fig. 4.4. The cables should be close to the tube axis, where the microwave mode has a node of the electric field. To account for the thermal expansion at low temperatures, thin and flexible gold wires are used between the contacts on the sample front or back surface and a twisted pair of coated wires to the outside.

Chapter 5

Dangling bonds in amorphous germanium

Dangling bonds (dbs) are the intrinsic defect states in group-IV semiconductors and were found to be responsible for both midgap acceptor and donor levels. Neutral dbs in Si have been studied in great detail, e.g., at the Si/SiO_2 interface[16, 45, 46, 47, 48, 49] and in amorphous silicon (a-Si).[24, 50, 51, 52, 53, 54, 55] In both cases, their electronic structure can be described as a linear combination of the valence orbitals of an undercoordinated central Si atom and of small contributions from the three backbonding hybrid orbitals. This was quantified experimentally via ESR measurements of hyperfine interactions of the dangling bond electron spin with the nuclear spins $I_{29} = 1/2$ of the central and the backbonding ^{29}Si atoms. Owing to the technological importance of metal/oxide/semiconductor (MOS) field effect transistors based on crystalline Si, and of large area electronics such as displays and solar cells based on hydrogenated amorphous silicon (a-Si:H), dbs in Si have been comparatively well studied.

In particular for photovoltaic applications, amorphous alloys of Si with Ge are frequently used. After deposition, such films suffer from a large concentration of electrically active dbs in the range of 10^{18-20} cm^{-3}, which can be reduced by hydrogenation down to 10^{16-17} cm^{-3}.[56, 57] The resulting hydrogenated a-$Si_{1-x}Ge_x$:H films are then suitable for electronic applications. As shown experimentally by electrically detected magnetic resonance (EDMR),[58] it is the Ge dangling bond that is responsible for most of the recombination processes also in Si-rich a-$Si_{1-x}Ge_x$:H alloys. This makes it important to understand dbs in a-Ge in detail. In contrast to crystalline and amorphous Si, no detailed model for the structure of the defect orbital is available from measurements of the hyperfine interaction, for neither crystalline or for amorphous Ge.

For both elemental semiconductors Si and Ge there exists only one isotope with nonzero nuclear spin and at low natural abundance. The composition of natural Si is ^{28}Si (92.2%), ^{29}Si (4.7%), and ^{30}Si (3.1%). Natural Ge consists of ^{70}Ge (20.5%), ^{72}Ge (27.4%), ^{73}Ge (7.8%), ^{74}Ge (36.5%), and ^{76}Ge (7.8%). It can be expected that

the hyperfine splitting of a db electronic spin is smaller for ^{73}Ge ($I_{73} = 9/2$) than that for ^{29}Si ($I_{29} = 1/2$), because the theoretical atomic hyperfine interactions from Hartree-Fock-Slater integrals at ^{29}Si are about twice as large as those at ^{73}Ge,[9, 32] and because dbs in a-Ge are expected to be more delocalized than in a-Si.[56] Unfortunately, the peak-to-peak linewidth $\Delta B_{\mathrm{pp}}^{\mathrm{exp}} = 48$ G observed for dbs in a-Ge at 9.35 GHz is much larger than $\Delta B_{\mathrm{pp}}^{\mathrm{exp}} = 8$ G for dbs in a-Si, so that the chances for the observation of resolved hyperfine satellites in a-Ge are low. The hyperfine contribution to the ESR linewidth of dbs in a-Ge was estimated in Ref. 59 from the method of moments[13, 26] to 17 G, assuming a localization radius of 5 Å. However, the authors suggested that these numbers should be verified using isotopically enriched samples.

In this chapter we investigate isotopically engineered amorphous Ge samples containing different concentrations of ^{73}Ge with the help of conventional ESR and EDMR at different microwave frequencies. We find a hyperfine broadening of 10 G at the natural isotope concentration, which is somewhat smaller than that predicted in Ref. 59, and determine the isotropic hyperfine interaction at the central defect atom to 29 G $\times\, g\mu_B$. From a numerical simulation of the EDMR linewidth over the complete ^{73}Ge concentration range, we are able to extract a spin localization radius of 3.5 Å for dbs in a-Ge. After the description of the experimental details and the electrical properties of the investigated samples in Sec. 5.1, the EDMR spectra observed are discussed in Sec. 5.2 for a-Ge films deposited from pure a-^{70}Ge material, from Ge with the natural isotope composition, and from ^{73}Ge-enriched samples at microwave frequencies from $0.434 - 9.35$ GHz. Analytical models and numerical simulations for the interpretation of the observed broadening are presented in Sec. 5.3 and then discussed with respect to the properties of dbs in a-Si in Sec. 5.4. Taking into account the similarity of dbs in crystalline and amorphous Si, the results presented below can also be used as a first estimate for the structure of dbs in Ge crystals or at the Ge/GeO_2 interface. In addition, this investigation is a case study of the effects of the ^{73}Ge nuclear spins on the electron spins of paramagnetic states, which are relevant for recent proposals for quantum computation applications.[60]

5.1 Experimental details

The a-Ge films under investigation were deposited on glass substrates (Corning 7059) by electron-beam evaporation of natural Ge and of isotopically enriched ^{70}Ge and ^{73}Ge target crystals with ^{73}Ge concentrations of 0.1% and 95.6%, respectively. The preparation of these crystals is described in more detail in Ref. 61. For the a-Ge films with intermediate ^{73}Ge concentrations of 31% and 51%, the appropriate amounts of ^{70}Ge and ^{73}Ge were electron-beam melted in a single Be crucible before deposition in order to ensure a homogeneous mixing. The substrates were cooled down to 77 K for the deposition of amorphous Ge films with a thickness around 1 μm. For the samples with low ^{73}Ge con-

centration, the densities of dbs could be determined by conventional ESR and were in the range of 10^{18-19} cm^{-3}. Defect densities of the samples with higher ^{73}Ge concentrations were similar, based on conductivity and optical absorption measurements. Care was used to avoid artificial broadening of the EDMR signal by magnetic field modulation and the incident microwave power. Unless otherwise specified, the measurement temperature was adjusted to around 70 K. No temperature-dependent broadening was observed in EDMR up to 100 K consistent with ESR studies on a-Ge:H, which report lifetime broadening of dbs in a-Ge above 150 K.(56, 62) At temperatures below 40 K, the detection of the EDMR signal is difficult because of the small sample conductivity.

For the electrical measurements, interdigitated Cr-Au contacts with finger spacings of 50 μm were deposited on 4×10 mm^2 sample pieces. Because of substantial peeling off from the glass substrate during lithography, somewhat larger contacts had to be prepared manually with silver paint for one sample with [^{73}Ge] = 31%. For the EDMR measurements, a dc voltage around 100 V was applied to the contacts, resulting in typical currents of the order of 1 μA at 70 K. Resonant current changes below 1 pA, which correspond to relative changes of the conductivity on a level of $\Delta\sigma/\sigma \approx 10^{-6}$, were resolved with good signal-to-noise ratio after amplification with a Stanford Research SR570 Low-Noise current preamplifier via magnetic field modulation, lock-in detection, and, in some cases, signal averaging for several days.

As shown previously for a-Si,(63, 64, 65) the spin dependence of the hopping processes between adjacent dbs can be exploited for a very selective and sensitive detection of their ESR signal, which would be impossible otherwise for the films with high ^{73}Ge concentrations under investigation here. In addition, ESR spectra of thin film samples typically suffer from background impurities in the glass substrate and in other parts of the spectrometer. This is avoided in EDMR of a-Ge, as in measurements of spin-dependent dark conductivity only the resonant changes of paramagnetic states close to the Fermi level contribute. Typically, a nonresonant background is observed in EDMR because of the magnetic-field dependence of the conductivity. A possibility for the separation even of broad EDMR spectra from this magnetoconductivity background is shown in Fig. 5.1. While the EDMR intensity scales approximately as $\Delta\sigma \propto T$ in the investigated temperature range, the magnetoconductivity features were found to scale rather similar to $\Delta m \propto T^2$. Therefore, the relative intensity $\Delta\sigma/\Delta m \propto T^{-1}$ is greatest at low temperatures, as shown in Fig. 5.1. Because of the high overall sample impedance, the best signal-to-noise and signal-to-background ratio is obtained at temperatures around 70 K.

The inset of Fig. 5.1 shows that the temperature-dependent dc conductivity falls off as $\sigma \propto \exp[(T/T_0)^{-1/4}]$, as expected for variable range hopping in unhydrogenated amorphous semiconductors with a large density of dbs close to the Fermi level.(56, 66, 67) According to Ref. 68, the average tunnelling range in such a material is proportional to $T^{-1/4}$, since with increasing temperature a larger number of localized states is involved in

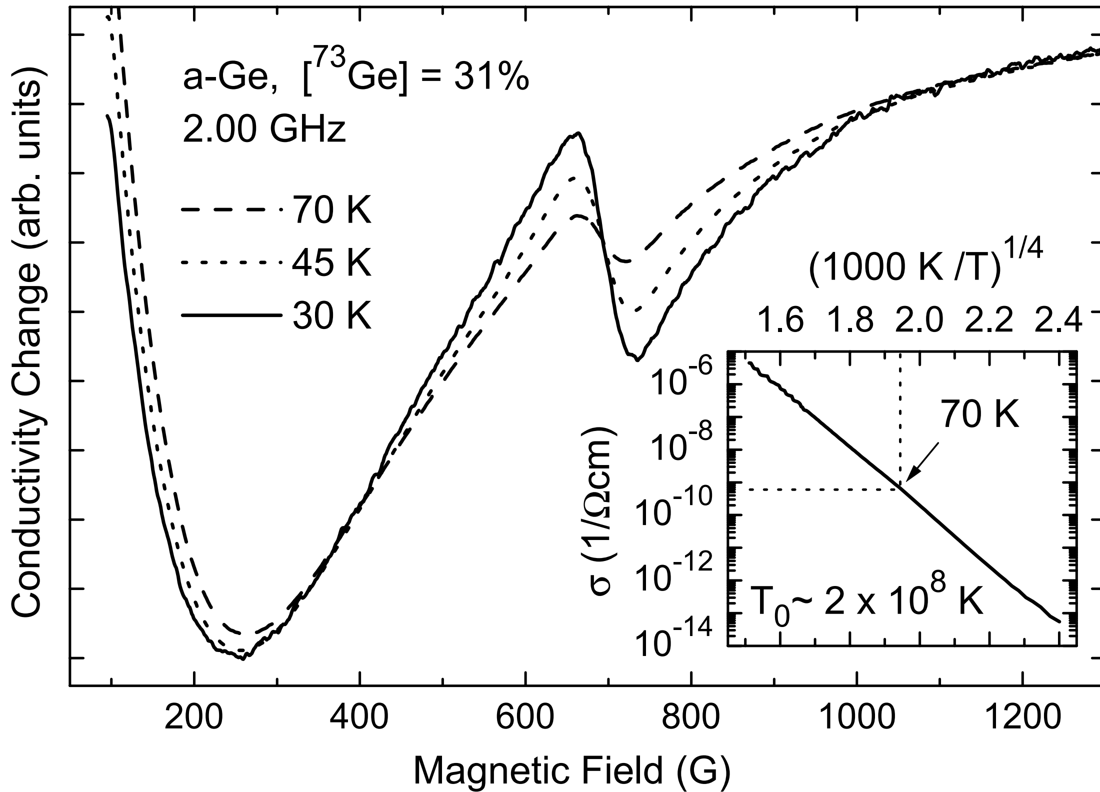

Figure 5.1: Example for the temperature dependence of the EDMR signal normalized to the background caused by magnetoconductivity. The broad EDMR can be separated from the nonresonant background via its different temperature dependence. The inset shows the temperature dependence of the dc dark conductivity with the $\exp[(T/T_0)^{-1/4}]$ dependence typical for variable range hopping. The microscopic interpretation of T_0 in terms of the density of states and the localization radius is discussed in the context of Eq. (5.12).

the tunnelling processes. To exclude significant exchange narrowing of the EDMR signals due to wave function overlap at large defect densities,(29) we additionally investigated hydrogenated a-Ge:H films with natural isotope concentration, where due to the much lower defect density of the order of 10^{17} cm^{-3}, the hopping rates are so small that no spin-dependent dark conductivity can be observed. To perform EDMR on these samples, charge carriers were exited into the bands by illumination with white light or with the visible lines of a 5 W argon ion laser, and the spin-dependent effects on recombination were monitored through photoconductivity measurements.(58) In contrast, no significant photoconductivity was observed in the unhydrogenated a-Ge films because of the higher defect density.

5.2 EDMR results

5.2.1 Isotopically pure a-^{70}Ge

The unhydrogenated a-^{70}Ge sample is virtually free from nuclear spins and therefore allows one to investigate the origin and magnitude of the contributions to the spin resonance linewidth other than hyperfine interaction. The remaining broadening mechanisms are dipolar and exchange broadening with neighboring dbs, lifetime broadening, as well as broadening by a distribution of g-factors. The former mechanisms are expected to depend only weakly on the magnetic field, whereas the last mechanism is directly proportional to the field and to the microwave frequency (see Sec. 5.3.1). As shown in Fig. 5.2, where the EDMR spectra are given as a function of the applied magnetic field B, the experimental linewidth for a pure a-^{70}Ge sample depends strongly on the employed microwave frequency and varies from only 2.6 G at 0.434 GHz to 43 G at 9.35 GHz. This indicates that it is mostly determined by g-factor broadening. Therefore, the same spectra are shown versus $g = h\nu/\mu_B B$ in Fig. 5.3, with Planck's constant h, Bohr's magneton μ_B, and the microwave frequency ν. Much closer similarity of the three spectra is indeed observed in this plot, as expected for g-factor broadening. However, also in Fig. 5.3 the linewidths and lineshapes still do not coincide completely.

The dashed lines in Figs. 5.2 and 5.3 show a simultaneous curve fit assuming a distribution of g-factors according to the same powder pattern for all spectra due to the random orientation of dbs in the amorphous network. This powder pattern is indicated by the dotted lines in Figs. 5.2 and 5.3 and is defined by the extremal g-factors $g_\perp = 2.026$ and $g_{||} = 2.013$ for the orientations of the external magnetic field parallel and perpendicular to the defect axis, i.e., the long axis of the dangling bond hybrid orbital.[9, 24] In addition, a Gaussian distribution of g-factors needs to be considered for the simulation of the observed lineshapes, similar to the fitting procedures of Refs. 24, 50, 51. Typically, the width $\Delta B_{\rm pp}^{\rm SO}(\theta)$ of such a distribution will depend on the orientation θ of the defect axis with respect to the external field. To reduce the number of possible fitting parameters, $\Delta B_{\rm pp}^{\rm SO}(\theta)$ was assumed here to be proportional to the g-factor shift $\Delta g(\theta) = g(\theta) - g_0$ from $g_0 = 2.0023$ of the free electron. Such a proportionality implies that the g-factor fluctuations causing the frequency-dependent broadening are caused by fluctuations of the spin-orbit interaction, which is also responsible for the g-factor shift with respect to the free electron value. The validity of this assumption is supported by the scaling of the linewidth $\Delta B_{\rm pp}^{\rm exp} = 8$ G of dbs in a-Si with the average g-factor shift $\bar{g}_{\text{a-Si}} - g_0 = 3.2 \times 10^{-3}$ in comparison to a-Ge dbs with $\Delta B_{\rm pp}^{\rm exp} = 48$ G and $\bar{g}_{\text{a-Ge}} - g_0 = 20 \times 10^{-3}$, which is proportional to the magnitudes of the spin-orbit coupling constants $\lambda_{\rm Si} = 149$ cm^{-1} and $\lambda_{\rm Ge} = 940$ cm^{-1}.[56, 69] The average g-factor $\bar{g} = 2.022$ of the powder patterns in Figs. 5.2 and 5.3 agrees with the reported values for $\bar{g} = \frac{1}{3}g_{||} + \frac{2}{3}g_\perp$, which were found in the range of 2.0018–2.023, and below 2.018 only for complex formation due to significant oxy-

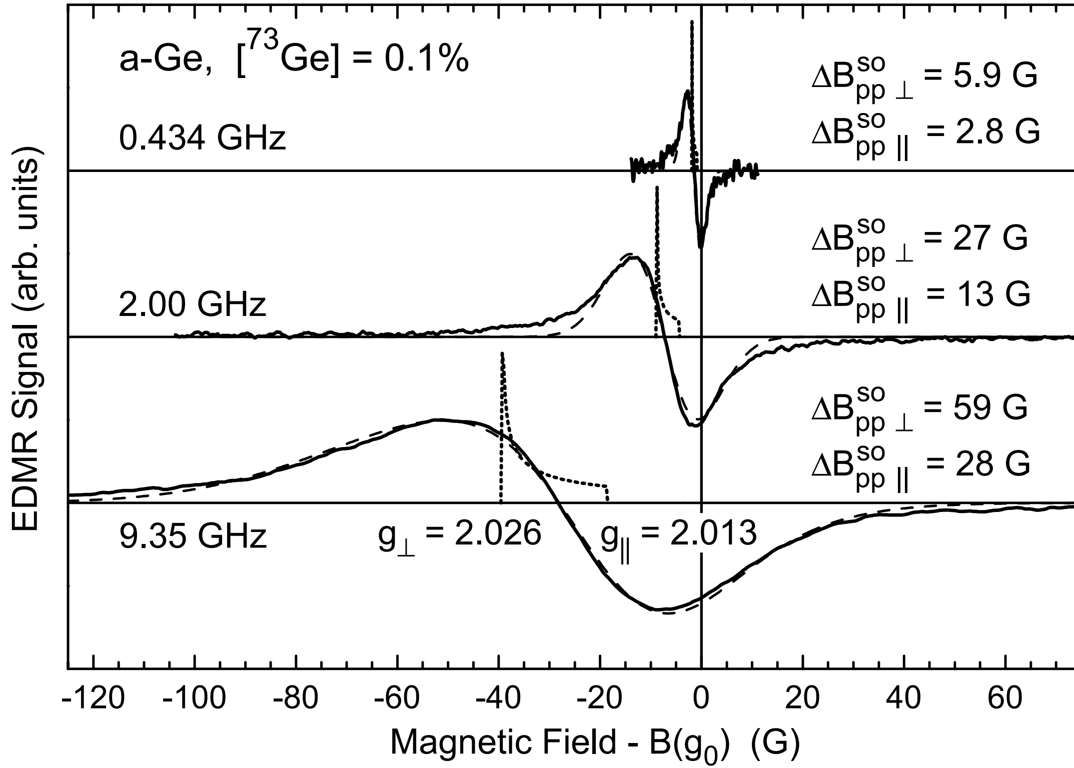

Figure 5.2: EDMR signal of pure a-^{70}Ge at different microwave frequencies. The magnetic field axes are offset such that the fields corresponding to the resonance of free electrons with $g_0 = 2.0023$ coincide. The dashed lines are fits based on the powder patterns indicated by the dotted lines and an additional Gaussian broadening $\Delta B^{\mathrm{SO}}_{\mathrm{pp}}(\theta)$ due to disorder. $\Delta B^{\mathrm{SO}}_{\mathrm{pp}||}$ and $\theta = 0°$ correspond to dbs oriented parallel to the magnetic field direction, and $\Delta B^{\mathrm{SO}}_{\mathrm{pp}\perp}$ and $\theta = 90°$ to dbs in perpendicular orientation.

gen contamination.[70, 71, 72] For dbs at the Ge/GeO_2 interface of crystalline germanium, $g_\perp = 2.022$ and $g_{||} = 2.005$ according to Ref. 73.

The width of the g-factor distributions visible in Fig. 5.3 (or the ratios of the linewidths and the corresponding microwave frequencies given in Fig. 5.2) seems to decrease at higher microwave frequencies, indicating a frequency-independent broadening mechanism of the order of 1 G. It can be estimated from the linewidths of the ^{73}Ge-enriched samples that such a broadening could only be accounted for by hyperfine interactions with ^{73}Ge, if the ^{73}Ge-concentration in this nominally pure a-^{70}Ge-sample was around 1%. This is not the case, as the residual ^{73}Ge concentration of the target crystal is only 0.1%, which suggests the presence of another frequency-independent broadening process in addition to the hyperfine interaction. Most probably, this process is the dipolar interaction between adjacent dangling bonds due to the high defect concentration in the investigated samples. An estimate for this dipolar broadening can be calculated based on the statistical theory of dipolar broadening (Sec. 5.3.2). For dipolar coupling between the electronic spins $S = 1/2$

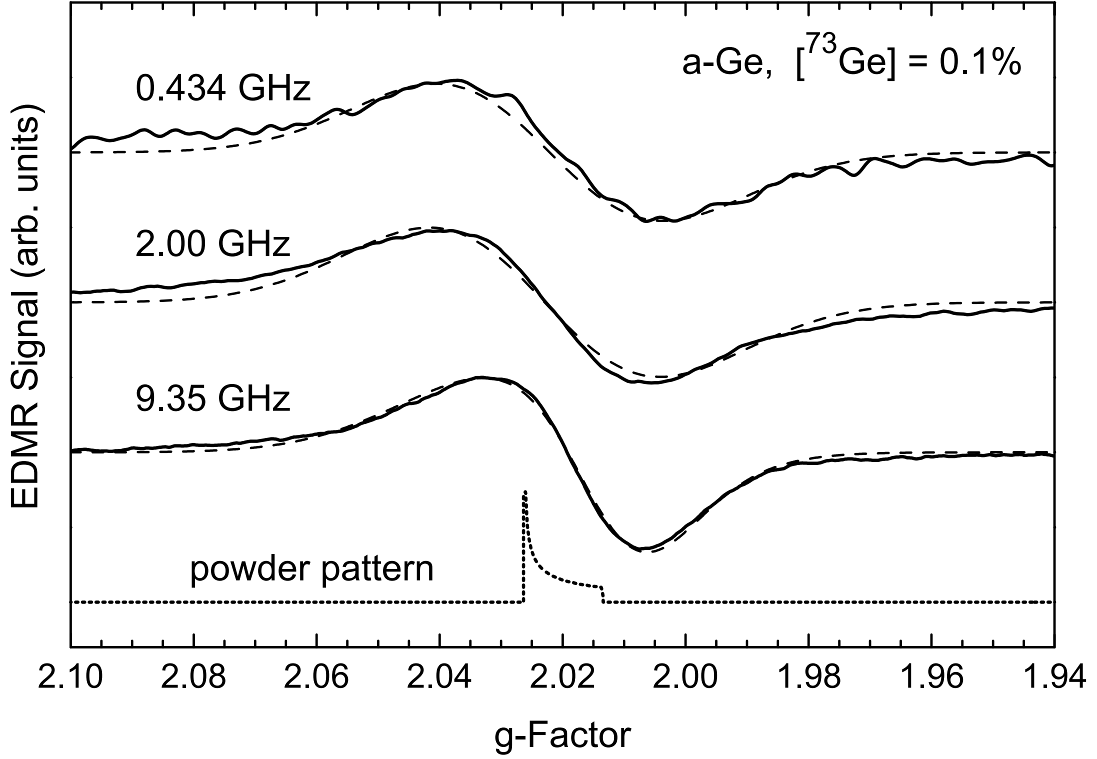

Figure 5.3: Spectra and fits of Fig. 5.2, but now plotted versus a decreasing g-factor axis. In the absence of nuclear spins, the linewidth is almost proportional to the microwave frequency, indicating that it is influenced dominantly by g-factor anisotropy. The smaller width at 9.35 GHz indicates a frequency-independent broadening mechanism, probably caused by dipolar electron-electron spin interactions of the order of 1 G at $N_S = 10^{19}$ cm^{-3}.

of adjacent dbs, the calculation of Ref. 59 predicts a Lorentzian line with a width

$$\Delta B_{\mathrm{pp}}^{\mathrm{dip}} = \tfrac{\pi}{9}\mu_0\mu_B g N_S = N_S \times 0.82 \times 10^{-19}\ \mathrm{G\ cm}^3. \tag{5.1}$$

Dipolar broadening of the order of 1 G is indeed expected from this calculation for the spin density N_S of this a-^{70}Ge sample, which is about 10^{19} cm^{-3}. Therefore, dipolar electron-electron spin interactions probably account for a significant fraction of the EDMR linewidth of the a-^{70}Ge films at 0.434 GHz. At X-band microwave frequencies, this contribution can be neglected for the analysis, because the observed linewidths are larger than 40 G. The effective dipolar distance would be reduced for an inhomogeneous distribution of dbs, so that Eq. (5.1) gives a lower limit for the effective dipolar broadening. As the linewidth broadening observed is close to this limit, we can exclude strongly clustered dbs in our a-Ge films, unless exchange narrowing exactly compensates for the dipolar broadening.

A further peculiarity of EDMR of amorphous Ge, which was already reported earlier in Ref. 58 for a-Ge:H with natural isotopic composition, however without a detailed analysis,

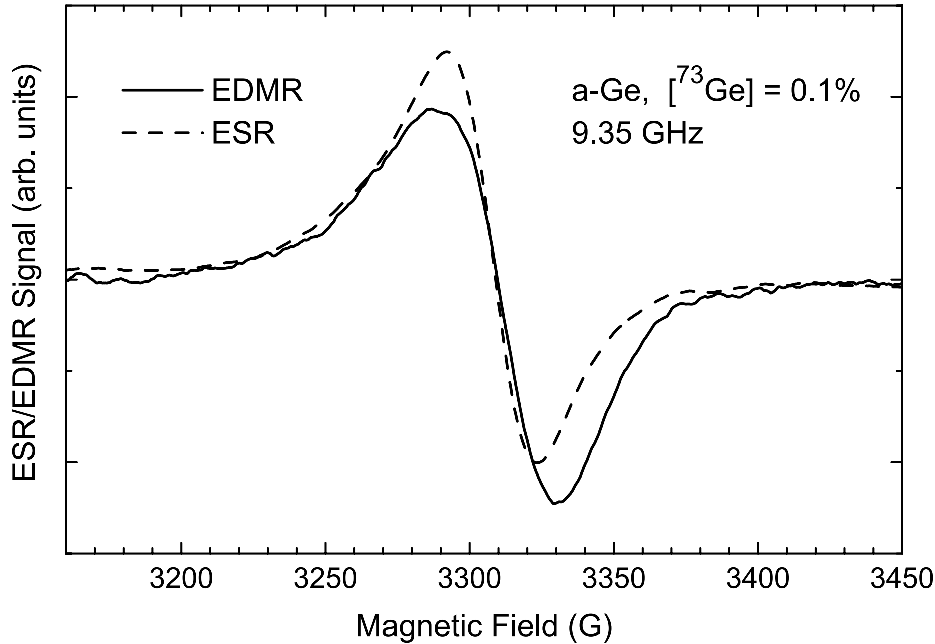

Figure 5.4: Different lineshape of the ESR and EDMR signals of the same a-^{70}Ge sample under identical measurement conditions. A similar difference was observed in Ref. 58 for a-Ge:H with natural isotope concentration.

is found in the nuclear-spin free a-^{70}Ge-film in an even more pronounced way. As shown in Fig. 5.4, the ESR and EDMR spectra of the same a-^{70}Ge film show a very different lineshape, although the experimental conditions such as the applied microwave power, the modulation amplitude, and the speed of the magnetic field sweep were the same in both experiments. In particular, the EDMR line is somewhat broader and more asymmetric than the resonance line observed in conventional ESR. In contrast to the experiments of Ref. 58, in which spin-dependent photoconductivity was measured under illumination, lifetime broadening due to recombination does not play a role here, where the hopping conductivity of an a-^{70}Ge sample was monitored in the dark. The possible influence of the hopping processes on the linewidths will be shown to be negligible in Sec. 5.2.2. It therefore appears most likely that the main contribution to the spin-dependent dark conductivity comes from a particular subensemble of dbs in a-Ge, whereas all spins present in the sample, possibly also complexes of dbs with oxygen,(72) contribute equally to the microwave absorption in conventional ESR measurements. A subensemble of dbs dominating the EDMR signal could for example be composed of those defects, which have a greater overlap than typical of their wave function with that of adjacent dbs. Consequently, the hopping rates will be increased at these dbs, which makes them more likely to participate in electronic transport, and the EDMR linewidth to be increased by dipolar interaction. Alternatively, a subensemble with increased coupling to neighboring spins could be characterized by relatively large g-factor fluctuations due to site-dependent fluctuations of the spin-orbit coupling. The hopping rate between such adjacent dbs is not high enough for the opposite effect on the linewidth to occur, a significant motional narrowing as observed in nearly metallic Si or SiC samples with similar concentrations of

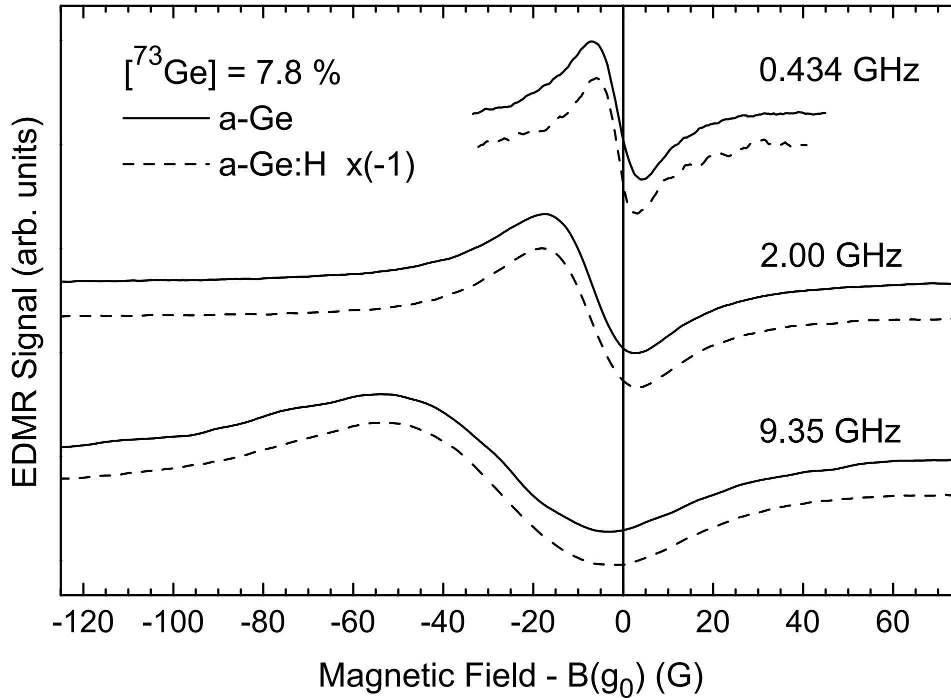

Figure 5.5: EDMR signals of a-Ge with natural isotope concentration at different microwave frequencies. The magnetic field axes are offset such that the fields corresponding to $g_0 = 2.0023$ coincide. The dashed lines are spin-dependent photoconductivity measurements of hydrogenated a-Ge:H samples with significantly lower defect density. Under resonance conditions, the dark conductivity of a-Ge is enhanced, while the photoconductivity of a-Ge:H is quenched. For better comparison, the EDMR signals of a-Ge:H are therefore inverted. The larger linewidth of unhydrogenated a-Ge compared to a-Ge:H is probably caused by dipolar interactions between the electronic spins at 0.434 GHz.

shallow donors.(29, 74) In the ^{73}Ge-enriched samples discussed below, the ESR background caused by defects in the substrate completely overwhelms the very broad ESR signals of the dbs. However, since the densities of dbs were around $10^{18} - 10^{19}$ cm^{-3} for all a-Ge samples studied, the same subensemble of dbs will participate in hopping transport in the different films, independent of the nuclear spin concentration. The additional broadening observed in samples with higher nuclear spin concentrations must therefore be related to hyperfine interactions.

5.2.2 a-Ge and a-Ge:H with natural isotope composition

The EDMR linewidths observed for the sample free of ^{73}Ge nuclear spins now enable us to identify the additional broadening due to hyperfine interactions in ^{73}Ge-enriched samples. A comparison of Fig. 5.5 with the EDMR spectra of a-Ge with natural ^{73}Ge concentration $c = 7.8\%$, and of Fig. 5.2 for pure a-^{70}Ge shows that the EDMR lines of natural a-

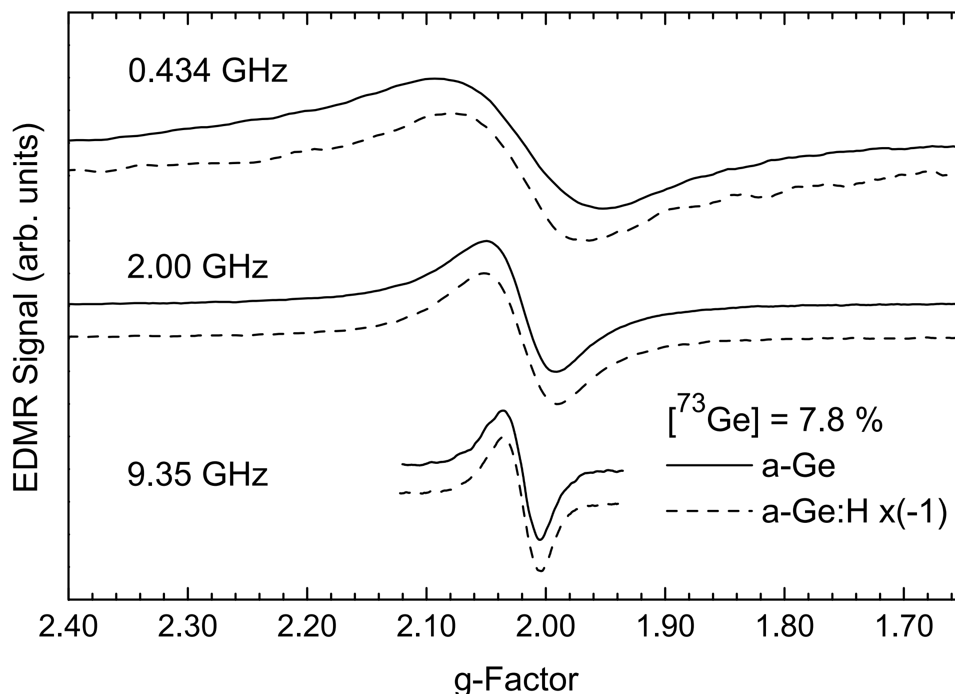

Figure 5.6: The EDMR spectra of a-Ge with natural isotope concentration of Fig. 5.5 plotted versus a decreasing g-factor axis. Note the much wider g-factor scale in comparison to Fig. 5.3. The EDMR signals of a-Ge:H were again inverted for better comparison. Whereas the unresolved hyperfine broadening due to the nuclear spins is negligible at 9.35 GHz, it is significant at lower microwave frequencies.

Ge broaden significantly at microwave frequencies of 0.434 and 2.00 GHz, while only a small broadening is caused by the ^{73}Ge nuclear spins at 9.35 GHz. The difference of the broadening effects is even more evident from a comparison of Figs. 5.6 and 5.3, where the spectra are again shown versus the g-factor. The linewidth at 0.434 GHz increases to 11 G by more than a factor of four in the sample with natural ^{73}Ge concentration compared to the nuclear-spin free a-^{70}Ge sample. However, the relative probability $c/(1-c)$ to find dbs at a central ^{73}Ge nucleus is still below 10% for this nuclear spin concentration. Therefore, this broadening must originate from hyperfine interactions with a large number of surrounding nuclei.

To compare the effects of different spin-dependent processes and the total defect density on the EDMR signal, hydrogenated a-Ge:H samples of natural isotopic composition were available. In Figs. 5.5 and 5.6, the spectra obtained via spin-dependent recombination in a-Ge:H are compared to the spectra obtained for spin-dependent hopping in a-Ge at the same ^{73}Ge concentration, but at a much lower density of dbs in the a-Ge:H sample. While an enhancement of spin-dependent hopping occurs in a-Ge under spin resonance conditions, a resonant quenching of the photoconductivity is observed in a-Ge:H.(58) For better comparison, the EDMR spectra for a-Ge:H have been inverted in

Figs. 5.5 and 5.6. For spin-dependent recombination at low defect concentrations, both the resonance of holes in the valence band tail, as well as a superposition of the resonances of dbs and electrons in the conduction band tail are observed in the spin-dependent photoconductivity of a-Si:H. However, at defect concentrations of 10^{17} cm^{-3} and above, the signal from dbs dominates in that material, as the spin-dependent hole diffusion process in the valence band tail is replaced by direct spin-independent tunnelling of the hole to a doubly occupied dangling bond.(75) The same appears to be the case in our a-Ge:H films, where no indication of the valence band tail resonances with $g = 2.054$ is found in spin-dependent recombination.(56) The nearly identical EDMR resonances of a-Ge:H with $N_S \approx 10^{17}$ cm^{-3} and a-Ge with $N_S \approx 10^{19}$ cm^{-3} at 2.00 GHz and 9.35 GHz show that at this ^{73}Ge concentration, hyperfine and g-factor broadening are much stronger than the dipolar broadening of adjacent dbs, and that the effects of exchange interactions and the lifetime dependence of hopping and recombination are negligible for the low-temperature linewidth.(59) Only at the lowest microwave frequency of 0.434 GHz, the EDMR spectra of a-Ge:H and a-Ge differ significantly (see Fig. 5.6). The observed linewidth change is opposite to the hyperfine broadening expected from the nuclear spins of hydrogen in a-Ge:H, which is expected to be below 1 G, similar to the observations of Ref. 76 for a-Si:H. Therefore, the different low-frequency linewidths are most probably again related to the electron-electron spin dipolar broadening in the unhydrogenated a-Ge sample, to which already the frequency-independent part of the EDMR linewidth of the ^{70}Ge sample was attributed before. Here, it is observed directly under the same experimental conditions as a linewidth difference in two samples with very different defect densities.

5.2.3 ^{73}Ge-enriched samples

A further increase of the concentration c of ^{73}Ge nuclear spins does not lead to a resolved hyperfine structure in EDMR, as shown in Figs. 5.7 and 5.8. Instead, the spectrum broadens continuously to a linewidth of about 300 G at 9.35 GHz for the pure ^{73}Ge sample. This type of broadening is remarkable, as sudden increases of the linewidth or the development of substructure in the outer parts of some spectra would be expected for any characteristic hyperfine interaction. Because of the magnetoconductivity background and the large EDMR linewidth, no resonances were resolved for 2.00 GHz at $c = 95.6\%$, and for 0.434 GHz at $c \geq 31\%$. Besides the EDMR linewidth, which varies over more than two orders of magnitude due to the variation of the concentration of nuclear spins, the lineshapes are changing significantly from a close to Lorentzian shape at $c \leq 51\%$ to a Gaussian shape at $c = 95.6\%$. The arrow in Fig. 5.8 indicates the onset of a shoulder in the spectrum with $c = 51\%$, which is interpreted as a remainder of the unresolved central Fermi contact interaction in the following sections. A similar shoulder around $\pm$(100-200) G from the center of the spectrum is weakly observed in the wings of the 2.00 GHz-spectrum of the sample with $c = 51\%$. In this case, it overlaps less with the central line,

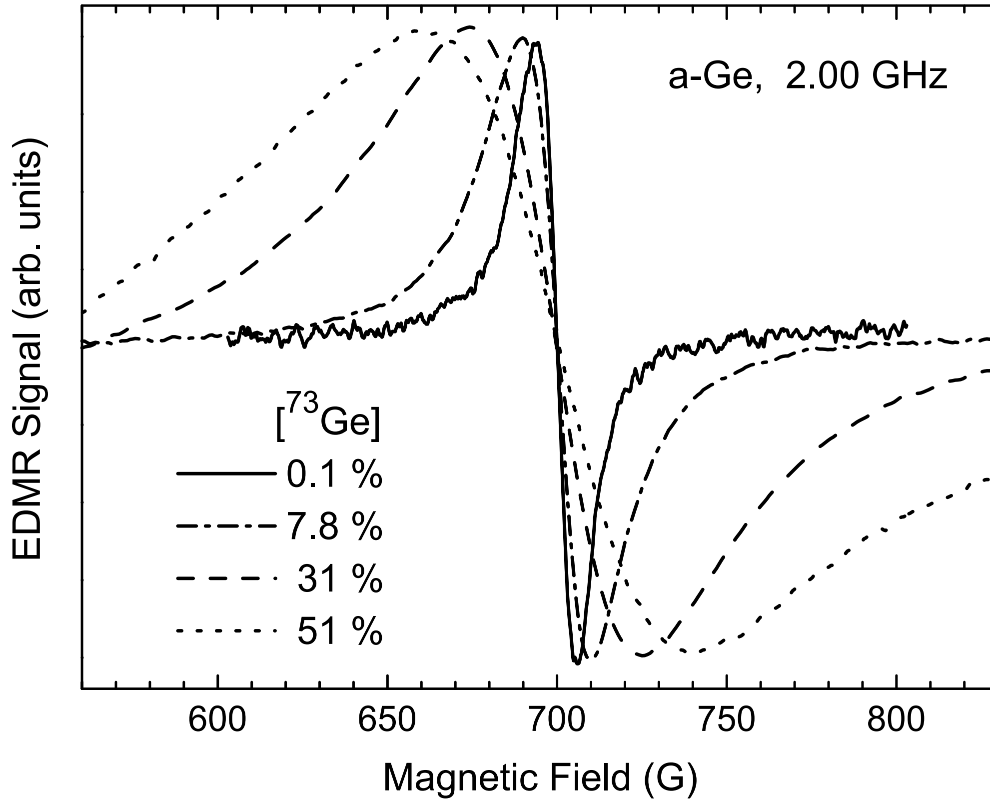

Figure 5.7: Broadening of the EDMR spectra measured at 2.00 GHz of a-Ge depleted of ^{73}Ge, with natural ^{73}Ge concentration, and enriched with ^{73}Ge. The spectra are normalized for the same peak-to peak amplitude and shifted to a common zero-crossing magnetic field.

but cannot be separated from the magnetoconductivity background unambiguously.

The peak-to-peak linewidths measured by EDMR in this work at different isotope concentrations and microwave frequencies are summarized in Tab. 5.1. As discussed above, the linewidths increase significantly with the ^{73}Ge concentration. The largest change is observed at 9.35 GHz between $c = 51\%$ and $c = 95.6\%$. The uncertainties of $\Delta B_{\mathrm{pp}}^{\mathrm{exp}}$ listed in Tab. 5.1 arise mostly from the possible errors during the subtraction of the magnetoconductivity background. Also included in Tab. 5.1 are the lineshape factors obtained via double integration from the measured derivative EDMR spectra according to Eq. (4.3). For the double integration, a spectral range of at least $8\times\Delta B_{\mathrm{pp}}$ was employed for all values except for the lineshape factors marked explicitly. Mostly Gaussian lineshape factors are found for the spectra at 9.35 GHz and low ^{73}Ge concentrations, as these spectra can be understood to be caused by a powder pattern and a Gaussian distribution of g-factors. At higher ^{73}Ge concentrations, the lineshape factors increase towards the Lorentzian value at all microwave frequencies. Only the very broad EDMR spectrum at $c = 95.6\%$ shows a clear Gaussian lineshape again. The reasons for this characteristic behavior will be discussed in detail in the following sections.

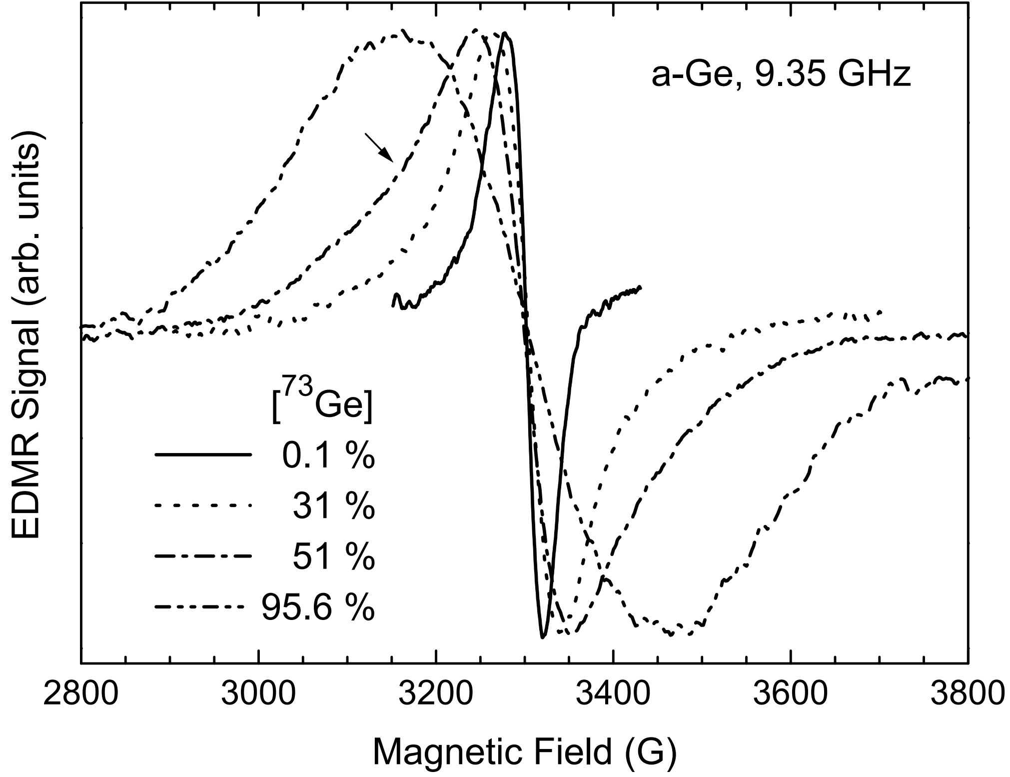

Figure 5.8: EDMR spectra at 9.35 GHz for the complete range of ^{73}Ge-concentrations. Note that the narrow spectrum with $c = 0.1\%$ is identical with the broadest spectrum of Fig. 5.2. The arrow indicates the onset of a shoulder in the spectrum with $c = 51\%$.

[^{73}Ge] (%)	Linewidth $\Delta B_{\rm pp}^{\rm exp}$ (G)			Lineshape factor l		
	0.4 GHz	2 GHz	9 GHz	0.4 GHz	2 GHz	9 GHz
a-Ge 0.1	2.6±0.2	12±1	43±2	2.4±0.3	2.6±0.3	1.6±0.2
a-Ge 7.8	11±1	21±1	48±2	2.2±0.4	2.8±0.2	2.1±0.2
a-Ge:H 7.8	9±1	21±1	47±2	2.8±0.4	2.9±0.3	2.2±0.2
a-Ge 31		52±3	73±4		3.0*±0.4	2.6±0.3
a-Ge 51		78±5	112±7		3.3*± 0.7	3.0±0.3
a-Ge 95.6			300 ± 10			1.1*± 0.2

Table 5.1: Observed peak-to-peak linewidths $\Delta B_{\rm pp}^{\rm exp}$ and lineshape factors l for the derivative EDMR spectra of Figs. 5.2–5.8. The uncertainties of $\Delta B_{\rm pp}^{\rm exp}$ arise mostly from the possible errors due to the the substraction of the magnetoconductivity backgrounds. For the double integration, a spectral range of $8 \times \Delta B_{\rm pp}^{\rm exp}$ was employed for all lines except when a narrow integration range of $3 - 6 \times \Delta B_{\rm pp}^{\rm exp}$ is indicated by (*). In these cases, approximate wings had to be estimated from the well resolved central part of the EDMR spectra.

5.3 Hyperfine interactions with ^{73}Ge

5.3.1 Spin Hamiltonian

The spin Hamiltonian of isolated, singly occupied dangling bonds with spin $S = 1/2$ is dominated by the Zeeman interaction given by the axial g-tensor $\hat{g}$ and the external magnetic field $\vec{B}$. Additionally, the Hamiltonian of Eq. (3.20) contains all hyperfine interactions $\hat{A}_n$ with the surrounding nuclear spins I_n. Clearly, variations in $\hat{g}$ lead to much larger Zeeman broadening at higher magnetic fields, whereas the hyperfine broadening is independent of B. For axial hyperfine tensors with only small anisotropic components, the effective hyperfine interactions are given by $A_n = A_{n,\text{iso}} + A_{n,\text{aniso}}(3\cos^2\theta - 1)$ for orientations of the hyperfine axes at an angle θ with respect to the magnetic field. At the microwave frequencies used, the resonance fields for ESR transitions are given approximately by

$$B = \frac{h\nu}{g\mu_B} - \sum_n \frac{A_n}{g\mu_B} m_n - \sum_n \frac{A_n^2}{2g\mu_B\, h\nu}\left[I(I+1) - m_n^2\right] + \ \ldots, \qquad (5.2)$$

where the magnetic quantum number takes the values $m_n = -I, \ldots, +I$ for the ^{73}Ge nuclei with nonzero nuclear spin $I = 9/2$. Higher-order terms and cross-coupling terms between different nuclear spins have been omitted in Eq. (5.2). The energy eigenvalues and the magnetic fields, at which the strongly allowed ESR transitions occur at $\nu = 0.434$ GHz and 2.00 GHz are shown in Fig. 5.9 for an isotropic Zeeman interaction with $g = 2.022$, i.e., for $h\nu/g\mu_B = 154$ and 707 G, and for an isotropic hyperfine interaction $A_{0,\text{iso}} = 29\text{ G} \times g\mu_B$ with a single nuclear spin. To first-order perturbation theory, the transition fields are given by $2I + 1$ equally spaced hyperfine satellites centered around the dominant Zeeman field. Additionally, all transitions are shifted towards lower magnetic field due to the second-order term of Eq. (5.2). For the example shown in Fig. 5.9 the first-order shifts are -130 G to $+130$ G, and the second-order shifts at 0.434 GHz are -12 to -67 G, which cannot be neglected at this microwave frequency. At 2.00 GHz, the second-order corrections are only -3 to -15 G, which is only 2% of the Zeeman field. Clearly, second and higher order terms due to hyperfine interaction of this magnitude must be taken into account in Eq. (5.2) for an accurate determination of the g-factor and the hyperfine splittings at low frequencies, similar to the hyperfine splittings around 280 G$\times g\mu_B$ of ^{73}Ge-atoms in the $[\text{GeO}_4]^-$ centers in α-quartz at X-band frequencies.[9, 77]

We will show below that hyperfine interactions as large as $29\text{ G} \times g\mu_B$ are present in a-Ge, but have significant influence on the linewidth only at $c > 60\%$. Since the EDMR spectrum of the sample with $c = 95.6\%$ could be separated clearly from the magnetoconductivity background only at $\nu = 9.35$ GHz, and since also the other hyperfine

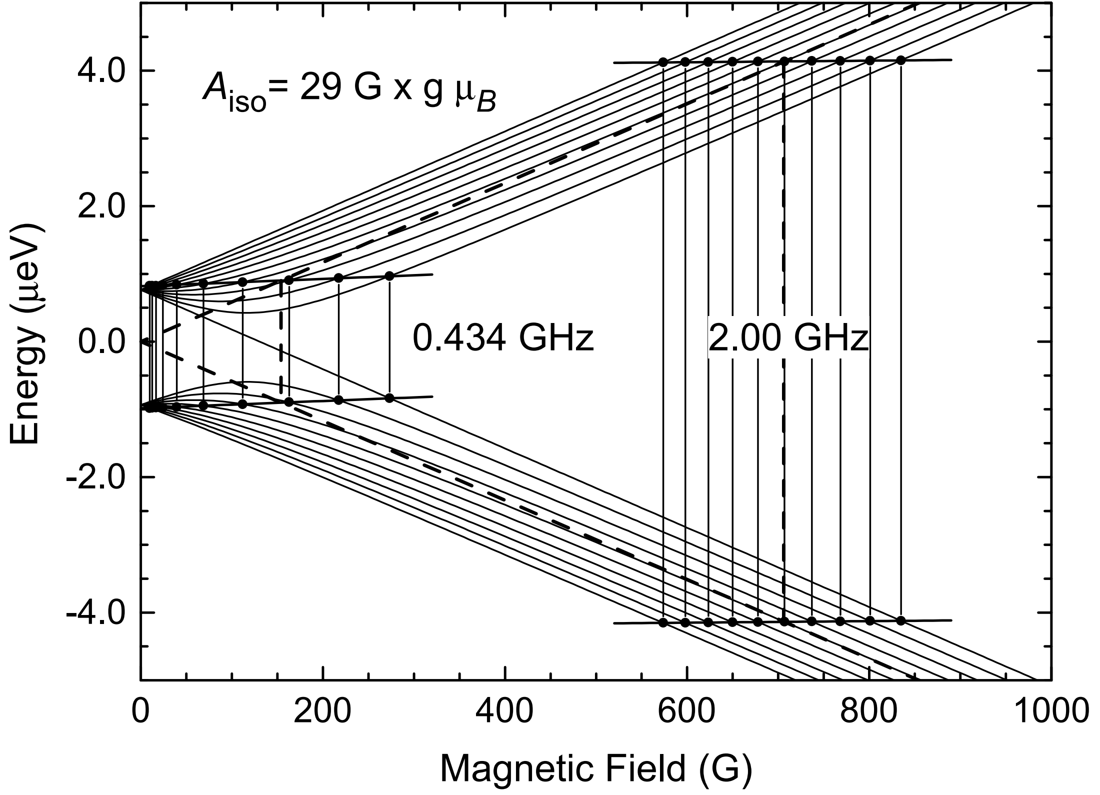

Figure 5.9: Breit-Rabi diagram for the spin Hamiltonian (3.20) with a single isotropic g-factor $g = 2.022$ and hyperfine interaction $A_{0,\text{iso}} = 29\ \text{G} \times g\mu_B$. The transition fields for electron spin resonance at 0.434 and 2.00 GHz are shown by the vertical lines. Indicated by the dashed lines are the energy levels and transition fields without perturbations by a nuclear magnetic moment.

broadenings listed in Tab. 5.1 do not exceed the respective resonant magnetic fields by more than 12%, it is sufficient to restrict the linewidth analysis to the first-order terms of Eq. (5.2) only.

A purely isotropic hyperfine interaction A_{iso} as discussed above is characteristic for spin states with spherically symmetric (s-like) dangling bond wave functions. The simplest approach for a complete microscopic description of a dangling bond wave function Ψ_{db} involves the linear combination of the 4s and 4p valence orbitals Ψ_s and Ψ_p of the outer shell of Ge atoms at the atomic sites $\vec{r}_n$

$$\Psi_{db}(\vec{r}) = \sum_n \alpha_n \Psi_s(\vec{r} - \vec{r}_n) + \sum_n \beta_n \Psi_{p_x,p_y,p_z}(\vec{r} - \vec{r}_n). \tag{5.3}$$

Neglecting the overlap of the different atomic orbitals within this superposition, and the core states and bonding orbitals like the 3d-states not included in this form of Ψ_{db}, a one-to-one correspondence between the hyperfine parameters $A_{n,\text{iso}}$ and $A_{n,\text{aniso}}$, and the projections α_n^2 and β_n^2 of the dangling bond wave function onto the atomic wave functions

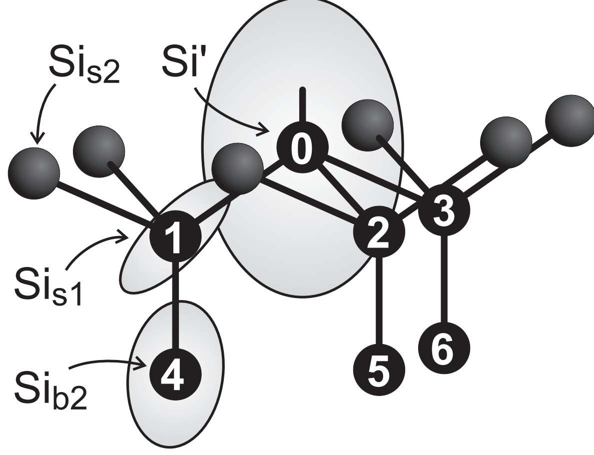

Figure 5.10: As an illustration for the concept of Eq. (5.3), the hyperfine tensors as calculated in Ref. 16 for the P_b wave function at the Si-SiO_2 interface are shown as ellipsoids, with $A_{0,\mathrm{iso}} = -129$ G $\times\, g\mu_B$, and $A_{0,\mathrm{aniso}} = -30$ G $\times\, g\mu_B$ at the defect atom labelled Si'. The hyperfine tensors found at the three backbonding atoms labelled Si_{s1} were $A_{1-3,\mathrm{iso}} = +1.2$ G $\times\, g\mu_B$, and $A_{1-3,\mathrm{aniso}} = -0.8$ G $\times\, g\mu_B$, and those at the next-nearest neighbors labelled Si_{b2} were $A_{4-6,\mathrm{iso}} = -10$ G$\times g\mu_B$, and $A_{0,\mathrm{aniso}} = -1.6$ G $\times\, g\mu_B$.

$\Psi_s(\vec{r} - \vec{r}_n)$ and $\Psi_p(\vec{r} - \vec{r}_n)$ is obtained for locally axial symmetry.[9, 24, 32] The isotropic hyperfine parameters $A_{n,\mathrm{iso}}$ are then interpreted as local Fermi contact interaction of the s-like components of the model wave function of Eq. (5.3). The anisotropic parameters $A_{n,\mathrm{iso}}$ are interpreted as the local dipolar interaction of the p-like components of the electronic spin with the ^{73}Ge nucleus with index n, so that

$$A_{n,\mathrm{iso}} = \alpha_n^2 A_{\Psi_s} = \alpha_n^2\, \frac{2\mu_0}{3} g\mu_B g_n \mu_n |\Psi_s(0)|^2$$

$$A_{n,\mathrm{aniso}} = \beta_n^2 A_{\Psi_p} = \beta_n^2\, \frac{2\mu_0}{5 \cdot 4\pi} g\mu_B g_n \mu_n \langle r^{-3} \rangle, \tag{5.4}$$

where $\mu_0 = 4\pi \times 10^{-7}\, \frac{\mathrm{Vs}}{\mathrm{Am}}$, g_n and μ_n denote the nuclear g-factor and the nuclear magneton, $|\Psi_s(0)|^2$ and $\langle r^{-3} \rangle$ are the characteristic atomic spin density and dipolar distance, and $n = 0$ is used to label the central defect atom (see Fig. 5.10). The atomic hyperfine interactions $A_{\Psi_s} = 843$ G $\times\, g_0\mu_B$ and $A_{\Psi_p} = 17$ G $\times\, g_0\mu_B$ have been calculated using Hartree-Fock-Slater integrals,[9] so that in principle the fractions α_n^2 and β_n^2 of the dangling bond wave function can be mapped out with the measured hyperfine parameters.

Although the symmetry information and therefore β_n^2 is not directly accessible in amorphous materials, the anisotropic contribution of the hyperfine interaction with respect to the symmetry axis of the g-tensor can in principle be extracted from differences in the satellite widths. In a-Si:H, the total spin density $\alpha_1^2 + \beta_1^2$ in the sp^3 hybrid of least one backbonding orbital to the atoms Si_{s1} with $n = 1 \ldots 3$ in Fig. 5.10 was estimated from the broadening of the central line and its hyperfine satellites. It was concluded that at the central defect atom $\alpha_0^2 = 6\%$ of the spin wave function is contributed from a $3s$ orbital and about $\beta_0^2 = 50\%$ of a nonbonding $3p$ orbital. About $\alpha_1^2 + \beta_1^2 \approx 10\%$ - 20% of the dangling bond spin wave function in a-Si:H comes from at least one backbonding sp^3 hybrid orbital.[24, 51, 52, 53] Similar to ^{29}Si, which is the only Si isotope with non-zero nuclear spin $I_{29} = 1/2$, only ^{73}Ge with a natural abundance of 7.8% has a non-zero nuclear spin

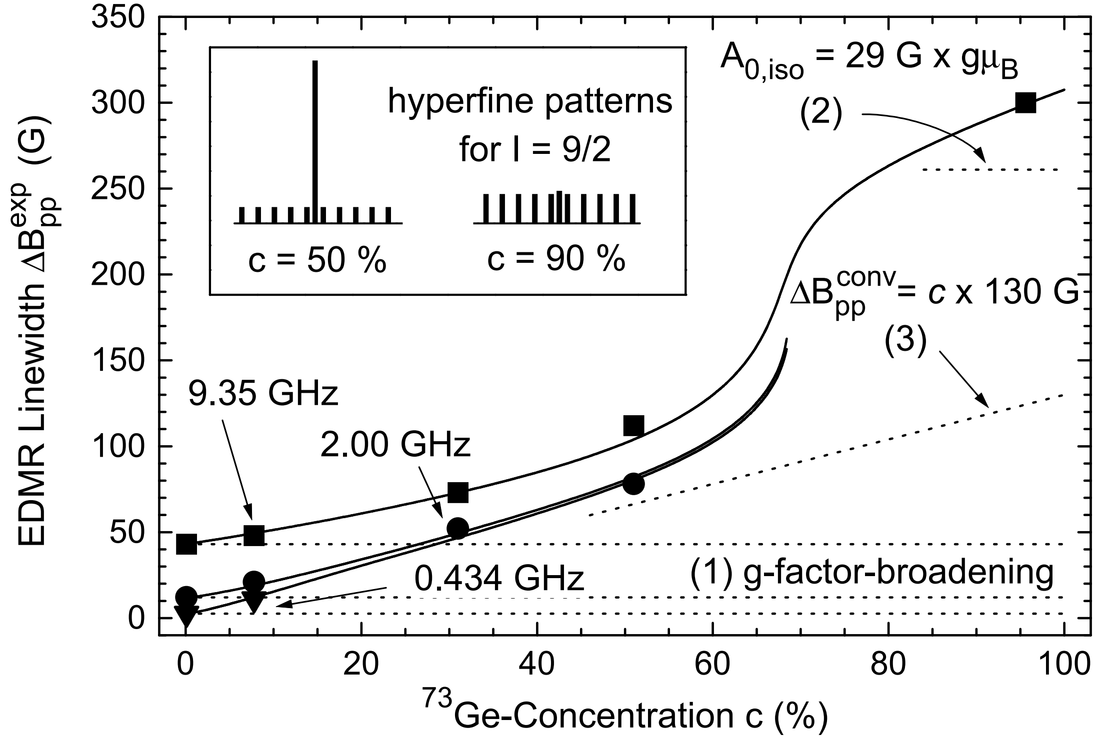

Figure 5.11: Experimentally determined peak-to peak linewidths $\Delta B_{\mathrm{pp}}^{\mathrm{exp}}$ of the spectra shown in Figs. 5.2-5.8. The continuous lines were calculated from a convolution assuming (1) a frequency-dependent Gaussian broadening due to a g-factor distribution, (2) a central hyperfine interaction of 29 G$\times g\mu_B$, which itself would lead to a spread of hyperfine satellites over 261 G, and (3) a Lorentzian broadening $\Delta B_{\mathrm{pp}}^{\mathrm{conv}}$ due to the surrounding spins, which increases linearly with the nuclear spin concentration c. The intensity patterns for $c = 50\%$ and 90% shown in the inset explain the qualitative change around $c = 70\%$ due to contribution (2), which causes the sudden increase of the linewidth by more than 100 G.

$I_{73} = 9/2$. The relative intensity of each of the $2I + 1$ hyperfine satellites at a given nuclear spin concentration c in a-Ge is expected to be $c/(2\ I_{73} + 1) = c/10$, which is five times smaller than $c/(2\ I_{29} + 1) = c/2$ in a-Si. In addition to this lower intensity, the smaller atomic hyperfine interactions of Ge compared to Si would lead to smaller hyperfine splittings in a-Ge,(9) even if the wave functions would be the same in both materials. Even smaller hyperfine splittings can be expected from the larger delocalization of the dangling bond wave function in a-Ge estimated from electrical measurements.(56)

In contrast to dbs in a-Si:H, no resolved satellite peaks are therefore observed for a-Ge in Figs. 5.7 and 5.8. However, characteristic changes in the EDMR linewidth $\Delta B_{\mathrm{pp}}^{\mathrm{exp}}$ are found upon ^{73}Ge dilution and enrichment, as summarized in Fig. 5.11, where the experimental peak-to-peak linewidth is shown for all a-Ge samples and resonance frequencies investigated. In a first approach, the large range of linewidths can be understood empirically by a convolution of three contributions, which are indicated by the dotted lines in

Fig. 5.11. The first contribution is an approximately Gaussian g-factor broadening independent of the ^{73}Ge concentration, but dependent on the employed microwave frequency. This contribution is known explicitly from the nuclear-spin free a-^{70}Ge film discussed in Sec. 5.2.1. Secondly, a hyperfine pattern is taken into account, which is caused by a single isotropic hyperfine constant $A_{\text{iso}} = 29\text{ G} \times g\mu_B$ arising from the Fermi contact interaction with the central defect atom. As shown by the inset in Fig. 5.11, the intensity of the hyperfine satellites of a single ^{73}Ge nucleus is small at $c \leq 50\%$ and comparable to the intensity of the central line only at $c \geq 90\%$, so that this contribution can be extracted best from the linewidth of the sample with $c = 95.6\%$. The third, at this point empirical component is a Lorentzian line whose peak-to-peak linewidth $\Delta B_{\text{pp}}^{\text{conv}} = c \times 130$ G varies linearly with the ^{73}Ge concentration c. This component is important for the increase of the linewidth from $c = 7.8\%$ to 51%. The resulting linewidths from the convolution of these three contributions are included as solid lines for the different measurement frequencies in Fig. 5.11. One of the most characteristic features of this calculation is the slow increase of the linewidths at low nuclear spin concentrations, and the sudden increase by more than 100 G around $c = 70\%$. As indicated by the inset of Fig. 5.11, this feature is not unexpected, and based on the intensity ratios of the hyperfine patterns of a single ^{73}Ge nucleus. The central resonance dominates the experimentally observed linewidth $\Delta B_{\text{pp}}^{\text{exp}}$ at ^{73}Ge concentrations below 70%, and the much broader envelope of the hyperfine satellites above. The only free parameters in such a convolution are the magnitude of the central hyperfine interaction, and the slope $\Delta B_{\text{pp}}^{\text{conv}}/c$ of the linearly increasing broadening component, which can be estimated from the observed linewidths $\Delta B_{\text{pp}}^{\text{exp}}$ at low microwave frequencies. Such a simple convolution seems to describe simultaneously all linewidths and lineshapes obtained. However, particularly the third component lacks a microscopic interpretation, and will therefore be discussed in detail in the following sections.

First, a limit will be defined in Sec. 5.3.2 for the number of interacting spins at a given ^{73}Ge concentration, for which EDMR spectra with a resolved envelope of such a hyperfine structure could be expected. Although this limit is based on a hypothetical example, it agrees fairly well with the more realistic numerical calculations presented in Sec. 5.3.4. Close to this limit, the well known analytical models of line broadening summarized in Sec. 5.3.3 are known to be unreliable, which are the method of moments for a convolution of many discrete hyperfine constants A_n, and statistical theory for a continuous distribution function of hyperfine constants $A(r)$. Therefore, the spin localization radius r_0 is obtained in Sec. 5.3.4 by comparing $\Delta B_{\text{pp}}^{\text{conv}}$ to the numerical calculations.

5.3.2 Convolution of multiple hyperfine interactions

The large broadening without resolved substructure observed at 0.434 GHz even at the natural ^{73}Ge concentration can only be explained by hyperfine interactions with a large number of Ge nuclei. At the defect concentration of the sample, the large majority of

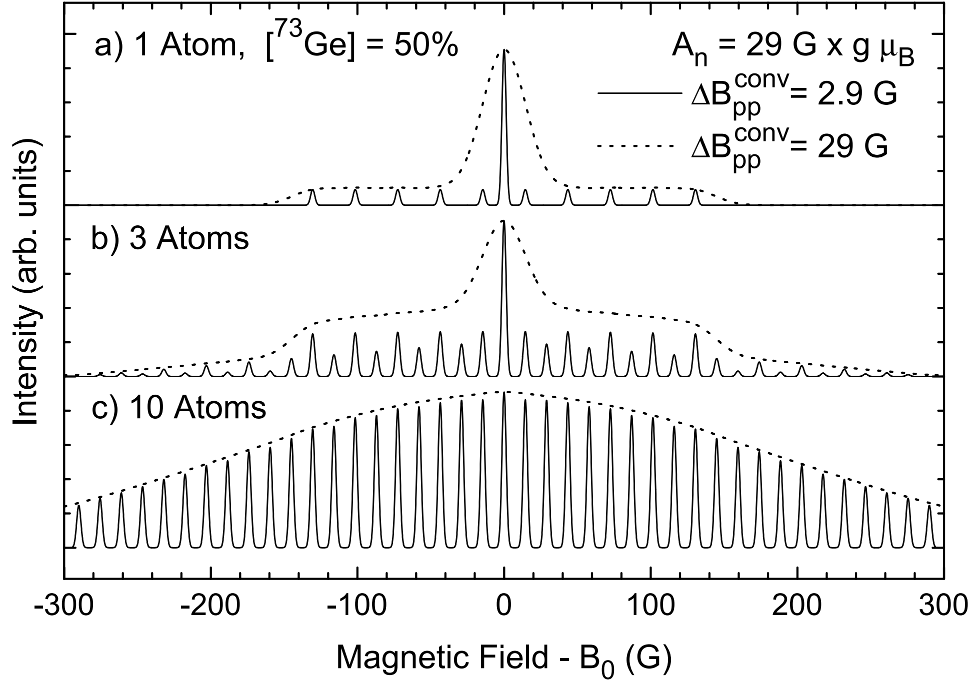

Figure 5.12: Hyperfine patterns of an electronic spin with 1, 3, or 10 atoms with a probability of $c = 50\%$ to have $I = 9/2$ and $A_n = 29$ G $\times g\mu_B$. All patterns have been normalized to the maximum intensity. The spectra have been calculated with two different Gaussian lineshapes with $\Delta B_{\rm pp}^{\rm conv} \times g\mu_B/A_n = 0.1$ and 1. Even without any resolved hyperfine lines ($\Delta B_{\rm pp}^{\rm conv} =$ 29 G), the shoulders resulting from the interaction with a single ^{73}Ge spin are visible if only a small number of nuclei with a hyperfine interaction $A_n/g\mu_B \approx \Delta B_{\rm pp}^{\rm conv}$ are participating in the hyperfine interaction.

atoms around the defect atom are fourfold coordinated with a hybridization close to sp^3, so that $\alpha_n^2 \approx \frac{1}{3}\beta_n^2$ and $A_{n,\rm iso} \gg A_{n,\rm aniso}$, since it is known from the atomic interactions that $A_{\Psi_s} \gg A_{\Psi_p}$. In a disordered material, the average over many sets of hyperfine constants must be calculated for a quantitative description of the observed EDMR spectra, as the orientation and the microscopic wave function are expected to vary from one defect site to another. Methods have been developed to account for many dipolar hyperfine interactions analytically. However, in particular for the present problem of a dominant Fermi contact interaction, the analytical approaches are not applicable for the complete range of the nuclear spin concentrations. Although all approaches yield very similar results in the low concentration limit and for concentrations close to $c = 1$, they disagree depending on the underlying assumptions in the regime of intermediate concentrations.(78)

The basic convolution problem is illustrated with the help of the very simple example shown in Fig. 5.12. For clarity, only a single hyperfine splitting $A_n = 29$ G$\times g\mu_B$ has been considered here at a nuclear spin concentration of $c = 50\%$. According to Eq. (5.2), the pattern produced by hyperfine interaction with one single Ge nucleus consists of $2I + 1$

equidistant satellites if this nucleus happens to be a ^{73}Ge atom with nuclear spin, and of a central resonance otherwise, as shown in Fig. 5.12a. This corresponds to the situation of a very localized dangling bond wave function interacting only with a single nucleus. Figs. 5.12b and c show the result of a threefold and tenfold convolution of this pattern with itself, which would be caused by the spread of the dangling bond wave function over three or ten nuclei with the same hypothetical hyperfine interaction $A_n = 29$ G $\times\, g\mu_B$. The intensity of the hyperfine satellites for these patterns increases as the probability of finding at least one nuclear spin increases with the number of nuclei involved. More than $2I + 1$ satellites are visible in the wings of the pattern of Fig. 5.12b due to the interaction with multiple nuclear spins. As the probability of an individual configuration of nuclear spins is shared among a large number of satellites at $I = 9/2$, their individual intensity is still lower than the central resonance up to rather high ^{73}Ge concentrations. The individual satellites are completely resolved in the example of Fig. 5.12 with an additional Gaussian broadening of $\Delta B_{\text{pp}}^{\text{conv}} = 0.1 \times A_n/g\mu_B$. However, they are smeared out with $\Delta B_{\text{pp}}^{\text{conv}} = A_n/g\mu_B$. The reason of such a broadening could, e.g., originate from a different set of nuclear spins with a smaller unresolved hyperfine splitting. Note that a different pattern would arise from fluctuations of the hyperfine constant A_n itself, which would dominantly broaden the outer hyperfine satellites. As shown in Fig. 5.12, the envelope structure of the satellite groups can still be resolved even if the individual broadenings $\Delta B_{\text{pp}}^{\text{conv}}$ are larger than the hyperfine splitting A_n. Approximately Gaussian lineshapes are obtained only with a large enough value $N \times c$ for the number of nuclei contributing with one nuclear spin.

A quantitative criterion for the number of Ge nuclei participating in a spectrum without resolved satellites, but with a structured envelope function can be estimated from the relative intensities of the narrow central line and the broad structures in Fig. 5.12. In the case of interaction with a single nucleus only (Fig. 5.12a), the area under the central resonance is proportional to the fraction $1 - c$. Therefore its intensity is proportional to $(1 - c)/\Delta B_{\text{pp}}^{\text{conv}}$, if all lines are convoluted with the same broadening function of width $\Delta B_{\text{pp}}^{\text{conv}}$. No resolved hyperfine satellites are expected for $\Delta B_{\text{pp}}^{\text{conv}} \geq A_n$. In this case, the shape of the envelope function depends on the broadening function only in the wings, and it is flat in the central region, as all hyperfine satellites occur with the same probability for hyperfine interactions with a single ^{73}Ge nucleus only. The area of this structure is proportional to the fraction c of interacting ^{73}Ge nuclear spins, so that its intensity is proportional to $c/[2I(A_n/g\mu_B) + \Delta B_{\text{pp}}^{\text{conv}}]$. The shape of the satellite intensity pattern is different for each number of interacting nuclei, e.g., rectangular for a single nucleus, triangular for two, and of Gaussian shape for many nuclei. Up to high ^{73}Ge concentrations, the contribution of configurations with more than one ^{73}Ge nucleus is small compared to the rectangular pattern formed by the interaction with only one nuclear spin because of the larger number of satellites. This can be seen in Fig. 5.12b, where a similar shape is

found for the broadened envelope function of three nuclei compared to the case of only one nucleus even at $c = 50\%$. The probability is $Nc(1-c)^{N-1}$ for finding exactly one nuclear spin out of N nuclei, which could interact with the dangling bond wave function. Therefore, the intensity of the rectangular structure caused by interactions with one nuclear spin is now increased to $I_1 \approx Nc(1-c)^{N-1}/[2I(A_n/g\mu_B) + \Delta B_{\rm pp}^{\rm conv}]$. At the same time, the intensity of the central line is reduced to $I_0 \approx (1-c)^N/\Delta B_{\rm pp}^{\rm conv}$. Neglecting the rounding effects on the spectrum by multiple interactions $I_2, I_3, \ldots$ with several nuclear spins, which become important at larger ^{73}Ge concentrations only, the ratio of intensities $I_0/I_1 \approx 1$ defines a critical number N_c of interacting nuclei, below which a resolved wing structure and above which a Gaussian lineshape is expected

$$N_c = \left[\frac{2I\ (A_n/g\mu_B)}{\Delta B_{\rm pp}^{\rm conv}} + 1\right]\ \frac{1-c}{c} \quad . \tag{5.5}$$

For a given number of atoms, one could similarly define a critical nuclear spin concentration, above which no resolved wings are observed. This criterion provides a first estimate for the number of interacting nuclei responsible for a significant broadening at a given concentration c. Although it is based on very simple considerations, it agrees very well with the numerical lineshape simulations discussed below, which also show that the lineshape changes from a line with characteristic wings to Gaussian shape above the critical number N_c of nuclei interacting with similar hyperfine interaction given by Eq. (5.5). This critical number is around 10 for $\Delta B_{\rm pp}^{\rm conv} \approx A_n/g\mu_B$ and $c = 50\%$, while a structureless Gaussian shape at ^{73}Ge concentrations of $c = 10\%$ would require around 90 nuclei with similar hyperfine interactions. The transition from the narrow central line to the broad Gaussian shape is not as distinct in this regime, as shown in Fig. 5.13. However, the peaked curve calculated for $n = 64$ and $c = 10\%$ still has rather Lorentzian than Gaussian shape. For ^{29}Si nuclei with the smaller nuclear spin $I_{29} = 1/2$, only one third of these nuclei would be sufficient to lead to a Gaussian line at the same nuclear spin concentration. The criterion (5.5) is similarly valid for the derivative lines observed in ESR experiments, which particularly emphasize the slopes at the edges of the central line and of the flat region of the hyperfine satellites.

5.3.3 Analytical lineshape calculations

Analytical expressions for the second moment M_2 and some higher moments $M_n = \int y(B)B^n dB / \int y(B)dB$ of the lineshape functions $y(B)$ have been calculated for the full range of nuclear spin concentrations taking into account dipolar variations of the hyperfine constants A_n.[26, 79, 80, 81, 82, 83] Because second moments add up linearly for convolutions of symmetrical lines, the second moment of any resonance pattern resulting from the interaction with a series of nuclei with $I = 9/2$, concentration c, and an arbitrary

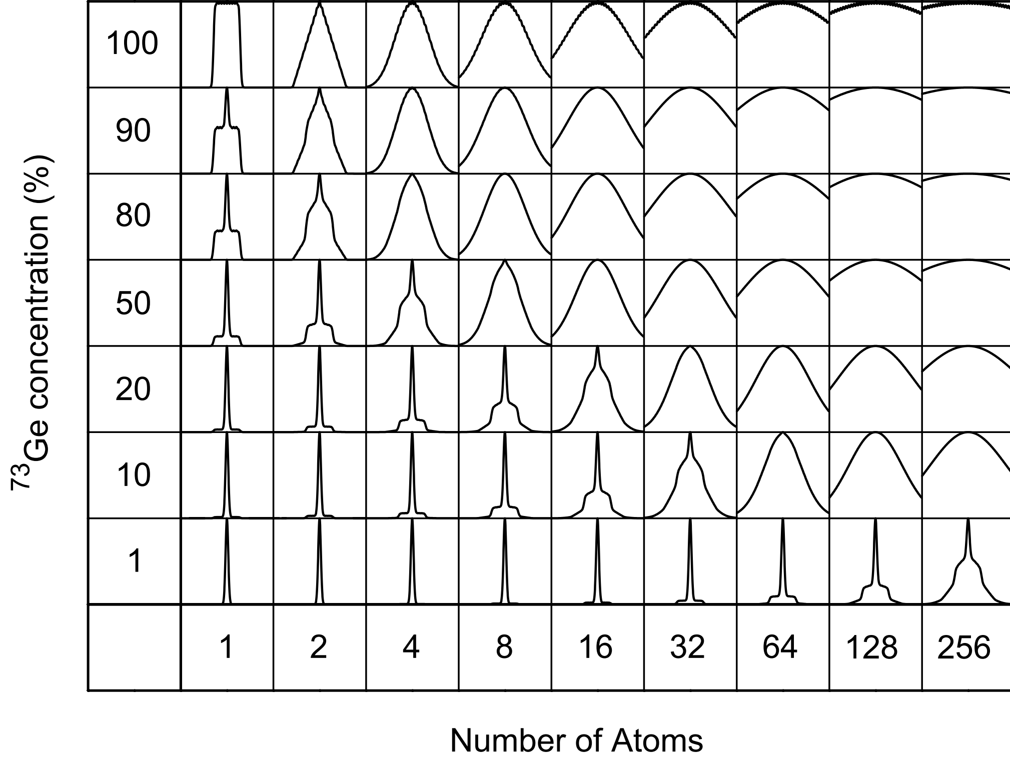

Figure 5.13: Hyperfine patterns calculated for various numbers of atoms with the same hyperfine interaction A_n and for several ^{73}Ge concentrations. Additional broadening with $\Delta B_{\mathrm{pp}}^{\mathrm{conv}} = A_n$ was assumed for this calculation. A Gaussian lineshape is obtained above the critical number of atoms defined by Eq. (5.5). Resolved wings are obtained with fewer atoms, or at a lower nuclear spin concentration. Note that the line shape expected, e.g., for 2 atoms at $c = 80\%$ is very similar to that for 256 atoms and $c = 1\%$. At a given isotopic composition, however, the line shape is indicative for the number of interacting nuclei, and the line width for their interaction strength.

set of hyperfine interactions A_n is given by

$$M_2(c) = c\,\frac{33}{4}\sum_n \left(\frac{A_n}{g\mu_B}\right)^2. \qquad (5.6)$$

According to Ref. 26, this expression even holds for the second moment of the transition fields of the true eigenstates of the Hamiltonian (3.20), which are not equidistant. For the dipolar interactions between point-like magnetic moments in a regular lattice, the rapidly decreasing $A_{n,\mathrm{aniso}} \propto (1-3\cos^2\theta_n)\, r_n^{-3}$ let the sum converge despite the increasing number $N(r_n) \propto r_n^3$ of interacting spins within a sphere of increasing radius r_n. Therefore, one expects $M_2 \propto c$ over the whole range of concentrations. For a purely Gaussian lineshape, the second moment can be compared directly to the experimentally observed linewidth, as $\Delta B_{\mathrm{pp}}^{\mathrm{Gauss}} \propto \sqrt{M_2}$ and therefore $\Delta B_{\mathrm{pp}}^{\mathrm{Gauss}} \propto \sqrt{c}$. For other lineshapes, the higher moments must be calculated, as they influence significantly the observable peak-to-peak linewidth

$\Delta B_{\rm pp}^{\rm exp} \approx \pi/3\sqrt{M_2^3/M_4}$.[13] For example, the moments of a Lorentzian line diverge, and become finite only after an arbitrary cut-off, which removes the divergence[13] and leads to $\Delta B_{\rm pp}^{\rm Lorentz} \propto M_2$ and to $\Delta B_{\rm pp}^{\rm Lorentz} \propto c$.

It has been shown from the analysis of dipolar interactions between identical $I = 1/2$ nuclear spins in a cubic lattice, that in such a system approximately Gaussian lineshapes are expected for $c > 0.1$, because in this regime $M_4 \propto c^2$. For $c < 0.01$ however, Lorentzian lineshapes are expected,[80] as in this regime $M_4 \propto c$. The empirical deconvolution of the experimental data shown in Fig. 5.11 is only possible with a broadening component $\Delta B_{\rm pp}^{\rm conv} \propto c$, corresponding to a Lorentzian lineshape, at least up to $c = 51\%$. The lineshape factors of the experimental EDMR spectra given in Tab. 5.1 also show that in the intermediate range of concentrations from 7.8% to 51%, where a linear increase of the linewidth is observed besides the g-factor broadening at high microwave frequencies, the EDMR lines are nearly Lorentzian. Such a hyperfine broadening is in agreement with Eq. (5.6), however it requires the low concentration limit to be extended over a much larger concentration range in a-Ge compared to the calculations of Ref. 80 for $I = 1/2$ nuclear spins in a regular lattice. This can be understood with the help of Eq. (5.5), taking into account the higher nuclear spin $I_{73} = 9/2$ and a smaller number N_c of effectively similar hyperfine constants in a-Ge. Besides due to structural disorder, N_c is smaller at large distances $r(n)$ here, as the hyperfine interactions of the dangling bond wave function probably fall off exponentially, i.e., faster than the long-range dipolar interactions.

It has been discussed previously by other groups that the few nearest neighbor spins are over-weighted in a linewidth calculation based on the method of moments, as the (rare) cases of nearest neighbors with nuclear spin contribute strongly to all finite moments. If the wings of the resonance lines cannot be measured with sufficient accuracy, the results from the method of moments can therefore be misleading.[82, 84] In this case, the statistical theory discussed in Refs. 13, 81, 82, 83, 84 provides a very powerful alternative to obtain the Fourier-transformed lineshape. This method is well suited for the continuum approximation required in an amorphous network. It becomes particularly simple in the low concentration limit, but might also be applied at high concentrations, eventually requiring the exclusion of a central volume, or concentrations close to $c = 1$.[85] Assuming symmetric, linear, and uncorrelated contributions from the hyperfine interactions at different atoms, the lineshape function $y(B)$ is given by

$$y(B) \propto \int_0^\infty \cos[(g\mu_B B - h\nu)x] \cdot \exp[-J(x)]\, dx \tag{5.7}$$

with

$$J(x) = \sum_{m_n} \int \frac{c\,\varrho(r)}{2I+1} \left[1 - \exp\left(i\,\frac{A(r)}{g\mu_B}\,m_n x\right)\right] dr^3$$

where x is the inverse hyperfine energy and $\varrho(r)$ the density of possible lattice sites.[82] In the case of dipolar interactions and a constant density ϱ, this integration results in

a Lorentzian line for the whole concentration range, in agreement with our assumptions in Fig. 5.11.[13, 84] At high nuclear spin concentrations, however, correlations in the occupation of the hypothetical continuum of possible nuclear positions become inevitable. Therefore, the assumption of an uncorrelated occupation of defect sites is valid only in the dilute limit. For a typically exponential fall-off of a delocalized dangling bond wave function, complicated hypergeometric functions are obtained from the volume integration, so that the derived lineshapes and scaling laws for the linewidth cannot be compared easily with the experimental data. As only few atoms with almost discrete hyperfine constants are expected to dominate the linewidth in this regime, instead numerical simulations for one or many discrete sets of hyperfine constants will be considered in the following section.

5.3.4 Numerical lineshape simulation

To circumvent the low concentration limit assumed for the derivation of Eq. (5.7) and to make predictions over the full concentration range, many hyperfine patterns similar to those of Fig. 5.12 with different hyperfine constants have been convoluted numerically via the fast Fourier transform algorithm. Averaging of several hundred atomic configurations is possible in small steps of c on a desktop computer with a resolution sufficient to study the effects of a variation of the hyperfine constants over more than three orders of magnitude. We start with the description of a simple numerical example without anisotropic contributions of the hyperfine interaction ($\beta_n^2 = 0$) and without fluctuations of α_n^2 to avoid the averaging process over many random configurations. For the wave function amplitudes at the nuclear spin sites r_n, a hydrogenic envelope function

$$\Psi_{db}(r_n) \propto e^{-r_n/r_0} \tag{5.8}$$

is used, which according to Eq. (5.3) and (5.4) leads to

$$A_{n,\text{iso}}(r_n) \propto \alpha_n^2 \propto \Psi_{db}^2(r_n) \propto e^{-2r_n/r_0}. \tag{5.9}$$

This kind of wave function is commonly assumed for the description of the delocalization of dbs in transport experiments, however, it is a very crude assumption compared to the set of hyperfine constants calculated for the P_b-center in Ref. 16 (see Fig. 5.10). It is not thought to be a realistic description of a true dangling bond wave function, but it is very helpful to understand the limits to which information can be extracted from the experimental data.

To define a set of hyperfine constants A_n via Eq. (5.9), the positions $\vec{r}_n$ of the host atoms need to be modelled in addition to the shape of the dangling bond wave function. The probability of finding a Ge atom at a certain distance r from a central Ge atom is given by the radial distribution function (RDF) $D(r)$, which has been determined from x-ray or electron diffraction experiments. The local environment of Ge atoms consisting

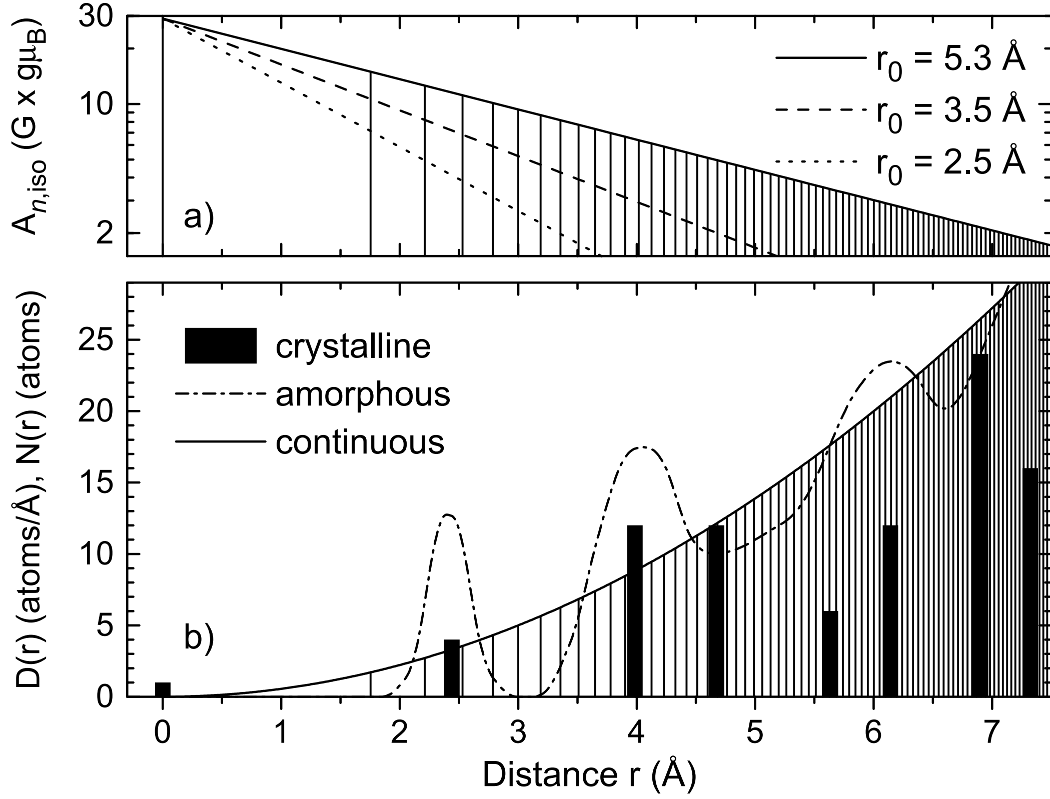

Figure 5.14: (b) Radial distribution functions of crystalline germanium ($N(r)$, bars), of a-Ge ($D(r)$, dash-dotted line, after Ref. 86), and of a homogenous medium with $D(r) = 4\pi r^2 \varrho$ (solid line). The discrete atomic positions $r_n = \sqrt[3]{3n/4\pi\varrho}$ are chosen from $D(r)$ for a homogeneous medium such that the area below each of the resulting segments corresponds to a single atom. (a) Set of hyperfine constants $A_{n,\mathrm{iso}}$ resulting from Fermi contact interaction of the dangling bond wave function of Eq. (5.8) with different localization radii r_0.

of the nearest neighbors and the next few shells of atoms in amorphous Ge still resembles that of crystalline Ge, however, broadened by structural disorder.[86] In particular, the maximum of the RDF around 2.44 Å in Fig. 5.14 can be identified with the four nearest Ge neighboring atoms, one of which is missing in the radial distribution function of dbs in a-Ge. For larger distances, $D(r)$ rapidly approaches the limit of a homogenous medium, for which $D(r) = 4\pi r^2 \varrho$ with the macroscopic atom density ϱ of a-Ge, which is similar to that of crystalline Ge ($\varrho = 0.0442$ Å^{-3}). Fig. 5.14 illustrates how a set of discrete nuclear positions r_n were chosen for the first numerical example discussed here. A new Ge atom with index n is placed at each distance r_n, at which the area under the continuous distribution function $\int D(r)dr = 4/3\pi r^3 \varrho = n$ corresponds to a full atom

$$r_n = \sqrt[3]{3n/4\pi\varrho}, \qquad n = 0, 1, \ldots . \tag{5.10}$$

This ensures, that at large distances the macroscopic atomic density $\varrho \approx 0.0442$ Å^{-3} is obtained. In this approximation, the nearest-neighbor positions are distributed between

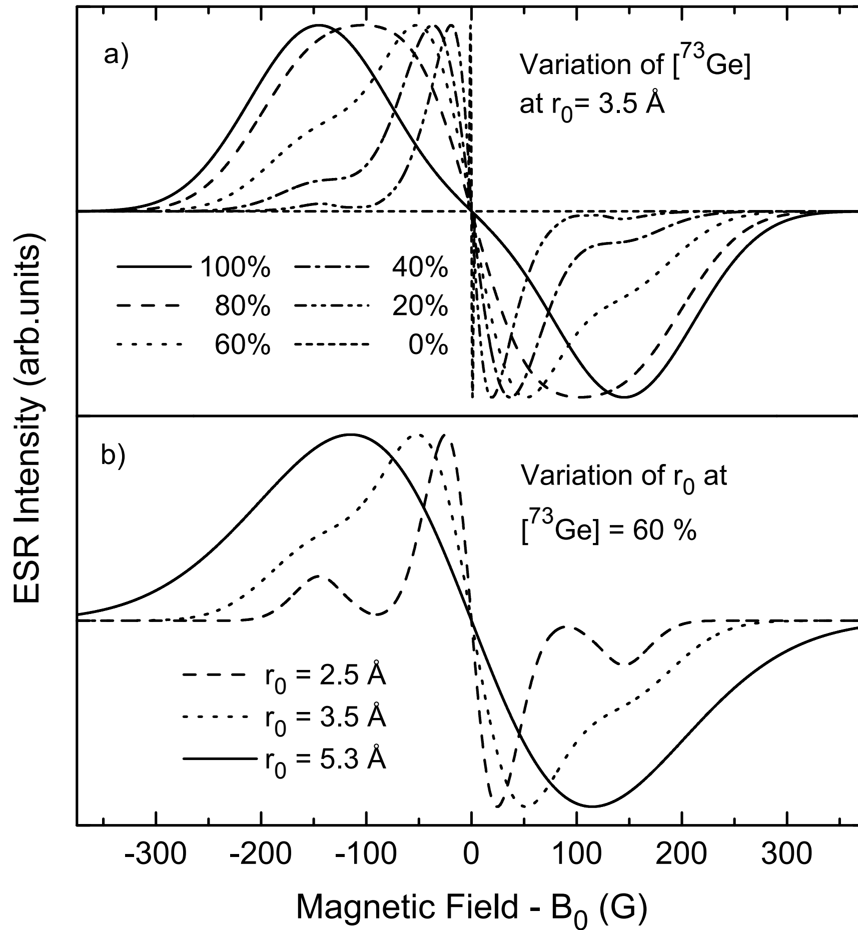

Figure 5.15: Simulated spin resonance spectra for the model of Fig. 5.14. The resolved shoulders originate from the hyperfine interaction $A_{0,\text{iso}} = 29\ \text{G} \times g\mu_B$ with the central ^{73}Ge defect atom. In the experimental spectra, these shoulders are averaged out because of fluctuations of the hyperfine constants, e.g. due to a dipolar hyperfine interaction $A_{0,\text{aniso}} \leq 5\ \text{G} \times g\mu_B$.

1.8–2.8 Å, which is a significantly larger spread than of 2.2–2.7 Å in the RDF of a-Ge. However, the results from simulations based on Eq. (5.10) were virtually the same as those from simulations with $r_{1-3} = 2.44$ Å. The errors introduced by the actual choice of r_n are therefore negligible, in particular compared to the effects of spin polarization discussed in Sec. 5.4.2. The resulting hyperfine constants from Eqs. (5.10) and (5.9) are shown in Fig. 5.14a for three different localization radii and $A_0 = 29\ \text{G} \times g\mu_B$. Note that for a spin density of dbs of about 10^{19} cm^{-3}, each defect occupies the volume of a sphere with a radius of 20 Å $\gg r_0$. The sum of the different sets of hyperfine constants of Fig. 5.14a is of interest for the normalization condition $\sum_n \alpha_n^2 + \beta_n^2 = 1$ of the dangling bond wave function. It is about 190 G for the set of hyperfine constants with $r_0 = 3.5$ Å, and about 85 G and 620 G for those with $r_0 = 2.5$ and 5.3 Å, respectively.

The derivative spectra, which result from the convolution of the hyperfine patterns obtained for the three sets of hyperfine constants of Fig. 5.14a are shown in Fig. 5.15. Whereas the second moments of the simulated spectra fulfill Eq. (5.6) for all concentrations, their lineshapes are obviously different than both Gaussian and Lorentzian curves. The overall shape of the simulated spectra is more similar to a Lorentzian curve up to $c = 60\%$, and to a Gaussian curve for higher c. A shoulder structure similar to that found

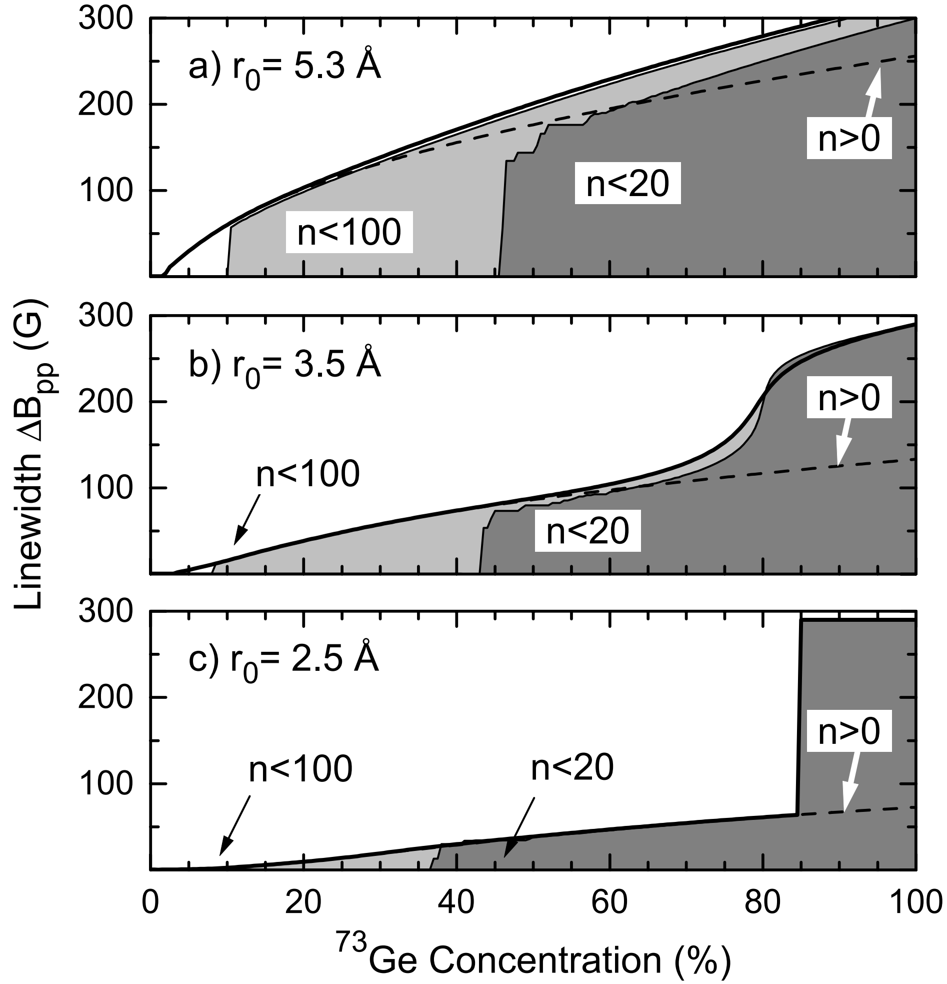

Figure 5.16: Peak-to-peak linewidth $\Delta B_{\text{pp}}^{\text{num}}$ extracted from the maximum and minimum field positions of the spectra obtained for the three sets of hyperfine constants of Fig. 5.14a. The satellite structures causing the step around 80% in the linewidth at localization radii of (c) $r_0 = 2.5$ and (b) $r_0 = 3.5$ Å vanish at a localization radius of (a) $r_0 = 5.3$ Å because of the larger number of similar hyperfine constants (see Fig. 5.14a). The dashed line was simulated without a central atom ($n > 0$), and the shaded areas indicate the linewidths calculated for the hyperfine constants with the nearest $n < 20$, and $n < 100$ nuclei.

in Fig. 5.12 and at the position of the experimentally observed wings of Fig. 5.8 is resolved at low concentrations. These shoulders determine the linewidths at $c \geq 80\%$. Obviously, the assumed hyperfine interaction $A_{0,\text{iso}} = 29$ G $\times\ g\mu_B$ of the central ^{73}Ge defect atom differs enough from $A_{n\geq 1} < 11$ G $\times\ g\mu_B$ assumed for the backbonding neighbors, so that in this model the shoulders of Fig. 5.12 remain visible.

The peak-to-peak linewidth $\Delta B_{\text{pp}}^{\text{num}}$ of the simulated derivative spectra can be determined numerically from the magnetic field separation of its global maximum and minimum. The theoretical linewidths obtained via this method for the three different radii of localization are shown in Fig. 5.16, with the linewidths corresponding to $r_0 = 3.5$ Å in

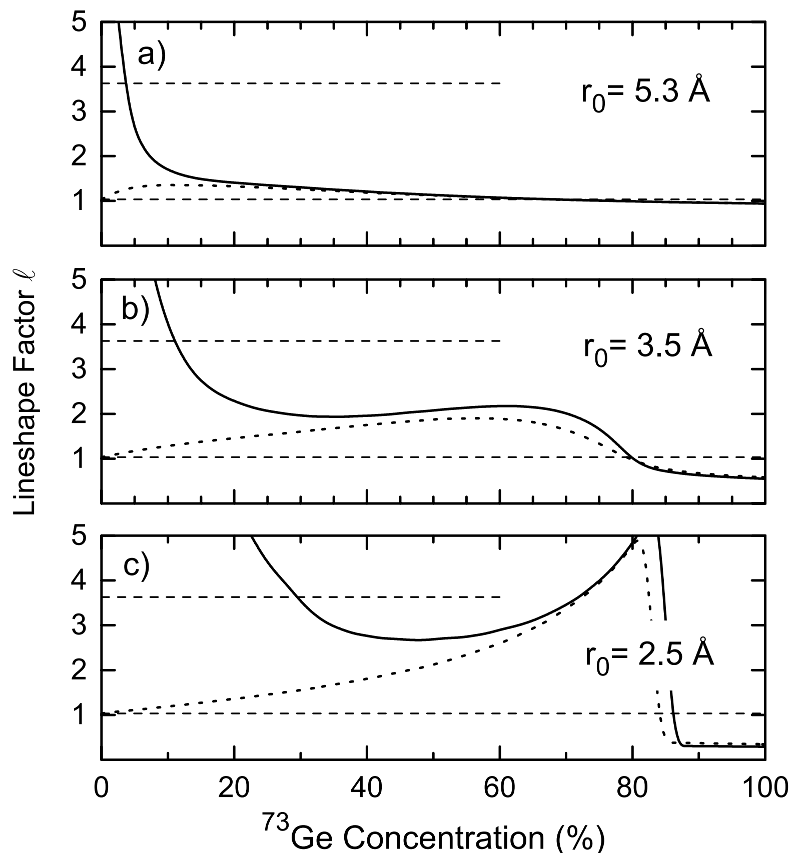

Figure 5.17: The lineshape factors l determined from the calculated spectra for the three sets of hyperfine constants of Fig. 5.14a (full lines). (a) For a localization radius $r_0 = 5.3$ Å, l is close to the Gaussian value of 1.033. (b,c) For smaller r_0, a Gaussian line is only expected for large ^{73}Ge concentrations. In the intermediate concentration range, l is closer to 3.628, which would be expected for a purely Lorentzian line. Also included are the lineshape factors expected for the three cases when Gaussian g-factor broadening $\Delta B_{\text{pp}}^{\text{SO}} \approx 40$ G at 9.35 GHz is included (dotted lines).

Fig. 5.16b. An increase of the linewidth approximately linear with the ^{73}Ge concentration is observed up to $c = 60\%$ for $r_0 = 3.5$ Å. Above $c = 80\%$, the linewidth rapidly approaches $\Delta B_{\text{pp}}^{\text{num}} \approx 300$ G. The resulting step of the linewidth around $c = 80\%$ is related to the cross-over between the central line of this pattern from dbs centered at nuclei with $I = 0$ and the $2I + 1$ equally intense contributions of hyperfine satellites already discussed in the context of Fig. 5.11.

This step is not present assuming a larger $r_0 = 5.3$ Å (Fig. 5.16a). In that case, the linewidth of the spectrum at $c = 60\%$ shown in Fig. 5.15b is large enough to cover the satellite pattern of the central atom, mainly because of the smaller difference between the largest hyperfine constant $A_0 = 29\text{ G} \times g\mu_B$ of the central atom and $A_1 \approx 15\text{ G} \times g\mu_B$ attributed to one of the backbonding neighbors in this model. As the linewidth of the central line for $r_0 = 5.3$ Å is around 200 G at $c = 60\%$, the satellites collapse with the central line for the solid curve in Fig. 5.15b. Because an accumulation of sufficient nuclei with similar hyperfine constants occurs for this localization radius according to Eq. (5.5) already for concentrations above 5%, the lineshapes are more Gaussian, as shown in Fig. 5.17a, where the lineshape factor l determined numerically from the simulated spectra is plotted with solid lines for the same model used in Fig. 5.15 and 5.16. As expected for a Gaussian lineshape, $\Delta B_{\text{pp}}^{\text{num}} \propto \sqrt{c}$ over almost the entire concentration range (see Fig. 5.16a).

In contrast, the satellite structure is clearly resolved for spectra simulated with a shorter localization radius $r_0 = 2.5$ Å. In this case, a central line is resolved between two distinct satellite peaks, which makes the definition of a single linewidth $\Delta B_{\rm pp}^{\rm num}$ difficult. Consequently, a jump of the linewidth occurs again, when the intensity of the outer satellites becomes larger than the intensity of the central line. At sufficiently low concentrations, the linewidth increases almost linearly with the ^{73}Ge concentration, as appropriate for a Lorentzian lineshape. The lineshape factors obtained numerically for these spectra are shown in Fig. 5.17c and are close to the Lorentzian value in the intermediate concentration range. They can be compared better with the experimental values of Tab. 5.1, if the additional broadening mechanisms at the different microwave frequencies are taken into account. The dominant mechanism at 9.35 GHz is g-factor broadening, as discussed in Sec. 5.2.1 with $\Delta B_{\rm pp}^{\rm SO} \approx 40$ G and an approximately Gaussian shape. The lineshape factors of the numerical spectra with such an additional broadening are shown by the dotted lines in Fig. 5.17. In agreement with the experimental data, the lineshapes start from a Gaussian shape at low nuclear spin concentrations, where g-factor broadening dominates, become Lorentzian at intermediate concentrations, and Gaussian again at $c > 80\%$.

The validity of Eq. (5.5) not only for one fixed hyperfine constant, but also for the sets of hyperfine constants discussed here, is shown numerically in Fig. 5.16 for a partial convolution of the hyperfine patterns of the nearest 20 or 100 neighboring nuclei only, and for the convolution of the complete set without the central defect atom. The steplike structure above $c = 80\%$ can be attributed unambiguously to the central atom, as it is not observed if the central atom is removed from the convolution. As seen by the steps in the curves with $n \leq 20$ and 100 atoms, the simulated linewidth is dominated by interactions with the central 20 nuclei for $c \geq 40\%$ and with the central 100 nuclei at $c \geq 10\%$. Both numbers are in good agreement with Eq. (5.5) for $\Delta B_{\rm pp}^{\rm conv} \approx 2I(A_n/g\mu_B)$.

Obviously, most of the information on individual hyperfine constants is lost during the convolution process. It is therefore not surprising that similar lineshapes and linewidths can be obtained numerically not only for the specific set of hyperfine constants shown in Fig. 5.14a, but also for other wave function envelopes with similar localization lengths and for other radial distribution functions consistent with the macroscopic density of a-Ge. A quasi-continuous RDF can be modelled numerically e.g. with a large number of dbs, each with its characteristic distribution function of atomic distances r_n and hyperfine constants A_n. The average ESR spectra for these dbs, and the corresponding linewidths and lineshapes are not much different from the results of Figs. 5.16 and 5.17. Independent of the specific defect model, the approximately Lorentzian lineshape and $\Delta B_{\rm pp}^{\rm num} \propto c$ up to $c = 60\%$, as well as the sudden increase to a linewidth of about 300 G are typical for those sets of hyperfine constants with $A_{0,\rm iso} = 29\ {\rm G} \times g\mu_B$ and a localization parameter around 3.5 Å. The available experimental data points, which indicate a hyperfine broadening of

10 G at $c = 7.8\%$, of 70 G at $c = 51\%$, and of 300 G at $c = 95.6\%$ could be reproduced best by those defect models containing 1–2 atoms with $A_n \approx 29$ G $\times\, g\mu_B$, 3–6 atoms with $A_n \approx 4 - 10$ G $\times\, g\mu_B$, and 100–200 atoms with $A_n \approx 0.5 - 1$ G $\times\, g\mu_B$, irrespective of the exact distribution functions. Within the given ranges, the larger number of nuclei is always to be used in conjunction with the smaller hyperfine constant. The ranges of validity were obtained by numerical simulations, but could have been determined as well with the numbers of nuclei from Eq. (5.5) for a given concentration and a typical set of hyperfine constants, and the linewidths from the ratio of the cumulated moments M_2 and M_4.

The sum of all isotropic hyperfine interactions with the dangling bond wave function is always in the range of 160–190 G for those sets of hyperfine constants, which are consistent with the experimental data. Also for the model of Fig. 5.14 this sum is about 190 G at a localization radius of 3.5 Å. Compared to the tabulated atomic hyperfine interaction of 843 G $\times\, g_0\mu_B$ for an ideal 4s-orbital, this suggests that about 19-23% of the db wave function occupies s-like atomic orbitals. Only 3.4% of an atomic s-wave function is found at the central Ge atom. The non s-like 77-81% of the wave function are expected to occupy p-like atomic orbitals, probably with an s/p ratio significantly smaller than 1/3 at the central atom and significantly larger at remote atoms. Note that the sums of the isotropic hyperfine constants of Fig. 5.14 for $r_0 \approx 2.5$ and 5.3 Å of 85 and 620 G $\times\, g\mu_B$ would be unrealistic, so that all $A_{n,\mathrm{iso}}$ would need to be scaled up or down for these cases by a factor of 2–4 to fulfill the normalization condition. Then, however the linewidth at $c = 100\%$ would be far from the experimentally observed values.

Until now, we have not taken into account any contributions of $A_{n,\mathrm{aniso}}$. Because all orientations of dbs are distributed randomly in amorphous materials, this will lead to powder pattern distributions of hyperfine constants between $A_{n,\perp} = A_{n,\mathrm{iso}} - A_{n,\mathrm{aniso}}$ and $A_{n,||} = A_{n,\mathrm{iso}} + 2A_{n,\mathrm{aniso}}$ in addition to the random fluctuations of $A_{n,\mathrm{iso}}$ due to disorder. Such fluctuations of $A_{0,\mathrm{iso}}$ are required to account for the observation of a structureless spectrum, even if $\Delta B_{\mathrm{pp}}^{\mathrm{exp}} \ll A_{0,\mathrm{iso}}$, which is the case at 0.434 GHz and 2.00 GHz and $c = 7.8\%$. Without such fluctuations, the simulations of Fig. 5.15a show a local minimum around $B_0 \pm 120$ G and a maximum around $B_0 \pm 150$ G. These features would overlap, if their position fluctuated by about 30 G, i.e., with fluctuations of A_n of at least 20% or 6 G $\times\, g\mu_B$. Because of the sharp peak of the powder pattern distribution at $A_{0,\perp}$, the interpretation of these fluctuations as anisotropic hyperfine interaction would require even larger fluctuations of $A_{0,\mathrm{aniso}} \geq 5$ G $\times\, g\mu_B$ in order to average out the wings of the spectra shown in Fig. 5.15a according to numerical simulations including $A_{0,\mathrm{aniso}}$. For very large values of $A_{0,\mathrm{aniso}}$, the true value of $A_{0,\mathrm{iso}}$ would be somewhat higher than 29 G $\times\, g\mu_B$ because of the asymmetry of the hyperfine powder patterns.

To summarize the results of the numerical simulations, the experimental linewidths and lineshapes can be explained by a dangling bond model wave function with $A_{0,\mathrm{iso}} =$

29 G $\times g\mu_B$ and a radius of localization $r_0 = 3.5$ Å, irrespective of the particular model employed. In agreement with the simple estimate from Eq. (5.5), at least 20 central nuclei are found to contribute to the linewidth at $c \approx 40\%$, and at least 100 central nuclei to the linewidth at $c \approx 10\%$. More complicated statistical models with fluctuating hyperfine constants or $A_{0,\text{aniso}} \geq 5$ G $\times g\mu_B$ are required to account for the structureless wings of the experimental spectra.

5.4 Discussion

Based on these conclusions for the hyperfine parameters of dbs in a-Ge from the hyperfine broadening of the EDMR signal, some specific aspects of the observed parameters will be discussed in more detail in the following sections. After a summary of the relevance of the other line broadening mechanisms in Sec. 5.4.1, the microscopic structure suggested from this work for dbs in a-Ge is discussed in Sec. 5.4.2, taking into account the effects of spin polarization. This defect structure is then compared to the localization radius obtained from transport experiments and to the structure of dbs in a-Si:H in Sec. 5.4.3.

5.4.1 Line broadening mechanisms

The model wave function of Eq. (5.3) takes into account only local Fermi contact and dipolar interactions of the dangling bond wave function with a particular ^{73}Ge nucleus. The influence of other interactions like the distant dipolar interactions of the electron spin centered at the defect site with the nuclear spins of the surrounding ^{73}Ge nuclei will be considered now. This long-range coupling can be calculated without further assumptions in the point-dipole approximation and is most significant for the remote nuclear spins I_n with small fractions of the total wave function. In analogy to the calculations of Refs. 13, 81, 82, 84, the Fourier transform of the ESR lineshape function caused by such dipolar coupling with $A_{\text{dipolar}}(r) = \frac{\mu_0}{4\pi} g_e \mu_e g_n \mu_n r^{-3}(3\cos^2\theta - 1)$ is given according to Eq. (5.7) for $I_n = 9/2$ in the continuum approximation and the low concentration limit by

$$J(x) = \exp\left(-\frac{5\pi\mu_0}{9\sqrt{3}} g_e \mu_e g_n \mu_n \; c\varrho \; |x|\right) \tag{5.11}$$

with the nuclear g-factor $g_n = -0.195$, and the Bohr and nuclear magnetons μ_B and μ_n. With the atomic density $\varrho = 0.0442$ Å^{-3}, this characterizes a Lorentzian lineshape function with a width of about 0.5 G $\times c$. At large nuclear spin concentrations, higher order terms in c enter Eq. (5.11), but still, the overall dipolar broadening from the nuclear spins is of the order of 1 G. Therefore, this contribution to the observed linewidths cannot account for a broadening $\Delta B_{\text{pp}}^{\text{conv}}/c = 130$ G, as required for the Lorentzian component (3) in the empirical model of Fig. 5.11.

The other broadening mechanisms such as broadening due to a distribution of g-factors, lifetime broadening, exchange or motional narrowing, and the dipolar coupling between adjacent electronic spins are independent of the nuclear spin concentration, so that the experimental spectra of the a-^{70}Ge sample can be used to determine the broadening due to these mechanisms. As is obvious from the spin Hamiltonian (3.20), the effect of the g-factor distribution is particularly large at high microwave frequencies. According to the linewidths given in Fig. 5.2 and in Tab. 5.1, g-factor broadening contributes with about 4.4 G $\times$ ν/GHz to the overall linewidth at 70 K.

For both a-Si and a-Ge, drastic increases of the ESR linewidth have been reported at temperatures above 100–200 K.[70, 72] This temperature-dependent lifetime broadening has been correlated with the known hopping rates from conductivity, as discussed in detail in Ref. 67. At 70 K and below, hopping in a-Ge is so slow that the ESR linewidth is determined only by other, temperature-independent linewidth contributions.[67, 70, 72]

As shown in Figs. 5.5 and 5.6, defect concentrations of the order of 10^{19} cm^{-3} lead to an increase of the EDMR linewidth by 1 G at maximum, confirming that the influence of exchange or motional broadening is negligible at the investigated concentrations. The magnitude of dipolar broadening due to other electronic spins, which have a larger magnetic moment $g_e\mu_B/g_n\mu_n = 1.88 \times 10^4$ than the ^{73}Ge nuclear spins was estimated in Eq. (5.1) with the help of the statistical method.[59] Due to the much smaller concentrations of dbs of around 10^{19} cm^{-3} or $2.3 \times 10^{-4} \times \varrho$, the broadening due to dipolar interactions between different dbs is again of the order of 1 G only.

Thus, the dipolar interaction with remote ^{73}Ge nuclei and between different dbs leads to line broadenings of the order of 1 G, whereas the distribution of g-factors leads to a frequency dependent broadening of 2-43 G. The effects due to hyperfine interactions are expected to dominate the observed linewidths in the ^{73}Ge enriched samples.

5.4.2 Spin polarization

According to Eq. (5.3), the hyperfine parameters $A_{n,\mathrm{iso}}$ and $A_{n,\mathrm{aniso}}$ are usually evaluated in terms of the fractions α_n and β_n of *s*- and *p*-like atomic orbitals contributing to the full dangling bond wave function. The corresponding spin densities α_n^2 and β_n^2 are obtained via Eq. (5.4) by comparison of the experimental parameters with the atomic values from Hartree-Fock calculations. Accordingly, $A_{0,\mathrm{iso}} = 29$ G $\times$ $g\mu_B$ corresponds to an *s*-like contribution of $\alpha_0^2 = 3.4\%$ at the central atom.

$A_{0,\mathrm{aniso}} \geq 5$ G can be estimated roughly from the missing structure of the experimental spectra at $c = 7.8\%$, which requires a certain random variation of A_0. If these variations were dominated by anisotropic hyperfine interaction, the *p*-wave fraction at the central atom would be $\beta_0^2 \geq 30\%$, and the s/p hybridization ratio at the central defect atom $\alpha_0^2/\beta_0^2 \leq 11\%$, as compared to the ratio of about 12% determined from $\alpha_0^2 = 6\%$ and $\beta_0^2 \approx 50\%$ for dbs in a-Si:H in Refs. 24, 51. For SiH_3 and GeH_3 radicals with negligible

delocalization and small spin polarization of the bonds, the ratios of hybridization $\alpha_0^2\beta_0^2$ were evaluated to be around 21% and 11.5%, respectively.[87, 88] As the value for GeH_3 is based on the rather small atomic Fermi contact interaction of $A_{\Psi_s} = 535$ G $\times\ g_0\mu_B$ from Ref. 32, even smaller fractions of α_0^2/β_0^2 around 7% would be obtained for dbs in GeH_3 radicals based on the more recent value $A_{\Psi_s} = 843$ G$\times g_0\mu_B$ of Ref. 9 used here. Therefore, the hybridization ratio at the Ge atom in GeH_3 is probably even lower, indicating nearly complete sp^2 configuration of the Ge-H bonds and a significant relaxation of the defect atom into the plane of the backbonding H atoms. Taking into account the smaller s/p ratio of dbs in a-Si:H with respect to the SiH_3 radical, one could expect a hybridization ratio even below 7% for dbs in a-Ge, resulting in $\beta_0^2 \geq 50\%$ and $A_{0,\text{aniso}} \geq 9$ G.

However, as indicated by the localization radius for $A_{n,\text{iso}}$ in Sec. 5.3.4, large parts of the dangling bond wave function in a-Ge seem not to be located on the dangling bond defect atom itself. For those sets of hyperfine constants compatible with the experimental data in Sec. 5.3.4, the sum of the isotropic hyperfine interactions with remote nuclei $\sum_{n\geq 1} A_{n,\text{iso}}$ is typically around 130–160 G $\times\ g\mu_B$, suggesting that about 15–19% of the dangling bond wave function occupies s-like states at Ge atoms other than the central defect atom. Assuming a hybridization ratio with an s fraction around 1/4 (sp^3 configuration) for these remote atoms, this would correspond to 60-76% of the complete defect wave function. The sum of the three contributions $\alpha_0^2 = 3.4\%$, $\beta_0^2 \geq 50\%$, and $\sum_{n\geq 1} 4\alpha_n^2 = 60 - 76\%$ is somewhat larger than 100%, but at least of the correct order of magnitude. The difference could indicate a lower p fraction than 3/4 at the remote atoms, or, alternatively, some of the atomic spin densities α_n^2 to be negative, which could not be distinguished in the experimental broadenings discussed above.

Negative spin densities are one of the effects of spin-polarization discussed in the literature for dbs in a-Si:H. Although the model wave function of Eq. (5.3) provides a reasonable approximation for the dangling bond charge density, the same wave function is probably inappropriate to give a realistic description of the dangling bond spin densities. Hartree-Fock calculations for the atomic hyperfine constants include the contributions from core polarization as a spin-dependent deformation of the Ge inner 1s-3s shells, described by configuration interactions.[32] As is known from the hyperfine interactions in small molecules, such a core polarization strongly depends on the unpaired spin density in the valence state. In different bonding configurations, the spin polarization might vary with respect to the atomic values. A single experimental hyperfine parameter α_n^2 or β_n^2 is then insufficient to quantify these multiple effects, so that the calculated localization based on $\alpha_n^2 + \beta_n^2$ is incorrect for the charge density in most cases.[16] Furthermore, even in the absence of net charge or unpaired spin density at one Ge atom, charge density on neighboring Ge atoms will cause locally unbalanced positive and negative spin densities at the central atom by local polarization of the bonds. This spin density then occurs with the opposite sign at the other atoms.

For the GeH_3 radical, this spin polarization of the bonds was measured from the proton interaction to contribute with 13 G $\times g\mu_B$ to the total isotropic hyperfine coupling of the ^{73}Ge nuclei of 75 G $\times g\mu_B$.[87, 88] Such a shift of positive spin density from the ligands to the central atom would be significant compared to $A_0 = 29$ G $\times g\mu_B$ and $A_1 = 10$ G $\times g\mu_B$ of the model wave function with $r_0 = 3.5$ Å, and hence the s-like charge density at the central atom is possibly even lower than 3.4%. In a-Ge, the spin polarization at the central atom is probably smaller than in GeH_3 because of charge delocalization. However, as pointed out in Ref. 16, also for dbs at the Si/SiO_2 interface the spin density at the neighboring atoms is almost cancelled by the transfer of spin density towards the central atom. This spin polarization also explains the difference between the charge and spin densities calculated for dbs in a-Si in Ref. 55, which predict a charge localization below 20%, but a spin localization around 50% at the central atom.

Because the fraction of the dangling bond wave function is largest at the central atom, the negative contributions to the spin density are largest on the backbonding atoms. At these atoms, the balance of opposing contributions may cause a reduction of the actual hyperfine interaction to zero or below, which once more justifies the assumption of a distinct isotropic hyperfine interaction $A_{0,\mathrm{iso}} \gg A_{n,\mathrm{iso}}$ at the central defect atom, which is one of the characteristic results of the numerical simulations of Sec. 5.3.4. The remote atoms, which determine the linewidth at smaller nuclear spin concentrations with their small hyperfine constants, are therefore an alternative and possibly more universal basis for the definition of the spin localization parameter of dbs in different materials, as they do not suffer such large spin polarization effects as the central defect atoms.

As a consequence of spin-polarization, a spin-unrestricted wave function in contrast to Eq. (5.3) cannot be easily identified with the experimentally accessible hyperfine parameters. Therefore, detailed theoretical calculations are required to interpret the experimental parameters quantitatively. Such calculations could also clarify, whether the postulated fluctuations of A_0 around $A_{0,\mathrm{iso}}$ can indeed be ascribed to anisotropic hyperfine interactions.

5.4.3 Charge localization

The low temperature transport properties of a-Ge are strongly influenced by the extent of the dangling bond defect wave function. The characteristic hopping rates of spin-independent transport are determined by charge, not spin localization. However, both types of wave functions must be considered in a realistic model for the dangling bond wave function, as pointed out previously for the P_b center and dbs in a-Si:H.[16, 55] The charge localization radius r_c of dbs in a-Ge:H has been determined from dc transport measurements in Ref. 56. According to the Mott model, the variable range hopping

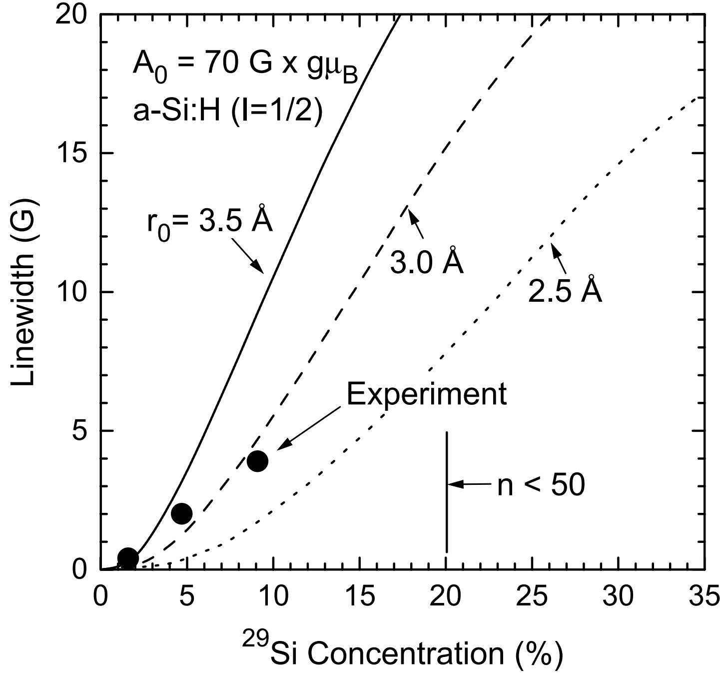

Figure 5.18: The peak-to-peak linewidths for dbs in a-Si:H at low ^{29}Si concentrations have been extrapolated from low-frequency measurements in Ref. 51. The simulations are based on the numerical model of Sec. 5.3.4, however with $I_{29} = 1/2$, and $A_{0,\mathrm{iso}} = 70\ \mathrm{G} \times g\mu_B$. More than 50 atoms contribute to the linewidths at nuclear spin concentrations below 20%. Apparently, the broadening at low nuclear spin concentrations is consistent with $r_0 = 3.0$ Å, as determined independently from the hyperfine broadening due to the 1-3 backbonding atoms.

conductivity for delocalized dbs described by Eq. (5.8) is given by

$$\sigma \propto e^{-\eta (T/T_0)^{-1/4}} \quad , \tag{5.12}$$

where $T_0^{-1} = r_c^3 N_F k_B$, and with the factor η in the range between 0.9 and 1.3, depending on the employed theoretical model. The density of states at the Fermi level N_F is linked to the spin density N_S via the density of states according to $N_F = N_S \times 11\ \mathrm{eV}^{-1}$, which can be obtained from deep level transient spectroscopy.[89] From Eq. (5.12), a localization radius of the order of 1 Å would be obtained with $T_0 = 2 \times 10^8$ K from the inset of Fig. 5.1. However, because unwanted influences of temperature cannot be excluded in measurements of $\sigma(T)$, the determination of r_c from T_0 is regarded as being very unreliable. Therefore, the dependence of $\sigma(N_F)$ on the spin density was evaluated for a-Ge:H in Ref. 56 at a fixed temperature $T = 200$ K with spin densities of dbs in range of 10^{17} to 10^{18} cm^{-3} after electron irradiation and stepwise annealing, resulting in a charge localization radius around $r_c = 11$ Å. The same hopping processes are also believed to be responsible for the lifetime broadening of the ESR signals at higher temperatures.[59, 66, 67, 70, 90]

The charge localization radius $r_0 = 11$ Å of dbs in a-Ge:H is about three times larger than the spin localization radius $r_0 = 3.5$ Å determined from the hyperfine broadening in this work. For dbs in a-Si:H, a charge localization radius around 4 Å has been determined from transport experiments at 200 K in Ref. 56, while the resolved hyperfine data of the central atoms in a-Si:H would be consistent with a spin localization radius of 3 Å.[50]

It remains to be shown, whether the localization parameters determined from the central hyperfine interactions at the few central atoms of the dbs in a-Si are equivalent to the parameter r_0 extracted from the more than 100 remote atoms in this work, and

independent of the relaxation at the central atom. The comparison of both models is possible for dbs in a-Si, for which both the hyperfine interactions at the central atom as well as the hyperfine broadening at low ^{29}Si concentrations[51] have been measured. Hyperfine broadenings of $\Delta B_{\mathrm{pp}}^{\mathrm{conv}}/c \approx 40$ G are predicted from numerical simulations for $c \leq 10\%$ with a model wave function for dbs in a-Si similar to that of Fig. 5.14a, but with $I_{29} = 1/2$ and $A_{0,\mathrm{iso}} \approx 70\ \mathrm{G} \times g\mu_B$, as measured in isotopically enriched a-^{29}Si:H in Ref. 50, and with $r_0 = 3.0$ Å. This is in good agreement with the experimental low-frequency data of Ref. 51, which shows $\Delta B_{\mathrm{pp}}^{\mathrm{exp}}/c \approx 40$ G for isotopically diluted a-Si:H samples, as shown in Fig. 5.18. No experimental data exists for dbs in a-Si:H in the intermediate concentration range $10\% < c < 90\%$. The critical number of nuclei of Eq. (5.5) is lower in a-Si than in a-Ge because of the smaller nuclear spin. Therefore, and because of the smaller localization radius, the linewidth in a-Si is not expected to rise linearly up to 50% for a hydrogenic model wave function, but to show a second step-like structure at ^{29}Si concentrations around 20% due to the backbonding atoms. In the investigated range of concentrations for a-Si:H, however, the spin localization radius derived from the central atom and the outer atoms agree.

The consistency of the spin localization radius and the central hyperfine constant can be checked independently via the normalization condition for the dangling bond wave function in a-Ge. The volume occupied by a delocalized spin wave function scales like r_0^3, so that the spin density at the central atom would be expected to be about $(3.5/3.0)^3 = 1.6$ times smaller for dbs in a-Ge compared to a-Si based on the localization radii, consistent with $\alpha_0^2 + \beta_0^2 \approx 50 - 70\%$ for a-Si and about 30-50%, which is most probable for a-Ge.

Therefore, both the broadening at low nuclear spin concentrations and the central hyperfine constants support a spin localization radius of $r_0 = 3.5$ Å for dbs in a-Ge compared to $r_0 = 3.0$ Å for dbs in a-Si. In a-Ge, however, this spin delocalization parameter is significantly smaller than the charge localization radius of 11 Å of Ref. 56, which shows that spin-unrestricted calculations will be indispensable to model the dangling bond wave functions in amorphous germanium.

5.5 Conclusions and outlook

Broadening of the spin resonance signal of dbs in a-Ge from 2.6 to 300 G was observed in EDMR investigations of isotope-engineered a-Ge samples over the whole ^{73}Ge concentration range from 0.1% to 95.6%. The contributions of g-factor broadening of $\Delta B_{\mathrm{pp}}^{\mathrm{SO}} = 4.4\ \mathrm{G} \times \nu/\mathrm{GHz}$ and of dipolar broadening of the order of 1 G were investigated separately from these hyperfine contributions with the help of measurements on a nuclear-spin free a-^{70}Ge sample. An additional hyperfine broadening of 10 G due to the ^{73}Ge spins is observed at the natural isotope concentration. Although no hyperfine satellites are resolved due to the continuously increasing linewidth and the large number

of contributing nuclear spins, a central hyperfine interaction of $A_{0,\mathrm{iso}} = 29$ G $\times g\mu_B$ and a spin localization radius $r_0 = 3.5$ Å have been extracted from numerical simulation of the ^{73}Ge concentration dependence of the spin resonance linewidth and lineshape. The spin density is found to be three times more localized than the charge density at the charge localization radius of a-Ge determined from transport measurements.

Further experimental investigations of dangling bond wave functions in a-Ge beyond this localization parameter will be difficult because of the lack of resolved hyperfine interactions. Only for the Fermi-contact interaction at one or two backbonding atoms, reliable values could possibly be obtained from detailed measurements of the linewidths and lineshapes in ^{73}Ge-enriched samples with $60\% < c < 90\%$, which were not available in this work. In a-Si:H, even more information about the spread of the db wave function over the next-nearest neighbors could be obtained from samples with intermediate ^{29}Si concentrations. To our knowledge, no *ab initio* calculations for the charge and spin wavefunctions of dbs in a-Ge have been made up to now. A significantly larger number of atoms compared to the calculations for dbs in a-Si(55) and at the Si/SiO_2 interface(16) will be required for calculations of the dangling bond wave function in a-Ge, at the Ge/GeO_2 interface, and in SiGe alloys. Meanwhile, such enormous computational efforts can be accomplished routinely with highly efficient program packages and modern supercomputers. The results of these calculations would greatly help to resolve the experimental uncertainties because of spin polarization, and to improve the model wave function, which was assumed to be hydrogenic for the lineshape simulations of this work.

The evaluation of the hyperfine broadenings in terms of Fermi-contact interactions with many nuclei developed during this work could stimulate similar investigations of point defects in many other systems, e.g. of dbs in microcrystalline germanium, at the GeO_2 interface, and in amorphous SiGe alloys. Furthermore, the results could help to estimate unresolved hyperfine broadenings of the ESR signals of shallow defects in binary semiconductors, like GaN, AlN, or SiC. These estimates could be confirmed later, if eventually isotope enriched or diluted samples become available.

Chapter 6

Shallow donors in diamond

Diamond has many outstanding properties as a potential semiconducting material. However, a major obstacle for the realization of bipolar diamond-based electronic devices is still the lack of shallow n-type dopants. Shallow donor states are formed e.g. in Si by P impurities and other elements of the fifth column of the periodic table with one extra valence electron compared to Si. Similarly, N has one extra electron compared to C, so that one could expect substitutional nitrogen N_C to form a shallow donor level in diamond. However, due to the electron transfer from the N impurity atom to one of the neighboring C atoms accompanied by a strong lattice relaxation, a 1.6 eV deep defect level is formed at N_C. The microscopic structure of this defect, called "P1 center", was first identified by ESR, as described in Sec. 3.3.3.[10, 11]

An alternative candidate for a shallow donor state in diamond is substitutional P, which unfortunately is much harder to incorporate into diamond than into silicon. The mismatch in atomic radii between P and C, which is the reason for the very high formation energy of this impurity, is illustrated in Fig. 6.1. Despite this difficulty, several groups have reported phosphorus incorporation into diamond during growth from the gas phase

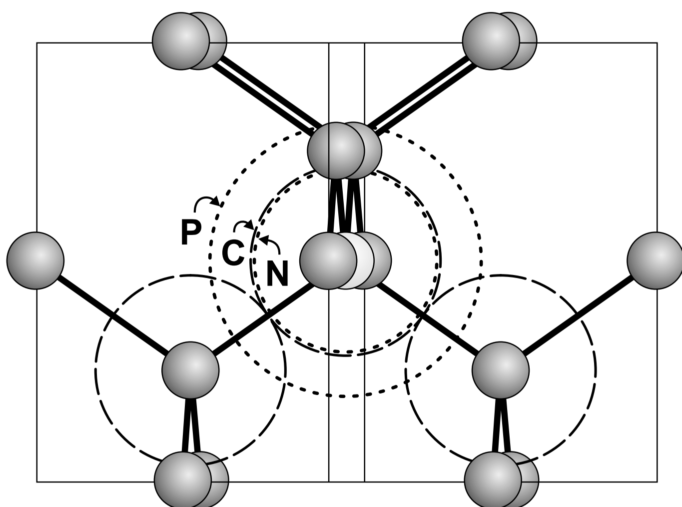

Figure 6.1: Unit cell of diamond seen from a ⟨110⟩ direction. The covalent radii of N and P are indicated by dashed lines at a substitutional site. Because the radius of P is 46% larger than the covalent radius of C, the formation energy of substitutional P is very high.[36, 91] As known from ESR studies on the P1 center,[10, 11] N undergoes a lattice relaxation towards one of the C neighbors, so that a deep defect is formed instead of a shallow donor.

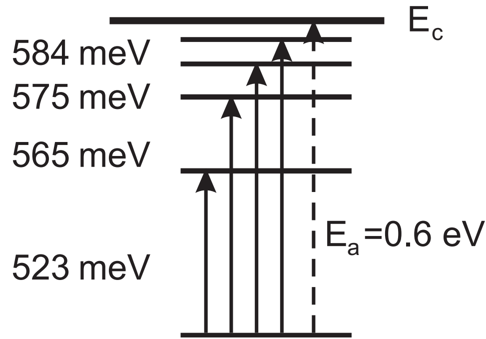

Figure 6.2: Infrared excitations to excited donor states observed in P-doped diamond.(94) The energies of all excited states can be approximated by effective-mass theory. However the ground state at $E_a \approx 600$ meV below the conduction band, as deduced from the thermal activation of the carrier concentration in Hall measurements(98) and from the energy of recombination of a donor-bound exciton around 5.2 eV(95, 96) is about three times larger than the effective-mass value of 218 meV.

without the lattice damage typically caused by ion implantation.(92, 93) A significantly more shallow donor state than the nitrogen defect level was observed in expitaxial samples grown using phosphine as a dopant source. N-type conductivity was found with activation energies of the Hall carrier concentration of 0.4 eV-0.6 eV.(92) For the same samples, infrared absorption peaks were observed at 0.52 eV and 0.56 eV, as summarized in Fig. 6.2, and were related to a photo-ionization onset in photoconductivity measurements.(94) Photoluminescence measurements of the recombination of donor-acceptor pairs and of the P-related exciton point to an energy depth of 630±50 meV of P-related donors.(95, 96) Recently, the first diamond-based bipolar device, an ultraviolet light-emitting diode, has been realized from a pn-junction at the interface between boron and phosphorus doped diamond layers.(97)

At present, the microscopic structure of the phosphorus donor in diamond is still incomplete. Compared to the estimated energy of an effective-mass donor in diamond, much larger optical and thermal ionization energies have been observed experimentally for states attributed to substitutional phosphorus,(99) but no lattice relaxation of the phosphorus atom away from the substitutional site could be detected in channelling experiments in the same n-type samples.(100) Hyperfine information from ESR experiments could provide a critical test for the symmetry and localization of this donor ground state.

6.1 ESR of phosphorus in diamond

One of the most sensitive probes for the symmetry and extend of the donor wave function are nuclear hyperfine coupling constants, which are experimentally accessible by electron spin resonance (ESR) and electron-nuclear double resonance (ENDOR). ESR of phosphorus-related states in diamond has been observed in poly-crystalline powders,(101) in crystals using a phosphorus catalyst,(102) and in CVD films implanted during growth(103) or after growth with subsequential annealing.(104) In the crystalline films, isotropic hyperfine lines with a characteristic splitting of 27-28 G were observed and attributed to the $I = 1/2$ nuclear magnetic moment of substitutional ^{31}P. Unfortu-

type	appearance	nitrogen contamination		nat. abundance
Ia	transparent	A,B-aggregates	500..2000 ppm	most natural samples
Ib	yellow – greenish	P1 centers (N_C)	50..500 ppm	most synthetic samples
IIa	transparent		$<$ 50 ppm	rare, natural gemstone
IIb	transp. – bluish	less N than B,	$\varrho < 10^4$ Ωcm	very rare

Table 6.1: Classification of diamonds as type Ia, Ib, IIa, and IIb according to their optical absorption features in the visible and infrared region (from Ref. 105). Type Ia, Ib, and IIa diamonds are highly insulating at room temperature because of the the large energy depth of nitrogen centers compared to the thermal energy.

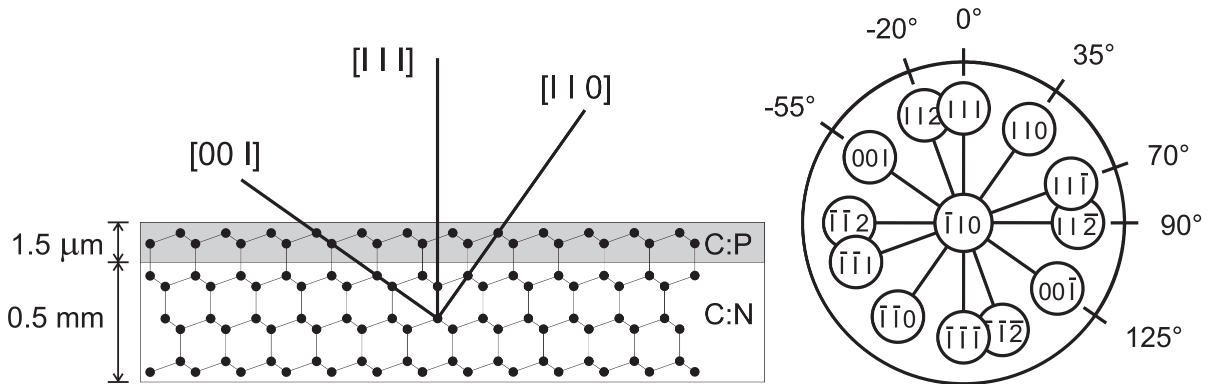

Figure 6.3: [100] rotation plane of the magnetic field for the investigation of ESR along all principle axes of a diamond crystal with a [111] oriented surface.

nately, these samples have a large number of implantation defects besides the phosphorus donors, so that n-type conductivity has never been observed for these samples. Only recently, 28 G split hyperfine lines were observed by ESR in P-implanted samples together with the characteristic infrared absorption at 0.52 eV and 0.56 eV,[(104)] which has also been found in the samples of Ref. 94, suggesting that shallow states give rise to this ESR signal.

Up to now, n-type samples doped from the gas phase were mostly grown on Ib diamond substrates. Unfortunately, the large amount of nitrogen P1 centers in these substrates is causing a huge background in conventional ESR experiments. Therefore, electrically detected magnetic resonance (EDMR), which provides high sensitivity and selectivity to spin-dependent transport at the Fermi level, seems to be the most promising approach to access paramagnetic states in P-doped epilayers.[(63)] As electrical detection is particularly sensitive to the paramagnetic states within the path of conductivity, efficient suppression of the P1 background from the insulating substrate can be achieved.

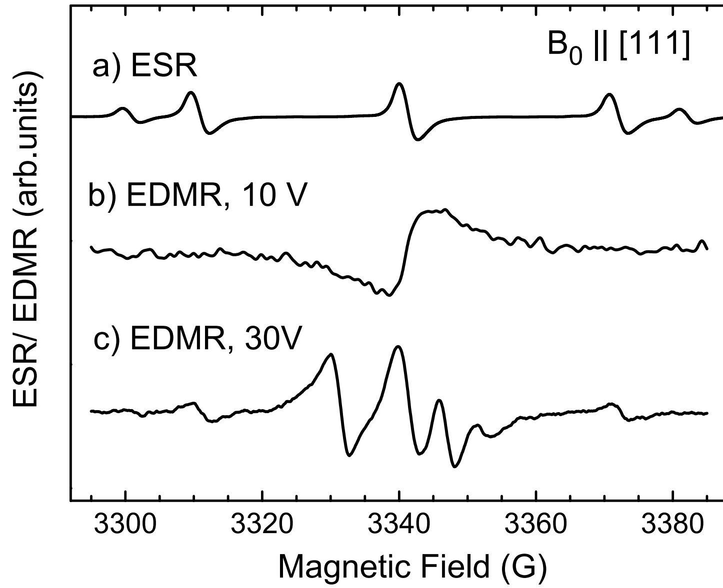

Figure 6.4: a) ESR signal dominated by P1 centers in the Ib substrate. b, c) EDMR spectra at bias voltages of 10 V and 30 V corresponding to 2 kV/cm and 6 kV/cm, assuming a homogeneous field distribution. In the regime of low electric field, carbon dangling bonds dominate spin-dependent transport, while at higher electric fields the signal shows a complex structure with several resonances. The normalized EDMR intensity is $\Delta\sigma/\sigma = \Delta I_{pp}/I_{DC} \approx 10^{-6}$ for the maximum components of the signal.

6.2 EDMR of n-type diamond

Doping of the particular homoepitaxial film investigated was performed by plasma-assisted chemical vapor deposition on a polished [111] surface of a $2 \times 2 \times 0.5$ mm^3 type Ib synthetic diamond with the relative gas concentrations $CH_4/H_2 = 0.075\%$ and $PH_3/CH_4 = 0.1\%$. Photoconductivity and infrared absorption measurements have been reported in Ref. 94, where this sample is labelled #4. The nominal phosphorus concentration of 5×10^{18} cm^{-3} of the film is below that of the metal-insulator transition expected for effective-mass donors in diamond. Approaching the metallic regime, the hyperfine satellites from the nuclear spin $I = 1/2$ of ^{31}P would be eliminated by delocalization due to exchange or due to fast hopping on the timescale of the spin lifetime.(29) In the investigated samples, hopping rates are much lower, but still high enough to contribute significantly to conductivity at room temperature and below. At higher temperatures the dark conductivity is found to be thermally activated with about 0.6 eV. Therefore, room temperature EDMR measurements seem to be a suitable tool to measure the hyperfine interaction at the ^{31}P donors in this n-type diamond film.

To ensure thermal equilibrium for charges metastably trapped within the diamond crystal, the sample was heated to about 600 K in the dark and subsequently transferred to the ESR system. Sample orientation and g-factor calibration were checked with the help of the anisotropic ESR signal from P1 nitrogen centers in the substrate shown in Fig. 6.4.(10) For EDMR measurements, coplanar interdigitated Au contacts with 50 μm spacing were deposited on top of the epitaxial film. The differential resistance of 10 MΩ at bias voltages above ± 20 V is consistent with the reported data for n and μ for this film.(94)

6.2.1 Bias dependence

Fig. 6.5 shows the IV-characteristics of the film at room temperature in the dark. Above ± 20 V, the behavior is almost ohmic as indicated by the dashed line that corresponds to a differential resistance of 10 MΩ and a conductivity of 10^{-6} Ωcm^{-1}. However, the IV-curve at lower bias voltages is nonlinear, indicating that the current is limited by some kind of barrier, such as the space charge region of a Schottky contact below breakthrough in reverse-bias. Obviously, any electrical measurement such as EDMR should be analyzed with regard to the bias voltage that determines the dominant resistance. In the regime of high voltages, the applied electric field is able to overcome the barriers so that the measured current is limited by the epilayer of interest, whereas in the low-field regime the space charge layers limit the overall current. The different EDMR signatures observed at high and low bias voltages shown in Fig. 6.4 support this qualitative explanation. While in the high-field regime at 30 V bias, a complex anisotropic signal is observed that will be discussed in more detail below, the low-field signal at 10 V bias can be identified directly by its isotropic g-factor $g = 2.0028$ and the peak-to-peak linewidth $\Delta B_{pp} \approx 7$ G. These parameters are commonly associated with carbon dangling bonds in amorphous hydrogenated carbon,(106) in polycrystalline diamond,(107) and in crystalline thin CVD diamond films after implantation.(103, 104) EDMR of carbon dangling bonds has been demonstrated previously in polycrystalline CVD diamond films with a high defect density.(108) In the present homoepitaxial film, the EDMR sensitivity to carbon dangling bonds is particularly high, as these defects limit conductivity through the space charge regions of the interdigitated contacts. Therefore, a small amount of such defects can be detected even in a single-crystal. The sign of the EDMR signal at low electric fields indicates a resonant quenching of the current due to a spin-dependent capture process of conduction band electrons.

In contrast, the signal at high electric field corresponds to a resonant enhancement of the current, which is typical for hopping transport at the Fermi level. As seen in the spectrum of Fig. 6.4, new features appear in the EDMR signal of the n-type layer when the bias voltage is increased to 30 V. In this regime, the electric field is sufficient to overcome the barriers at the contacts and to obtain the EDMR signal of the n-type epilayer. At the same time, the background spectrum of the carbon dangling bonds at the contacts is reduced. EDMR spectra measured under these conditions for the three fundamental crystal orientations with respect to the magnetic field B_0 are shown in Fig. 6.6. Within the overlapping resonances, the outer pairs of satellites are recognized clearly as part of the P1 spectrum observed simultaneously in conventional ESR. Although the substrate has a higher thickness than the epilayer, its room temperature dark conductivity is too low for a contribution to an EDMR signal with $\Delta\sigma \approx 1$ pA. This could indicate that deep P1 centers are present in the epitaxial film. Alternatively, since the identical signal is strongly observed in the substrate ESR, heating of the sample upon microwave absorption has to

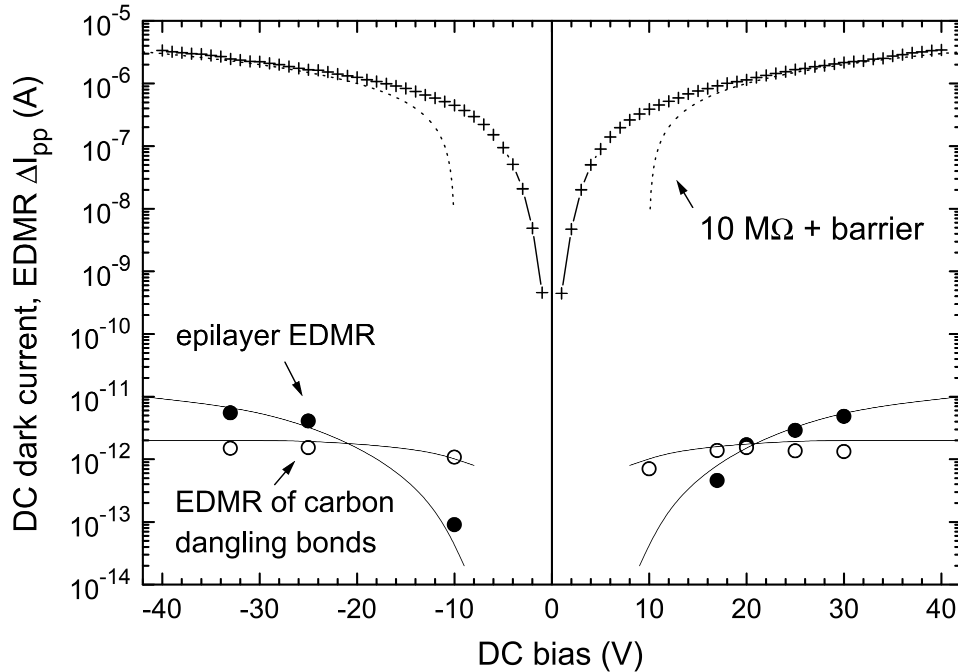

Figure 6.5: Room temperature IV-characteristics of the phosphorus doped diamond film with 50 μm interdigitated finger contacts (++). The dotted line indicates the IV-characteristics of an ohmic resistor, but offset from zero voltage due to a voltage drop of about 10 V at the non-ideal contacts. Open and closed circles show the intensities of the two signal components in EDMR.

be considered as another possible origin for the increased conductivity at spin resonance. Such thermal crosstalk could not be distinguished from spin-dependent hopping for the P1-related EDMR signal.

6.2.2 Anisotropy at high bias voltage

Besides the signal due to P1 centers, all spectra measured at high bias voltage show an isotropic line at 3329 G and several anisotropic lines with C_{3v} symmetry at about 3347 G. For these features, thermal crosstalk can be excluded, as no absorption is visible at those field positions in conventional ESR. If both lines were interpreted separately, their g-factors would be $g = 2.009$ and $g \approx 1.998$, which is outside the typical range of g-factors known for diamond.(25) More consistently, they might be interpreted as a hyperfine pair caused by the interaction with the nuclear spin $I = 1/2$ of the ^{31}P atom. In this case, the spin Hamiltonian for the unpaired electron with axial symmetry is given by

$$\mathcal{H} = \mu_B \vec{B}_0 \hat{g} \vec{S} + \vec{S} \hat{A} \vec{I} \tag{6.1}$$

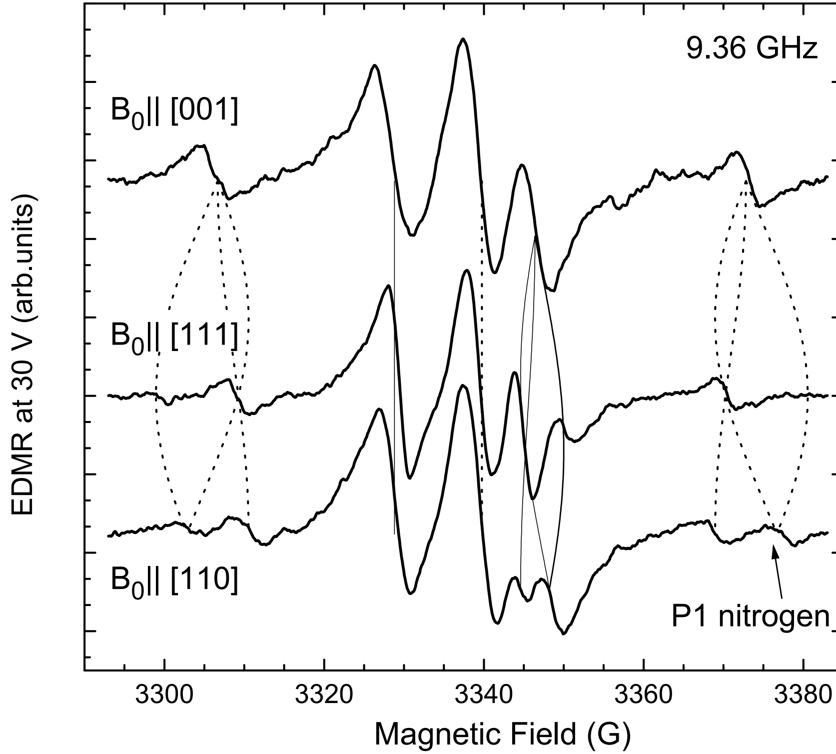

Figure 6.6: Anisotropy of the EDMR signal at 30 V. The crystal is rotated around a [110] axis. The outer transitions and the central line around 3340 G belong to P1 triplets that dominate the ESR signal of the Ib substrate and to dangling bond centers. The inner set of lines is attributed to hyperfine satellites of a phosphorus-related center, which has a very low spin density on the ^{31}P nucleus.

with the axial tensors $\hat{g}$ and $\hat{A}$, and Bohr's magneton μ_B. To first order, the magnetic fields at which transitions occur are[19]

$$B_0 = \frac{h\nu}{g\mu_B} \pm \frac{A}{2g\mu_B} \tag{6.2}$$

with

$$g = \sqrt{g_{||}^2 \cos^2\theta + g_{\perp}^2 \sin^2\theta} \quad \text{and} \tag{6.3}$$

$$A = \frac{1}{g}\sqrt{A_{||}^2 g_{||}^2 \cos^2\theta + A_{\perp}^2 g_{\perp}^2 \sin^2\theta}, \tag{6.4}$$

Planck's constant h, the microwave frequency ν, and the angle θ between the magnetic field and the defect axis. Without g-factor-anisotropy, all pairs of hyperfine lines would appear symmetrically around one central magnetic field, as it is the case for the P1 center. For small anisotropic contributions from g and A, both angular dependencies can be separated, so that

$$A \approx A_{\text{iso}} + A_{\text{aniso}}(3\cos^2\theta - 1). \tag{6.5}$$

As indicated in Fig. 6.6, we interpret the experimental resonance positions by a combination of the anisotropies in g and A, which cancel on the left satellite, so that here the splitting is below the experimental linewidth of $\Delta B_{pp} \approx 5$ G. In contrast, the anisotropies add up on the three satellites on the right, separating these lines with only little overlap. Accordingly, we find an axial center with C_{3v} symmetry, $g_{\perp} = 2.0026$, $g_{||} = 2.0042$,

$A_{\rm iso} = 17.6$ G, and $A_{\rm aniso} = 1.8$ G. Two of the four symmetry-related sites coincide for the investigated orientations. Assuming the parameters given above, the positions and intensities of the measured spectra are described satisfactorily. To our knowledge, a similar set of parameters has not been reported for paramagnetic centers in diamond before. In particular, they are distinct from the phosphorus-related centers of Tab. 6.2. One of these centers (NIRIM 8)[(102)] has been identified as P-C-N^+ complex with most of the electron density localized at the nitrogen atom. The same complex is possibly present in the polycrystalline powder of Ref. 101 with the outer satellites broadened beyond detection. The second, almost isotropic center from Ref. 103 and 104 has been observed recently together with the characteristic infrared absorption at 0.52 eV and 0.56 eV also present in the n-type samples of this study, suggesting that shallow states give rise to this ESR signal.[(104)] Because the implanted samples have a large number of additional defects besides the phosphorus-related states, n-type conductivity has not been confirmed for them yet. The set of parameters for the new EDMR center is also different from the hydrogen-vacancy complexes H1 and H2,[(107)] and the μ^*- and μ-centers that correspond to interstitial and bond-centered hydrogen in diamond. Scaled from the ratio of nuclear g-factors, these would have the hyperfine constants $A^*_{\rm iso} = 23.4$ G and $A^*_{\rm aniso} = 21.1\ {\rm G} \times g\mu_B$, or $A_{\rm iso} = 421\ {\rm G} \times g\mu_B$. The line positions are also different from the forbidden hyperfine transitions within the P1 manifold.[(25)] The natural abundance of $I = 1/2$ nuclei other than ^{31}P and ^{1}H is too small to account for the observed resonance pattern.

The measured Fermi contact and dipolar hyperfine parameters are converted into atomic spin densities α^2 and β^2 in the atomic $3s$ and $3p$ orbitals of phosphorus with Eq. (3.17) and (3.18) and the help of the Hartree-Fock-Slater integrals $A_{\rm iso} \approx 4748$ G and $A_{\rm aniso} \approx 131$ G of Tab. 3.1 from Ref. 9 for unpaired s an p electrons. The ratio of the measured constants and these numbers directly gives the hybridization ratio sp^x with $x = \beta^2/\alpha^2$ and the total spin density $\alpha^2 + \beta^2$ at the phosphorus atom. Note, that in the defect molecule picture, the hybridization ratio $x = 3$ corresponds to a bond angle of 109.47° and sp^3-coordination of the backbonding atoms, whereas $x \gg 3$ corresponds to a bond angle close to 90° and sp^2-coordination. The results for the P-related EDMR center are listed in Tab. 6.2. The last but one row shows that for the center reported here, the remaining spin density at the phosphorus atom is about 1%, similar to the phosphorus-nitrogen complex of Ref. 102. Consequently, the unpaired donor electron has been transferred almost completely to nearby atoms. The spin density at the impurity atom is even lower than in the case of the strongly distorted P1 center, where about 20% of the spin density resides at the donor atom and most of the wave function is shifted to one carbon neighbor.[(25)]

In Ref. 109 a stable Phosphorus-Vacancy (P-V) complex is predicted, which has axial symmetry and very low spin density at the donor atom, as the large phosphorus impurity occupies the space of two adjacent carbon atoms. However, this defect complex is

expected to be in its neutral charge state only from 0.6 eV to 1.1 eV above the valence band edge.[110] In n-type samples, this complex would act as an acceptor, become diamagnetic, and therefore be invisible for ESR. Since for similar samples a large fraction of phosphorus atoms was found on substitutional rather than on bond-centered sites in channelling experiments,[100] and because of the small number of β^2, this center should not be expected as the origin of the observed EDMR signal. Unfortunately, no further hyperfine satellites are observed within the experimental resolution, which could clarify the location of the remaining 98% of the electron wave function. Most likely, atoms with a low fraction of nuclear spins such as ^{13}C are involved, so that the satellite intensity is well below the noise level of our experiment. In conclusion, only the axial symmetry and the spin density at the phosphorus atom were obtained for this electronically active center close to the Fermi level.

6.2.3 Additional signal after illumination

One additional series of EDMR measurements was performed with the sample in a metastable state after illumination without subsequential heating in the dark, leaving it in thermodynamical non-equilibrium. This pretreatment did not affect the DC conductivity significantly, but as shown in Fig. 6.7, it revealed a new EDMR center with the hyperfine satellites of at least two non-equivalent sites. This signal disappeared after measuring the sample orientation by x-ray diffraction and subsequential heating to 600 K in the dark, which hindered us to check the full signal anisotropy, which is assumed to be axial along [111] similar to the spectra of Fig. 6.6. The magnetic field was not oriented along one of the principal crystalline axis for the spectrum of Fig. 6.7, but its direction cosines towards the [111] axis were recovered to be $\cos^2\phi = 0.94, 0.27, 0.15$, and 0.00 from the ESR of P1 centers in the same sample orientation close to a [112] axis. Assuming $I = 1/2$ and axial symmetry along a [111] axis, the hyperfine tensor is given by $A_{\text{iso}} = 380$ G and $A_{\text{aniso}} = 15$ G. Due to the large isotropic component, the first-order approximation to the resonance fields from above has to be corrected by second order terms that shift both satellites to lower magnetic fields

$$B_0 = \frac{h\nu}{g\mu_B} \pm \frac{A}{2g\mu_B} - \frac{A^2}{4h\nu g\mu_B} \pm \ldots \tag{6.6}$$

Considering this so-called Breit-Rabi shift, the g-factor of this EDMR signal is $g = 2.006$, which shows clearly that the satellites are not part of the central structure, which probably is a convolution of the various centers within $g = 2.0042$ to 2.0026 from above, broadened in Fig. 6.7 due to the experimental conditions. Compared to the hyperfine interaction of an isolated phosphorus atom, the hybridization ratios β^2/α^2 and the total spin density $\alpha^2 + \beta^2$ are evaluated and listed in the last row of Tab. 6.2. This center is more isotropic and about 10 times more localized at the phosphorus atom than the previous one. Also

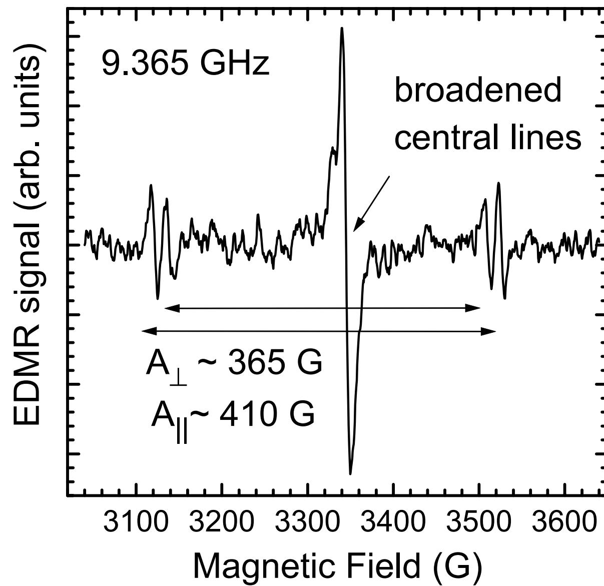

Figure 6.7: EDMR signal of the second ^{31}P-related center with large, but still anisotropic hyperfine interaction. This center was observed in a sample state without prior heating in the dark, so that thermal equilibrium has not been reached on the timescale of the experiment of one week. For this spectrum, the sample was oriented with the magnetic field along a [112] axis, as reconstructed from the ESR signal of the P1 center in the substrate. The central line around 3340 G is a broadened convolution of the signals shown in Fig. 6.6.

for this electron, no additional hyperfine interaction was observed within the experimental signal-to noise ratio.

6.3 Discussion of the EDMR signals

In general, a low spin density at the donor atom would be characteristic for shallow donor electrons, which might extend over hundreds of lattice sites. In the case of phosphorus in silicon, the ^{31}P Fermi contact interaction is only 42 G, corresponding to about 0.9% of an atomic 3s wave function.(5) By ENDOR, the hyperfine interaction of this donor electron with many surrounding shells of Si atoms has been determined and consistently interpreted in terms of an improved effective-mass model.(6) In diamond, the effective-mass approximation successfully predicts the excited donor level energies, and at least gives a reasonable trend for the description of the ground state energy.(99) A simple extrapolation of this effective-mass model to substitutional P in diamond is discussed in the following.

6.3.1 Effective-mass donors in diamond

The most sensitive check for the approximated wave function certainly is the Fermi contact interaction at the central nucleus. In the effective-mass approximation, the donor wave function is build from a combination of the hydrogenic envelope function $F(r)$ and Bloch functions at the conduction band minima at $\vec{k}_0$ along the D axes of the Brillouin zone. In the absence of better crystal wave functions, these Bloch functions are best approximated

with the help of atomic solutions $u(\vec{r})$ of the Hartree-Fock equation,[5] so that

$$\Psi(\vec{r}) = \sqrt{\tfrac{1}{6}} \sum_{j=1}^{6} F(\vec{r})^j u(\vec{r})^j \exp(i\vec{k}_0^j \vec{r}), \tag{6.7}$$

where the summation is over all conduction band minima. The probability density at the phosphorus donor with a central wave function $u(r)$ is described in this approximation by the envelope-function F, the scaling of which is done by an ellipsoidal hydrogenic potential with the anisotropic effective masses m_t^* and m_l^*. Outside of the central cell, the dielectric constants $\varepsilon_{\mathrm{Si}}^*$ and $\varepsilon_{\mathrm{C}}^*$ of silicon and diamond, respectively, are screening the strong coulombic potential. As the ratio m_t^*/m_l^* is similar for silicon and diamond, the hydrogenic energy levels $E^* \propto m^*/\varepsilon^{*2}$, the radius of localization of the envelope function $a^* \propto \varepsilon^*/m^*$, and the probability density $|\psi(0)|^{*2} \propto a^{*-3} \propto (m^*/\varepsilon^*)^3$ scale simply with the ratios $\varepsilon_{\mathrm{C}}^*/\varepsilon_{\mathrm{Si}}^* = 5.7/11.7 \approx 0.5$ and $m_{\mathrm{C}}^*/m_{\mathrm{Si}}^* \approx 1.5$.[99] The scaling factor for the extrapolation from silicon to diamond is $(m_{\mathrm{C}}^*/m_{\mathrm{Si}}^*)/(\varepsilon_{\mathrm{C}}^*/\varepsilon_{\mathrm{Si}}^*) \approx 1.5/0.5 = 3$, which means, that the probability density and hyperfine constant have to be scaled by a factor $3^3 = 27$ from silicon to diamond. Starting with $\alpha^{*2} \approx 0.9\%$ in silicon, the portion of the donor wave function on the donor atom would be of the order of 24% in diamond, and the expected isotropic hyperfine interaction larger than 1000 G $\times\, g\mu_B$. Due to the increased contribution from the central cell with an even smaller dielectric constant, the experimental ground-state energy appears underestimated by this simple approximation. For this reason, the true localization and hyperfine constant should be even larger for P in diamond. Corrections in the opposite direction are discussed in Ref. 103 due to the relative electronegativities, which might reduce the wave function amplitude at the phosphorus atom in diamond compared to the situation in silicon. Additionally, the admixture of antisymmetric combinations of wave functions from opposite conduction minima to the donor ground state wave function leads to a reduction of the central hyperfine constant in Si:P.[111] This “valley orbit” coupling mechanism can be expected to be less pronounced for diamond compared to silicon because the excited states are at larger energies there.[99]

6.3.2 Hyperfine values from the literature

For comparison, the observed hyperfine parameters and the corresponding spin densities of both centers are summarized in Tab. 6.2 together with the spin Hamiltonian parameters of P-related ESR signals reported previously for phosphorus-doped diamond samples without n-type conductivity.

Strong P1-like hyperfine satellites were observed in addition to the phosphorus-related ESR signals in poly-crystalline diamond powder,[101] and in single crystals grown from phosphorus catalyst.[102] Therefore, it was suggested in Ref. 102 that these signals could possibly be related to a N1-like defect complex involving an ionized phosphorus atom

method of P incorporation	g	A_{iso} ($g\mu_B$G)	α^2 (%)	A_{aniso} ($g\mu_B$G)	β^2 (%)	$\alpha^2 + \beta^2$ (%)	$\frac{\beta^2}{\alpha^2}$
high pressure [101]	2.0025	20.8	0.4	1.2	0.9	1.3	2
from catalyst [102]	≈2.003	≈20	0.4	≈1	0.9	1.3	2
coimplanted [103]	2.0023	27	0.6	-	-	0.6	0
impl. & ann. [104]	2.0024	28	0.6	-	-	0.6	0
from the gas phase,	anisotr.	17.6	0.4	1.8	1.4	1.7	3.7
PECVD [this work]	2.006	380	8.0	15	11	19	1.7

Table 6.2: Spin Hamiltonian parameters of phosphorus-related centers in diamond obtained from ESR and EDMR experiments. The relative spin densities have been evaluated with the help of the atomic values from the Hartree-Fock-Slater integrals $A_{\text{iso}} = 4748$ G $\times\, g\mu_B$ and $A_{\text{aniso}} = 131$ G $\times\, g\mu_B$ of Tab. 3.1.(9)

next to a substitutional nitrogen impurity. Such a complex would have about 25% of the spin density localized on the nitrogen atom, and the remaining 73% of the spin density on adjacent carbon atoms (see Sec. 3.3.3). The low spin density of 2% at the phosphorus atom in such a complex is not related to an extended donor wave function, but rather to the significantly higher electronegativity of at least one of the neighboring atoms. Other defect complexes with vacancies,(109) or hydrogen atoms(91, 110) as nearest neighbors have been predicted from theory, however, without quantification of spin densities or hyperfine constants. All theoretical calculations suggest that these defect complexes are deeper in energy than substitutional phosphorus donors. Weaker exciton binding energies have been observed only for the isoelectronic P-B complexes, which are not expected to have donor or acceptor activity.(96)

According to the calculations of Ref. 112, the C-P bond lengths around a substitutional phosphorus atom are expected to have between 109% to 112% of the ideal C-C bond length. However, calculations with a larger numbers of atoms eventually find equal bond lengths and T_d symmetry for the isolated substitutional phosphorus donors.(91, 112) It would therefore be intriguing to assign the isotropic center observed in P-irradiated diamond samples(103, 104) to substitutional phosphorus donors. However, as these samples do not show n-type conductivity because of the high level of radiation damage, their Fermi level is probably not located at 0.6 eV below the conduction band. This would be consistent with the observation of other defects besides the 27 G split hyperfine satellites in ESR.(103, 104) If, however, the Fermi level is below the phosphorus donor level, most donor electrons must be expected to be trapped at other defects, leaving the shallow donors ionized, diamagnetic, and therefore invisible to ESR. Finally, the hybridization ratios β^2/α^2 of the centers listed in Tab. 6.2 can be compared to that of the P1 center introduced in Sec. 3.3.3 with $\beta^2/\alpha^2 \approx 3.8$. The phosphorus-related centers observed in

this work seem to undergo a less pronounced axial distortion, which would be consistent with a more symmetrically delocalized electron wave function.

6.4 Conclusions

Effective-mass like delocalization determining the ^{31}P hyperfine splitting in silicon clearly does not account for the extremely low spin density, smaller than 2%, observed in the case of the first diamond center described in this chapter (Fig. 6.6) and in those reported previously by conventional ESR. Significantly higher spin densities of $\alpha^2 + \beta^2 \approx 19\%$ are found for the second center (Fig. 6.7). However, the anisotropic part $\beta^2 \approx 11\%$ of this signal still suggests a strong relaxation for this donor state, too.

It is evident from the detection scheme used that the defects observed via EDMR in this work are strongly involved in room temperature transport in this n-type diamond film. Theoretical modelling of the microscopic structure and hyperfine constants of these phosphorus-related states in diamond would therefore be highly desirable.

6.5 Outlook: Alternatives to n-type diamond

At present, phosphorus is known as the shallowest donor in diamond. However, the preparation of purely diamond-based bipolar devices is a challenge because of the low solubility and large ionization energy of phosphorus atoms in diamond. In contrast, p-type doping of diamond is readily available via boron acceptors located at 374 meV above the valence band edge. This situation is the opposite of what is known about many other wide band gap materials, such as GaN, AlN, or ZnO. For these materials, n-type conduction occurs naturally, and p-type doping is a major challenge. It is therefore of interest to combine both natural preferences, and to replace the n-type diamond films with layers of other n-type materials like AlN:Si, in which the Si donors are known to form DX centers at 320 meV below the conduction band edge.(113)

Growth and characterization of such a heterojunction device between a cubic [001]-oriented boron-doped IIb diamond substrate and a wurtzite [00.1]-oriented silicon-doped AlN epitaxial film has been reported recently.(114) The structural quality of this AlN film was surprisingly good, considering the mismatch of lattice symmetries and periods, and of the thermal expansion coefficients. Under forward bias, ultraviolet electroluminescence at 4.8 eV has been observed from this AlN/diamond interface, and was ascribed to the recombination of electrons and holes. In addition, strong blue light emission was observed around 2.7 eV, and ascribed to recombination at defect states at the interface.(114)

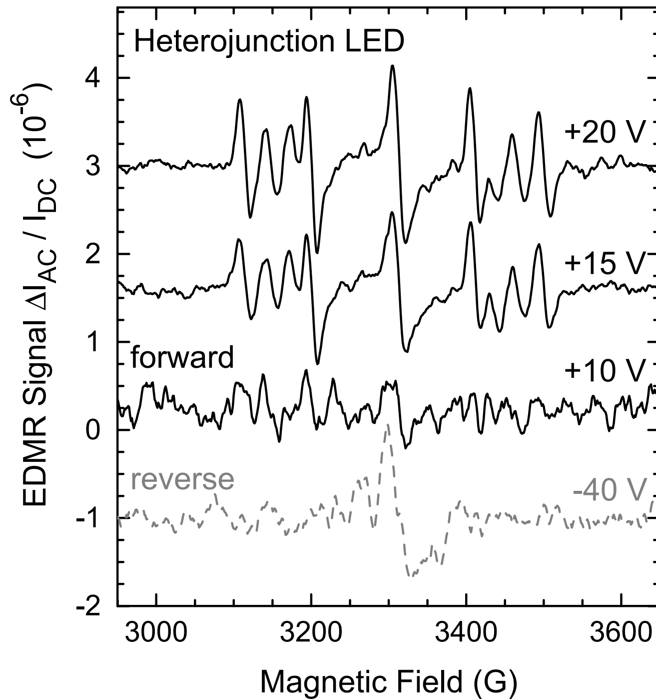

Figure 6.8: Bias dependence of the EDMR signal from an AlN/diamond heterojunction. All EDMR intensities ΔI_{AC} have been normalized to the DC currents I_{DC}. The multiple resonance lines observed at sufficiently large forward bias are ascribed to recombination at deep defect centers. A qualitatively different EDMR signal is observed in reverse direction. This is most probably related to spin-dependent processes in the leakage current through the space charge region.

6.5.1 Spin-dependent recombination

Apparently, the minority carriers injected into the p-n junction under forward bias are very likely to be trapped at defects and are therefore lost for radiative recombination in the ultraviolet energy range. The defect states responsible for this parasitic recombination process can be identified via EDMR measurements of the spin-dependent contributions to this recombination process, as described in Sec. 4.3.

As shown in Fig. 6.8, EDMR observed under forward bias in such a diode is indeed sensitive enough to detect defects which cannot be observed in conventional ESR. EDMR experiments on the AlN/diamond heterojunction of Ref. 114 at several bias voltages are shown in Fig. 6.8. The asymmetry of this EDMR signal with respect to the bias conditions confirms that the active defect states are confined to a region close to the heterointerface. High leakage currents under reverse bias were already noticed from the IV-characteristics of this particular LED device.[(114)] Possibly, the interface defects involved in this leakage path dominate the EDMR signal under reverse bias. However, from the bias dependence alone it is unclear whether the active defect levels under forward and reverse bias are located on the AlN side of the interface, at the interface itself, or on the diamond side of the interface.

6.5.2 Anisotropy of the EDMR signal

The symmetry of the defect state observed under forward bias can be obtained from EDMR measurements at various orientations of the sample with respect to the magnetic

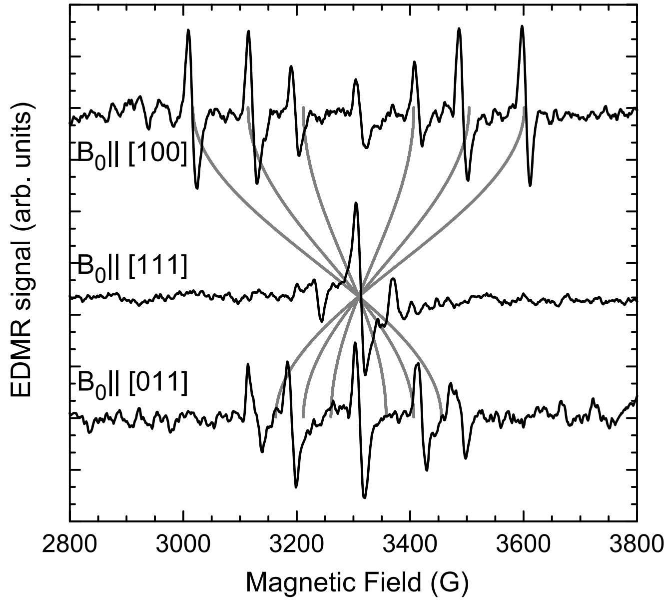

Figure 6.9: The largest splitting of the EDMR signal under forward bias occurs at magnetic field orientations close to [100]. The grey lines indicate the anisotropy pattern calculated for fine-structure interactions along [100] and equivalent axes. Better agreement with the experimental data is obtained with a [912]-oriented fine-structure pattern, as shown in Fig. 6.10.

field, as is shown for magnetic field orientations along the principal cubic axes in Fig. 6.9. The observed pattern has the symmetry properties of the bulk diamond lattice, as EDMR signals similar to the spectrum labelled with $B_0||[100]$ in Fig. 6.9 have been observed not only for the orientation of the magnetic field along the [100] direction tilted by about 6° with respect to the surface normal, but also for one of the perpendicular [010] directions in the sample plane. In the case of hexagonal AlN, such a similarity would necessarily imply $D_\perp = D_{||}$, and therefore the absence of axial anisotropy. Different EDMR spectra are observed for intermediate orientations, e.g. for one of the four equivalent [111] axes tilted by 54.74° towards the sample plane, and for one of the four [011] axes in the sample plane and for one of the two [110] axes within the sample plane. This symmetry information has been verified experimentally from EDMR signals of two rotation planes, namely a rotation around the $[0\bar{1}1]$ axis from [100] via [111] to [011] and a rotation around the [001] axis from [100] via [110] to [010].

The overall intensity of the satellite lines exceeds the central line by far. Therefore, the spin state under investigation has probably spin $S = 1$, and the central line does not originate from the same defect as the outer lines. Possibly, this central line is the same, as that observed under reverse bias. The first-order angular variation pattern calculated for a defect with $S = 1$ and fine structure interactions

$$\begin{aligned} &D_{zz} = -540 \text{ MHz} \times h, \quad D_{yy} = 360 \text{ MHz} \times h, \quad \text{and} \quad D_{xx} = 180 \text{ MHz} \times h \\ &\text{oriented along the principal tetragonal axes} \quad \vec{e}_z||[100] \quad \text{and} \quad \vec{e}_y||[010] \end{aligned} \tag{6.8}$$

is shown by the grey lines in Fig. 6.9. A defect with this symmetry could fit the observed six satellite lines at $B_0||[100]$ approximately. However, the description fails to describe the observed spectra at most other crystal orientations. Up to now, no defect with this symmetry has been observed in diamond, despite the large number of defects with $S = 1$

reported in the literature.[25, 115] Only few low-spin defects like the tetra-interstitial cluster I_4 in silicon have been observed with this uncommon symmetry.[116] Therefore, and because even larger fine structure splittings are observed at small tilt angles away from the [100] axis, the angular anisotropy pattern for a lower defect symmetry with

$$D_{zz} = -600 \text{ MHz} \times h, \quad D_{yy} = 400 \text{ MHz} \times h, \quad \text{and} \quad D_{xx} = 200 \text{ MHz} \times h$$
$$\text{and the principal axes} \quad \vec{e}_z || [912] \quad \text{and} \quad \vec{e}_y || [\bar{1}\bar{1}5] \tag{6.9}$$

has been considered and is shown by the grey lines in Fig. 6.10. Also shown there is a set of EDMR spectra at intermediate magnetic field orientations for an axis of rotation, which is tilted by about 5° from the $[0\bar{1}1]$ axis. This pattern fits the observed line positions and intensities much better than the pattern calculated with the fine structure parameters of Eq. (6.8). Apparently, most line positions could be fitted reasonably well with a $S = 1$ center and the fine structure tensor of Eq. (6.9). A more accurate determination of the components of the fine structure tensor and its principle axes are at present hindered by the large number of lines and the limited signal-to-noise ratio of this experiment. No other defects with similar fine structure parameters have been reported in diamond before.[25, 115]

A very rough estimate for the extent of this defect structure is possible via the point dipole approximation of Sec. 3.2.1 and with $D = \frac{3}{2}D_{zz} \approx -320$ G $\times\, g\mu_B$. According to Eq. (3.14), the dipolar distance between two non-overlapping spins with a total spin $S = 1$ is

$$r = \sqrt[3]{3\mu_0 (g\mu_B)^2 / 8\pi D} = 4.42 \text{ Å} \quad . \tag{6.10}$$

This dipolar distance is almost equal to the size of $a = 3.57$ Å of the unit cell of diamond, which would be a typical extent of a defect complex with [100] symmetry (see Fig. 3.1c). The true dipolar distance could be overestimated from the simple point-dipole approximation because of charge delocalization effects and the considerable off-axis component $E = \frac{1}{2}(D_{xx} - D_{yy}) \approx -36$ G $\times\, g\mu_B$.

The microscopic model for this new recombination center observed under forward bias at the AlN/diamond heterojunction is still incomplete. However, it is clear from the EDMR data that this center is located on the diamond side of the p-n junction. Because the growth conditions of AlN are not expected to induce many additional defects in the IIb diamond substrate, the defect complexes were probably already present in the substrate before the growth of the AlN film. This assumption would not be in conflict with the lack of an ESR signal from the diamond substrate, as the defect complex could be diamagnetic in the Boron-doped p-type material. Only in the space charge region of the investigated p-n junction, the Fermi level could be lifted far enough to transfer additional electrons to this defect complex and make it visible for EDMR. This suggests that the growth of a high-quality p-type diamond film below the n-type AlN:Si film is indispensable for better performance of future diamond-based heterojunction devices. It also makes clear that the

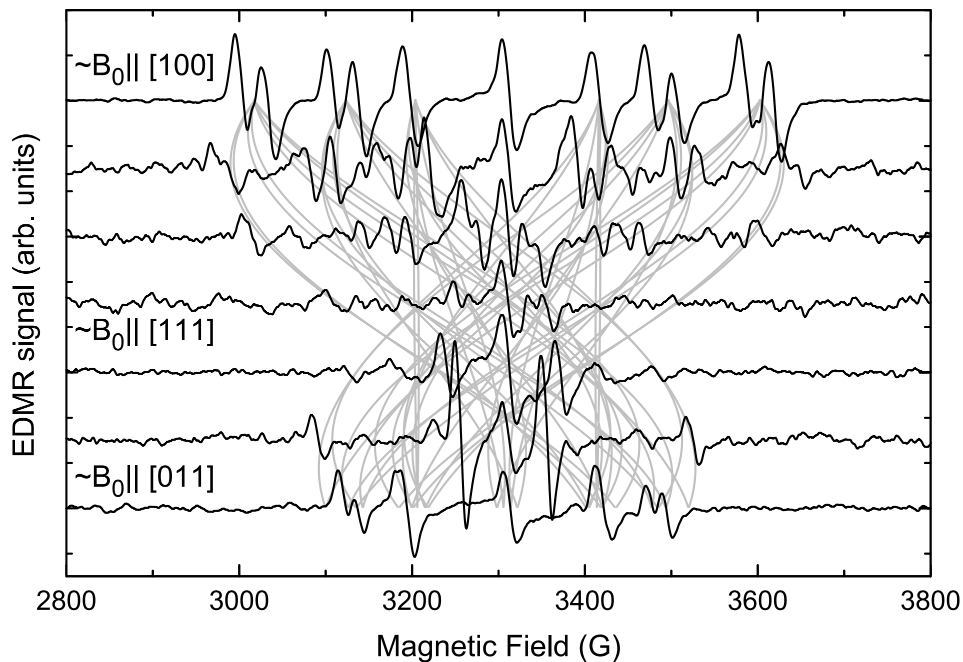

Figure 6.10: Anisotropy pattern of the EDMR signal measured under forward bias with a rotation axis tilted by about 5° from the [0$\bar{1}$1] axis. At the orientation closest to [100], the outer satellite groups split into pairs, which might indicate that the innermost satellites do not belong to the same defect as the outer two groups of satellites. No appropriate set of spin Hamiltonian parameters was found for such a scenario. Therefore, the grey lines again indicate the line positions calculated with the parameters of Eq. (6.9), neglecting the misalignment of the sample.

challenge of making n-type diamond films depends not only on the availability of suitable shallow donors in diamond, but also on the quality of the diamond film itself. As long as deep compensating defects can not be avoided, the characterization and application of n-type diamond films will remain problematic.

Chapter 7

The $Mn^{3+/2+}$ acceptor level in group III nitrides

As discussed in the previous chapters, hyperfine interactions of point defects are very useful in order to verify theoretical predictions for their electronic properties like thermal activation energies or optical absorption cross sections, which are based on calculations of the corresponding defect wave functions.[2, 117, 118] In contrast, the investigation of the acceptor level of Mn impurities in GaN discussed in this chapter is motivated by the shape of the electron spin wave function and the spin-spin interactions themselves. As discussed in Sec. 3.2, direct dipolar coupling between electronic spins of several defects is weak, e.g. of the order of $10\ \mathrm{G} \times g\mu_B \approx 10^{-3}\ \mathrm{K} \times k_B$ for spin concentrations around $10^{20}\ \mathrm{cm}^{-3}$. Stronger coupling is only possible if some spin density or induced spin polarization of one defect can also be found at the next impurity site, so that several spin states overlap. Strongly delocalized spin states have been observed e.g. in dilute magnetic semiconductors, which become ferromagnetic even at high temperatures. Various coupling mechanisms, such as spin-spin interactions mediated via band states, bound magnetic polarons, or virtual transitions to the valence band have been suggested to mediate the remarkably strong ferromagnetic interactions (see Sec. 7.5). However, the dominant mechanism is still under debate. From a fundamental point of view, a better understanding of the ferromagnetic coupling could be obtained from materials for which the coupling is particularly strong, and from a systematic variation of the essential properties of the spin wave functions in a series of similar materials.

Technologically, there is great interest in the optimization of the spin wave function properties to improve the stability of the magnetic interaction up to room temperature. Semiconductor materials showing ferromagnetism at high temperatures are one of the basic prerequisites for the realization of a new class of electronic devices, which utilize both the charge and spin degrees of freedom, and are therefore also called "spintronic" devices.[119, 120] Using spin injection into a non-magnetic light emitting diode, the generation of spin polarized currents has e.g. been demonstrated with the help of ferromagnetic

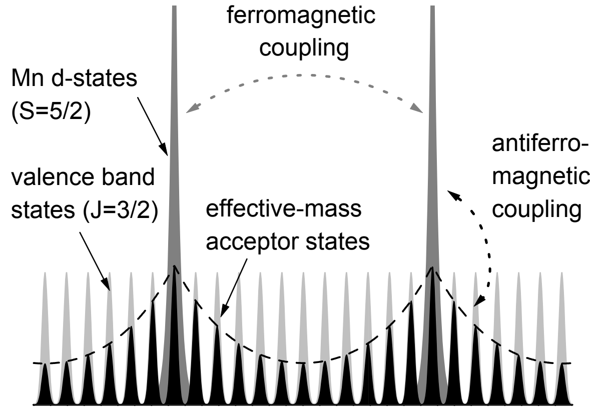

Figure 7.1: The neutral Mn acceptor state in GaAs is composed of an effective-mass acceptor state and of a core of highly localized $3d$ electrons. As shown by ESR in Ref. 134, the antiferromagnetically coupled neutral acceptor state with $j = S - J = 1$ is lowest in energy. Ferromagnetic interactions exist between the acceptor states of adjacent Mn sites in case of overlapping hole states.

$Ga_{1-x}Mn_xAs$ contacts at low temperatures.(121) Particularly high Curie temperatures T_c have recently been predicted for the diluted magnetic semiconductor (DMS) material GaN:Mn and other wide bandgap-semiconductors upon heavy Mn doping, if Mn doping could provide a sufficient number of localized spins as well as itinerant holes in the valence band.(122, 123) Due to the large potential of room-temperature ferromagnetic semiconductors in spintronic devices, this perspective has triggered significant research activities.(124, 125, 126, 127, 128, 129, 130, 131, 132, 133) Recently, ferromagnetism at high temperatures has indeed been reported in epitaxial GaN:Mn films,(125) but despite their high Mn concentration, these films still show n-type conductivity, which contradicts the assumption that Mn provides valence band holes similar to a shallow acceptor level in GaN. In contrast, it has been established previously that effective-mass acceptor states are formed by substitutional Mn_{Ga} in GaAs:Mn in such a way that bound holes do not recombine with the core electrons from the half-filled $3d$ shell. As shown in Fig. 7.1, the neutral Mn acceptor in GaAs instead consists of a core of highly localized $3d$ electrons *and* of an extended hole state with their respective magnetic moments coupled antiferromagnetically.(134) Long-range ferromagnetic coupling between the randomly distributed Mn spins is enabled via the large spatial extent of the effective-mass holes.

As in the case of GaAs,(134) electron spin resonance (ESR) experiments are essential to examine the microscopic nature of the Mn electronic states in wide band-gap semiconductors. The ESR results obtained on the Mn^{2+} spin states in GaN and AlN films in this work will be presented in Sec. 7.3, and discussed with respect to ESR studies reported previously for Mn^{2+} in nominally undoped GaN bulk crystals.(135, 136, 137) No indication for the ESR signal of neutral acceptors was observed in our films. This does not necessarily indicate a diamagnetic Mn^{3+} ground state. Most probably the crystal field splitting of the corresponding Kramers doublets could become broadened or shifted out of the energy range of an ESR spectrometer. Therefore, the Mn^{3+} ground state and excited states have been investigated by optical measurements at much larger energies. Optical studies of GaN:Mn reported previously,(128, 138) have also indicated a deep Mn-related

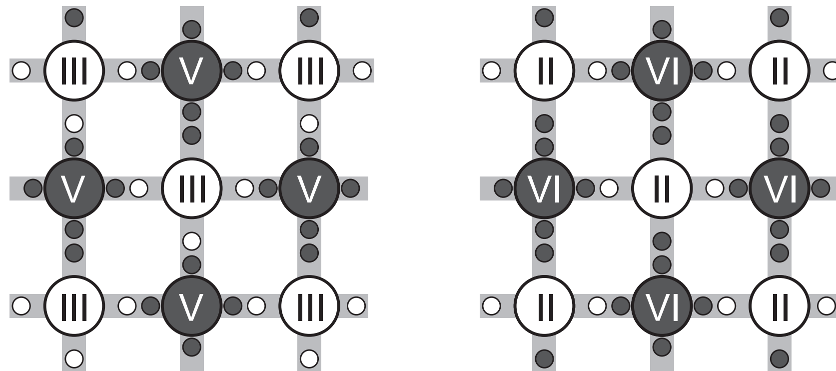

Figure 7.2: Schematic configuration of valence electrons in tetrahedrally coordinated III–V and II-VI semiconductor materials. In a covalent picture, the number of valence electrons contributed from each element to the bonds is given by its column in the periodic table. The bonds then become polarized because of the different electronegativity of the bonding partners. In the hypothetical case of complete ionization, this corresponds to threefold and twofold ionized cations, e.g. Ga^{3+} or Zn^{2+}.

level and identified it tentatively with Mn^{2+}. However, a reliable microscopic identification of the optically active Mn-related gap state is essential to understand whether the exchange mechanism given in Ref. 122, which is based on the coexistence of Mn^{2+} spins and extended holes, could take place in GaN:Mn.

After a brief introduction to the concepts and the nomenclature used in the literature for transition-metal states in semiconductors in Sec. 7.1, and a summary of the most important details of the growth of the GaN:Mn films investigated in Sec. 7.2, the information about the Mn^{2+} ground state in GaN and AlN obtained from ESR experiments will be discussed in detail in Sec. 7.3, and the information about the location of the $Mn^{3+/2+}$ acceptor level and an excited $(Mn^{3+})^*$ state obtained from optical measurements in Sec. 7.4. The consequences which can be drawn from these observations for the prospects of carrier-mediated ferromagnetism in GaN will then be outlined in Sec. 7.5.

7.1 Transition-metal states in semiconductors

For the description of transition-metal states in semiconductors, the physics of a continuum of electronic states must be combined with the physics of a many-electron system in a consistent way. The nomenclature for the resulting transition-metal states, and the typical problems arising from a simplified description of such different systems adopted for the experimentally observable parameters, will be introduced at a qualitative level in this section. More profound introductions into this field can be found in Refs. 15, 118, 139, 140, which are highly recommended for a more detailed discussion.

In III–V and II–VI semiconductors with zinkblende or wurtzite crystalline structures,

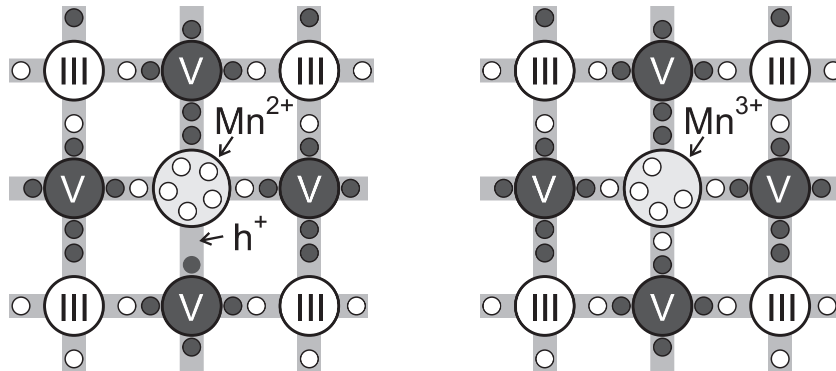

Figure 7.3: A Mn atom with five $3d$ electrons and two $4s$ valence electrons on a group III lattice site lacks one valence electron. This results in a hole, which is located either in the bonds, i.e. in the valence band (left side), or is transferred to the Mn $3d$ shell (right side). A combination of the properties of these two extremes is expected for realistic hole states.

the elements from one column of the periodic table, e.g. the group III cations, are tetrahedrally coordinated with elements from the other row of the periodic table, e.g. the group-V anions, as shown for the zinkblende structure in Fig. 3.1. As shown schematically in Fig. 7.2, three of four valence electrons per atom are contributed from the group III elements in III-V materials, and two from the group II elements in II-VI materials. Unlike in group-IV materials, where both bonding partners are equivalent, the electron clouds of the bonds are polarized, and shifted towards the group V or group VI anions because of their higher electronegativity. To preserve charge neutrality during substitution of the cations with transition-metal impurities, it is important to track the number of electrons contributed to the valence states from each element before substitution. This is most easily done in the ionic picture, using the (formal) oxidation states Ga^{3+} and N^{3-} of the bonding partners. In reality, the bonding partners are of course much less ionized than the anions and cations in salts like $Na^{+}Cl^{-}$.

The electronic configuration of neutral Mn atoms is $[Ar]3d^{5}4s^{2}$, where [Ar] denotes the electronic configuration of Ar, i.e. filled inner shells up to $3p^{6}$. Regarding only the two outer electrons as valences and the five $3d$ electrons as core states, Mn is therefore isoelectronic to the group II elements of Fig. 7.2 and can be substituted for other group II elements without any electronic change. In III–V semiconductors, however, Mn lacks one of the valence electrons, which was contributed from the group III cation before substitution. In the semiconductor language, this would be considered as a divalent acceptor impurity on a trivalent site, which introduces a hole in the valence band, as shown on the left hand side of Fig. 7.3. As the formal charge associated with the Mn^{2+} core is more negative by one electron compared to the formal charge of the group III cations, the valence band hole is not completely free to move through the crystal, but is weakly attracted to the Mn atom. However, its shape and extend is dominated by the

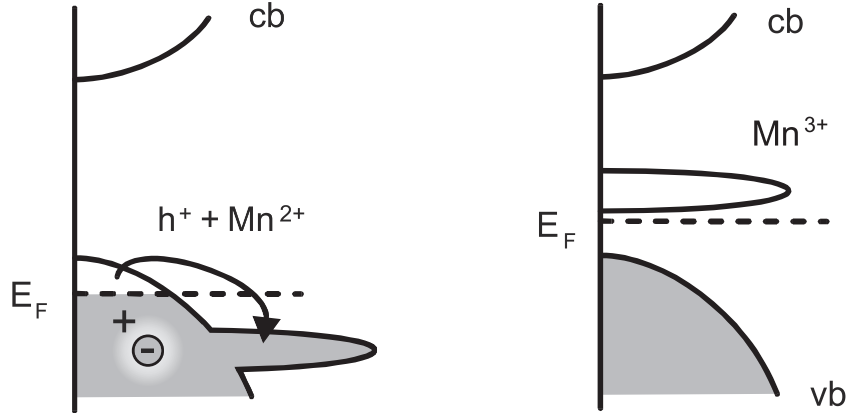

Figure 7.4: Energy diagrams for the two cases shown in Fig. 7.3. The d states of Mn are filled with electrons from the valence band only, if they are located below the valence band edge (left side). In a hole picture this charge transfer can be written formally as $\mathrm{Mn}^{3+}(d^4) \rightarrow \mathrm{Mn}^{2+}(d^5)+\ \mathrm{h}^+$. In GaAs, the thus created band-like holes are then weakly attracted by the local negative charge of the Mn^{2+} centers, so that a weakly coupled effective-mass like state is formed. As shown on the right, the reverse process $\mathrm{Mn}^{2+}(d^5)+\ \mathrm{h}^+ \rightarrow \mathrm{Mn}^{3+}(d^4)$ is expected to occur for transition-metal states located within the band gap. In this case, the Fermi level remains above the valence band edge, and the presence of Mn^{2+} is possible only with additional electrons from the conduction band, i.e., $\mathrm{Mn}^{3+}(d^4) + \mathrm{e}^- \rightarrow \mathrm{Mn}^{2+}(d^5)$. In such a system, the 3d states act as localized trap states for carriers in the bands.

sp^3-like valence band states, similar to the effective-mass states introduced in Sec. 2.1.1. It is itinerant, e.g. it occupies the valence band when ionized from the Mn^{2+} site, as shown in a schematic energy diagram in Fig. 7.4. This situation has been confirmed experimentally for Mn acceptors in GaAs:Mn.(134)

On the right hand side of Fig. 7.3, the hole in the valence band has been filled by one electron from the Mn 3d shell. This charge transfer of the hole from the valence band to the $\mathrm{Mn}^{2+}(d^5)$ core leads to a $\mathrm{Mn}^{3+}(d^4)$ core instead. It is energetically favorable, if the valence band states are at lower energy than the Mn 3d shell, as shown on the right hand side of Fig. 7.4. Compared to complete band structure calculations, the reduction of the Mn acceptor state to purely d-like core states and purely sp^3-like valence states appears somewhat artificial, as the true valence electron density is composed of all of these states. Realistic defect wave functions are therefore expected to combine the properties of the limiting cases shown in Figs. 7.3 and 7.4. However, very different ionization energies and ground state degeneracies are expected in the limiting cases, as in the Mn^{2+}+h^+ ground state, the Mn^{2+} core has a spin $S = 5/2$ and no angular momentum, and the valence band hole has the total angular momentum $J = 3/2$. The antiferromagnetically coupled ground state of Mn^{2+}+h^+ has a total angular momentum $j = S - J = 1$, as shown in Ref. 134. In contrast, the spin of Mn^{3+} is expected to have the spin $S = 2$ and the angular momentum $L = 2$. The latter is, however, quenched by the crystal field or the Jahn-Teller

III–V	$3d^3$	$3d^4$	$3d^5$	$3d^6$	II–VI
A^{--}			Cr^{1+}	Mn^{1+}	A^-
A^-		Cr^{2+}	Mn^{2+}	Fe^{2+}	A^0/D^0
A^0/D^0	Cr^{3+}	Mn^{3+}	Fe^{3+}		D^+
D^+	Mn^{4+}	Fe^{4+}			D^{++}
Spin	3/2	2	5/2	2	

Table 7.1: Nomenclature for transition-metal states according to the oxidation states of free Cr, Mn, and Fe ions, and the corresponding charge states of single and double donors and acceptors in semiconductors. The wave functions are labelled by their formal d-electron configuration, although the neighboring host atoms contribute significantly to the impurity ground state wave function. Similar as for the free ions, the high-spin ground states predicted by Hund's rule are observed for these transition-metal impurity states and included in the table.

effect in most cases, e.g. for GaAs:$Cr^{2+}(d^4)$.[15]

The negatively charged acceptor state Mn^{2+} will occur in both cases, if additional electrons are provided from the conduction band or from shallow donors:

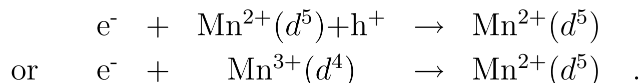

$$\begin{array}{lcccl} & e^- + & Mn^{2+}(d^5)+h^+ & \rightarrow & Mn^{2+}(d^5) \\ \text{or} & e^- + & Mn^{3+}(d^4) & \rightarrow & Mn^{2+}(d^5) \quad . \end{array}$$

Single and double donor levels $D^{0/+}$ and $D^{+/++}$, and single and double acceptor levels $A^{0/-}$ and $A^{-/--}$ are associated with the different oxidation states of Cr, Mn, and Fe transition-metal impurities in III-V and II-VI semiconductors, as compiled in Tab. 7.1. Therefore, the ionization processes of donors and acceptors can be observed as the charge-transfer processes

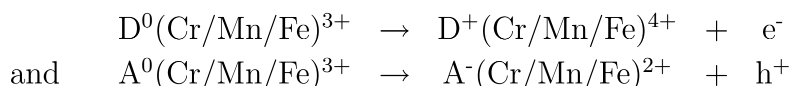

$$\begin{array}{lcccl} & D^0(Cr/Mn/Fe)^{3+} & \rightarrow & D^+(Cr/Mn/Fe)^{4+} & + \; e^- \\ \text{and} & A^0(Cr/Mn/Fe)^{3+} & \rightarrow & A^-(Cr/Mn/Fe)^{2+} & + \; h^+ \end{array}$$

in III–V materials, and as

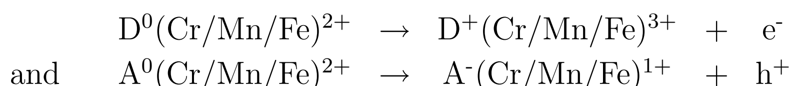

$$\begin{array}{lcccl} & D^0(Cr/Mn/Fe)^{2+} & \rightarrow & D^+(Cr/Mn/Fe)^{3+} & + \; e^- \\ \text{and} & A^0(Cr/Mn/Fe)^{2+} & \rightarrow & A^-(Cr/Mn/Fe)^{1+} & + \; h^+ \end{array}$$

in II–VI materials. Since most spectroscopic properties of the impurity states resemble those of the free ions, screened by the host material, similar properties can be expected for the neutral Mn^{2+} state in II–VI materials, and the negatively charged Mn^{2+}-acceptor in III–V materials.[118, 140, 141, 142] Consequently, the wave functions are labelled according to their formal d-electron configuration, even if the neighboring host atoms contribute significantly to the impurity ground state wave function. Similar to the free ions, the high-spin ground states predicted by Hund's rule are observed for these transition-metal impurity states and included in the Tab. 7.1.

T_d	$\{E\}$	$\{3C_2\}$	$\{6\sigma\}$	$\{6S_4\}$	$\{8C_3\}$	Basis functions
A_1	1	1	1	1	1	xyz
A_2	1	1	−1	−1	1	$x^4(y^2 - z^2) + y^4(z^2 - x^2) + z^4(x^2 - y^4)$
E	2	2	0	0	−1	$\{(x^2 - y^2), z^2 - \frac{1}{2}(x^2 + y^2)\}$
T_1	3	−1	−1	1	0	$\{x(y^2 - z^2), y(z^2 - x^2), z(x^2 - y^2)\}$
T_2	3	−1	1	−1	0	$\{x, y, z\}$

Table 7.2: Character table of the tetrahedral point group T_d with the basis functions of the irreducible representations A_1, A_2, E, T_1, and T_2 (from Ref. 1). The 24 symmetry operations of T_d are divided into five classes containing the identity operation $\{E\}$, the two-fold rotations $\{3C_2\}$ and the four-fold improper rotations $\{6S_4\}$ about the [100] axes, the reflections $\{6\sigma\}$ on the (110) planes, and the three-fold rotations $\{8C_3\}$ about the [111] axes. Note, that the Koster notation Γ_1, Γ_2, Γ_3, Γ_4, and Γ_5 is often preferred to the molecular notation A_1, A_2, E, T_1, and T_2 for band structure calculations. The character tables of the double group required to include spin-orbit interactions are also given in Ref. 1.

C_{3v}	$\{E\}$	$\{3m\}$	$\{2C_3\}$	Basis functions
Λ_1	1	1	1	$x + y + z$
Λ_2	1	−1	1	$xy(x - y) + yz(y - z) + zx(z - x)$
Λ_3	2	0	−1	$\{(x - y), \sqrt{\frac{2}{3}}[z - \frac{1}{2}(x + y)]\}$

Table 7.3: Character table of the point group C_{3v}, which has a lower symmetry and less irreducible representations than T_d (from Ref. 1). In particular, the symmetry classes $\{3C_2\}$ and $\{6S_4\}$ are missing here. Besides this, the irreducible representations Λ_1, Λ_2, Λ_3 correspond to A_1, A_2, and E of the T_d point group. Using the orthogonality betweens the rows of Tab. 7.2, one finds that under trigonal distortion the representations T_1 and T_2 of T_d split into $\Lambda_2 + \Lambda_3$ and $\Lambda_1 + \Lambda_3$, respectively.

Up to now, the Mn d-states were treated to be located at a single energy level above or below the valence band edge, neglecting electron-electron interactions completely. However, the interactions between the d electrons of free transition-metal ions are known to be of the order of tens of eV. According to Hund's rules, the high-spin states of Tab. 7.1 are expected as ground states of the complex many-electron transition-metal systems. In the absence of crystal fields, the total orbital degeneracy and the angular momentum of these states is labelled by the spectroscopic notation with capital letters S, P, D, F, G, ... for the total angular momentum $L = 0, 1, 2, 3, 4, \ldots$, respectively, according to the L-S or Russell-Saunders coupling scheme. As the effect of spin-orbit coupling is small compared to the energy differences between orbitals with different values of L, this additional interaction is usually treated by perturbation theory for ions of the transition-metal series.

The arrangement of the nearest cations in III–V or II-VI semiconductors is approxi-

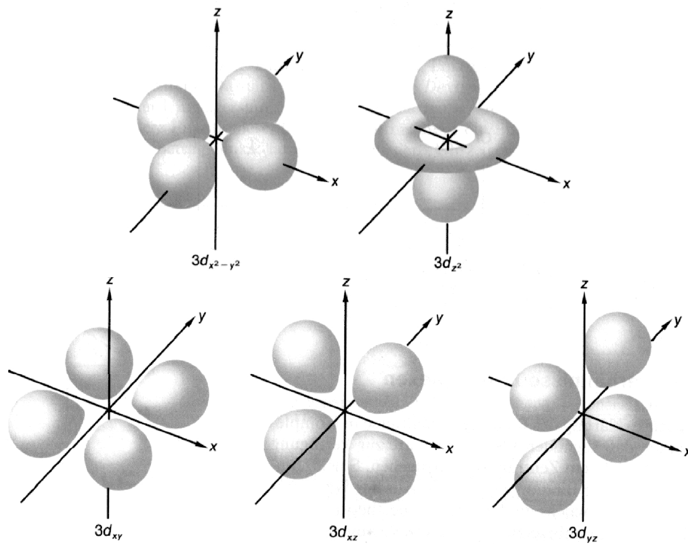

Figure 7.5: In a tetrahedral environment the orbitals of a single d-electron are split into the e-orbitals $d_{x^2-y^2}$ and d_{z^2}, and the t_2 orbitals d_{xy}, d_{xz}, and d_{yz} known from textbooks on quantum mechanics. As the t_2-orbitals would be closer to four anions in a tetrahedral configuration, their energy is higher for electrons on substitutional cation sites in tetrahedrally coordinated semiconductors (from Refs. 143, 144).

term $(2L+1)$	S (1)	P (3)	D (5)	F (7)	G (9)	... ...
T_d	A_1	T_2	$E + T_2$	$A_2 + T_1 + T_2$	$A_1 + E + T_1 + T_2$	...
C_{3v}	Λ_1	$\Lambda_1 + \Lambda_3$	$\Lambda_1 + 2\Lambda_3$	$\Lambda_1 + 2\ \Lambda_2 + 2\ \Lambda_3$	$2\ \Lambda_1 + \Lambda_2 + 3\ \Lambda_3$	...

Table 7.4: Irreducible representations spanned by the tetrahedral point group T_d and the C_{3v} point group of the wurtzite lattice. As introduced in Tabs. 7.2 and 7.3, the one-dimensional representations are designated by $A_{1,2}$, and $\Lambda_{1,2}$, the two-dimensional representations by E and Λ_3, and the three-dimensional representations by T_1 and T_2.

mately tetrahedral, i.e. the environment and orbital eigen-states belong to the T_d symmetry group with only small corrections of lower symmetry. Therefore, the multiplicities and symmetries of the $2L + 1$-fold degenerate many-electron states can be summarized in Tab. 7.4 according to the irreducible representations defined by the character table (Tab. 7.2) of T_d.[1, 145] For a system with only one d electron like $Mn^{6+}(d^1)$ or $Ti^{3+}(d^1)$, there are two e orbitals $d_{x^2-y^2}$, and d_{z^2}, which belong to the two-dimensional irreducible representation E of the five-dimensional rotation group, and three t_2 orbitals d_{xy}, d_{xz}, and d_{yz}, which belong to the three-dimensional irreducible representation T_2. These well-known atomic one-electron d-orbitals are shown in Fig. 7.5. For an octahedral configuration of negative point charges on the coordinate axes, the energy of the e orbitals with their charge density concentrated mainly on the coordinate axes will be increased more than the energy of the t_2 orbitals, whose charge density is mainly concentrated between the axes. In the opposite way, a cubic or tetrahedral arrangement of point charges between the coordinate axes is expected to make the e orbitals energetically favorable with respect to the t_2 orbitals. Both arrangements are closely related, considering that additional positive point charges can be introduced in between the negative point charges

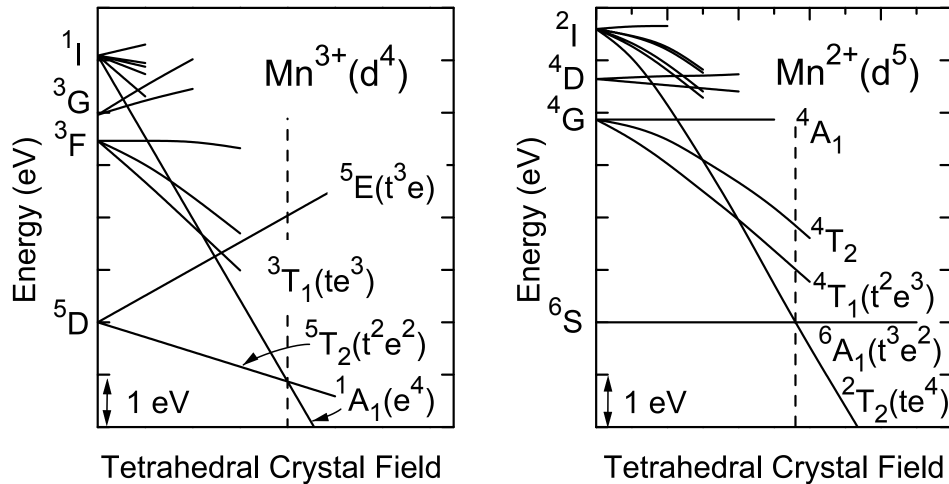

Figure 7.6: The degeneracies of transition-metal states in a crystal field of tetrahedral symmetry are depicted in "Tanabe-Sugano" diagrams[(146)] and labelled according to the irreducible representations of Tab. 7.4, which is a somewhat different nomenclature than the original one of Ref. 146. The free ion states are labelled S, P, D, ... according to their total angular momentum, and are indexed by their spin degeneracies $2S + 1$. According to Hund's rules, the free ion state with highest spin and lowest angular momentum is at the lowest energy. In the presence of a tetrahedral crystal field, these orbital degeneracies are lifted, and the states must be classified by the irreducible representations $A_{1,2}$, E, and $T_{1,2}$ of the T_d symmetry group. The symmetry considerations apply even in a semiconductor environment, although the point-charge approximation of crystal field theory breaks down there.

to preserve charge neutrality. These are naturally arranged on the corners of a cube for an octahedral arrangement of negative point charges on the face centers of the cube, and vice versa. The main difference between tetrahedral and octahedral crystal fields besides this opposite sign is, that for point charges at the same distance the tetrahedral crystal field is only 4/9 as large as the octahedral crystal field. The energy considerations for the single-electron orbitals also apply for many-electron systems, if the effects of the crystal field is much stronger than electron-electron interactions responsible for the level splitting of the free ion. In this high-field limit, the energy of an electronic configuration is dominated by the number of electrons occupying t_2 and e orbitals respectively. For large tetrahedral crystal fields, the lowest energy is therefore expected for the highest number of electrons in e orbitals. This configuration does not necessarily correspond to a high-spin ground state according to Hund's rules.

The energy levels at intermediate crystal fields are summarized in the so-called "Tanabe-Sugano" diagrams calculated first in Ref. 146, and shown schematically for Mn^{3+} and Mn^{2+} in Fig. 7.6. The states are labelled according to their spin degeneracy with the upper left index, and with capital letters for the $A_{1,2}$, E, and $T_{1,2}$ representations according to their orbital degeneracy (see Tab. 7.4). The energy splitting of the free ion terms,

can be adjusted via the so-called Racah-parameters. For other than the trivial cases of an empty or completely filled d shell, the diagrams must be calculated by matrix diagonalization for each particular number n of d-electrons separately. The configurations $d^n(t^x e^{n-x})$ with $n = 1 \ldots 9$ electrons in tetrahedral crystal fields are characterized by the number of electrons in t-orbitals $x = 0 \ldots 6$, and the number of electrons in e-orbitals $n - x = 0 \ldots 4$, which dominate the energies in the limit of high crystal fields. The Tanabe-Sugano diagrams for the configurations $d^n(t^x e^{n-x})$ in tetrahedral fields, as shown in Fig. 7.6, are qualitatively the same as the corresponding diagrams for n holes, i.e. $10 - n$ electrons, in an octahedral crystal field, which are more commonly found in the literature,[9, 13, 145] as far as spin-orbit interactions are neglected. The $(t^x e^{n-x})$ many-electron terms then correspond to the $(t^{6-x} e^{4-(n-x)})$ terms in the hole picture. Similarly, the lowest T_2 and E terms with four of the five spin-up orbitals occupied have the same degeneracy as one single electron occupying a t_2 or e orbital, however, the energy difference between the two levels is reversed, as the remaining spin-up level remains unoccupied, i.e. occupied by a single t_2 or e-like hole, for which the electrostatic repulsion discussed before for a single electron turns into electrostatic attraction. This explains the similarities of the $d^1(e^1)$ ground state orbital with the $d^6(^5E, t^3e^3)$ ground state and the $d^4(^5E, t^3e^1)$ excited state, and of the $d^1(t^1)$ excited state orbital with the $d^6(^5E, t^4e^2)$ excited state and the $d^4(^5E, t^2e^2)$ ground state.

For clarity, all energies are shown in Fig. 7.6 without subtraction of the respective ground state energy. In the more usual diagrams, the slopes of all lines change at the dashed line, where one of the low-spin states reaches a lower energy than the high-spin ground state at lower fields. Typically, the crystal fields present in semiconductors are too weak to reach this limit, although they are often predicted erroneously from LSDA calculations.[2, 118] However, this limit is often reached in molecules. The energy axes have been scaled with the electron repulsion Racah parameters $B_{\mathrm{Mn}^{2+}} = 960\ \mathrm{cm}^{-1}$ and $B_{\mathrm{Mn}^{3+}} = 1140\ \mathrm{cm}^{-1}$ of the free Mn ions. For GaN:Mn^{2+}, a reduction down to $B_{\mathrm{GaN:Mn}^{2+}} = 726\ \mathrm{cm}^{-1}$ has been estimated in Ref. 22. For comparison with other transition-metal ions, it is interesting to note that $B_{\mathrm{Cr}^{2+}(d^4)}$ is typically about 20% smaller than $B_{\mathrm{Mn}^{3+}(d^4)}$, and $B_{\mathrm{Fe}^{3+}(d^5)}$ about 10% larger than $B_{\mathrm{Mn}^{2+}(d^5)}$. There is some confusion in the literature[9] concerning the low-spin ground state of $Mn^{3+}(d^4)$ at high tetrahedral crystal fields. According to Ref. 147, not the $^3\mathrm{T}_1(te^3)$, but the $^1\mathrm{A}_1(e^4)$ level crosses the $^5\mathrm{T}_2(t^2e^2)$ level first, so that the ground state has either the spin degeneracy $S = 2$ or $S = 0$. The $T_{1,2}$ levels in tetrahedral symmetry split even further in crystal fields of lower symmetry like the C_{3v} configuration of the wurtzite lattice of GaN (see Tab. 7.4).

In Sec. 7.3, we will show that the ground state of Mn^{2+} has spin $S = 5/2$ and no orbital degeneracy in group III nitrides, i.e. its electronic configuration is $^6\mathrm{A}_1(t^3e^2)$ without the influence of spin-orbit interaction and of axial crystal fields. These perturbations result in the admixture of excited states to the spherically symmetric $^6\mathrm{A}_1$ ground state, which

enter the spin Hamiltonian parameters, and can be understood quantitatively by the superposition model of crystal fields.[148] The $^6A_1 \leftrightarrow {}^4T_1$ transition to the first excited state $^4T_1(t^2e^3)$ is spin-forbidden, but it has been observed for Mn^{2+} in other materials. In GaN, this state is probably located within the conduction band. As discussed in Sec. 7.4, an excited state of Mn^{3+} is observed for GaN:Mn and AlN:Mn, which is most probably the $^5E(t^3e)$ state of Fig. 7.6. This observation strongly supports the assignment of Mn in group III nitrides to a deep trap state, which makes the achievement of carrier-mediated ferromagnetism improbable for GaN:Mn, as discussed in Sec. 7.5.

7.2 Growth of GaN:Mn films

The samples under investigation were grown by plasma-induced molecular beam epitaxy (PIMBE) on 2 inch c-plane oriented sapphire, as described in detail in Ref. 149. The substrates were metallized on the backside by Ti/Pt (800 nm/ 80 nm) to ensure a homogeneous temperature profile over the whole wafer.[150] After growth of a 10 nm thick AlN nucleation layer, Mn-doped GaN films with Ga-face polarity and a thickness of about 1.2 μm were deposited at a growth rate of 1.5 Å/s. In order to vary the Mn concentration of different GaN samples without changing the growth rate, the substrate temperature was lowered from 820 to 690°C, and the beam equivalent pressure (BEP) of the Ga-flux from 1.3×10^{-5} to 4×10^{-6} mbar, respectively in a series of eight samples. A series of AlN:Mn samples was grown at a substrate temperature of 850°C and varying the Mn flux only. For all GaN:Mn samples discussed here, the Mn-flux was kept constant at about 2.0×10^{-7} mbar BEP. Nitrogen radicals were provided by an Oxford plasma source operated at an input power of 425 W and a nitrogen flux of 2 sccm, which resulted in process pressure of 3×10^{-5} mbar inside the MBE chamber. All samples were grown under metal rich conditions, which caused the formation of metallic Ga, Mn, or GaMn droplets at low substrate temperatures. The droplets were removed from the GaN:Mn epilayer surface by HCl etching at 50°C. To investigate the effect of additional codoping with shallow donors, some samples were grown at the conditions mentioned above with simultaneous incorporation of Mn and Si at a substrate temperature of 820°C.

The crystalline quality of all films was investigated by x-ray diffraction (XRD) with the results shown in Fig. 7.7. Typically, the full width at half maximum of the (00.2) reflex for GaN:Mn layers was about 500 arcsec for rocking curves (Ω scans) and 50 arcsec for 2Θ-Ω scans. Only at the lowest growth temperature (690°C), metal clusters were observed in the GaN film with an optical microscope, and the presence of a second phase, possibly Mn_3N_2, became visible in the x-ray diffraction pattern (upper trace in Fig. 7.7). The widths of the (00.2) x-ray diffraction peaks confirm the structural quality of the GaN and AlN films. They would correspond to variations of the out-of plane lattice constant c of about 0.04%, if they were caused by a spread of c only.

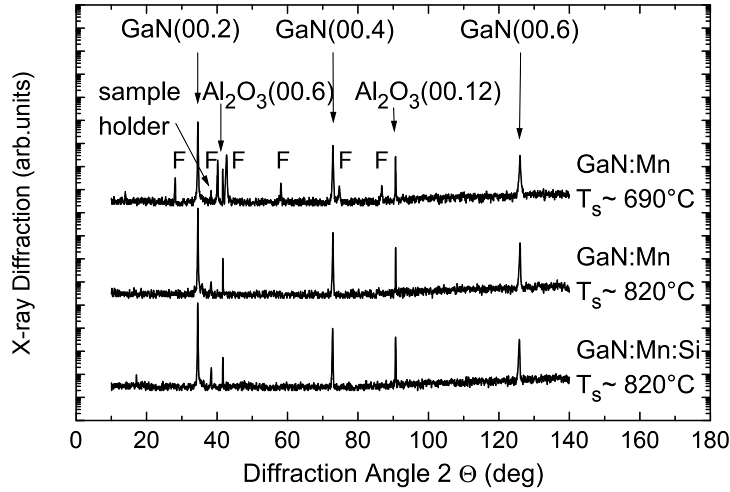

Figure 7.7: XRD patterns of a GaN:Mn film grown at a substrate temperature of 690°C, and of GaN:Mn and GaMn:Si films grown around 820°C. Typically, the full width at half maximum of the (00.2) reflex for GaN:Mn layers is about 500 arcsec for rocking curves (Ω scans) and 50 arcsec for 2Θ-Ω scans. Only at the lowest growth temperature (690°C) a second phase (indicated by F) is visible in XRD.

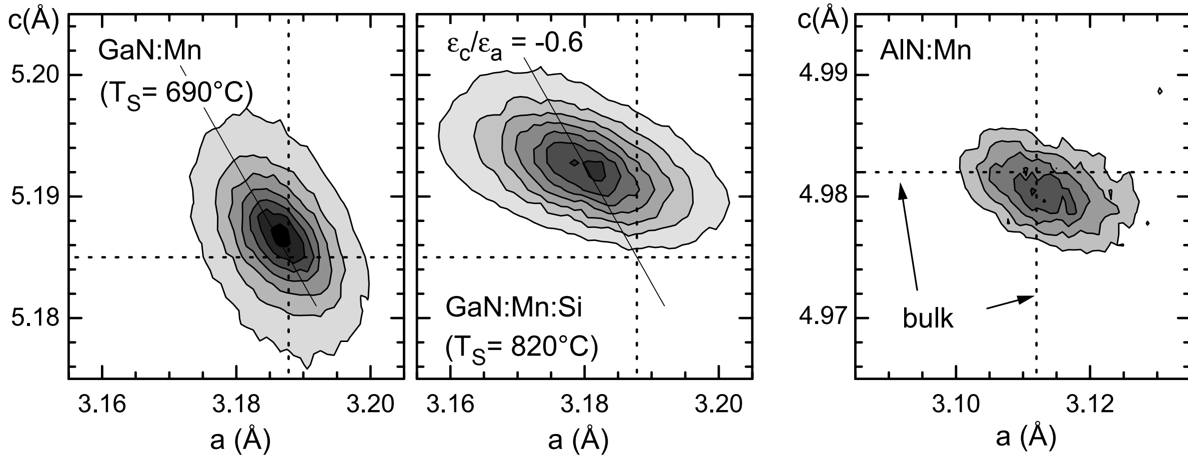

Figure 7.8: Reciprocal space maps of the asymmetric (20.5) reflex of GaN:Mn grown at $T_s = 690°C$, of GaN:Mn:Si grown at $T_s = 820°C$, and of AlN:Mn. The bulk lattice constants are indicated by dotted lines. Because of the lattice mismatch to the sapphire substrate and the mismatch of the respective thermal expansion coefficients, the a lattice constant of the GaN films is reduced and the c lattice constant increased compared to the bulk values.

As reported for example in Ref. 151, the lattice mismatch to the sapphire substrate and the mismatch of the respective thermal expansion coefficients causes biaxial strain in GaN and AlN thin films. In addition, hydrostatic strain is expected at high doping concentrations. Therefore, the in-plane lattice constant a of expitaxial GaN films on sapphire is typically compressed with respect to the bulk value $a_0 = 3.1878$ Å, and c is expanded with respect to $c_0 = 5.1850$ Å.[151] These changes were monitored in reciprocal space maps of the asymmetric (20.5) reflex for all samples investigated here. The relative deviations of the in-plane lattice constant $\varepsilon_a = (a - a_0)/a_0$ varied from -0.04% to -0.25%, and the deviations in growth direction $\varepsilon_c = (c - c_0)/c_0$ from 0.03%

to 0.15%, with the codoped GaN:Mn:Si samples grown at 820°C showing the largest strain. A linear dependence between both relative changes with $\varepsilon_c/\varepsilon_a = -0.6 \pm 0.02$ is observed for the investigated films, which corresponds to the effective Poisson ratio $\nu = -(\varepsilon_c/\varepsilon_a)/[(\varepsilon_c/\varepsilon_a) - 2] = 0.23$ reported earlier in Ref. 151

Electrical measurements on the uncompensated GaN:Mn layers were performed with interdigitated Ti/Al contacts with a spacing of 50 μm. Their high resistivity prohibits unambiguous Hall measurements on this type of samples. Even at Mn concentrations around 10^{20} cm^{-3}, their resistivity is so high that the formation of an impurity band and a metal-insulator transition can be excluded. This allows estimation of an upper limit of the localization radius of the acceptor states to less than 1 nm. The dark conductivity is thermally activated with about 370 meV, with absolute conductivities ranging from $\sigma(T = 170\text{ K}) \approx 3 \times 10^{-14}$ $(\Omega\text{cm})^{-1}$ to $\sigma(T = 500\text{ K}) \approx 10^{-6}$ $(\Omega\text{cm})^{-1}$. Possibly this activation energy is determined by hopping conductivity through other defect levels rather than the Mn impurities under investigation. The low dark conductivity enables a dynamic range of many orders of magnitude for the photoconductivity measurements discussed in Sec. 7.4.1.

7.2.1 Elastic recoil detection

The total amount of Mn incorporated into the samples was determined by elastic recoil detection (ERD)[(152)] and is shown by closed symbols in Fig. 7.9. Because of the high ion energies of 100-250 MeV used here, ERD is insensitive to the Mn position, either in the GaN lattice, in micropipes, or small metallic clusters. Note that ERD does not require a calibration standard like secondary ion mass spectroscopy (SIMS), and is sensitive to Mn concentrations of about 10^{17} cm^{-3}. Within the depth resolution of 30 nm of ERD, the samples were found to be homogeneously doped with Mn. The concentration of other unintentionally introduced impurities was 10^{18} cm^{-3} for O and 10^{17} cm^{-3} for Si at maximum. In the non-codoped GaN:Mn samples, the Mn concentrations observed were between 5×10^{19} and 6×10^{20} cm^{-3}, and decreased slightly with an increase in growth temperature. Possibly a small contribution by other phases like Mn_4N, Mn_2N, MnN, MnO, and Mn_3N_2 is included in this total Mn concentration at low growth temperatures besides substitutional Mn on Ga lattice sites.[(153)] Therefore, the ERD results provide an upper limit for the real substitutional Mn concentration. In samples codoped with Mn and Si, concentrations of 3×10^{19} cm^{-3} were determined by ERD for both dopants.

The concentration of Mn atoms per cm^3 is often quoted in the literature as a fraction of the number of Ga sites in GaN. There are two Ga sites in the unit cell of GaN with a volume

$$c \times a \times \tfrac{a}{2}\sqrt{3} = 5.185\text{ Å} \times (3.1878\text{ Å})^2 \times 0.8660 = 45.63\text{ Å}^3 \quad . \tag{7.1}$$

Therefore, the concentration of Ga sites in GaN is 4.38×10^{22} cm^{-3}, and a concentration

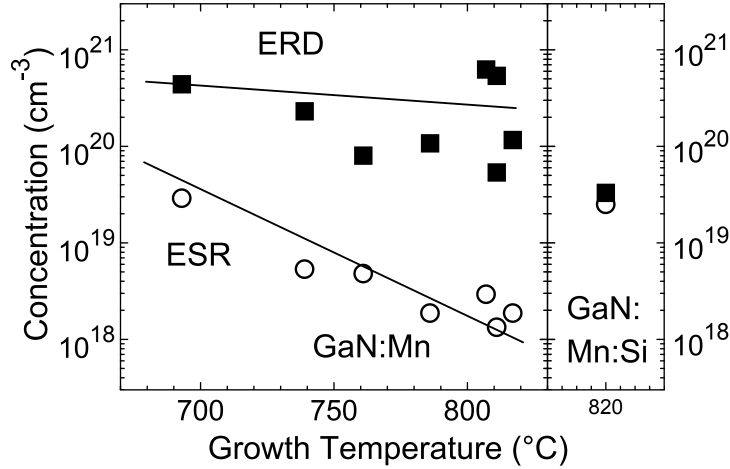

Figure 7.9: Total Mn concentration determined by ERD in comparison with spin densities measured by ESR. The large difference observed for GaN:Mn at high growth temperatures is attributed to the dominance of the Mn^{3+} charge state. Codoping with Si donors removes this difference in concentration because Mn^{3+} is converted to Mn^{2+} by compensation.

of Mn atoms of 10^{20} cm^{-3} corresponds to an occupation of 0.23% of the Ga sites with Mn atoms.

It still is unclear at this point whether these Mn atoms indeed occupy substitutional Ga sites of the GaN crystal structure, or perhaps aggregate in microscopic Mn-containing clusters embedded in the GaN matrix. The defect wave function and the magnetic and optical properties of substitutional Mn atoms will furthermore depend strongly on the oxidation state, which cannot be determined from ERD. Experiments concerning the structural environment, spin states, and the electronic structure of Mn ions in group III nitrides will be discussed in detail in the following sections. Before going into detail, we will first give a brief outline of the conclusions which can be drawn from the various experimental observations:

SQUID measurements (see Sec. 7.2.2) of the magnetic properties of our GaN:Mn thin films are challenging because of the small sample volumes around 5×10^{-3} cm^{-3}. Additionally, the paramagnetic and diamagnetic contributions from the sapphire substrate, and possible ferromagnetic inclusions make it difficult to interpret the mostly paramagnetic magnetization curves. The SQUID results are, however, consistent with the Mn concentrations observed in ERD, if one assumes that Mn is present as Mn^{2+} or Mn^{3+} in our films.

ESR experiments (see Sec. 7.3) provide direct microscopic information about the $S = 5/2$ high spin state of paramagnetic Mn^{2+} impurities in GaN, which substitute for Ga with a slightly distorted tetrahedral symmetry. ESR experiments on strained films confirm that the observed axial distortion is caused by a displacement of the Mn^{2+} ions of about 8.5 pm from the substitutional Ga sites.

The Mn^{2+} concentrations evaluated from the observed ESR intensities in Sec. 7.3.5 are included in Fig. 7.9. For the pure GaN:Mn samples, these concentrations are far below the total Mn concentrations determined by ERD. For the Si-codoped samples,

however, the Mn^{2+} concentrations determined via ESR agree well with the total Mn concentrations from ERD. This confirms that not the negatively charged acceptor state $Mn^{2+}(A^-)$, but the neutral acceptor state $Mn^{3+}(A^0)$, or a $Mn^{2+}+h^+(A^0)$ complex (see Fig. 7.3) are present in the pure GaN:Mn samples. Unfortunately, A^0 seems to be invisible in X-band ESR.

Optical absorption measurements (see Sec. 7.4) of the pure GaN:Mn samples with $[Mn]_{ERD} \approx 10^{20}$ cm^{-3}, but with $[Mn^{2+}]_{ESR} \approx 2 \times 10^{18}$ cm^{-3} show two characteristic absorption bands at 1.5 eV and 1.8 eV. Based on photoconductivity measurements, the two transitions are assigned to a $^5T_2 \rightarrow {}^5E$ internal excitation of Mn^{3+}, and to the charge-transfer process $Mn^{3+} + h\nu \rightarrow Mn^{2+}+h^+$, respectively. According to this assignment, the $Mn^{3+/2+}$ acceptor level is located at 1.8 eV above the valence band edge of GaN, which can be understood qualitatively from the concepts established previously for other transition-metal impurities in semiconductors. Based on these concepts, the prospects for carrier-mediated ferromagnetism will be discussed in Sec. 7.5 in view of the qualitative difference between the very deep $Mn^{3+/2+}$ acceptor level in GaN:Mn compared to GaAs:Mn, where Mn is known to form effective-mass like acceptor states.

7.2.2 SQUID measurements

As is usual in studies of diluted magnetic semiconductors,(124, 125, 138) the magnetization of the samples was investigated by superconducting quantum interference device (SQUID) measurements at temperatures down to $T = 2$ K and at magnetic fields up to 7 T. The temperature dependence of the magnetization of two GaN:Mn samples grown at $T_s = 820°$C and $T_s = 740°$C is shown in Figs. 7.10 and 7.11. For the samples grown at high temperatures, it can be well described by the Brillouin function

$$M(T,B) = Ng\mu_B \left[(S+\tfrac{1}{2}) \coth \frac{g\mu_B B(S+\frac{1}{2})}{k_B T} - \tfrac{1}{2} \coth \frac{g\mu_B B}{2k_B T} \right] \tag{7.2}$$

for the equilibrium magnetization of an ensemble of paramagnetic states. This magnetization follows Curie's law at high temperatures and saturates at low temperatures and large magnetic fields

$$M(T,B) \approx \begin{cases} Ng\mu_B S & \text{at } g\mu_B B \gg k_B T \\ N\dfrac{g^2\mu_B^2 B}{k_B T} S(S+1) & \text{at } g\mu_B B \ll k_B T \end{cases} . \tag{7.3}$$

For $g \approx 2$, the critical temperature per applied field is about $g\mu_B/k_B \approx 1.3$ K/T, which makes it possible to estimate the spin density N from the saturation magnetization at $T = 2$ K and $B = 7$ T.

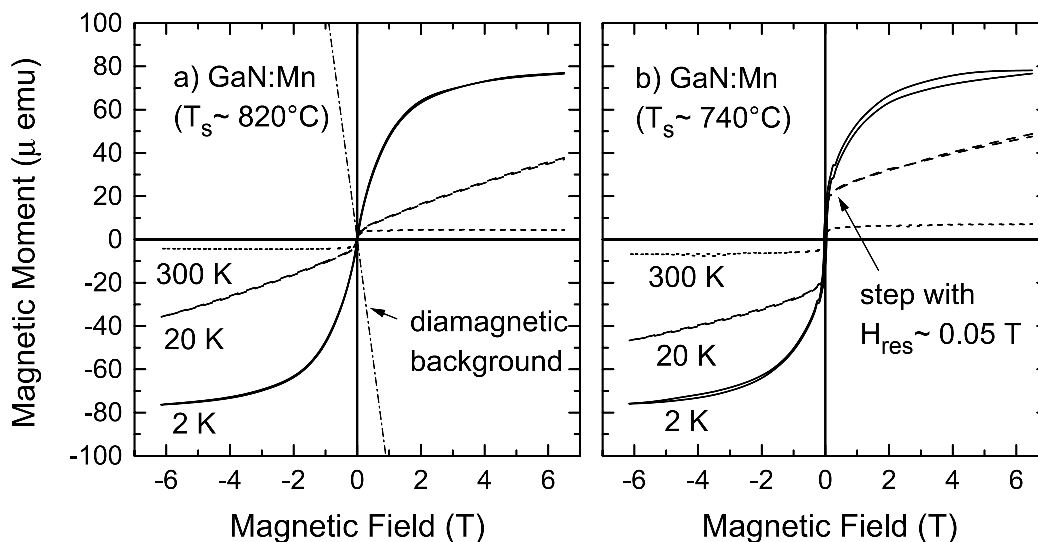

Figure 7.10: Magnetic moments detected by SQUID measurements at T = 2 K, T = 20 K, and T = 300 K of GaN:Mn samples grown at T_s = 820°C and T_s = 740°C. The large diamagnetic background from the sapphire substrate has been subtracted from all curves. The jump at zero magnetic field in all curves is most probably caused by trapped flux quanta in the superconducting magnet that show up as magnetization after a linear background subtraction. A close-up of the region around zero magnetic field is shown in Fig. 7.11.

The results for GaN:Mn at the two extreme growth temperatures T_s = 690°C and 820°C, for GaN:Mn:Si and for an undoped GaN reference sample are shown in Fig. 7.12. As in Figs. 7.10 and 7.11, the linear diamagnetic background due to the sapphire substrate was subtracted from all curves. From the Brillouin shape of the magnetization curves, it is clear that all samples investigated here are mostly paramagnetic. However, a small step-like contribution to the magnetization curve is observed up to room temperature for the GaN:Mn sample grown at T_s = 690°C. We attribute this to a ferromagnetic Mn_xN_y minority phase similar to the phases reported for microcrystalline GaN samples before etching in aqua regia.[124, 153] A paramagnetic contribution is also observed in the magnetization curve of the undoped GaN sample. This contribution is related to transition-metal impurities in the sapphire substrate, which are also clearly visible in ESR, and which are not eliminated by linear background correction of the diamagnetic contribution of the substrate. Despite the low concentration of these impurities, their contribution to the total magnetization cannot be neglected, because the thickness of the substrate is much larger than that of the GaN film. However, to enable a better comparison between the signals from the GaN:Mn samples and the background contribution from the substrate, the reference data have also been divided by the volume of the GaN film rather than by that of the substrate. Taking into account this background contribution and assuming a high-spin

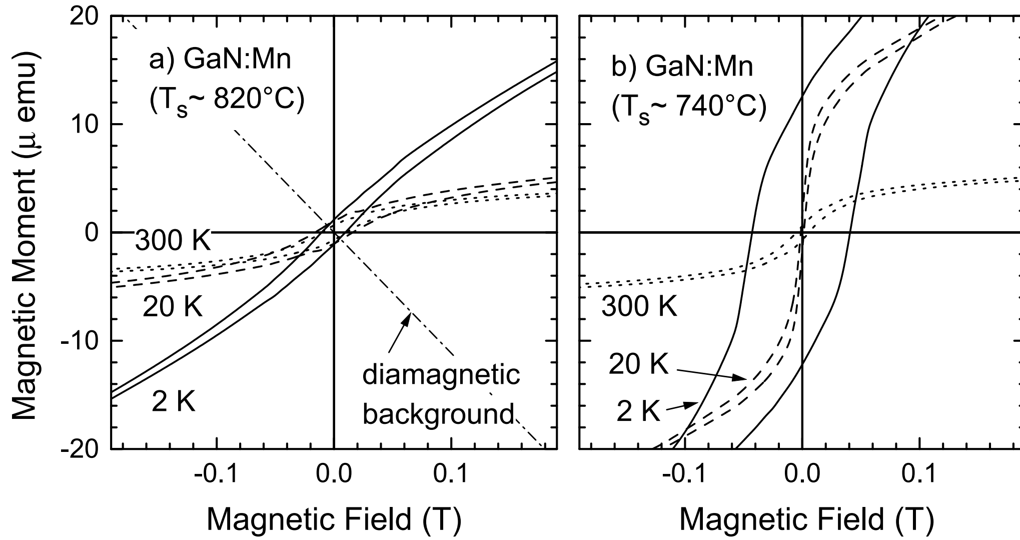

Figure 7.11: The magnified curves of Fig. 7.10 show more clearly the jump at zero magnetic field and the hysteresis below $T = 20$ K of the sample grown at $T_s = 740°$C. As discussed in detail in Ref. 154, part of this magnetic moment is observed to decay slowly on a timescale of hours at $T = 2$ K, and therefore indicates a spin-glass state of GaN:Mn.

configuration of the Mn ions with $S = 2 - 2.5$ and $g \approx 2$ for both Mn^{2+} or Mn^{3+} centers, we find good agreement between the total Mn concentrations $[\mathrm{Mn}] = M_{\mathrm{sat}}/(g\mu_B S)$ with the Bohr magneton $\mu_B = 9.3 \times 10^{-21}$ emu, determined from the saturation magnetization M_{sat} indicated on the right axis of Fig. 7.12, and the total Mn concentrations determined by ERD. As is obvious from the temperature-dependent SQUID measurements shown in Fig. 7.10, about 20-30% of the Mn atoms are incorporated into ferromagnetic minority phases also in the GaN:Mn sample grown at $T_s = 740°$C. In contrast, nearly all of the Mn contributes to the paramagnetism in the GaN:Mn and GaN:Mn:Si samples grown at higher substrate temperatures. SQUID measurements, however, do not provide the possibility of determining the magnetic moments or the g-factors of the contributing Mn^{2+} or Mn^{3+} oxidation states separately. This is only possible with the help of ESR measurements.

7.3 ESR of GaN:Mn^{2+} and AlN:Mn^{2+}

ESR identification of Mn^{2+} in GaN has previously been reported in unintentionally doped bulk crystals prepared by the sublimation sandwich method at small Mn concentrations of 10^{17} cm^{-3}.[135, 136, 137] This growth method is quite useful for the preparation of large GaN crystals,[155] however, most device-quality epitaxial GaN films are presently grown by molecular beam epitaxy (MBE) or metal-organic chemical vapor deposition (MOCVD) because of higher purity and better doping control. Although at first sight the ESR spec-

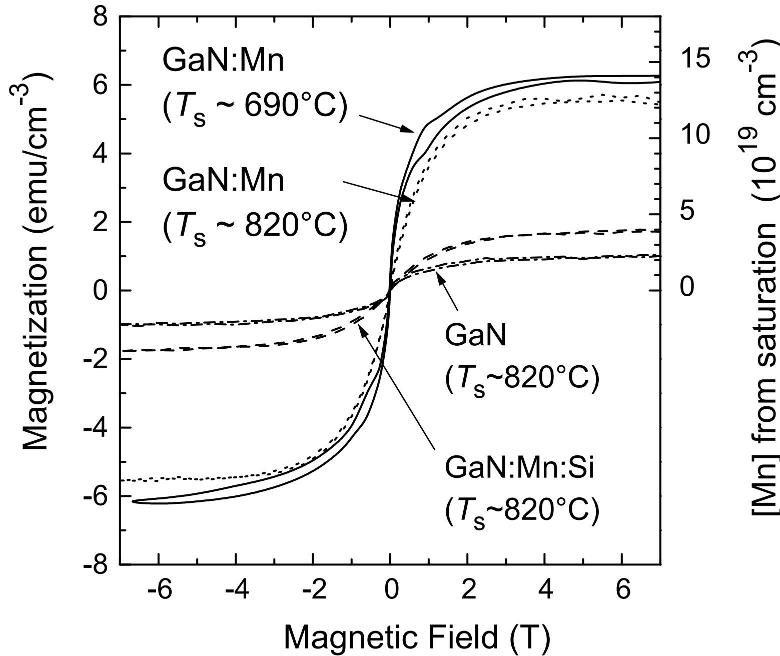

Figure 7.12: Magnetization at $T = 2$ K of the three representative GaN:Mn and GaN:Mn:Si samples. The magnetization of the GaN reference sample is caused by paramagnetic impurities in the sapphire substrate that are clearly resolved in ESR (see also Fig. 7.31). The Mn concentrations indicated on the right axis of the figure are obtained from the saturation magnetization with $g \approx 2$ and $S \approx 2 - 2.5$.

tra of our highly doped MBE-grown GaN:Mn^{2+} films are similar to those reported for the lower doped bulk crystals, the extracted fine- and hyperfine-structure parameters differ significantly. The differences in the axial fine-structure parameter can be dominantly ascribed to the biaxial strain from the substrates, as described below. Because in our samples the degree of relaxation varies with the film thickness and the growth conditions, the influence of the crystal field on the Mn^{2+} ground state can be studied without application of external pressure. Some features of the numerical simulation reported in Refs. 135, 136, 137 are neither present in the experimental spectra nor in our numerical results. However, some additional "forbidden" transitions neglected in Refs. 135, 136, 137 have been observed in our experimental spectra. To review their origin and to describe the spin properties of Mn^{2+} in GaN and AlN more accurately, a refined experimental and numerical investigation of the spin Hamiltonian is presented here.

So far, only few other ESR studies on Mn in group III nitrides are available. In addition to Refs. 135, 136, 137, Mn-related ESR was reported in microcrystalline GaN grown by the ammonothermal method and doped intentionally with different concentrations of Mn.(124) In this study, the identification was restricted to the isotropic part of the ESR spectrum, and therefore no direct evidence for the oxidation state of Mn could be extracted. Intentionally doped GaN:Mn crystals have been prepared by MOCVD (127, 128) and MBE ,(125, 126) but to our knowledge, these samples have not been studied by ESR yet. In polycrystalline AlN, some Mn-related ESR spectra with g-factors in the range of 1.8-10 were reported together with Mn^{2+}- and Mn^{4+}- related photoluminescence.(156) Again, no ESR anisotropy of Mn-related centers in AlN crystals was reported up to now, which is necessary for a detailed analysis of the spin Hamiltonian. Preliminary ESR re-

sults have also been published in Ref. 125 for the ferromagnetic GaN:Mn films of Ref. 157. These results indicate the presence of a paramagnetic phase in these films with spin properties similar to those reported for GaN:Mn^{2+} in Refs. 135, 136, 137. Additionally, the ferromagnetic resonance (FMR) signal of an unidentified second phase was observed,(157) which is very similar to the FMR signal of MnAs clusters in GaAs:Mn.(158) No experimental evidence of the presence of corresponding Mn–N clusters in GaN:Mn was found in Ref. 157, however, the methods employed were insensitive to clusters of nm-size.(154)

In the following, we first analyze in detail the spin Hamiltonian parameters of the pure GaN:Mn^{2+} and AlN:Mn^{2+} films, which are mostly relaxed. Later, these values are compared with the spin Hamiltonian parameters of the more strained GaN:Mn^{2+}:Si films and those of the bulk GaN:Mn^{2+} crystal of Refs. 135, 136, 137. The spin densities of the pure and Si-codoped GaN:Mn^{2+} and GaN:Mn^{2+}:Si films are evaluated in Sec. 7.3.2.

7.3.1 Crystal field spin Hamiltonian

Starting from the [Ar]$3d^5 4s^2$ electronic configuration of free Mn atoms, Mn^{2+} denotes the Mn oxidation state with a half-filled $3d^5$ shell. Within a semiconductor lattice, this formally twofold ionic charge is distributed over the neighboring host valences and screened by the valence-band electrons, so that the ionization threshold is effectively reduced in comparison to free Mn ions.(31, 118) The electronic spin $S = 5/2$ of the five $3d$ electrons of the Mn^{2+} Kramers ion is conserved and typically combined to a $^6A_1$ ground-state configuration with orbital momentum $L = 0$. This ground state is additionally coupled to the nuclear spin $I = 5/2$ of the natural isotope ^{55}Mn.

Generally, it is incorrect to employ crystal field theory to describe the zero-field splitting of impurity ground states in semiconductors because of the presence of continuum electronic states that hybridize with the atomic Mn orbitals.(15, 118) However, the phenomenological form of the crystal field spin Hamiltonian is still correct, even if the true origin of the occurring parameters fails to agree with real crystal fields.(15) Therefore, the effective Mn^{2+} ground state manifold of $(2S+1)(2I+1) = 36$ spin states can be described by the Hamiltonian (13, 18, 159, 160)

$$\begin{aligned}\mathcal{H} \;=\;& \mu_B \vec{B} g \vec{\mathcal{S}} + D\left(\mathcal{S}_z^2 - \tfrac{35}{12}\right) + \vec{\mathcal{S}} A \vec{\mathcal{I}} \\ &+ \tfrac{1}{6}\,\tilde{a}\left(\mathcal{S}_\xi^4 + \mathcal{S}_\eta^4 + \mathcal{S}_\zeta^4 - \tfrac{707}{16}\right) + \tfrac{7}{36} F\left(\mathcal{S}_z^4 - \tfrac{95}{14}\mathcal{S}_z^2 + \tfrac{81}{16}\right) \\ &+ P\left(\mathcal{I}_z^2 - \tfrac{35}{12}\right) - \mu_n \vec{B} g_n \vec{\mathcal{I}} \end{aligned} \tag{7.4}$$

with all parameters introduced in the following. As an example, the Breit-Rabi diagram of the eigen-energies plotted as a function of the external field $\vec{B} \parallel \vec{e}_z \parallel c$ (lattice vector of the wurtzite crystal) is shown in Fig. 7.13 using the parameters for $g, D, A, \ldots$ determined for AlN:Mn^{2+} below.

The 36 eigen-states are denoted by m_s and m_i according to their $\mathcal{S}_z$ and $\mathcal{I}_z$ quantum numbers at large magnetic fields. As indicated, the allowed transitions follow the selection

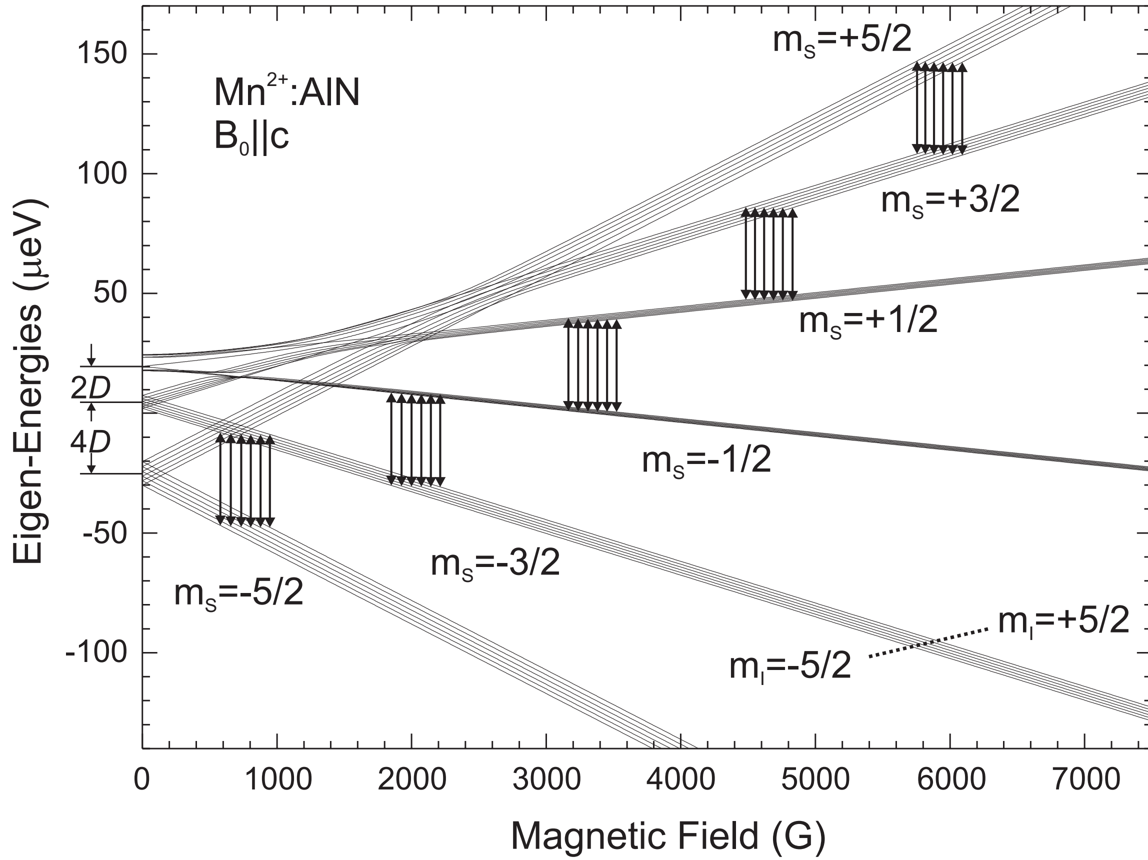

Figure 7.13: Breit-Rabi Diagram for Mn^{2+} in AlN with the magnetic field $\vec{B}_0$ oriented parallel to the c-axis of the film. At this orientation, the spin quantization axis is well oriented along this direction at low and high magnetic fields because of the combined effect of the Zeeman and the axial fine-structure interactions. The parameters used are $g_{\mathrm{AlN}} \approx 2.000$, $D_{\mathrm{AlN}} \approx -8$ μeV, $A_{\mathrm{AlN}} \approx -0.8$ μeV, and $h\nu \approx 40$ μeV.

rule $\Delta m_s = \pm 1$ and $\Delta m_i = 0$ in this orientation. In X-band ESR experiments, the total eigen-energies are mainly determined by the Zeeman energies up to $g\mu_B B m_s \approx 100$ μeV for $m_s = +5/2$ and $B = 3300$ G. The axial crystal field parameterized by D dominates the fine-structure of the levels in the zero-field limit. It distributes the electronic spin states into three Kramers doublets separated by about 20 μeV, as indicated in Fig. 7.13. The hyperfine interaction A of the electronic spin with the nuclear spin of ^{55}Mn further splits the energies levels by an amount of the order of 2 μeV. The fine-structure parameters $\tilde{a}$ and F of the cubic crystal field for $S = 5/2$ states are even smaller and of the order of 0.1 μeV only. $\mathcal{S}_\xi$, $\mathcal{S}_\eta$, and $\mathcal{S}_\zeta$ are the spin operators rotated onto the axes of the cubic crystal field, as discussed below. Further contributions such as the nuclear Zeeman interaction of the ^{55}Mn nuclei characterized by $g_n\mu_n \approx 0.000\,377 \times g_0\mu_B$ (see Tab. 3.1), and the nuclear quadrupolar interaction characterized by P give rise to even smaller energy corrections. The nuclear spin parameters g_n and P cancel out for the "allowed" electron spin resonance

transitions, for which m_i remains unchanged, but they contribute significantly to the positions of the "forbidden" transition doublets of Eq. (7.18). Therefore, they should be included in Eq. (7.4). However, since the nuclear properties g_n and P are extremely similar in different materials, both parameters were taken from ZnO:Mn^{2+}(161) to also describe the Mn^{2+} states in GaN and AlN.

The large number of ESR transitions, which is expected within this ground state manifold has been studied in detail for hexagonal ZnO:Mn^{2+} crystals earlier. The transition intensities calculated numerically from Eq. (7.4) for ZnO:Mn^{2+} with $D_{\mathrm{ZnO}} = -252.5\ \mathrm{G} \times g\mu_B$, $A_{\mathrm{ZnO}} = -79.3\ \mathrm{G} \times g\mu_B$, $\tilde{a}_{\mathrm{ZnO}} = +6.6\ \mathrm{G} \times g\mu_B$, $F_{\mathrm{ZnO}} = +1.0\ \mathrm{G} \times g\mu_B$, $g_n\mu_n = 0.000\,377 \times g\mu_B$, and $P = 0.17\ \mathrm{G} \times g\mu_B$ are shown in Fig. 7.14 together with experimental ESR spectra of a ZnO bulk substrate crystal contaminated with Mn^{2+} and Fe^{3+} impurities at concentrations around $10^{16}\mathrm{cm}^{-3}$. The linewidths observed in these bulk crystals is even narrower than 0.1 G, which makes it much easier to analyze this signal compared to the overlapping signals of the GaN:Mn^{2+} and Aln:Mn^{2+} samples discussed below.

In the ideal wurtzite structure, the coordination of the four nearest nitrogen neighbors is tetrahedral, but the symmetry is lowered to C_{3v} in the group III nitrides. The most general fine-structure Hamilton for a Mn^{2+} center with such trigonal symmetry can be written as

$$\mathcal{H}_{\mathrm{fs}} = B_2^0\mathcal{O}_2^0 + B_4^0\mathcal{O}_4^0 - \tfrac{2}{3}\ B_4(\mathcal{O}_4^0 + 20\sqrt{2}\mathcal{O}_4^3) \tag{7.5}$$

with the crystal field operators from Ref. 13 [see Eq. (7.88) and Tab. 16]

$$\begin{aligned} \mathcal{O}_2^0 &= 3\ \mathcal{S}_z^2 - S(S+1) \\ \mathcal{O}_4^0 &= 35\ \mathcal{S}_z^4 - 30\ S(S+1)\mathcal{S}_z^2 + 25\ \mathcal{S}_z^2 - 6\ S(S+1) + 3\ S^2(S+1)^2 \\ \mathcal{O}_4^3 &= \tfrac{1}{4}\left[\mathcal{S}_z(\mathcal{S}_+^3 + \mathcal{S}_-^3) + (\mathcal{S}_+^3 + \mathcal{S}_-^3)\mathcal{S}_z\right] \quad . \end{aligned} \tag{7.6}$$

According to Ref. 14, an opposite sign appears at the last term of Eq. 7.5 in case of a left-handed coordinate system with exchanged x and y in-plane coordinate axes, as used e.g. by Ref. 18 [see Eq. (4.54)] and others.(162) The more common form(13, 14, 159) of Eq. (7.4) is obtained from Eq. (7.5) with

$$\tilde{a} = 120\ B_4; \qquad D = 3\ B_2^0; \qquad F = 180\ B_4^0 \tag{7.7}$$

and the Spin operators

$$\begin{aligned} \mathcal{S}_\xi &= -\sqrt{\tfrac{2}{3}}\ \mathcal{S}_x + \sqrt{\tfrac{1}{3}}\ \mathcal{S}_z \\ \mathcal{S}_\eta &= \sqrt{\tfrac{1}{6}}\ \mathcal{S}_x + \sqrt{\tfrac{1}{2}}\ \mathcal{S}_y + \sqrt{\tfrac{1}{3}}\ \mathcal{S}_z \\ \mathcal{S}_\zeta &= \sqrt{\tfrac{1}{6}}\ \mathcal{S}_x - \sqrt{\tfrac{1}{2}}\ \mathcal{S}_y + \sqrt{\tfrac{1}{3}}\ \mathcal{S}_z \end{aligned} \tag{7.8}$$

along the cubic axis indicated in Fig. 7.15, and with

$$\mathcal{S}_\xi^4 + \mathcal{S}_\eta^4 + \mathcal{S}_\zeta^4 - \tfrac{1}{5}S(S+1)(3S^2 + 3S - 1) = -\tfrac{1}{30}(\mathcal{O}_4^0 + 20\sqrt{2}\mathcal{O}_3^3) \quad . \tag{7.9}$$

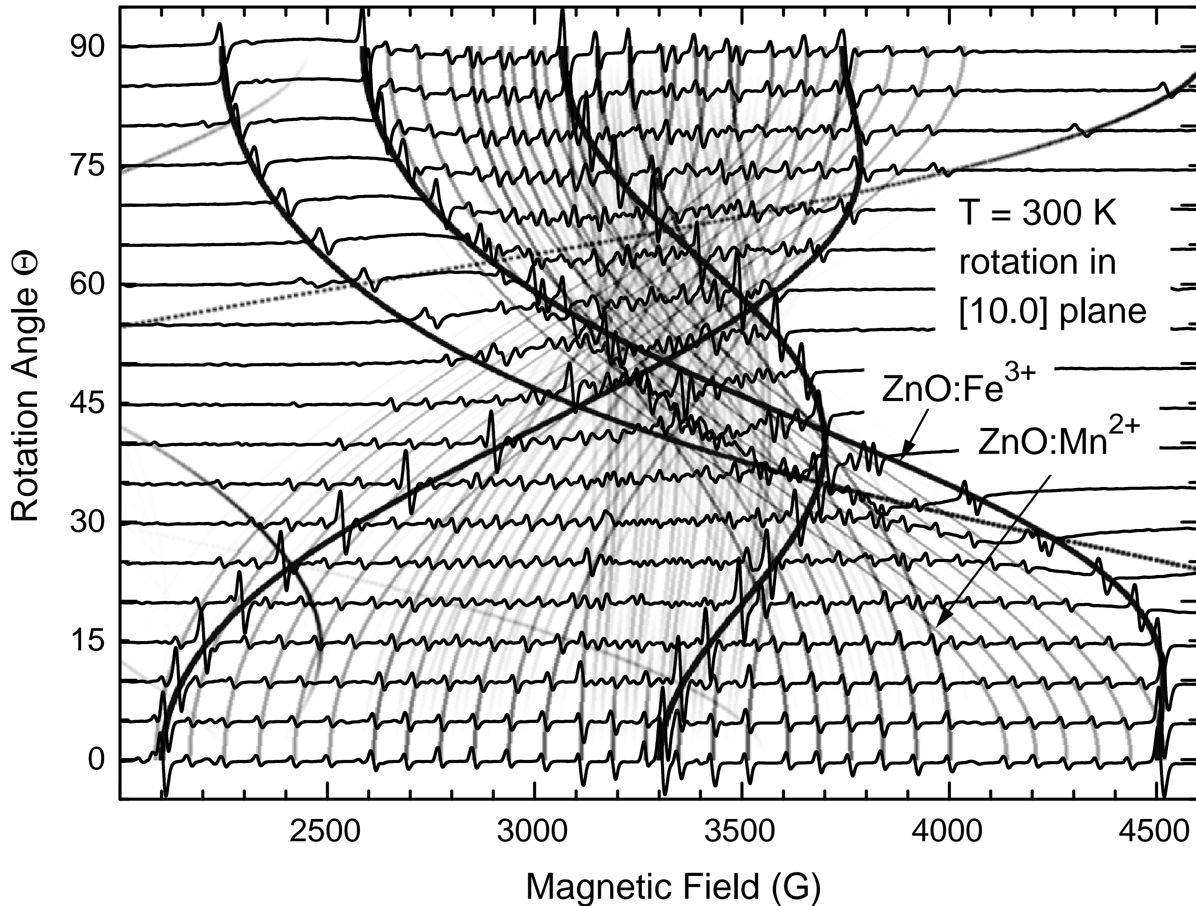

Figure 7.14: Measured ESR signal (solid lines) and calculated transition intensities of ZnO:Mn^{2+} for a rotation of the magnetic field in the (10.0) plane. In the perpendicular $(1\bar{2}.0)$ plane, the number of lines would even be twice as large. An additional, more intense and highly anisotropic signal belonging to Fe^{3+} impurities is observed as well in these crystals. These were simulated with the spin Hamiltonian of Eq. (7.4), however with $D = -637\ \mathrm{G} \times g\mu_B$ and without hyperfine interactions.

Several other notations, e.g. a parameter $D' = D/3$ as used e.g. in Ref. 163, and many typical errors in the use of these parameters are summarized in Ref. 14.

The axial distortion, which is expressed by the crystal field parameter D, is assumed to be oriented along the sample c-axis in agreement with the observed ESR signals discussed below. For the notation (7.4) of the spin Hamiltonian, the z coordinate axis is chosen along this axis of D and fixed with respect to the sample, although the axis of spin quantization will rather be oriented along $\vec{B}$. To investigate all possible relative orientations, the angle θ between $\vec{B}$ and the c-axis of the sample is varied between 0 and 90° by a rotation of $\vec{B}$ within the $(1\bar{2}.0)$ and (10.0) planes, as shown in Fig. 7.15.

For the tetrahedral substitutional sites, those two rotations are indistinguishable in quadratic terms like the Zeeman and hyperfine interaction, as the corresponding energy

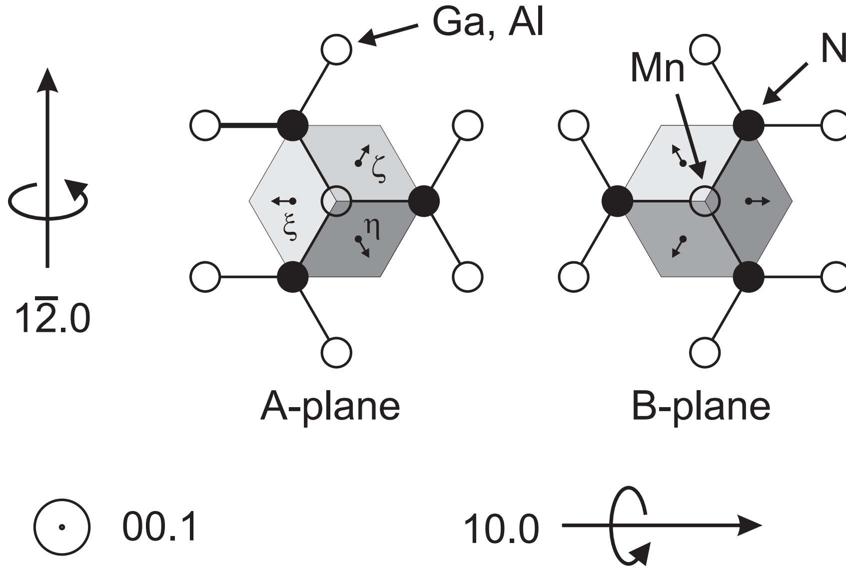

Figure 7.15: The two magnetically nonequivalent A and B lattice sites of the wurtzite lattice. The largest cubic fine-structure splitting between the Mn^{2+} ESR of the two sites is expected for magnetic fields tilted by $\theta = 60°$ from the (00.1) axis towards (10.0). However, this splitting is below the experimental linewidth of the experimental data reported for group III nitrides here.

ellipsoids do not reflect the threefold crystalline symmetry around c. This is different for the cubic crystal field described with three perpendicular axes ξ, η, and ζ, which are tilted by 35.26° with respect to the (00.1) plane and oriented parallel to the edges of the cubes, as indicated in Fig. 7.15.[159, 160, 161] There are two distinct cubes for the A and B site of the wurtzite AB stacking sequence, each containing one central atom and four nearest tetrahedral neighbors on the corners. The orientation of these cubes with respect to the external field $\vec{B}$ can be expressed by a single parameter $\phi = l^2m^2 + m^2n^2 + n^2l^2$ with l, n, m being the direction cosines of ξ, η, and ζ, respectively, with respect to the field axis.[13, 160] As can be deduced from Fig. 7.15, this parameter is symmetric with respect to the sign of θ for rotations within the (10.0) plane and asymmetric for rotations within the ($1\bar{2}.0$) plane for A and B sites, respectively. Geometrical considerations result in

$$\begin{aligned}\phi_{10.0} &= \frac{1}{96}[21 + 4\cos(2\theta) + 7\cos(4\theta)] \quad , \\ \phi_{1\bar{2}.0} &= \phi_{10.0} \pm \frac{\sqrt{2}}{96}[8\sin(2\theta) - 4\sin(4\theta)] \quad . \end{aligned} \tag{7.10}$$

As the anisotropy of the cubic crystal field is described in terms of ϕ only, its symmetry reappears in the solutions of the spin Hamiltonian. The maximum difference between the eigen-energies of the magnetically inequivalent A and B sites of the wurtzite lattice is expected for a maximal splitting of $\phi_{1\bar{2}.0}$ at $\theta = 60°$ in the ($1\bar{2}.0$) plane.[160]

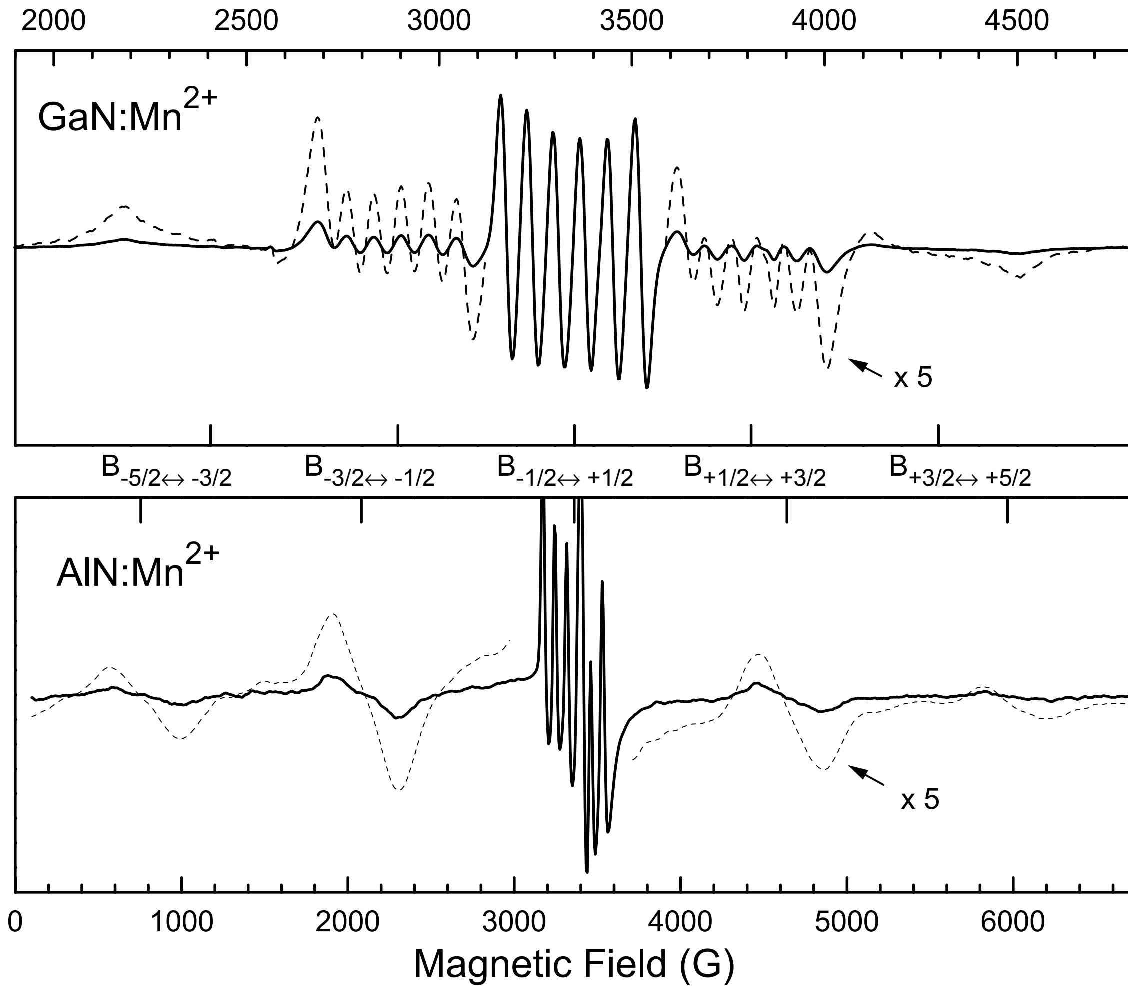

Figure 7.16: X-band ESR spectra of Mn^{2+} with the magnetic field oriented parallel to the c-axis of GaN and AlN at $T = 6$ K. In both spectra, five $(2S)$ groups of six $(2I + 1)$ hyperfine satellites indicate the presence of $^{55}Mn^{2+}$. Increased broadening of the outer fine-structure groups reveals fluctuations in the zero-field splitting of about 5%. In the spectra shown, microwave saturation helps to suppress the background ESR dominated by impurities in the sapphire substrate.

7.3.2 Spin Hamiltonian analysis with $\vec{B} \parallel c$

Most of the properties of Mn^{2+} in GaN and AlN are conveniently extracted from the spectra of Fig. 7.16 at $\theta = 0°$, where the splitting of adjacent lines is maximum. In this orientation, the electronic part of the Spin Hamiltonian can be diagonalized analytically, as the axis of the crystal field D coincides with the magnetic field axis.[159, 160] The parameters from the analysis of the spectrum at $\theta = 0°$ are then used in Sec. 7.3.3 to investigate the full anisotropy of the spin Hamiltonian. Neglecting hyperfine interactions,

one obtains the analytical eigen-energies

$$\begin{aligned} W_{\pm 5/2} &= \pm g\mu_B B + \tfrac{1}{3}D - \tfrac{1}{2}(\tilde{a}-F) \\ &\quad \pm\sqrt{[\pm\tfrac{3}{2}\, g\mu_B B + 3D + \tfrac{1}{6}(\tilde{a}-F)]^2 + \tfrac{20}{9}\tilde{a}^2} \quad , \\ W_{\pm 3/2} &= \pm\tfrac{3}{2}\, g\mu_B B - \tfrac{2}{3}\, D + (\tilde{a}-F) \quad , \\ W_{\pm 1/2} &= \mp g\mu_B B + \tfrac{1}{3}D - \tfrac{1}{2}(\tilde{a}-F) \\ &\quad \pm\sqrt{[\pm\tfrac{3}{2}\, g\mu_B B - 3D - \tfrac{1}{6}(\tilde{a}-F)]^2 + \tfrac{20}{9}\,\tilde{a}^2} \quad . \end{aligned} \tag{7.11}$$

According to the first-order approximation of large microwave energies $h\nu \gg |D| \gg |\tilde{a}-F|$, the cubic crystal field parameters always occur in a combination $\tilde{a}-F$, so that additional measurements at intermediate angles are required for the determination of these parameters separately. The solutions for the resonance condition $h\nu = W_{m_s} - W_{m_s-1}$ define the magnetic-field positions $B_{m_s\leftrightarrow m_s-1}$ of the resonances $|m_s\rangle \leftrightarrow |m_s-1\rangle$. The parameters $g = h\nu/(\mu_B B_{+1/2\leftrightarrow -1/2}) \approx 2.000$, and D and $\tilde{a}-F$ are then calculated in terms of these fields, which are indicated in Fig. 7.16 by the centers of gravity of the fine-structure resonance groups:

$$\begin{aligned} |D| &= (g\mu_B/56)\ |5\ (B_{+5/2\leftrightarrow +3/2} - B_{-3/2\leftrightarrow -5/2}) \\ &\quad +4\ (B_{+3/2\leftrightarrow +1/2} - B_{-1/2\leftrightarrow -3/2})| \quad , \\ |\tilde{a}-F| &= (g\mu_B/28)\ |-3\ (B_{+5/2\leftrightarrow +3/2} - B_{-3/2\leftrightarrow -5/2}) \\ &\quad +6\ (B_{+3/2\leftrightarrow +1/2} - B_{-1/2\leftrightarrow -3/2})| \quad . \end{aligned} \tag{7.12}$$

For the spectrum of a GaN:Mn^{2+} film with $c = 5.187$ Å and $a = 3.187$ Å shown in Fig. 7.16, we find

$$\begin{aligned} |D_{\mathrm{GaN}}| &= (236 \pm 2)\ \mathrm{G} \times g\mu_B = 220 \times 10^{-4}\ \mathrm{cm}^{-1} \times hc \quad , \\ |\tilde{a}-F|_{\mathrm{GaN}} &= (6 \pm 3)\ \mathrm{G} \times g\mu_B = 5 \times 10^{-4}\ \mathrm{cm}^{-1} \times hc \quad , \end{aligned}$$

and correspondingly for an AlN:Mn^{2+} film with $c = 4.981$ Å and $a = 3.112$ Å

$$\begin{aligned} |D_{\mathrm{AlN}}| &= (648 \pm 3)\ \mathrm{G} \times g\mu_B = 605 \times 10^{-4}\ \mathrm{cm}^{-1} \times hc \quad , \\ |\tilde{a}-F|_{\mathrm{AlN}} &= (10 \pm 4)\ \mathrm{G} \times g\mu_B = 9 \times 10^{-4}\ \mathrm{cm}^{-1} \times hc \quad . \end{aligned}$$

In units of frequency, the larger fine-structure zero-field splitting $\delta \approx 4|D|$ between the electronic Kramers doublets with $|m_s| = 3/2$ and $|m_s| = 5/2$ at $B = 0$ is obtained as $\delta \approx 0.66$ GHz for GaN and $\delta \approx 1.8$ GHz for AlN. As experimentally the outer fine-structure splittings $|B_{+5/2\leftrightarrow +3/2} - B_{+3/2\leftrightarrow +1/2}|$ and $|B_{-1/2\leftrightarrow -3/2} - B_{-3/2\leftrightarrow -5/2}|$ are larger than the inner splittings $|B_{+3/2\leftrightarrow +1/2} - B_{+1/2\leftrightarrow -1/2}|$ and $|B_{+1/2\leftrightarrow -1/2} - B_{-1/2\leftrightarrow -3/2}|$, it can be deduced from Eq. (7.11) that D and $\tilde{a}-F$ have opposite signs. The relative sign of D with respect to g, the latter of which is assumed to be positive because of the small deviation from g_0, has to be deduced by other means, as discussed below.

Up to now, the hyperfine interaction between electronic and nuclear spins has been neglected in the calculation of the eigen-energies. Treating this additional interaction as a small perturbation, the magnetic-field offsets $\Delta b_{m_s,m_i \leftrightarrow m_s-1,m_i}$ of the transitions $|m_s, m_i\rangle \leftrightarrow |m_s-1, m_i\rangle$ from the transitions $|m_s\rangle \leftrightarrow |m_s-1\rangle$ resulting from Eq. (7.11) have been calculated to third order in A in Ref. 161

$$\begin{aligned}\Delta b_{m_s,m_i \leftrightarrow m_s-1,m_i} &= B_{m_s,m_i \leftrightarrow m_s-1,m_i} - B_{m_s \leftrightarrow m_s-1} \\ &= -\tfrac{A}{g\mu_B}\ \Big\{ m_i + \tfrac{A}{h\nu}\ \left[(m_s - \tfrac{1}{2})\ m_i + \tfrac{1}{2}\ (\tfrac{35}{4} - m_i^2) \right] \\ &\quad + \tfrac{A^2}{(h\nu)^2}\ \left[(\tfrac{35}{4} - m_i^2)(2m_s - 1) - \tfrac{1}{2}\ m_i(\tfrac{35}{4} - 3m_s^2 + 3m_s - 2) \right] \\ &\quad + \tfrac{AD}{(h\nu)^2}\ \left[(\tfrac{35}{4} - m_i^2)(2m_s - 1) - m_i(\tfrac{35}{4} - m_s^2 + m_s - 1) \right] \Big\} \quad . \end{aligned} \tag{7.13}$$

The hyperfine constant $|A|$ is given approximately by the splitting of about 70 G within one of the fine-structure groups. At X-band energies, higher-order terms are shifting the hyperfine resonances significantly, increasing both the apparent g-factor and the effective hyperfine splitting. In Fig. 7.17, the resonance positions of the $m_s = 1/2$ central fine-structure group are shown according to first-, second-, and third-order perturbation theory, i.e. including terms proportional to $\frac{A}{h\nu}$, to $\left(\frac{A}{h\nu}\right)^2$, and to $\left(\frac{A}{h\nu}\right)^3$ or $\frac{A^2 D}{(h\nu)^3}$ of Eq. (7.13), respectively. The result of a numerical diagonalization of the complete spin Hamiltonian (7.4) for GaN and AlN is also shown. The numerical shifts $\Delta b_{m_s,m_i \leftrightarrow m_s-1,m_i}$ within this group are of the order of -6 to 0 G (-7 to $+7$ G) for GaN:Mn^{2+} (AlN:Mn^{2+}). The constant first-order splitting $A/(g\mu_B)$ has been reduced by a factor of five in Fig. 7.17 for better visibility of the higher-order effects. Obviously, the change in $|D|$ between both materials influences both, the average positions as well as the splitting of the central hyperfine sextet. According to the exact numerical calculations, $|A| = (69 \pm 1)\text{G} \times g\mu_B = 65 \times 10^{-4}\ \text{cm}^{-1} \times hc$ is obtained both for the GaN and AlN spectra of Fig. 7.16. After calibration of the magnetic field positions with diphenyl-picrylhydracyl (DPPH, g = 2.0036), corrected g-factors $g = 1.9994 \pm 0.0008$ for Mn^{2+} in GaN and $g = 2.0004 \pm 0.0008$ in AlN are obtained.

For other transitions than $|+1/2, m_i\rangle \leftrightarrow |-1/2, m_i\rangle$, also the second-order corrections $[-\left(\frac{A}{h\nu}\right)^2 (m_s - \frac{1}{2})\ m_i]$ of (7.13) modify the effective hyperfine splitting, as they contain terms proportional to m_i. From the differences in hyperfine splitting, the relative sign of A with respect to that of D can be determined, as, e.g., the transitions $|+3/2, m_i\rangle \leftrightarrow |+1/2, m_i\rangle$ are shifted towards lower or higher magnetic field for positive or negative sign of D, respectively. To illustrate this, the spectrum of GaN:Mn^{2+} has been reversed in the inset of Fig. 7.18 in a way that some inner and outer hyperfine pairs overlap. For these groups, a larger splitting between adjacent hyperfine lines is observed at lower magnetic fields (full line) than in the reversed signal that occurs at higher magnetic fields (dashed line). The stronger overlap of the high-field satellites is also responsible for their smaller ESR amplitude compared to the low-field satellites. These observations show that the sign of A is negative, if the transition $|+3/2, m_i\rangle \leftrightarrow |+1/2, m_i\rangle$ occurred at higher magnetic

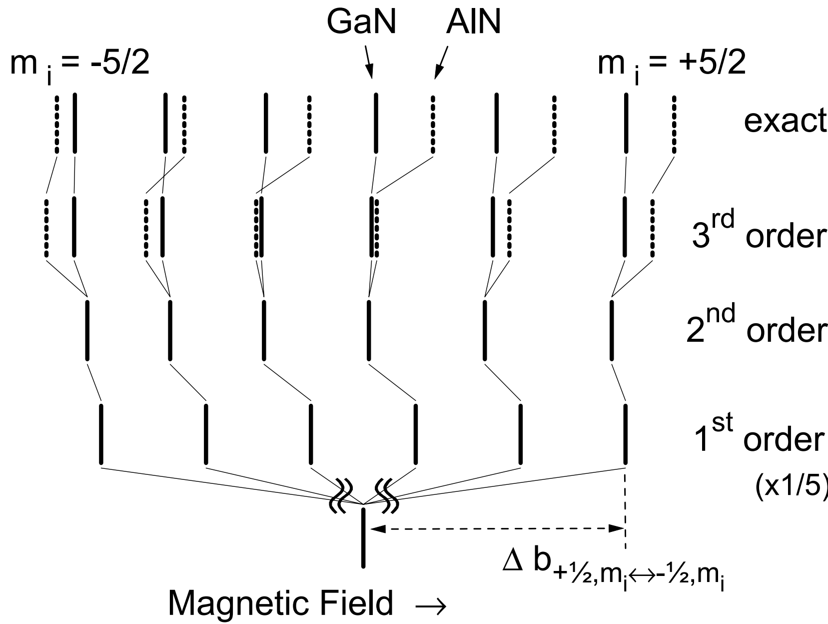

Figure 7.17: For the Mn^{2+} spin system with both fine and hyperfine interactions, the resonance positions $B_{1/2\leftrightarrow-1/2}$ without nuclear spin are shifted by $\Delta b_{1/2,m_i\leftrightarrow-1/2,m_i}$, defined in Eq. (7.13) according to perturbation theory. The numerical calculation shows that mixing terms with the axial crystal field D of higher order become important in AlN:Mn^{2+} even at $\theta = 0°$. The first-order splitting has been reduced to $A/5$ in this plot.

fields, i.e. if D was negative. Such a combination of negative D and A is depicted in the level diagram of Figs. 7.13 and 7.17.

However, it still remains to be shown that D is indeed negative in GaN and AlN. To determine the sign of D, one needs to clarify whether the transitions with positive m_s occur at high or low magnetic fields. Because the transition intensity $I_{m_s\leftrightarrow m_s-1}$ is proportional to the population difference between the levels $|m_s\rangle$ and $|m_s-1\rangle$, the situations for positive and negative D can be distinguished at low temperatures. Below microwave saturation, and for $k_BT \gg hv \gg |D|$, the thermal occupation of the levels $|m_s\rangle$ and $|m_s-1\rangle$ is given by a Boltzmann series:[18]

$$I_{m_s\leftrightarrow m_s-1} \propto \frac{N_{m_s-1}-N_{m_s}}{\sum_n N_n} = \frac{1-\exp\frac{-h\nu}{k_BT}}{\sum_n \exp\frac{W_{m_s-1}-W_n}{k_BT}} \approx \frac{1}{6}\left(\frac{h\nu}{k_BT}\right) - \frac{m_s-1/2}{6}\left(\frac{h\nu}{k_BT}\right)^2 . \quad (7.14)$$

To first order in $h\nu/k_BT$, the occupation differences follow Curie's law for all levels, but as energetically lower pairs of levels have both a higher average population as well as a higher difference in population, their ESR absorption are larger in second order. At X-band frequencies, $h\nu/k_B \approx 0.43$ K, so that at 2.8 K, which is the lowest temperature achievable with our cryostat, we expect relative second-order changes of about 30% for the outer transitions $|\pm 5/2, m_i\rangle \leftrightarrow |\pm 3/2, m_i\rangle$ and about 15% for the inner transitions $|\pm 3/2, m_i\rangle \leftrightarrow |\pm 1/2, m_i\rangle$. Two integrated ESR spectra recorded at 2.8 and 6 K are shown normalized for the first-order Curie term in Fig. 7.18. The satellites in the region of lower

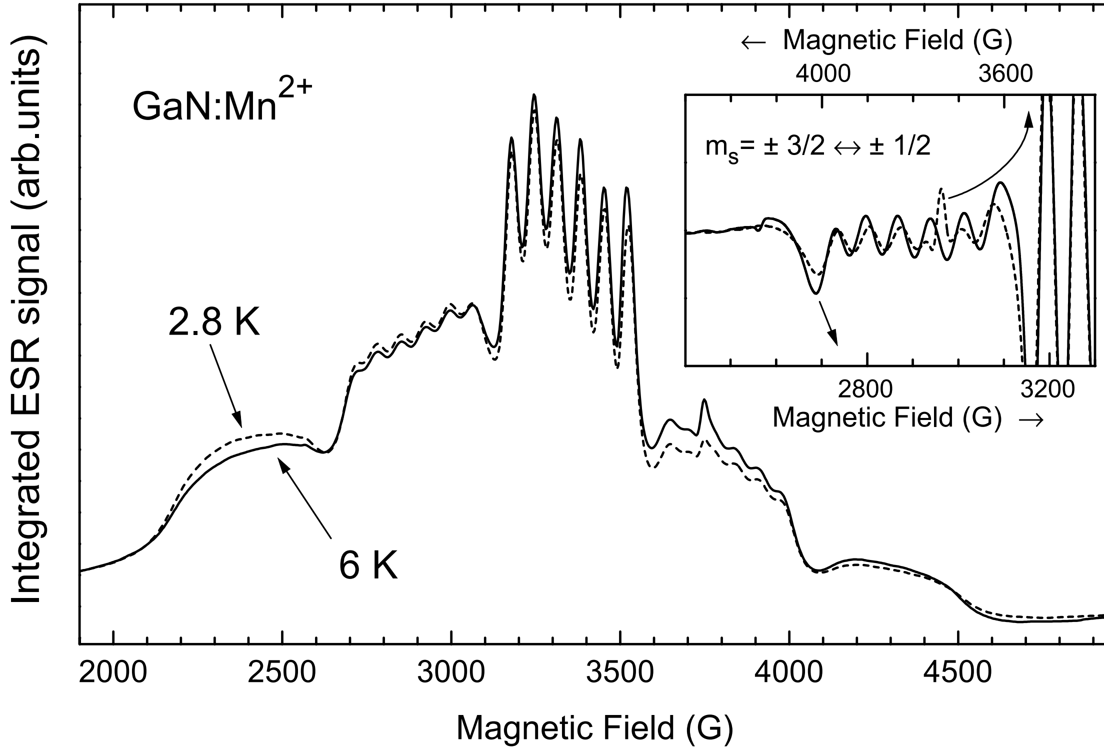

Figure 7.18: Integrated GaN:Mn^{2+} spectra with the intensities corrected for the measurement temperature. The intensity ratio of the fine-structure groups is consistent with the ideal ratio 5:8:9:8:5 of an $S = 5/2$ spin system discussed below. The intensity ratio at lower temperatures requires the assignment of these transitions to the m_s quantum numbers, as shown in Fig. 7.13. Microwave power has been reduced in these spectra in order to avoid microwave saturation. Therefore, some substrate resonances, e.g. a narrow line at 3750 G are not suppressed completely. The inset shows that second-order effects increase the hyperfine splitting of the low-field transitions $|m_s = -1/2\rangle \leftrightarrow |m_s = -3/2\rangle$ compared to the transitions $|m_s = 3/2\rangle \leftrightarrow |m_s = 1/2\rangle$, which have been plotted on a reversed magnetic-field axis. Therefore, the sign of A is determined to be negative, as that of D.

magnetic fields grow faster than linearly in $h\nu/k_BT$ with decreasing temperature. Thus, they can be identified to belong to negative m_s. According to Fig. 7.13, this ordering of the fine-structure lines indicates a negative sign of D. From the earlier conclusions about the relative signs, A follows to be negative and $\tilde{a} - F$ to be positive, respectively.

As shown in Fig. 7.19, the spin resonance signal of Mn^{2+} in GaN and AlN can be measured up to room temperature. Within the experimental errors, no change was observed in the spin parameters and densities. The paramagnetic susceptibility is well described by Curie's law at all accessible temperatures, confirming the presence of an unchanged amount of isolated Mn^{2+} states below their ionization temperature (see Fig. 7.19a). The inhomogeneous linewidth of the central fine-structure group, which is about 30 G in GaN and about 15 G in AlN, did not change up to room temperature, which indicates a small

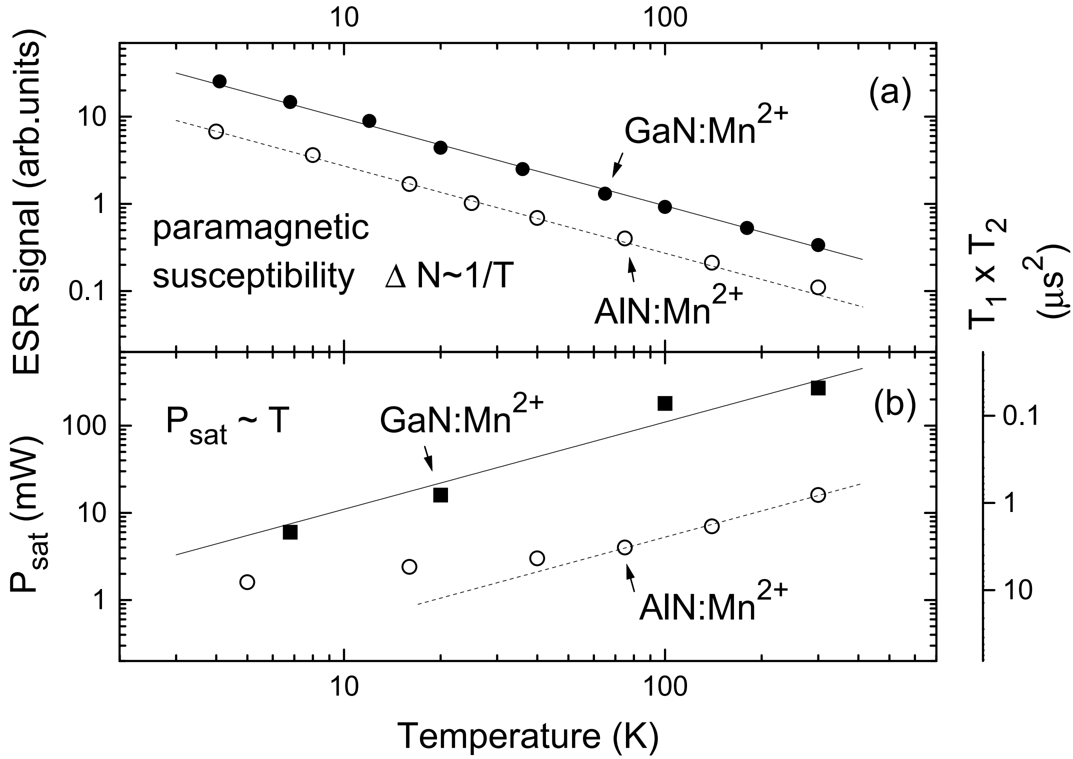

Figure 7.19: Temperature dependence of (a) the ESR signal intensity and (b) the microwave saturation power, which is representative of the spin relaxation rates. The GaN:Mn^{2+} and AlN:Mn^{2+} ESR signals can be traced up to room temperature, indicating a low coupling of the Mn^{2+} spins to the surrounding lattice.

contribution of spin-lattice relaxation processes in group III nitrides to the linewidth. By the continuous saturation method, it is possible to obtain a rough estimate of the product $T_1 \times T_2$ of the spin-lattice relaxation time T_1 and the spin-spin relaxation time T_2, as displayed in Fig. 7.19b. The observed approximately inverse proportionality to temperature would be consistent with a direct spin-lattice relaxation process without a phonon bottleneck.[(164)] Recently, changes of the spin-lattice relaxation time T_1 with the carrier density have been observed in degenerately doped n-type bulk GaN:Mn crystals[(165)] and attributed to the Korringa mechanism of Ref. 166. This enabled an estimate of an upper limit for the very small *sd*-exchange interaction around 14 meV.

The resonances of the central fine-structure group are well resolved in the sample orientation $\vec{B} \parallel c$, while the hyperfine resonances of the fine-structure satellite groups tend to overlap each other. As any spread due to a mosaic structure of the GaN film is small for orientations of B parallel to the principal crystalline axis, the excess linewidth of these satellites is most probably caused by an inhomogeneous distribution of fine-structure constants.

The good agreement of the experimental ESR intensities and of the magnetic-field

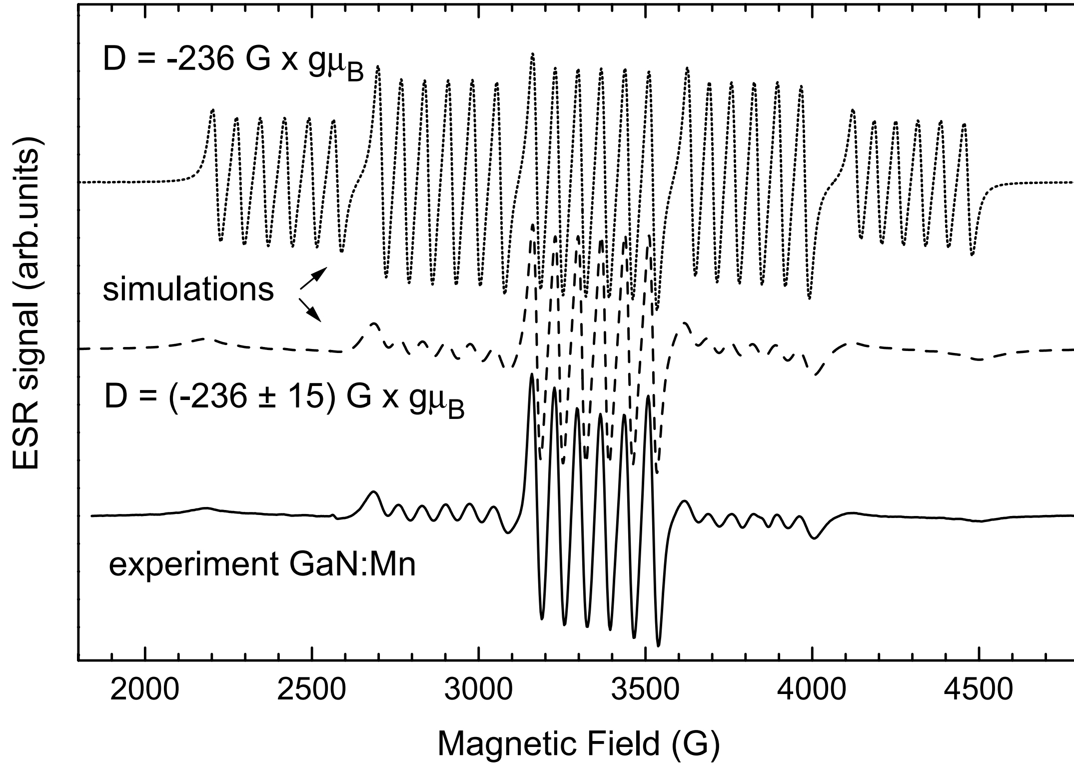

Figure 7.20: Simulated and measured ESR spectra of GaN:Mn^{2+} for the sample orientation $\vec{B} \parallel c$. The upper spectrum (dotted line) was simulated for a single axial crystal field $D = -236$ G $\times\, g\mu_B$ and a residual linewidth of 25 G. A weighted average of similar spectra for a Lorentzian distribution of axial crystal parameters around -236 G $\times\, g\mu_B$ with a full width at half maximum of 30 G $\times\, g\mu_B$ results in the middle spectrum (dashed line), which is very similar to the experimental spectrum shown at the bottom (solid line).

positions for $\vec{B} \parallel c$ with simulated spectra for a Lorentzian distribution of axial crystal fields D with a FWHM of 30 G is shown in Fig. 7.20. According to Eq. (7.11), the separation of the fine-structure satellites from the unperturbed resonance position $B_{-1/2\leftrightarrow+1/2}$ is roughly proportional to D, so that the broadening of the fine-structure satellites is proportional to the variation of that separation for a distribution of D. Experimentally, the central transition group is best resolved also at intermediate orientations of the magnetic field with respect to the sample c-axis, where the magnetic field separation of the fine-structure groups is small, as discussed below. Therefore, possibly also fluctuations of the cubic crystal field parameters $\tilde{a}$ and F must be considered. The observed variations of the crystal field are probably caused by residual inhomogeneous strain within the GaN layers.[13, 135, 136, 137] It would be interesting to compare this with independent measurements of local strain, e.g., from micro-Raman spectroscopy or excitonic photoluminescence. No additional broadening due to electrostatic or magnetic interaction with neighboring Mn centers as claimed in Ref. 124 was observed at the Mn concentrations of

our GaN films. Despite the differences in amplitudes, the same resonance positions are obtained for spectra simulated for an average crystal field and the distribution shown in Fig. 7.20.

Due to the differences in linewidth, the relative intensities of the fine-structure groups can be compared best after numerical double integration. The theoretical intensity for the five transition groups $|m_s \leftrightarrow m_s - 1\rangle$ is proportional to the transition matrix elements from time-dependent perturbation theory. In the strong field limit, they are given by $S(S+1) - m_s(m_s - 1)$.(13, 18) Therefore, with $S = 5/2$, the intensity ratios for the five fine-structure transition groups are 5:8:9:8:5, which are satisfactorily reproduced by the experimental ratios 5:8:11:7:3±1, as can be seen in Fig. 7.18.

7.3.3 Arbitrary orientations

One of the advantages of ESR spectroscopy in single crystals is the symmetry information, which is accessible by rotation of the sample with respect to the external magnetic field. The resonance positions for $\theta > 0°$ allow a critical check of the spin Hamiltonian parameters determined earlier and the verification of the orientation of the axial crystalline field along the c-axis of the epitaxial layers. The presence of other interactions of Mn spins such as exchange interactions besides the fine and hyperfine interaction of Mn^{2+} or possible ESR signals from centers which might overlap with the signal from Mn^{2+} at $\theta = 0°$ can also be investigated by such experiments.

Approximate solutions for the transitions between the eigen-states of the spin Hamiltonian have been calculated via perturbation theory by Ref. 167, including the forbidden transitions with $|\Delta m_i| > 0$ discussed below. Those results were supplemented in Ref. 141 by the forbidden half-field transitions with $|\Delta m_s| > 1$. Today, the available computing power conveniently enables the exact numerical diagonalization of the spin Hamiltonian matrix. The resonance field positions and transition intensities were obtained with the help of a MATHEMATICA (168) code developed during this work and are shown in Figs. 7.21 and 7.22 with the theoretical intensity of the transitions coded by a gray scale.

The experimentally observed resonance positions are included in the same plot, with the intensity of the transition coded by the diameters of the dots. The good agreement with the experimental resonance positions measured for Mn^{2+} in GaN and AlN confirms the symmetry of the spin Hamiltonian assumed earlier and the parameters that were determined above from the spectra at $\vec{B}||$c. Neglecting the contributions from the nuclear spins, the analytical resonance positions $B(\theta)_{m_s \leftrightarrow m_s - 1}$ have been calculated to second

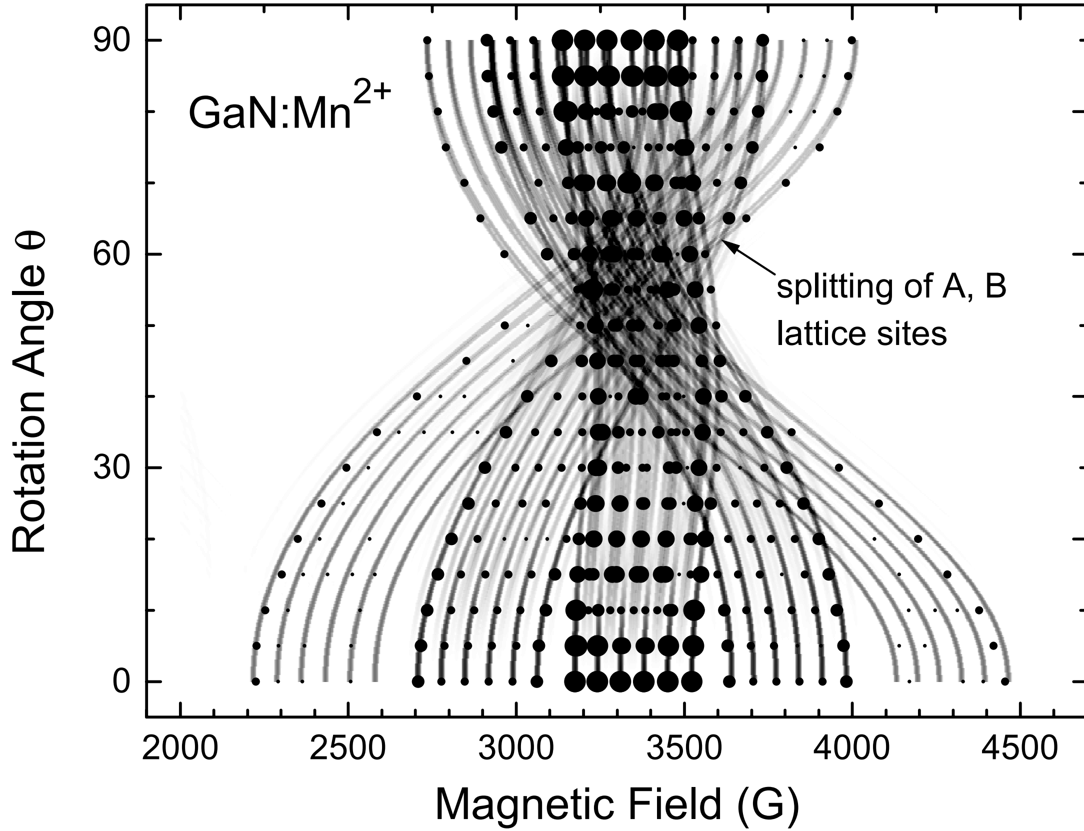

Figure 7.21: Anisotropy of the ESR resonance fields of GaN:Mn^{2+} for sample rotations within the $(1\bar{2}.0)$ plane. The experimental resonance positions are indicated by different dot sizes corresponding to their relative intensities. The underlying gray-scale map shows the transition intensities calculated by numerical diagonalization of the spin Hamiltonian. The significantly smaller linewidth of the central $|m_s = 1/2\rangle \leftrightarrow |m_s = -1/2\rangle$ fine-structure group makes it possible to distinguish this group from the other resonances even in the strongly overlapping regime around $\theta = 60°$.

order in D and to first order in $\tilde{a}$ and F in Refs. 13 and 18

$$\begin{aligned}
B(\theta)_{\pm 5/2 \leftrightarrow \pm 3/2} &= \big[h\nu \mp 2D(3\cos^2\theta - 1) \\
&\qquad \mp 2p\tilde{a} \mp \tfrac{1}{6}\, Fq\big]/(g\mu_B) - 32\Delta_1 + 4\Delta_2, \\
B(\theta)_{\pm 3/2 \leftrightarrow \pm 1/2} &= \big[h\nu \mp D(3\cos^2\theta - 1) \\
&\qquad \pm \tfrac{5}{2}\, p\tilde{a} \pm \tfrac{5}{24}\, Fq\big]/(g\mu_B) + 4\Delta_1 - 5\Delta_2 \quad , \\
B(\theta)_{+1/2 \leftrightarrow -1/2} &= h\nu/(g\mu_B) + 16\Delta_1 - 8\Delta_2 \quad ,
\end{aligned} \tag{7.15}$$

with the geometry parameters $p = 1 - 5\ \phi$ and $q = 35\cos^4\theta - 30\cos^2\theta + 3$, and the second-order fine-structure shifts

$$\begin{aligned}
\Delta_1 &= D^2/(g\mu_B h\nu)\cos^2\theta\sin^2\theta \qquad \text{and} \\
\Delta_2 &= D^2/(4g\mu_B h\nu)\sin^4\theta \quad .
\end{aligned}$$

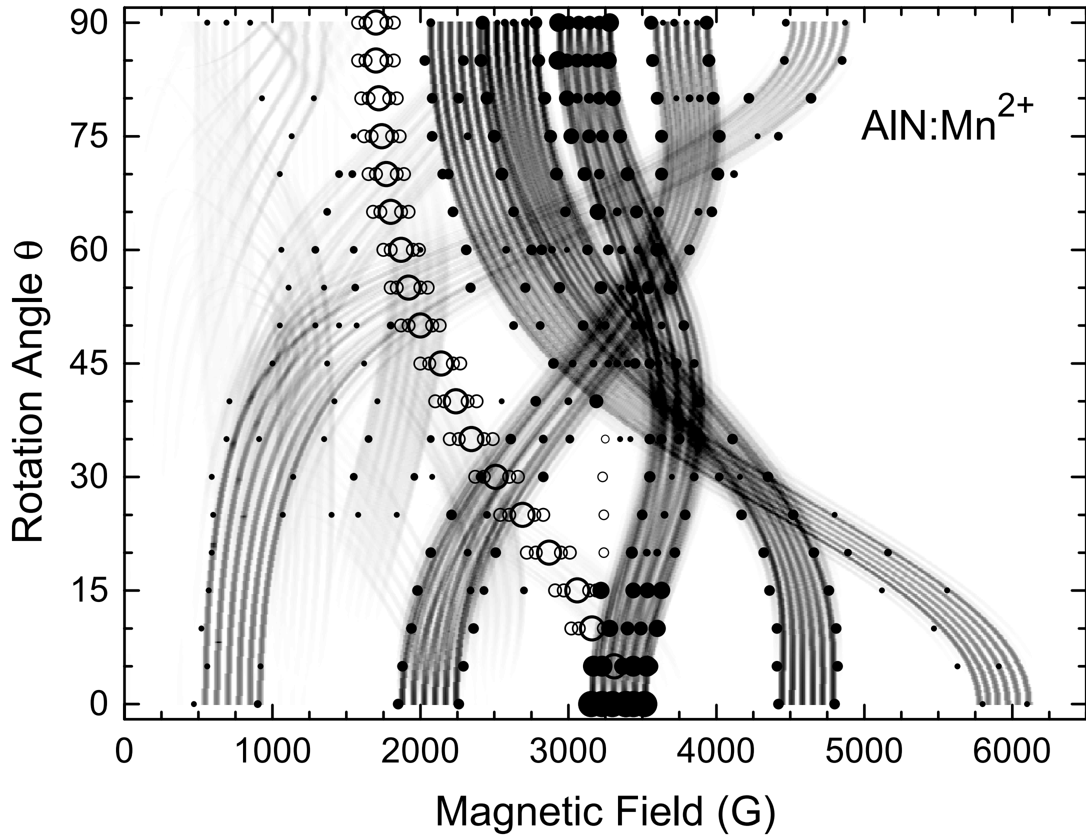

Figure 7.22: Anisotropy of the ESR resonance fields of AlN:Mn^{2+}. The hyperfine-structure of the outer resonance groups is mostly unresolved because of variations in the fine-structure parameters. However, the lineshapes are sometimes still indicative of a group of overlapping lines. In these cases, the positions of the left and right wings of the resonances are indicated by the dots instead of the central resonance positions. Resonances at the positions marked with open circles have been found in the bare sapphire substrate as well, and are therefore not related to the AlN:Mn^{2+} film under investigation.

The direction cosines ϕ are defined in Eq. (7.10) for the (10.0) and $(1\bar{2}.0)$ rotation planes, respectively. The resulting cubic crystal field splitting between the A and B lattice sites is visible in the simulations of Figs. 7.21 and 7.22; however, no difference between ESR spectra recorded in the two rotation planes was observed experimentally (not shown). From the analytical line positions of Eq. (7.15), the maximum splitting due to the cubic crystal field occurs at $\theta = 60^\circ$ for the $|\pm 3/2, m_i\rangle \leftrightarrow |\pm 1/2, m_i\rangle$ transition, and is of the order of 6 G for $|\tilde{a}| < 10$ G $\times\, g\mu_B$, which can be assumed in the nitride epitaxial films in analogy to ZnO.[160] Therefore, it is not unexpected to find no experimental difference between the (10.0) and $(1\bar{2}.0)$ rotation planes. The splitting between the A and B lattice sites cannot explain the splitting of the central fine-structure group indicated in the simulations of Refs. 135, 136, 137.

The asymmetry of the resonance pattern of AlN:Mn^{2+} (Fig. 7.22) is much more pro-

nounced than that of the resonance pattern of GaN:Mn^{2+} (Fig. 7.21). This is a consequence of the much larger spin Hamiltonian parameter D from Eq. (7.12). Analytically, Eq. (7.15) provides a good approximation to the ESR spectra of GaN:Mn^{2+}, as $\frac{|D|}{h\nu} \approx 7\%$ there. The competition between the Zeeman- and fine structure interactions is much stronger in AlN:Mn^{2+}, where $\frac{|D|}{h\nu} \approx 20\%$, and the transitions $|-5/2\rangle \leftrightarrow |-3/2\rangle$ occur almost at zero magnetic field. At intermediate orientations, the quantization axis is therefore tilted away from the direction of $\vec{B}$ by the influence of the internal axial crystal field. Therefore, the hyperfine shifts $\Delta b_{m_s,m_i \leftrightarrow m_s-1,m_i}$ of the allowed transitions in Eq. (7.13) have to be corrected by higher order terms in A and mixing cross-terms with D, as calculated to second order in Refs. 13 and 161 for the center group $|+1/2, m_i\rangle \leftrightarrow |-1/2, m_i\rangle$

$$\begin{aligned}\Delta b(\theta)_{1/2,m_i \leftrightarrow -1/2,m_i} \quad = \quad & -\frac{A}{g\mu_B}\Big\{ m_i + \frac{A}{2h\nu}\left(\tfrac{35}{4} - m_i^2\right) \\ & + \left(\frac{D}{h\nu}\right)^2 \left[36\sin^2(2\theta) - 2\sin^4(\theta)\right]\ m_i \Big\} \quad . \qquad (7.16)\end{aligned}$$

Note, that for $D \approx \frac{1}{10}\, h\nu$, as it is the case in these X-band experiments, the magnitude of the third term is almost half of that of the first, so that this correction is indeed required for the analytical field positions.

An even more pronounced effect of the off-diagonal terms $\mathcal{I}_x\mathcal{S}_x + \mathcal{I}_y\mathcal{S}_y$ in the spin Hamiltonian is shown in Fig. 7.23, where numerical results for the eigen-energies and the strongest magnetic dipole transitions for AlN:Mn^{2+} at $\theta = 60°$ are shown. Compared to Fig. 7.13, multiple level repulsions and an increased number of hyperfine transitions are observed. As at $\theta > 0°$ the selection rules for the forbidden magnetic dipole transitions are modified due to the mixing of electronic and nuclear quantum numbers, the intensity of the "forbidden" $\Delta m_i \neq 0$ transitions eventually becomes even larger than that of the formerly "allowed" transitions with $\Delta m_i = 0$. According to Refs. 161 and 167, the ratio between the intensity I_f of the first "forbidden" transition $|m_s, m_i\rangle \leftrightarrow |m_s - 1, m_i \pm 1\rangle$ and I_a of the "allowed" transition $|m_s, m_i\rangle \leftrightarrow |m_s - 1, m_i\rangle$ is given to second-order perturbation theory by

$$I_f/I_a \approx \left[\frac{3}{4}\frac{D}{h\nu}\sin(2\theta)\left(1 + \frac{35}{12\ m_s(m_s-1)}\right)\right]^2 \cdot (35/4 - m_i^2 + m_i) \quad . \qquad (7.17)$$

Comparison with the exact numerical intensities for GaN in Fig. 7.24 shows that although qualitatively similar, this analytical result is insufficient to describe the central hyperfine group of Mn^{2+} in GaN correctly at tilt angels of $\theta \approx 10°$, at which the "forbidden" transitions with $\Delta m_i = \pm 1$ (dashed lines in Fig. 7.24) have grown strongly at the expense of the "allowed" transitions (full lines). At larger tilt angles, only the outmost "allowed" transitions $|+1/2, \pm 5/2\rangle \leftrightarrow |-1/2, \pm 5/2\rangle$ remain visible, and many "forbidden" transitions with $|\Delta m_i| > 1$ occur at intermediate angles. Note that the resonance positions for GaN in Fig. 7.24 have not been assumed fixed as in the simplified calculation of Ref. 167.

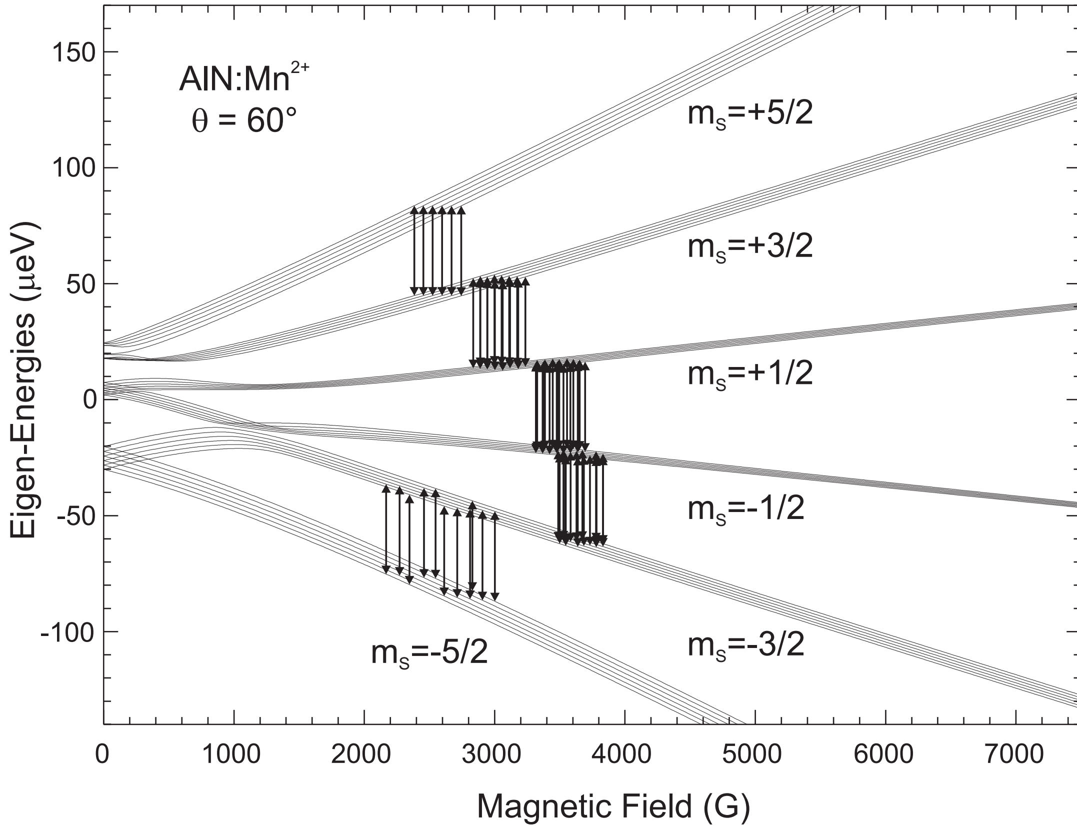

Figure 7.23: Breit-Rabi Diagram for AlN:Mn^{2+} with the magnetic field oriented at $\theta = 60°$ with respect to the *c*-axis of the film and otherwise identical parameters as in Fig. 7.13. At this orientation, the spin quantization axis results from a competition between the Zeeman and the axial fine-structure interaction. The arrows indicate only the strongest magnetic dipole transitions. As shown in Fig. 7.22, additional weak half-field transitions with $\Delta m_s > 1$ are expected at this orientation.

However, in order to reduce the number of 36 possible traces, the outer and inner transitions for each Δm_i were averaged to a single line. In the case of AlN, the axial crystal field is tilting the quantization axes even stronger away from the magnetic-field orientation. Therefore, the intensities of the "forbidden" transitions with $\Delta m_i = \pm 1$ increase even more rapidly compared to GaN upon rotation of the sample with respect to the magnetic field and exceed the "allowed transitions" already at $\theta \approx 5°$. The numerical results for the central fine-structure group of both GaN and AlN are shown as gray-scale maps in Figs. 7.25 and 7.26. It can be seen from these figures that in contrast to the simulations in Refs. 135, 136, 137, the forbidden lines do not split gradually from specific allowed lines at $\theta = 0°$, but rather vanish at magnetic field positions in between those of the allowed transitions.

In GaN, the experimental linewidth is too large to spectrally resolve both "allowed" and "forbidden" transitions. Rather, the increased number of lines tend to interfere with

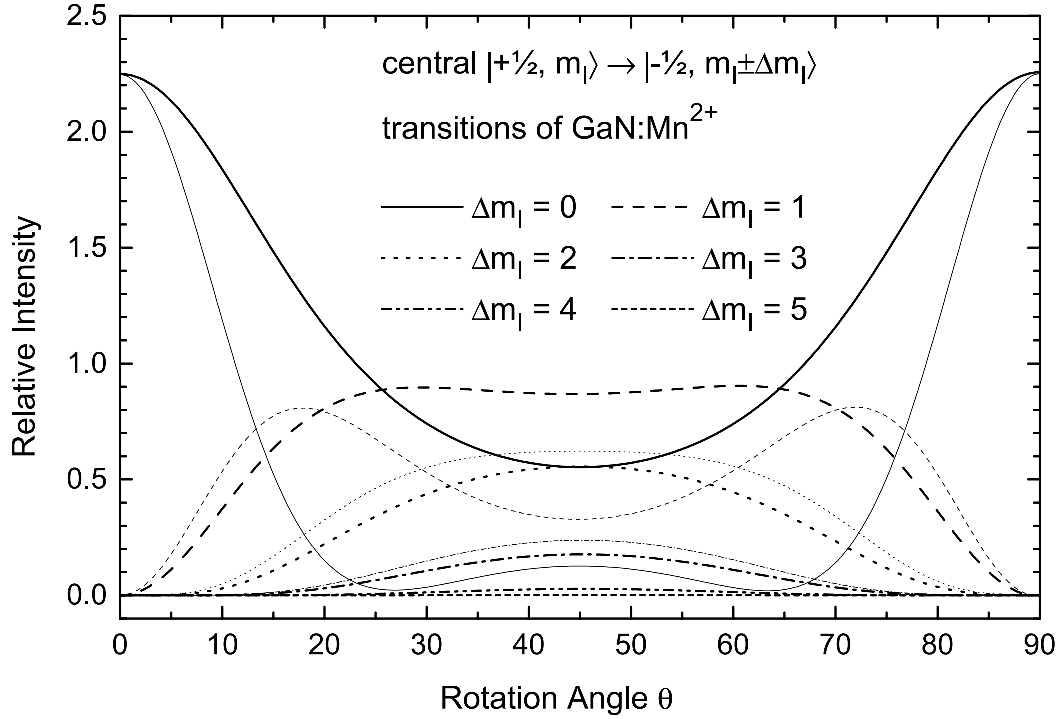

Figure 7.24: Angular variation of the $|+1/2, m_i\rangle \leftrightarrow |-1/2, m_i \pm \Delta m_i\rangle$ transition intensities for GaN:Mn^{2+} at a fixed X-band microwave frequency. In order to reduce the number of 36 possible traces, both the two "allowed" and four "forbidden" outer transitions $|\pm 1/2, \pm 5/2\rangle \leftrightarrow |\mp 1/2, \pm 5/2 \mp \Delta m_i\rangle$ were averaged to a single line. Similarly, the intensities of the remaining inner transitions have been averaged and are shown with a second thinner line of the same type for each $|\Delta m_i|$.

each other, as can be seen in Fig. 7.25, where the inner resonances cancel out at $\theta \approx 10°$. It is also evident that at $\theta \approx 20°$ five new resonances appear between the two outmost resonance fields, which correspond to the outer of the six "allowed" transitions at $\theta \approx 0°$. In ZnO:Mn^{2+}, the spectral resolution was limited by similarly broad lines,[160] until high-quality and strain-free crystals made it possible to separate the extremely large number of narrow individual resonance positions shown in Fig. 7.14.[169] In GaN or AlN, this might be impossible due to ligand hyperfine coupling with the highly abundant nitrogen isotope ^{14}N with $I = 1$, while the natural abundance of the only oxygen isotope ^{17}O with nuclear spin is very low in ZnO.

Due to somewhat smaller linewidths in the central transition group in AlN, some "forbidden" transitions with $\Delta m_i = \pm 1$ are resolved for small misorientations $\theta < 5°$ (Fig. 7.26). To second order perturbation theory,[161] the doublets $|+1/2, m_i\rangle \leftrightarrow |-$

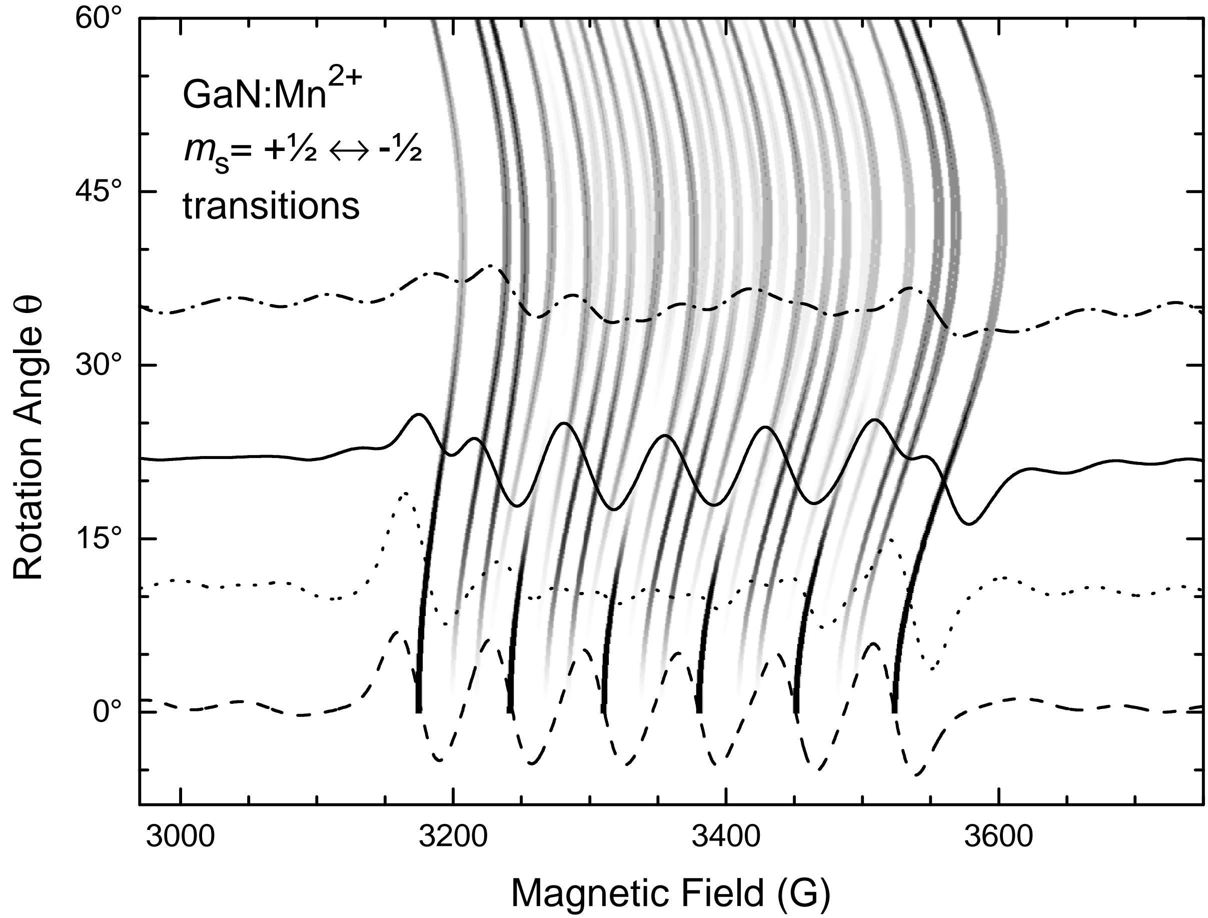

Figure 7.25: Magnified view of the inner fine-structure group $|+1/2, m_i\rangle \leftrightarrow |-1/2, m_i \pm \Delta m_i\rangle$ of GaN:Mn^{2+}. In the ESR spectra, the "forbidden" hyperfine satellites are interfering destructively with the "allowed" transitions at tilt angles around $\theta \approx 10°$. The gray-scale map shows the transition intensities of the central fine-structure group obtained from the exact numerical diagonalization without the outer groups, which are broadened experimentally because of the variation of the fine-structure parameters. A large number of resonances at intermediate angles is caused by the appearance of "forbidden" fine-structure transitions, rather than by axial or cubic crystal field splittings of the inequivalent wurtzite lattice sites.

$1/2, m_i - 1\rangle$ and $|+1/2, m_i - 1\rangle \leftrightarrow |-1/2, m_i\rangle$ are split by

$$\begin{aligned}
&\Delta b(\theta)_{1/2,m_i\leftrightarrow -1/2,m_i-1} - \Delta b(\theta)_{1/2,m_i-1\leftrightarrow -1/2,m_i} \\
&\quad = 17A^2/(2g\mu_B h\nu) + 2h\nu(g_n\mu_n/g\mu_B)/g\mu_B \\
&\qquad -25A^3/[g\mu_B(h\nu)^2]\cdot(m_i - \tfrac{1}{2}) \\
&\qquad +8DA^2/[g\mu_B(h\nu)^2]\cdot(m_i - 1/2)\cdot(3\cos^2\theta - 1) \\
&\qquad -2P/g\mu_B(m_i - \tfrac{1}{2})\cdot(3\cos^2\theta - 1) \quad . \qquad (7.18)
\end{aligned}$$

Each of the listed terms contributes shifts of several G to the forbidden transition doublet splitting and therefore cannot be neglected in the calculation of these transition fields.

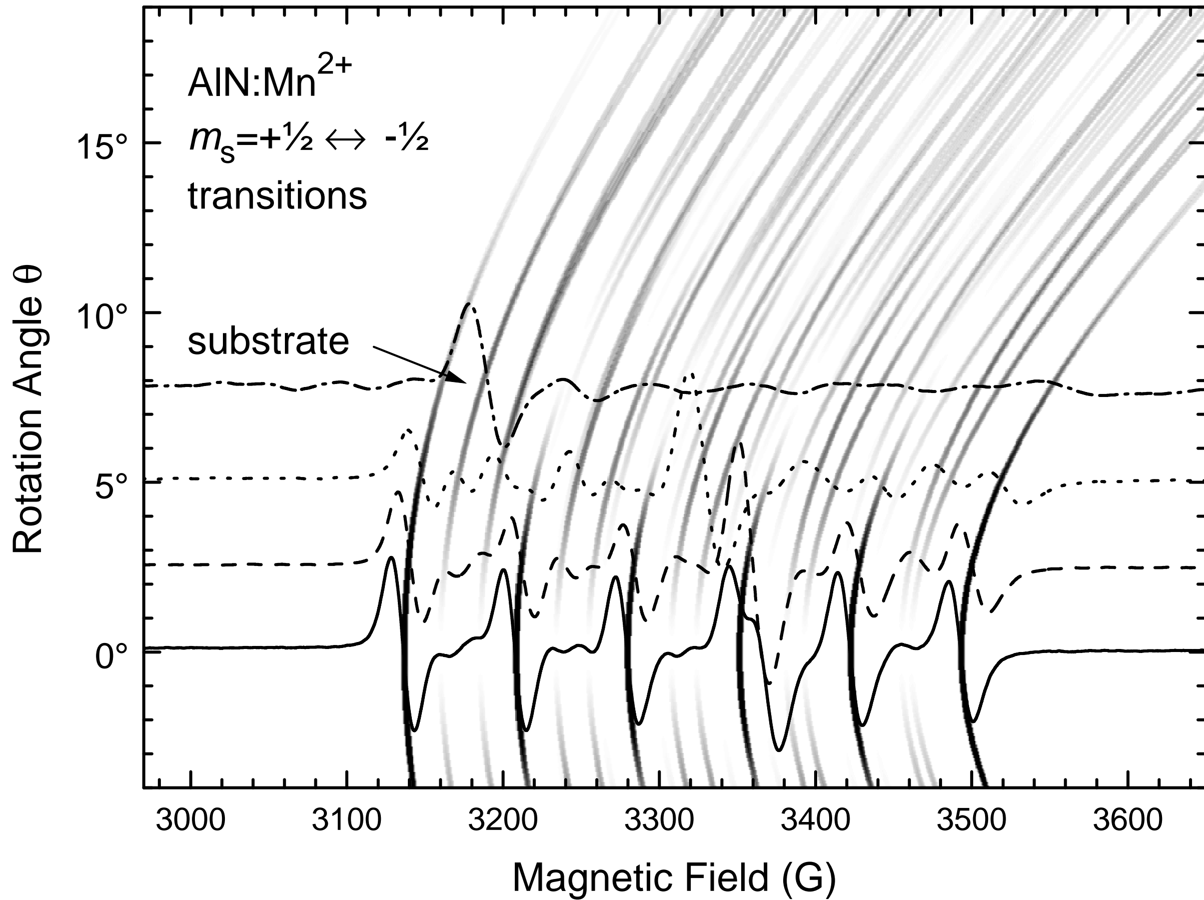

Figure 7.26: Magnified view of the inner fine-structure group $|+1/2, m_i\rangle \leftrightarrow |-1/2, m_i \pm \Delta m_i\rangle$ of AlN:Mn^{2+}. In the ESR spectra, the "forbidden" hyperfine satellites interfere destructively with the "allowed" transitions at tilt angles around $\theta \approx 5°$. The "forbidden" lines are small, but still visible at the orientation closest to $\theta = 0°$. The distinct line moving to lower magnetic fields with increasing tilt angle θ can be attributed to impurities in the sapphire substrate.

The observed spacing of the five pairs of transitions decreases from 30 G on the low-field side to overlapping lines on the high-field side (Fig. 7.26). This is consistent with the ratio $(g_n\mu_n)/(g\mu_B) \approx 0.000\,377$ and the reported nuclear quadrupolar moment of ^{55}Mn, which is $P = 0.17$ G $\times\, g\mu_B$ in ZnO.[160, 169]

In summary, no indication of interactions between adjacent centers was found at a doping level around 10^{20} cm^{-3}. The effective spin Hamiltonian for isolated Mn^{2+} centers sufficiently describes all features of the observed ESR spectra in GaN and AlN at an arbitrary orientation. In contrast, exchange narrowing is observed in the ESR spectra of GaAs:Mn^{2+} at doping concentrations around 0.1% indicating the wave function overlap required for spintronic devices.[170]

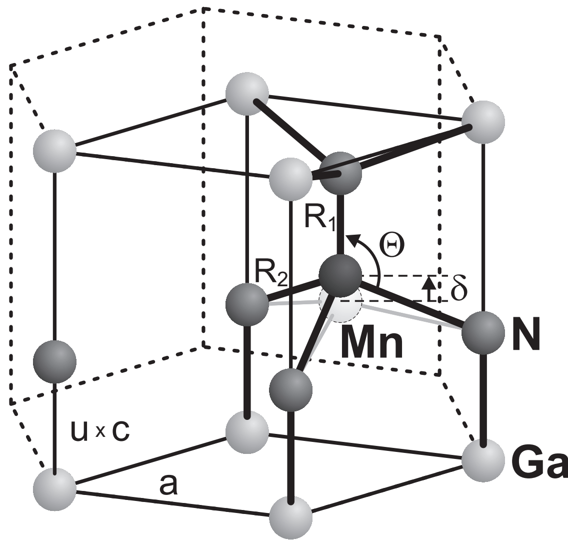

Figure 7.27: Unit cell of the hexagonal lattice of GaN with one Mn atom substituting a Ga cation. The strong axial crystal fields observed by ESR indicate a displacement δ of Mn^{2+} along the c-axis of 0.085 Å, which is as large as 4% of the Ga-N bond length of 1.95 Å an even larger displacement of 0.13 Å in AlN:Mn^{2+}.

7.3.4 Discussion of the ESR parameters

Manganese is expected to occupy the substitutional cation site in GaN and AlN,[118] as shown schematically in Figs. 7.3. The geometry of the surrounding ligands is shown in Fig. 7.27. Other lattice sites have been reported for Mn in group III arsenides[171] and will be discussed further below. On the substitutional site, partly ionic and partly covalent bonds to the four nitrogen neighbors bind three electrons of the free Mn [Ar]$3d^5 4s^2$ configuration, resulting in the deep neutral acceptor state Mn^{3+} (A^0), e.g., in GaP,[172] or the antiferromagnetically coupled shallow Mn^{2+}-hole complex in GaAs:Mn,[134] as introduced in Sec. 7.1. Due to the Jahn-Teller instability of its orbital ground state, large distortions are expected for Mn^{3+} similar to Cr^{2+}.[172, 173] Because there is no unperturbed Kramers doublet in the $S = 2$ ground state manifold of these oxidation states, the electron spin resonance transitions are possibly shifted outside the range of X-band spectrometers.[173] Additionally, the multiple lines are possibly broadened inhomogeneously by strain effects, so that the spin resonance signature of Mn^{3+} has been observed in a few III–V semiconductors only, most notably GaP.[172] In this work, the neutral Mn^{3+} oxidation state was reduced to the negatively charged acceptor Mn^{2+} (A^-) by the presence of residual donors in GaN:Mn grown at low growth temperatures, or by the Si donors in the GaN:Mn:Si samples.[174]

Theoretical predictions of the parameters g and D of the spin Hamiltonian need to consider spin-orbit coupling in perturbation theory up to very high orders.[22] Without the symmetry-breaking presence of nearby ionic charges, the expected deviations of g from the free-electron value $g_0 = 2.0023$ are small. For substitutional Mn^{2+}, the g-factor is typically somewhat reduced from g_0 because of spin-orbit coupling due to the admixture of excited states and due to small covalent contributions, in agreement with our observations.[13, 22]

Various mechanisms have been suggested to contribute to the observed spin Hamiltonian parameter D. The dominant contributions are crystal fields causing spin-orbit interaction in higher orders, and intermixing from excited Mn^{2+} configurations.(148, 175) On the substitutional sites, both contributions are of the order of 10 μeV in magnitude, but of opposite sign. In contrast, the magnitude of D typically exceeds the Zeeman splitting by far for defect complexes.(148, 176) In the group III nitrides, the axial crystal field is probably enhanced by the different bond lengths and the asymmetric charge compensation of Mn^{2+} along the c lattice direction.(177) However, theoretical estimates of the zero-field splitting D based on higher-order perturbation formulas of the spin-orbit mechanism turned out to be one order of magnitude too small in GaN.(22) As, at the same time, D is at least one order of magnitude smaller than expected for a defect complex, it was concluded from the experimental result in Refs. 135, 136, 137 for bulk GaN:Mn crystals, that the Mn^{2+} ion does not occupy the exact Ga^{3+} site, but is displaced by δ towards the N ligand along the c lattice direction,(22) as shown in Fig. 7.27. Unfortunately, some equations appear inconsistent in the printed version of Ref. 22. Correcting the obvious typographic errors, the axial crystal field parameter due to spin-orbit coupling in the weak-field scheme(148) is given by

$$D_{\text{weak}} \approx \frac{-3\zeta_d^2 B_{20}^2 - 63\zeta_d^3 B_{20}}{70\ P^2 D'} + \frac{-10\zeta_d^2 B_{40}^2 + 7\zeta_d^2 B_{43}^2}{126\ P^2 G} \tag{7.19}$$

with the trigonal crystal field parameters

$$\begin{aligned} B_{20} &\approx \bar{A}_2 \Big[\, 2\left(\frac{R_0}{R_1}\right)^{t_2} + 3\ (3\cos^2\Theta - 1)\left(\frac{R_0}{R_2}\right)^{t_2}\Big], \\ B_{40} &\approx \bar{A}_4 \Big[\, 8\left(\frac{R_0}{R_1}\right)^{t_4} + 3\ (35\cos^4\Theta - 30\cos^2\Theta + 3)\left(\frac{R_0}{R_2}\right)^{t_4}\Big], \\ B_{43} &\approx -6\sqrt{35}\ \bar{A}_4 \sin^3\Theta\cos\Theta\left(\frac{R_0}{R_2}\right)^{t_4} \quad , \end{aligned} \tag{7.20}$$

the spin-orbit coupling coefficient $\zeta_d \approx 317$ cm^{-1}, $P \approx 25.3 \times 10^3$ cm^{-1}, $D' \approx 26.9 \times 10^3$ cm^{-1}, $G \approx 21.9 \times 10^3$ cm^{-1}, $\bar{A}_2 \approx 10.5 \times 10^3$ cm^{-1}, and $\bar{A}_4 \approx 878$ cm^{-1}, which can be obtained from the Racah parameters estimated for Mn^{2+} in GaN in Refs. 13 and 22 at the reference distance $R_0 = \frac{1}{4}R_1(0) + \frac{3}{4}\ R_2(0)$, and with the exponents $t_2 \approx 3$ and $t_4 \approx 5$. The distance $R_1(\delta)$ from the Mn^{2+} ion to the N neighbors along c and the distances $R_2(\delta)$ to the three other neighbors oriented at $\Theta(\delta)$ from the Mn site are given by

$$\begin{aligned} R_1(\delta) &= u\ c - \delta, \\ R_2(\delta) &= \sqrt{a^2/3 + [c(u-1/2) - \delta]^2}, \\ \Theta(\delta) &= \arccos\frac{c(u-1/2) - \delta}{R_2(\delta)} \quad , \end{aligned} \tag{7.21}$$

with the u-parameter $u_{\text{GaN}} \approx 0.377$(178) as indicated in Fig. 7.27, and the lattice constants $c_{\text{GaN}} = (1+\varepsilon_c)$ 5.1850 Å, and $a_{\text{GaN}} = (1+\varepsilon_a)$ 3.1878 Å (see Fig. 7.27).(151) As a_{GaN} and

c_{GaN} were measured by x-ray diffraction at room temperature, both lattice parameters have been reduced by approximately 0.06% to account for the cooling down to 6 K,[179] at which the ESR parameters were evaluated. A more precise approach for the calculation of the lattice parameters of bulk GaN at low temperatures would need to include the anisotropy of about 13% of the thermal expansion coefficients perpendicular and parallel to the c-axis of GaN, which are $\alpha_{\mathrm{GaN},\perp} \approx 4.3\times10^{-6}$/K and $\alpha_{\mathrm{GaN},||} \approx 3.8\times10^{-6}$/K at room temperature.[179, 180, 181] The in-plane thermal expansion coefficient of GaN films grown on sapphire substrates is effectively determined by the thermal expansion coefficient of the sapphire substrate $\alpha_{\mathrm{Al_2O_3},\perp} \approx 5.4 \times 10^{-6}$/K, which strongly increases the effective anisotropy of the thermal expansion coefficients. As a consequence of this external in-plane compression, the effective out-of-plane thermal expansion coefficient is reduced even further, so that the anisotropy of the thermal expansion can be expected to be as large as 40%. This would require additional corrections around 0.02% of ε_a and ε_c at low temperatures for all investigated samples, in contrast to the bulk samples of Refs. 135, 136, 137.

With the parameters discussed in Ref. 22, the reported displacement $\delta = 0.07$ Å can be reproduced only, if the variation of $\Theta(\delta)$ is ignored. Using the $\Theta(\delta)$-dependence of Eq. (7.21), the assumed crystal field parameters of Ref. 22, the u-parameter of Ref. 178, and the measured lattice constants c_{GaN} and a_{GaN}, the observed spin Hamiltonian parameter D is consistent with a displacement of $\delta_{\mathrm{GaN}} = +0.085$ Å from the Ga site. For AlN:Mn^{2+}, a displacement $\delta_{\mathrm{AlN}} = +0.13$ Å would be suggested by the measured lattice constants with $u_{\mathrm{AlN}} \approx 0.382$[178] and the identical set of crystal field parameters, which were estimated based on the optical properties of AlN:Mn^{2+} and on the similarity of the Mn-N bond in GaN:Mn and AlN:Mn. The approximately quadratic dependence of the $D(\delta)$ predicted from Eq. (7.19) is shown in Fig. 7.28, where the experimental values of D are indicated with horizontal lines. Apparently, these could also be obtained with $\delta_{\mathrm{GaN}} = -0.15$ Å and $\delta_{\mathrm{AlN}} = -0.22$ Å. Such negative displacements are, however, inconsistent with the slope $dD_{\mathrm{GaN}}/d\varepsilon_a$ observed for strained GaN films, as discussed below. Certainly, the accuracy of the deduced displacements is limited by the various assumptions that are needed for the evaluation of Eq. (7.19). It is impossible to verify these assumptions and the validity of the crystal field approach with a single experimental crystal field parameter, because the displacements δ are unknown *a priori*, and were chosen to fit this experimental parameter. Also, the good agreement of the weak- and strong-field schemes in Ref. 22 merely supports the validity of the perturbation approximation. It does not verify the assumed parameters and the dominant influence of the spin-orbit coupling over the other contributing mechanisms.

However, this can be verified independently with the help of ESR measurements on strained GaN films, for which the lattice distortions ε_a and ε_c are known. Similar experiments have been performed and discussed previously for Mn^{2+} in some other host

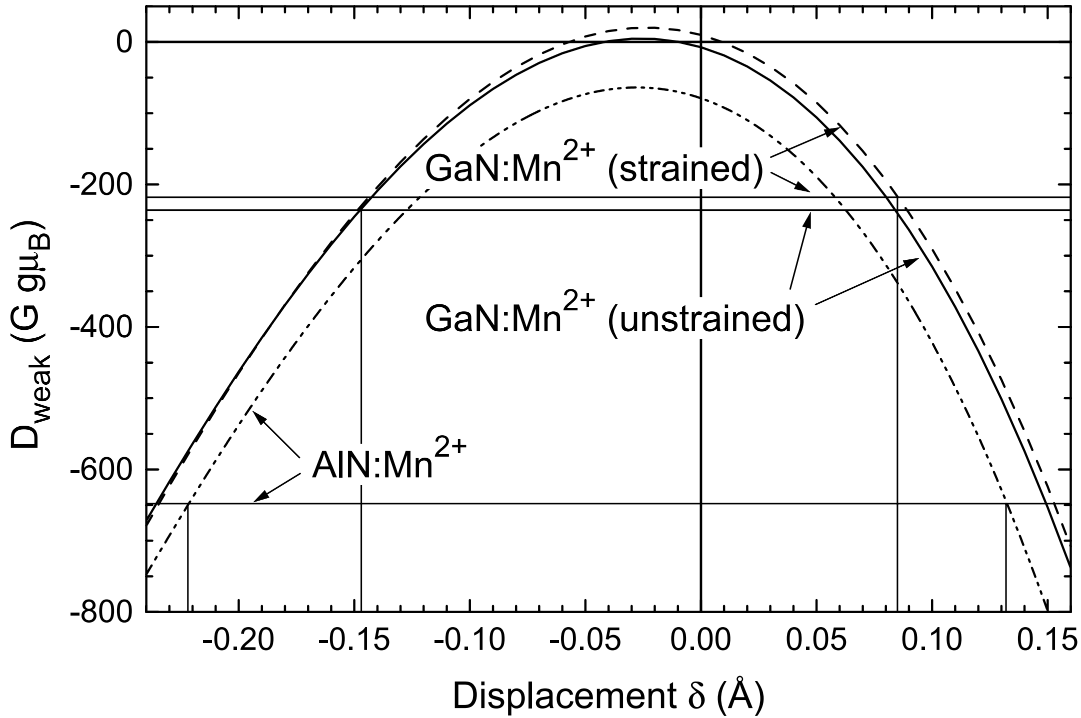

Figure 7.28: Axial crystal field parameters D_{weak} predicted from the weak-field scheme as a function of the displacement δ of Mn^{2+} from the substitutional Ga sites in bulk GaN:Mn^{2+} and AlN:Mn^{2+}. The measured values of $D_{\mathrm{GaN}} = -236$ G$\times g\mu_B$ and $D_{\mathrm{AlN}} = -648$ G$\times g\mu_B$ indicated by the horizontal lines would be consistent with $\delta_{\mathrm{GaN}} = +0.085$ Å and $\delta_{\mathrm{AlN}} = +0.13$ Å, but also with somewhat larger negative displacements. However, the experimentally observed strain dependence is more consistent with the positive displacement δ for GaN:Mn^{2+}.

crystals.[148, 175, 182] ESR spectra obtained on several of our GaN:Mn^{2+} and GaNMn^{2+}:Si films are shown in Fig. 7.29. Although all spectra are appear similar at first sight, a systematic narrowing is observed from the bottom spectra to the top. The axial crystal field parameters D evaluated from these spectra are summarized in Fig. 7.30. As discussed before, a variation of the strain is caused in these samples by the heteroepitaxy and the high doping concentrations. The inset of Fig. 7.30 shows that the ratio of the strains in these films is $\varepsilon_c/\varepsilon_a = -0.6$, as expected.[151]

Also shown at the position of the bulk lattice constant of GaN is the axial crystal field parameter measured on a bulk GaN:Mn^{2+} crystal in Refs. 135, 136, 137. The ESR amplitude of the fine-structure satellites of this bulk sample is suppressed similar to the fluctuations responsible for the broadening shown in Fig. 7.20. Therefore, fluctuations of D and the presence of residual strain must be expected also in this bulk crystal. The reevaluation of the published data of Refs. 135, 136, 137 turns out to be consistent with a value of $|D|$ below 250 G$\times g\mu_B$ as well, which would give a better agreement with the fine-structure parameters determined in this work. The dashed lines in Fig. 7.30 were

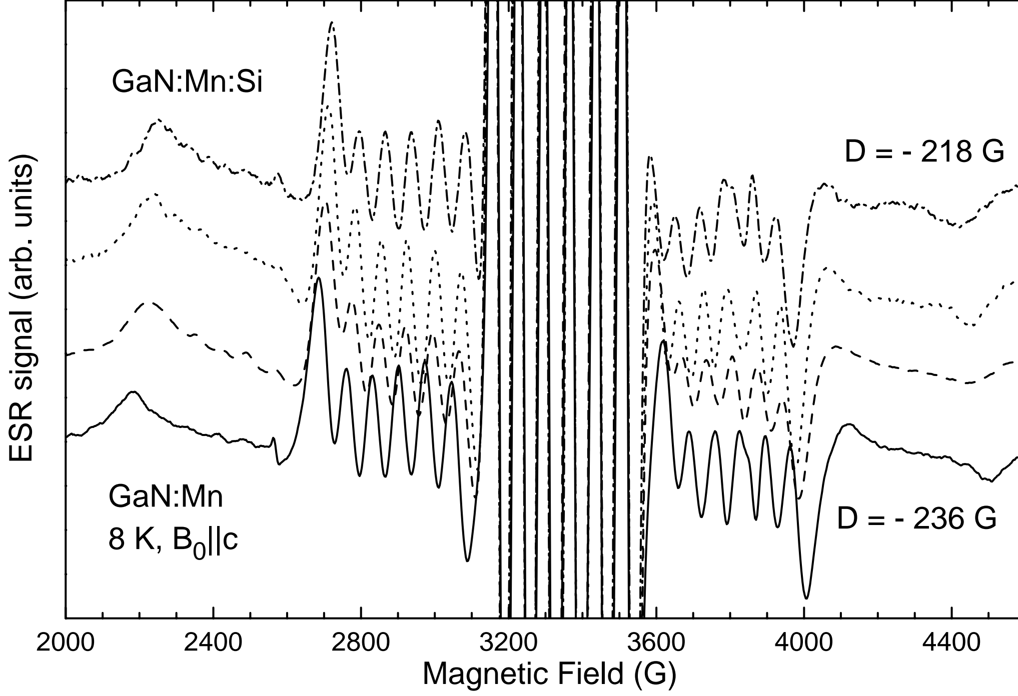

Figure 7.29: ESR spectra for $\vec{B}_0||c$ of the GaN:Mn sample grown at $T_s = 690°$C and of several GaN:Mn^{2+}:Si samples grown at $T_s = 820°$C with larger strain. The splitting between the outer and middle transition groups on the left and right hand sides becomes narrower from the spectra shown at the bottom to those at the top. Evaluation of D according to Eq. (7.12) results in values of D_{GaN} from -218 G $\times\, g\mu_B$ to -236 G $\times\, g\mu_B$, in correlation with the strain observed by XRD.

calculated according to Eq. 7.19 with $\delta = 0.084$, 0.085, and 0.086 Å, and $\varepsilon_c = -0.6\ \varepsilon_a$. The middle line corresponds to

$$D(\delta \approx +0.085\ \text{Å},\ \varepsilon_c \approx -0.6\ \varepsilon_a) \approx (-240 - 1.0 \times 10^4\ \varepsilon_a)\text{G} \times g\mu_B \quad , \qquad (7.22)$$

without the assumption of any additional free parameters. The first-order dependence of $D(\delta, c, a, u)$ at $\delta = +0.085$ Å, $\delta = 0.0$ Å, and $\delta = -0.15$ Å is summarized in Tab. 7.5. For the opposite displacement of $\delta_{\mathrm{GaN}} = -0.15$ Å, the slope $dD/d\varepsilon_a$ would be six times smaller and therefore inconsistent with the experimental data. The quantitative agreement of Eq. (7.22) with the measured data convincingly supports the validity of the superposition model for the spin-orbit coupling of Ref. 22. Nonlinear contributions to $D(\varepsilon_a)$ would be expected from covalent contributions to the spin-orbit coupling,[(184)] or from strain effects on δ and u, which were assumed as constants here.

An overview of recent results for the isotropic hyperfine splitting A_{GaN} calculated with the Green's function method is given in Ref. 31. This splitting is mostly caused indirectly

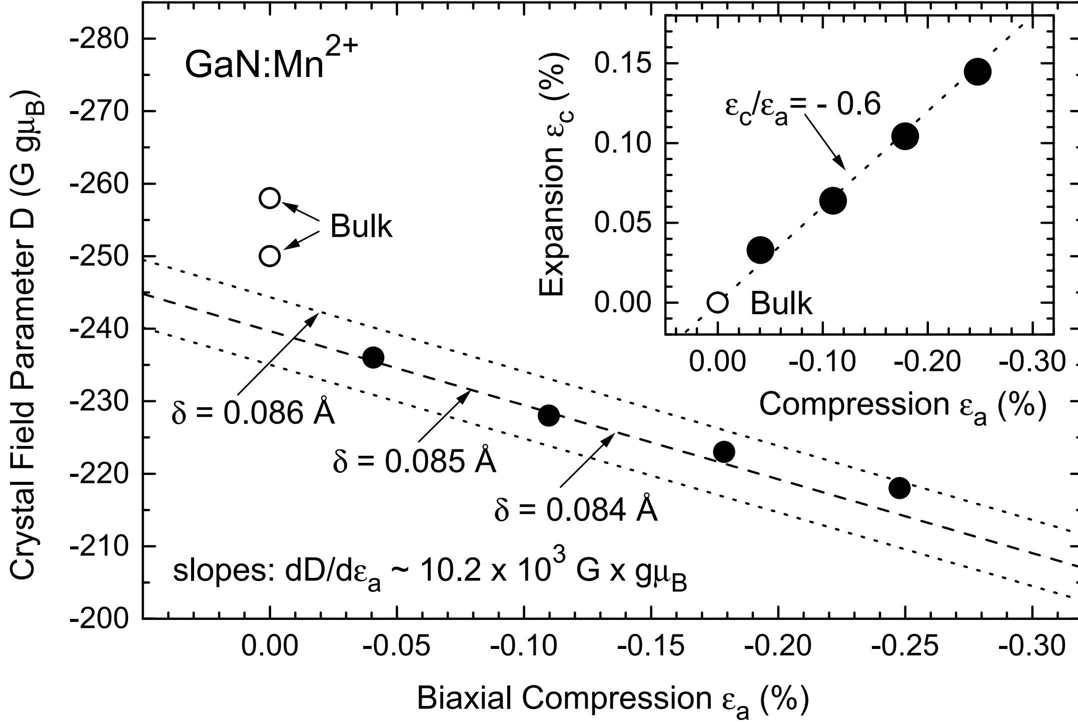

Figure 7.30: The inset shows the variation of the lattice constants of several GaN:Mn and GaN:Mn:Si samples measured by reciprocal space maps of the asymmetric (20.5) reflex as shown in Fig. 7.8. The linear dependence between the relative changes $\varepsilon_c/\varepsilon_a = -0.6$ corresponds to an effective Poisson ratio $\nu = 0.23$.[(151)] The results obtained for bulk GaN in Refs. 135, 136, 137 and evaluated from the data of Ref. 183 are included with the bulk lattice parameters. The dashed and dotted lines are calculated with Eq. (7.19) and the parameters of Ref. 22 without additional free parameters. The good agreement with the experimental data supports the validity of the superposition model for the spin-orbit coupling.

δ_0 (Å)	D_0 (G$\times g\mu_B$)	$\partial D/\partial\varepsilon_c$ (G$\times g\mu_B$)	$\partial D/\partial\varepsilon_a$ (G$\times g\mu_B$)	$\partial D/\partial u$ (G$\times g\mu_B$)	$\partial D/\partial\delta$ (G$\times g\mu_B$/Å)
0.085	-240	7.4×10^3	-5.8×10^3	23×10^3	-4.7×10^3
0.00	-7.1	4.8×10^3	-4.7×10^3	5.0×10^3	-1.0×10^3
-0.15	-245	3.0×10^3	0.12×10^3	-19×10^3	$+3.8 \times 10^3$

Table 7.5: First order-dependence of the axial crystal field parameter $D(\varepsilon_c, \varepsilon_a, u, \delta)$ on the lattice parameters according to Eq. (7.19). At $\delta = 0.085$ Å, the combination of biaxial compression ε_a and axial expansion ε_c result in $dD/d\varepsilon_a \approx -10 \times 10^3$ G $\times\, g\mu_B$, as observed experimentally (see Fig. 7.30). The model is not restricted to a constant displacement δ during the deformation of the crystal. One might e.g. consider a linear variation $\partial\delta/\delta \propto \partial a/a = \partial\varepsilon_a$ during the deformation of the lattice. However, the expected additional contribution to $dD/d\varepsilon_a$ would be of the order of $\partial D \times (\partial\delta/\delta)^{-1} \approx -0.4 \times 10^3$ G $\times\, g\mu_B$ and therefore negligible compared to the direct influence from the deformation.

	χ_l (eV)	$p(\chi_l)$ (%)	A (G$\times g\mu_B$)	D (G$\times g\mu_B$)	g	Reference
GaAs (zb.)	2.0	23	-56	$(< 2\ )$	2.004	170, 185
ZnS (zb.)	2.6	20	-68	–	2.003	13, 186
ZnS (wz.)	2.6	20	-70	-113	2.002	186
GaN (wz.) bulk	3.0	17	±75	±257	1.999	135, 136, 137
relaxed film	3.0	17	-69	-236	1.999	this work
strained film	3.0	17	-69	-218	1.999	this work
AlN (wz.)	3.0	17	-69	-648	2.000	this work
ZnO (wz.)	3.5	14	-79	-253	2.001	160, 169, 187

Table 7.6: The chemical trend of the isotropic hyperfine constant A is related to the relative electronegativities of the ligands χ_l and the Mn ions $\chi_{\mathrm{Mn}} \approx 1.5$ eV and to Pauling's covalency parameter $p(\chi_l)$ for the nearest neighbors of the Mn atoms. The axial crystal field is given for the wurtzite materials and for strained GaMnAs, with the conversion factors $1\ \mathrm{G} \times g\mu_B = 0.934 \times 10^{-4}\ \mathrm{cm}^{-1} \times hc = 2.80\ \mathrm{MHz} \times h = 11.6$ neV. The values listed above for bulk GaN are those of Table 1 of Ref. 135. (The conversion factor was possibly omitted in the evaluation of the hyperfine splitting $|A_{\mathrm{GaN}}| = 75\ \mathrm{G} \times g\mu_B = 70 \times 10^{-4}\ \mathrm{cm}^{-1} \times hc$ of Refs. 135, 136, 137, as a splitting of approximately 70 G was discussed in the text and is shown in the experimental data of Ref. 135.)

by a Fermi contact interaction of $3d$-induced s orbital spin polarization at the ^{55}Mn nucleus. In the free Mn^{2+} atom, the total core polarization of the inner $1s$, $2s$, and $3s$ orbitals sums up to about -110 G$\times g\mu_B$,[(171)] generating a local magnetic field opposite to the external quantizing field. The induced negative spin density is partly compensated by a positive $4s$ spin density of about $+90$ G$\times g\mu_B$. In a covalent bond, however, this positive contribution is reduced, as the spins are paired off in the binding $4s4p^3$ hybrid orbitals. Therefore, a lower electronegativity of the surrounding ligands leaves a larger negative overall spin density at the Mn nucleus. This subtle balance can be exploited to estimate the valence-band spin polarization at the Mn site, which might be of special interest for the determination of the exchange constants required for ferromagnetism in diluted magnetic semiconductors. Additionally, delocalization of the $3d$ electrons and direct $4s$ admixture of the order of 1% can reduce the magnitude of A significantly. These contributions seem to be overestimated in the calculations of Ref. 31, where $|A| = 40\ \mathrm{G} \times g\mu_B$ has been predicted for Mn^{2+} in GaN, in contrast to the value of $69\ \mathrm{G} \times g\mu_B$ reported here. The same difference between theory and experiment is found by the authors of Ref. 31 for other transition-metal states.

Alternatively to *ab initio* calculations, the expected hyperfine splitting can be estimated with the help of chemical trends between closely related materials. According to Ref. 171, the electronegativities χ_l (see Table 7.6) of the four ligands and of the Mn

ion $\chi_{\mathrm{Mn}} \approx 1.5$ eV can be used to calculate Pauling's covalency parameter $p(\chi_l)$ of the Mn-ligand bond

$$p(\chi_l) = [1 - 0.16(\chi_l - \chi_{\mathrm{Mn}}) - 0.035(\chi_l - \chi_{\mathrm{Mn}})^2]/4 \quad . \tag{7.23}$$

Selected semiconductor materials with anion electronegativities χ_l close to that of nitrogen are listed in Tab. 7.6, together with the covalency $p(\chi_l)$ of the Mn-anion bond and the hyperfine constants for substitutional Mn^{2+} on the cation site. Obviously, the hyperfine constants for GaN:Mn^{2+} and AlN:Mn^{2+} fit in between the numbers for ZnS and ZnO, as would be expected from the electronegativity of N, which is between those of S and O. Twice as large hyperfine constants have been reported for Mn^{2+} on tetrahedral interstitial lattice sites in GaP and GaAs,(171) which confirms the substitutional nature that was assumed above. With respect to the covalency and hyperfine constants, similarities to Mn in II–VI semiconductors rather than to III–V materials such as GaAs are expected, as long as the neutral Mn^{3+} centers can be reduced to Mn^{2+} by residual donors or Si codoping, as in the samples discussed here.

7.3.5 $\mathbf{Mn^{2+}}$ spin density

From the calibrated ESR amplitudes, absolute $\mathrm{Mn}^{2+}_{\mathrm{Ga}}$ concentrations can be determined with an accuracy of about a factor of two.(188) In some of the samples investigated, the width of individual ESR lines is broder than the hyperfine splitting. Therefore, overlapping of adjacent hyperfine lines has to be taken into account even for the best resolved center group, whose peak-to-peak linewidth ΔB_{pp} varied between 30 and 60 G, without any obvious correlation to the spin density or growth temperature.

Typical X-band ESR spectra of this center group recorded at $T = 10$ K and an incident microwave power of 1 mW are shown in Fig. 7.31. Also included is the ESR spectrum of paramagnetic impurities in the sapphire substrate recorded at higher temperature and lower microwave power. For crystal orientations other than those with the crystalline c axis along the external magnetic field, the sapphire ESR spectrum splits into many characteristic resonances and is thus clearly distinct from the ESR signal of the GaN:Mn films. It is easily saturated with an increase in microwave power because of its longer spin relaxation time and it can therefore be suppressed under the experimental conditions used to record the GaN:Mn ESR spectra shown also in Fig. 7.31. However, it will be prominent in the total magnetization measurements. Simulations of the width, lineshape and amplitude of the prominent center group of transitions were chosen as the most reliable way of evaluating overall spin densities. All results were calibrated with the ESR signal of Si:P,(7) taking into account the ratio of the transition matrix elements

$$r_s = \tfrac{1}{2} g^2 \frac{S(S+1) - m_s(m_s - 1)}{2S + 1} = 3 \tag{7.24}$$

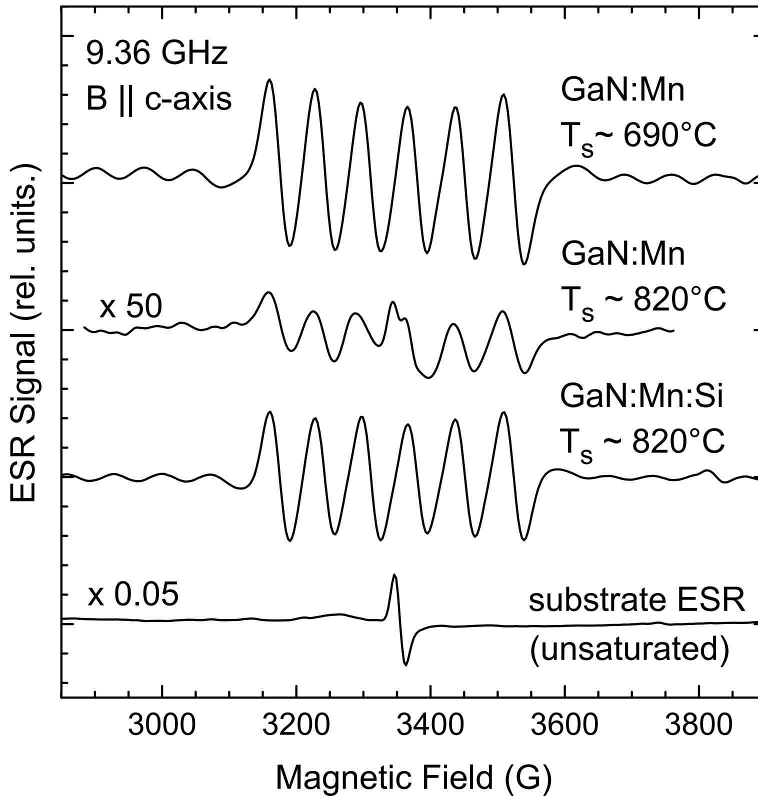

Figure 7.31: The spin density of GaN:Mn grown at $T_s \approx 820°C$ (second spectrum) is almost two orders of magnitude smaller than that of GaN:Mn grown at $T_s \approx 690°C$ (first spectrum) and compensated unintentionally by structural defects. High Mn^{2+} spin densities are also observed in samples grown at $T_s \approx 820°C$, which were compensated intentionally by Si codoping (third spectrum). For comparison, also the ESR signal of the paramagnetic impurities in the sapphire substrate is shown (last spectrum), which was recorded at higher temperature and lower microwave power to avoid microwave saturation. It can be distinguished clearly from the GaN:Mn signal because of its characteristic anisotropy.

for the $S = 5/2$ system under investigation compared to the spin-1/2 system of Si:P,[(188)] and for $m_s = 1/2$ for the center group of transitions. As included in Fig. 7.9 of Sec. 7.2.1 (open symbols), we observed Mn^{2+} spin densities in the range of $10^{18} - 3 \times 10^{19}$ cm^{-3} in our samples.

No signal of Mn oxidation states other than Mn^{2+} was observed by ESR, probably because of excessive broadening due to residual strain. This situation has been discussed previously for the neutral Mn acceptor state in GaP and GaAs.[(139)] The $^6A_1$ orbital singlet of the Mn^{2+} (A^-) ground state is unaffected by crystal fields, whereas the Mn^{3+} (A^0) ground state $^5T_2$ multiplet is subject to Jahn-Teller distortion in tetrahedral crystal fields and, additionally, to trigonal strain in GaN,[(134)] as shown schematically in Fig. 7.32. Because of these distortions, the zero-field splittings typically become as large as several cm^{-1}.[(172)] Note that no central Kramers doublet remains unperturbed for a paramagnetic state with an odd number of eigen-states. Even larger zero field splittings would be expected for displacements of Mn^{3+} from the Ga lattice sites of the order of $\delta \approx +0.085$ Å as discussed for Mn^{2+} in in the context of Fig. 7.30. Indeed, displacements of the order of 3% have been observed for neutral substitutional Mn in GaN:Mn in extended x-ray absorption fine structure (EXAFS) studies.[(189)] Therefore, the resonant transitions are

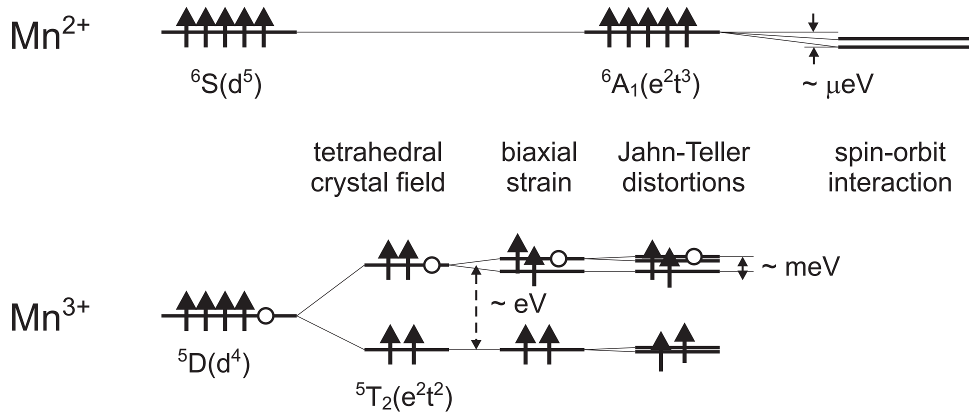

Figure 7.32: One-electron schemes for the ground state splitting of Mn^{2+} and Mn^{3+}. The $^6A_1$ ground state of Mn^{2+} is not affected by tetrahedral crystal fields, trigonal distortions, random strains, and Jahn-Teller distortions because of its lack of angular momentum. Therefore, the Mn^{2+} spin states are only marginally split at zero magnetic field because of second and higher order perturbations via the excited states. In contrast, the $^5T_2$ ground state of free Mn^{3+} ions has nonzero orbital momentum, which is quenched in crystals because of the multiple perturbations. This causes the presence of several excited states not far from the Mn^{3+} ground state, which enhances spin-orbit interactions. Inhomogeneous strains can therefore lead e.g. to large variations of the g-factor and the zero-field splitting D. ESR detection becomes particularly difficult, when the zero field splittings exceeds the Zeeman energy of 40 μeV.

possibly shifted out of the range of an X-band spectrometer or broadened excessively due to residual strain, as shown in Fig. 7.33. Inhomogeneous broadening probably also inhibited the observation of a FMR signal similar to that for the films in Ref. 157 for the film grown at $T_s = 690°C$, for which ferromagnetic minor phases were observed by SQUID measurements. As shown in Fig. 7.9, the total Mn concentration determined by ERD is significantly higher than the Mn^{2+} spin density in non-codoped GaN:Mn, but becomes similar to $[Mn^{2+}]$ within experimental accuracy in codoped GaN:Mn:Si. All further ESR signals found were identified as due to paramagnetic transition-metal impurities in the Al_2O_3 substrate, and no indication for interstitial Mn and Mn-Mn clusters was observed by ESR, although these clusters have been predicted to have lower formation energies than isolated substitutional Mn impurities.[(190)]

7.4 Identification of the Mn^{3+} state

Whereas ESR experiments on Mn^{2+} provide detailed microscopic information about the localized spins, no information can be deduced from ESR about the Mn-bound holes, which are absent in the case of a negatively charged acceptor, as they are either compensated or transferred to the valence band. While total Mn concentrations around 10^{20} cm^{-3} are present in the GaN:Mn samples, as shown in Fig. 7.9, the Mn^{2+} concentration mea-

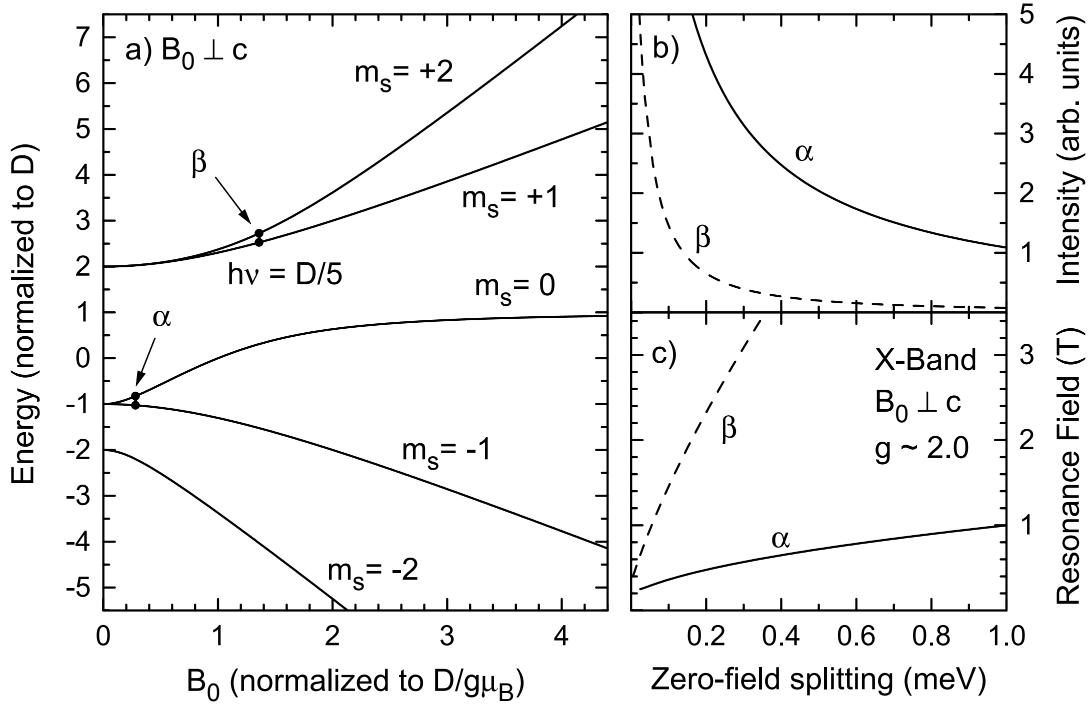

Figure 7.33: (a) Breit-Rabi diagram for the $S = 2$ ground state of Mn^{3+} with a large zero-field splitting D compared to the Zeeman energy $g\mu_B B_0$. The zero-field splitting of d^4 states is typically much larger than the microwave energy,[173] so that only the transitions α and β within the two undisturbed Kramers doublets remain possible, as indicated in (a) for a typical value for Mn^{3+} of $h\nu = D/5$. In contrast, $h\nu \approx 5D$, as observed for AlN:Mn^{2+} is a very large interaction for a $Mn^{2+}(d^5)$ orbital singlet. The transitions α and β are forbidden at most orientations, and have nonzero intensities only for $\theta \approx 90°$. Their intensities for this orientation are shown in (b) assuming $g \approx 2.0$ and X-band microwave frequencies. The corresponding resonance fields are shown in (c). As the resonance fields depend on the magnitude of D for both transitions, broadening on the order of 1000 G would result from relative variations of D on the order of 10%, which makes the detection of ESR impossible.

sured by ESR is below 2×10^{18} cm^{-3}, indicating that less than 2% of the Mn impurities were negatively charged by the capture of an extra residual electron from the GaN host crystal. In contrast, the number of negatively charged Mn^{2+} acceptors is increased to 3×10^{19} cm^{-3} in intentionally codoped GaN:Mn:Si samples with [Mn]≈[Si]≈ 3×10^{19}cm^{-3}, where additional electrons are provided from the shallow Si donors. Within the experimental error of ERD and ESR, the compensation is complete in these samples. Compared to other GaN:Mn samples grown under similar conditions, the Mn^{2+} concentration of the Si-codoped films is increased by almost two orders of magnitude to about 100%, as shown in Fig. 7.9. In the pure GaN:Mn samples, the remaining 98% of the Mn centers are therefore supposed to be in the neutral Mn^{3+} (or Mn^{2+}-h^+) acceptor state, since a higher total concentration of Mn is found in ERD, but at the same time a significantly lower Mn^{2+}

concentration is found in ESR. In samples with lower growth temperatures, more Mn^{2+} is detected in ESR, which can be explained by an increasing number of structural defects that act as compensating donors and convert Mn^{3+} to Mn^{2+} via the charge transfer $Mn^{3+} + D^0 \rightarrow Mn^{2+} + D^+$. This is consistent with Hall-measurements and measurements of the Seebeck coefficient of these samples, and with the n-type conductivity of GaN:Mn samples reported in Refs. 124, 125 and 126.

The neutral Mn acceptor states in pure GaN:Mn films are invisible for X-band ESR experiments. Therefore, optical experiments were used to investigate these states, as discussed in the following sections.

7.4.1 Optical absorption measurements

Figure 7.34 shows room-temperature optical absorption spectra of Mn-doped GaN, GaN:Si, and AlN samples with [Mn]$\approx 10^{20}$ cm^{-3}, measured with photothermal deflection spectroscopy (PDS) in the region of low absorbance, and with transmission and reflection measurements at higher absorbance close to the band gap. Details of these experiments can be found in Ref. 149. The spectrum of the pure GaN:Mn sample shows a characteristic absorption band A with onset $h\nu_A \approx 1.8$ eV, and a peak B around $h\nu_B \approx 1.5$ eV. In the codoped GaN:Mn:Si samples of Fig. 7.34, the only optical absorption feature is the band gap absorption above 3.4 eV. Additional low-temperature transmission measurements of peak B in the pure GaN:Mn samples have recently been performed in the spectral region of 1.37–1.57 eV by A. Hoffmann's group at the Technical University Berlin. Typical results of these measurements are shown in Fig. 7.35. Most interestingly, the FWHM of the absorption peak is reduced to only 3 meV as compared to 200 meV at room temperature. The peak position and linewidths vary significantly between the studied samples, most probably related to variations of the residual strain. A splitting seems to take place in samples grown at temperatures above 800° C. This could either be related to a large strain-induced crystal field splitting, or more likely to a laterally inhomogeneous strain distribution in these samples. Reciprocal space maps of the investigated sample pieces could help to clarify this issue. The main Mn-related absorption features have been reported previously with a lower dynamical range in optical absorption and by deep level optical spectroscopy (DLOS).[128, 191] In these previous studies, the absorption band A, for which the onset was determined as $h\nu_A \approx 2.0$ eV, was tentatively assigned to the emission of an electron to the conduction band. By comparing the transition energy to those of other transition-metal states,[118] the initial gap state for both transitions was assumed to be the Mn^{2+} oxidation state. For the resonant absorption peak B, a zero-phonon line at $h\nu_B \approx 1.42$ eV was resolved at temperatures around 20 K.

In Refs. 128, 191, a zero-phonon line at 1.42 eV was resolved for transition B at lower temperatures with vibrational modes at 20 and 73 meV that are well-described by the mass defect approximation. The broadening at temperatures above 60 K has been

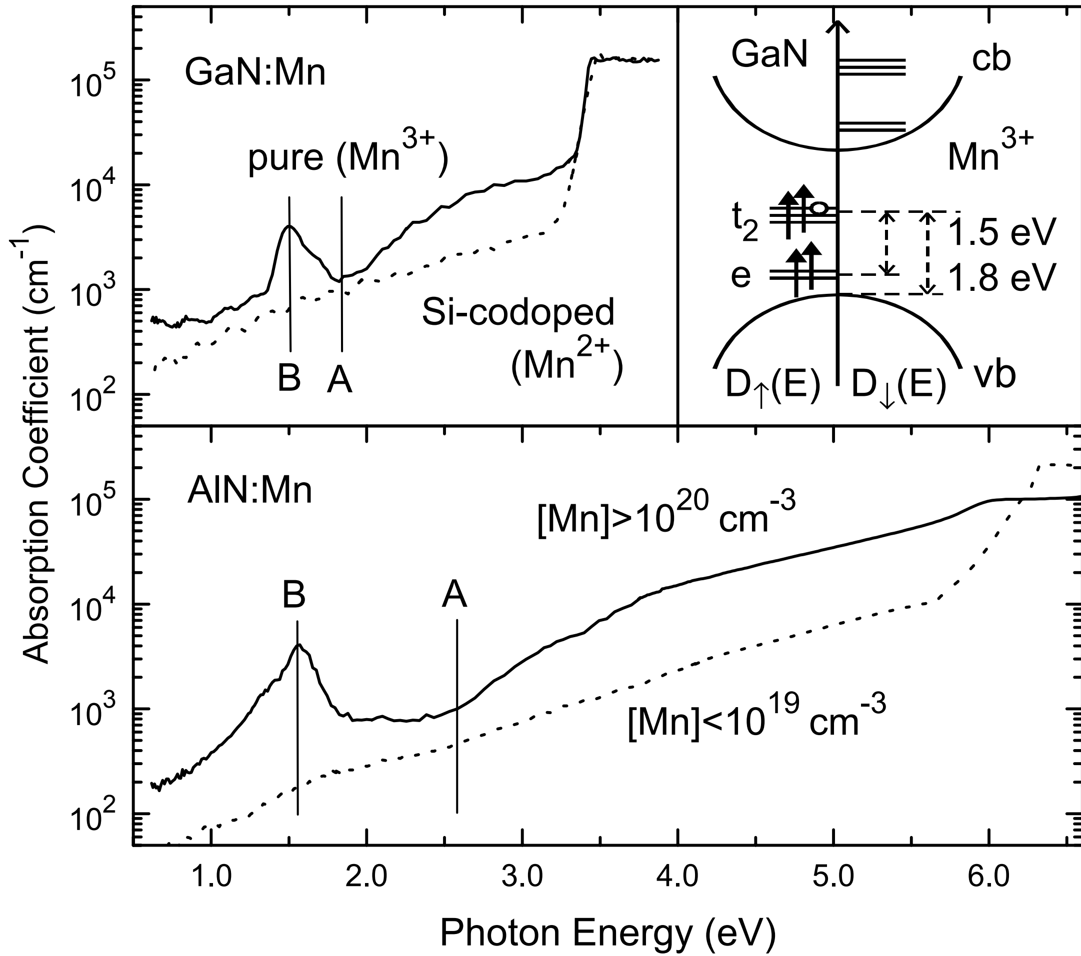

Figure 7.34: Optical absorption of GaN:Mn, GaN:Mn:Si, and AlN:Mn with [Mn] $\approx 10^{20}$ cm^{-3}. Transition A with an onset around 1.8 eV in GaN is assigned to the direct emission of holes from Mn^{3+} acceptors to the valence band, and transition B around 1.5 eV to the internal spin-allowed $^5E \rightarrow ^5T$ transition of the deep neutral Mn^{3+} state, as shown in the inset with the spin-polarized one-electron densities of states $D_\uparrow(E)$ and $D_\downarrow(E)$.

ascribed to the excitation of phonon modes during the optical transition in Ref. 128. Fig. 7.35 reveals that the position of the zero phonon line (ZPL) strongly depends on residual strain in the GaN thin films, similar to the axial crystal field ESR parameter D of Mn^{2+} discussed previously.

The transition energies of 1.4-1.8 eV suggest that the $Mn^{3+/2+}$ acceptor level involved is located deep within the band gap of GaN. It would be desirable to identify the type of optical absorption process directly via light-induced electron spin resonance (LESR) similar to the investigations in Ref. 192. However, as might be expected for very high Mn doping concentrations, the light intensity provided by the available light sources (100 W halogen lamp, 100 W xenon lamp, or the 514 and 488 nm lines of a 5 W argon ion laser) were insufficient to ionize a detectable fraction of Mn acceptors, although they spectrally

overlap the Mn^{3+}-related optical absorption bands. Recently, LESR consistent with the results summarized in Fig. 7.9 have been observed on bulk GaN:Mn crystals with 2-3 orders of magnitude lower Mn doping concentrations than our GaN:Mn films.[193]

In Ref. 128, transition B at 1.5 eV was tentatively assigned to the emission of a hole to the valence band, so that the energy gap of GaN of 3.4 eV resulted as the sum of the transition energies of 2 eV (A) and 1.4 eV (B). This interpretation can be summarized by

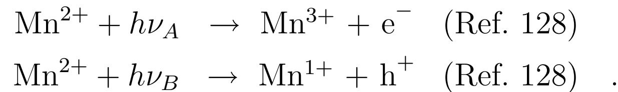

$$\begin{aligned} \mathrm{Mn}^{2+} + h\nu_A &\rightarrow \mathrm{Mn}^{3+} + \mathrm{e}^- \quad \text{(Ref. 128)} \\ \mathrm{Mn}^{2+} + h\nu_B &\rightarrow \mathrm{Mn}^{1+} + \mathrm{h}^+ \quad \text{(Ref. 128)} \quad . \end{aligned}$$

This previous model is even questionable on the basis of the data of Ref. 128. First, one would expect a similarly broad absorption band both for the photoionization into the continuum of the valence and conduction band. However, at low temperatures, the width of the resonant peak B and its phonon replica is only 3-10 meV, whereas the photoionization A has a width of almost 2 eV. Secondly, the energy gap as the result of a summation of electron and hole emission energies would imply a correlation energy close to zero, which is extremely unlikely for the axially distorted Mn^{2+} oxidation state observed in ESR. Furthermore, since much larger concentrations of Mn^{2+} are found by ESR in GaN:Mn:Si samples, which do not show the Mn-related absorption (dashed curve in Fig. 7.34), this assignment has to be revised. Instead, the initial state of both transitions seems to be the neutral Mn acceptor state.

The observed behavior of transition B indicates that it occurs due to an internal absorption of the Mn^{3+} system without emission of carriers into one of the GaN:Mn bands. A similar absorption peak at about 1.5 eV is also observed for AlN:Mn in Fig. 7.34 and assigned to the same Mn^{3+} internal transition. A photoionization shoulder similar to A is observed in AlN:Mn as well, but shifted to higher energies around 2.6 eV, as expected for a transition from a deep Mn level into the valence or conduction band. The relative intensities of the two features are similar in both materials. In the case of AlN, no systematic codoping was performed, and the second spectrum for AlN with lower total Mn concentration is shown only as an indication of the typical background absorption of our undoped AlN samples. The spectral differences at the band edge are probably due to a reduced material quality for high Mn concentrations or due to the limited dynamical range of the optical measurements.

An even clearer picture of the Mn-related transitions is obtained from the photoconductivity measurements of pure GaN:Mn samples shown in Fig. 7.36 as a function of temperature. Only those absorption processes that affect the number of carriers in the bands contribute to photoconductivity. At all temperatures, the broad absorption band A above 1.8 eV is observed, confirming that carriers are excited directly to the valence or conduction band. This associates the energy position of the onset $h\nu_A$ either with the

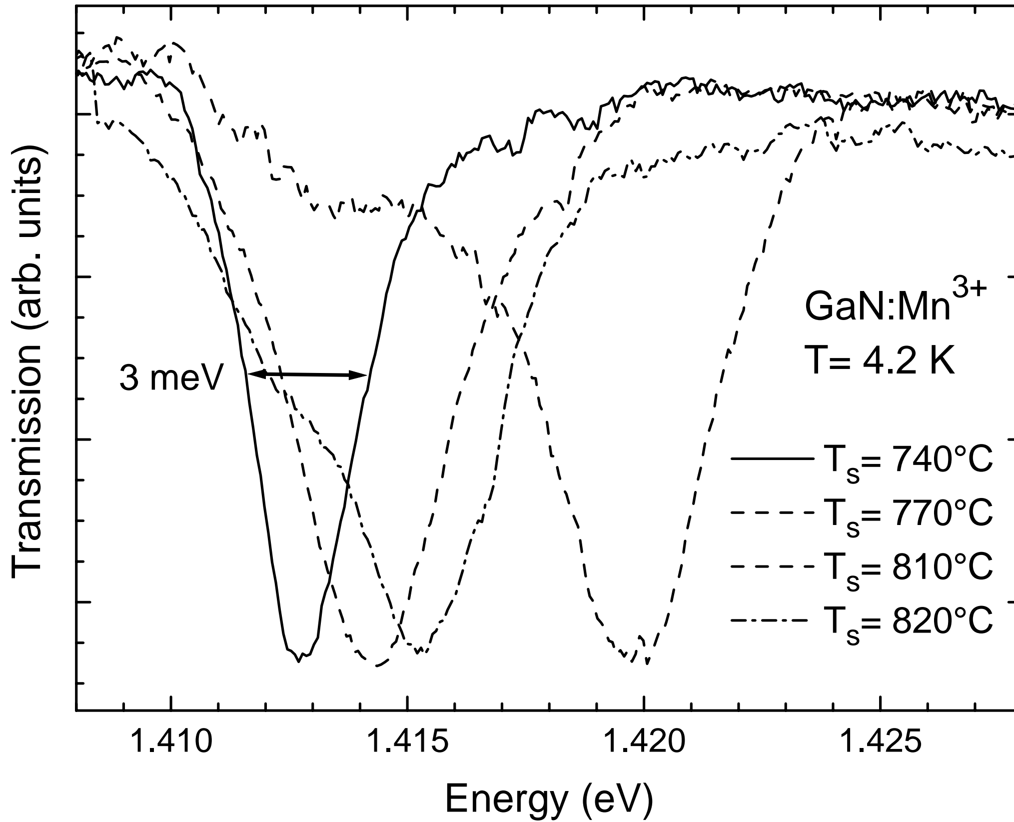

Figure 7.35: Low temperature measurements with high energy resolution of transition B in several GaN:Mn samples. The peak intensities have been normalized in this plot, but correlate well with the total Mn concentration in these samples, as determined by ERD. The peak energy varies between 1.412 and 1.420 eV, depending on the growth temperatures T_s. This could possibly be related to the higher strain of samples grown at higher temperatures. The two peaks observed in those samples grown at temperatures above 800° C could be related to a crystal field splitting or to laterally inhomogeneous strain distribution in these samples.

$Mn^{3+/2+}$ acceptor or a $Mn^{3+/4+}$ donor level, and transition A with the

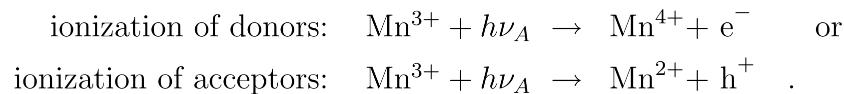

$$\text{ionization of donors:} \quad Mn^{3+} + h\nu_A \rightarrow Mn^{4+} + e^- \quad \text{or}$$
$$\text{ionization of acceptors:} \quad Mn^{3+} + h\nu_A \rightarrow Mn^{2+} + h^+ \quad .$$

Of both interpretations, the large absorption coefficient $\alpha_{\max} \approx 5 \times 10^3$ cm^{-1} at [Mn]$\approx 10^{20}$ cm^{-3} suggests hole emission from Mn^{3+} acceptors, which involves stronger *pd* coupling to the valence band. The large optical absorption cross-section of both processes is indicative for the *pd* mixing of the Mn^{3+} ground state, as otherwise either the internal *d* shell transition or the direct transition to the valence band would be parity-forbidden by dipole selection rules. Note that the ionization energies of the ground state and the excited state at 1.8 and 0.3 eV are far from the values for effective-mass acceptors in GaN,

whose ground state is expected to be only a few hundred meV above the valence-band edge.

In addition to the emission of holes from the neutral $Mn^{3+}(A^0)$ acceptor states in pure GaN:Mn at 1.8 eV, one could also expect to observe the emission of electrons from the negatively charged acceptor states $Mn^{2+}(A^-)$ in n-type GaN:Mn:Si. This transition has indeed been observed at 2.1 eV in n-type GaN:Mn bulk crystals,(183) which were unintentionally doped at a degenerate level. However, the optical cross-section of this *sd*-like transition was at least an order of magnitude weaker than the optical cross-section of the *pd*-like transition A discussed above. Because of the substantial lattice relaxation involved in the Mn^{2+} and Mn^{3+} states,(189, 194) the sum of both transition energies 3.9 eV turns out to be much larger than the band gap of GaN of 3.4 eV.

The energy position of the transition B is unaffected by the temperature shift of the GaN band gap, which again points to an internal d shell transition. The dependence of the intensity of the photoconductivity at this photon energy on temperature shows that transition B is not related to a direct photoionization. Instead, a two-step photothermal process is observed. The internal optical excitation B of Mn^{3+} to an excited state $(Mn^{3+})^*$ is followed by a thermal ionization of $(Mn^{3+})^*$ to Mn^{2+} and a free hole h^+ with a thermal activation energy $E_A \approx 0.3$ eV (see inset of Fig. 7.36). This is confirmed by the total energy difference $h\nu_A = h\nu_B + E_A = 1.8$ eV between the final and initial state of transition A. To summarize, the photoionization processes in GaN:Mn have been identified as

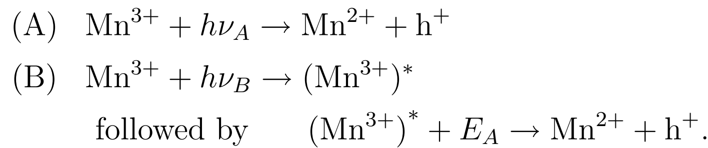

$$\begin{aligned} &(A) \quad Mn^{3+} + h\nu_A \rightarrow Mn^{2+} + h^+ \\ &(B) \quad Mn^{3+} + h\nu_B \rightarrow (Mn^{3+})^* \\ &\qquad \text{followed by} \qquad (Mn^{3+})^* + E_A \rightarrow Mn^{2+} + h^+. \end{aligned}$$

Further evidence for the latter assignment is presented below, based on the band alignment of various III–V materials. Although transition A can be measured in photoconductivity over a wide dynamical range, the precision of $h\nu_A$ is limited by the failure of standard models to describe the shape of the complete photoionization band. Because the energy dependence of the transition matrix elements is not known *a priori*, the energy $h\nu_A = 1.8$ eV was estimated from the onset of A, assuming low-energy tails similar to those below the band gap and below the zero-phonon line of transition B. Photoconductivity experiments on AlN:Mn, similar to those shown for GaN:Mn in Fig. 7.36, would require very high temperatures to show the thermal excitation of transition B because of the large energy difference $h\nu_A - h\nu_B \approx 1.1$ eV in AlN:Mn. This thermal excitation is not necessary to observe the optical absorption spectra shown in Fig. 7.34.

A schematic one-electron level scheme for these processes is shown in the inset of Fig. 7.34. The tetrahedral crystal field of the surrounding N ligands splits the five d orbitals of the Mn ion into two e orbitals and three t_2 orbitals. The latter are split once more by the trigonal distortion present in group III nitrides (see Tab. 7.3). In a more

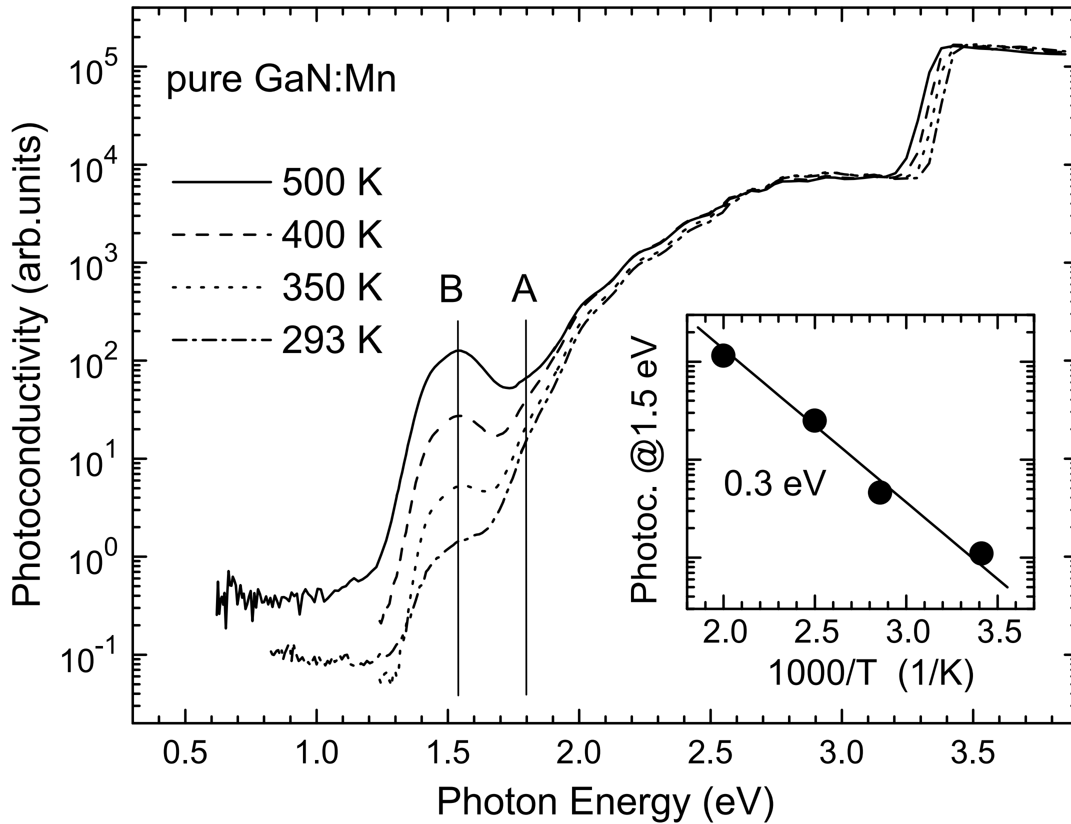

Figure 7.36: Temperature dependence of the spectrally resolved photoconductivity spectra of GaN:Mn. Photoionization across the band gap is observed around 3.4 eV. At high temperatures, this threshold decreases by 0.4 meV/K, in good agreement with the numbers reported for the excitonic luminescence in Ref. 195. Absorption around 1.8 eV enables the emission of holes from deep neutral Mn^{3+} acceptors, which occurs photothermally in a two-step process B via an internal transition to an excited $(Mn^{3+})^*$ state assigned to the zero-phonon absorption line of Ref. 128, followed by thermal emission with an activation energy $E_A \approx 0.3$ eV, as seen in the inset.

appropriate covalent model, the t_2 orbitals are hybridized with those of the surrounding nitrogen atoms, shifting the occupied bonding t_2 orbitals (not shown) into the valence band, and the antibonding t_2 orbitals above the two nonbonding e orbitals.[196, 197] The spin-up and spin-down levels are drawn separately on the left and right sides of the energy axis in Fig. 7.34, as they are offset by the exchange energy ΔE_{ex}. In the case of the Mn^{3+} ground state with $^5T_2$ symmetry, four electrons occupy the localized Mn states within the band gap. One t_2 orbital remains unoccupied or, in other words, is occupied by a strongly acceptor-bound hole. If additional electrons are provided via codoping, the Mn acceptor receives another electron and is converted into Mn^{2+} ($^6A_1$), as observed by ESR.

For Mn^{3+}, one of the t_2 orbitals remains unoccupied, or in the hole picture occupied by a mostly d-like hole. Under illumination with photons of about 1.5 eV energy, an

e electron is excited into the t_2 orbital. Thus, transition B can be interpreted as the $^5T_2 \rightarrow ^5E$ transition of one electron (or hole) between the t_2 and e gap levels with the same spin orientation. This process is spin-allowed, consistent with the observed large optical absorption cross-section $\sigma \approx 10^{-16}$ cm^2. Several phonon modes can be excited during this transition, as seen in Ref. 128. In the excited state, a d-like hole occupies the e-level closer to the valence-band edge. At high temperatures, the hole in the e-level eventually acquires enough thermal energy to escape to the valence band or, in the electron picture, the neutral Mn^{3+} acceptor accepts one electron from the valence band and is converted to Mn^{2+}. Accordingly, the photoionization process A can be understood as an excitation of electrons from the valence band into the unoccupied t_2 level, or as hole emission from the neutral Mn acceptor into the valence band.

To summarize, the transition to the excited $(Mn^{3+})^*$ state must be ascribed to an internal excitation of the many-electron system of the deep $Mn^{3+}(d^4)$ acceptor. These excited states are expected to be very similar to those of the isoelectronic $Cr^{2+}(d^4)$ ions, for which the $^5T_2 \rightarrow {}^5E$ internal excitations have been observed in ZnS:Cr and GaP:Cr at 0.6 eV and 0.9 eV, respectively.[115, 118, 198] Higher excited states have been observed for Cr^{2+} as well, however, their transitions to the $^5T_2$ ground state are expected to be weak in absorption due to spin-selection rules. Compared to the Cr^{2+} system, the $^5T_2 \rightarrow {}^5E$ internal transition of GaN:Mn^{3+} occurs at a significantly higher energy of 1.42 eV.[128] Probably this energy difference is related to the different crystal fields of GaN and GaP. In addition, the splitting due to the covalent coupling with the ligand dangling bonds seems to be particularly strong for GaN:Mn, as discussed below. In contrast, the spin-forbidden internal transition $^6A_1 \rightarrow ^4 T_1$ of Mn^{2+} or Fe^{3+} is typically observed in photoluminescence only. In some materials, the Mn spin-down e orbitals are located within the conduction band, as drawn in Fig. 7.34. Therefore, this $^6A_1 \rightarrow {}^4T_1$ transition is not observed in GaAs, unless the band gap is increased under pressure or by alloying, for example, for $Al_xGa_{1-x}As$ with $x > 0.3$.[199] In AlN, this transition has been ascribed to a green Mn-related luminescence band around 2.0 eV.[156] If ΔE_{ex} were similar in GaN:Mn^{2+}, the unoccupied spin-down e orbitals of Mn^{2+} would be within the conduction band similar to GaAs:Mn^{2+}. However, the PL energy of a zero-phonon line ascribed to this internal transition was reported to be as low as 1.53 eV in GaP:Mn^{2+},[23] so that further experimental studies are required to identify this transition in GaN:Mn^{2+}.

Not only the internal Mn levels, but also their relative position within the gap can be compared between different materials. The energy required for a charge transfer at the $Mn^{3+/2+}$ level can be estimated from the internal-reference related band offsets.[200, 201] Since the valence-band offset between GaN and GaP is known to be about $\Delta_{VB} \approx 1.4$ eV,[202] the energy position of the $Mn^{3+/2+}$ acceptor level can be extrapolated to GaN with the help of the known acceptor ionization energy $E_{GaP} = 0.4$ eV of GaP:Mn^{3+},[23, 118, 172] as shown in Fig. 7.37. The resulting energy $E_{GaN} \approx E_{GaP} + \Delta_{VB} =$

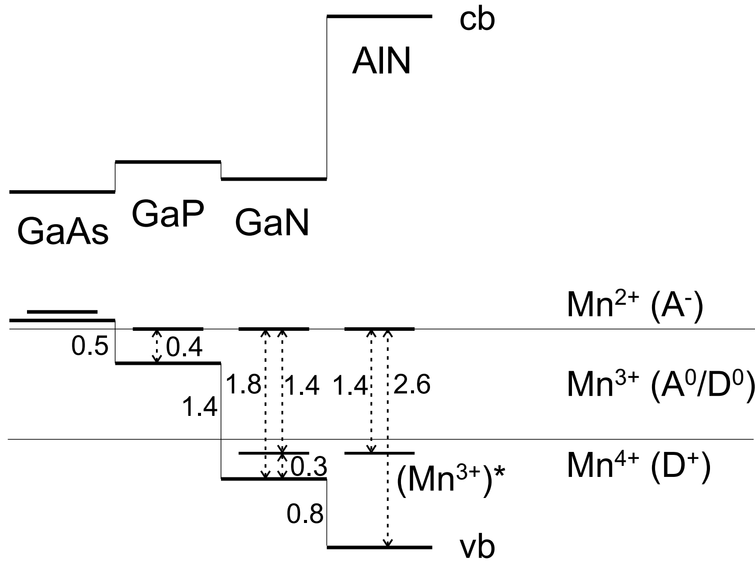

Figure 7.37: Band alignment of the $Mn^{3+/2+}$ acceptor levels in several III–V materials with energy differences given in eV. The valence-band offsets have been taken from the literature.[202] A $Mn^{3+/4+}$ donor level below the $Mn^{3+/2+}$ acceptor level and close to the observed $(Mn^{3+})^*$ acceptor level was predicted by *ab initio* calculations in Ref. 31.

0.4 eV + 1.4 eV is consistent with the energy of 1.8 eV of both photoionization processes A and B. The same level alignment also works reasonably well for AlN with $E_{\text{AlN}} \approx 0.4$ eV + 2.2 eV.[202] Although strong hybridization probably makes this extrapolation invalid for GaAs, it is interesting to note that the valence-band edge would be located above the Mn t_2 orbitals in GaAs, which would make it energetically favorable for valence-band electrons to enter these, or in other words, for holes to occupy extended effective-mass acceptor states Mn^{2+}-h^+ instead of the localized d orbitals, enabling the long-range mediation of magnetic interactions in ferromagnetic DMS, as indeed observed.

7.4.2 Tight-binding picture

As obvious from Fig. 7.37, the properties of Mn^{3+} and $(Mn^{3+})^*$ are very likely to be similar in GaN and AlN. However, significant differences are expected between the Mn acceptor states in GaN:Mn and GaAs:Mn, where Mn acceptors form a very shallow state. Classical crystal field theory, which is very useful in describing transition-metal states in insulators, cannot be applied to semiconductors easily because of the continuum of states in the valence and conduction bands. However, as shown based on a spin-polarized unrestricted Hartree-Fock model for the transition-metal impurity and a tight-binding Green function calculation for the host crystal in Ref. 142, and as shown more recently via LSDA calculations with GGA in Ref. 197, the properties of transition-metal impurity states in a semiconductor result from the strong coupling of the majority spin $t_{2\uparrow}(d_{yz})$ orbitals of the Mn^{3+} ion on the Ga site to the $sp^3{}_\uparrow$ hybrid orbitals of the ligand atoms associated with a Ge vacancy V_{Ga}^{3-}.

The optical transitions observed in the absorption spectra of GaN:Mn^{3+} in Fig. 7.34 accordingly can be understood on the basis of the single-electron scheme of Fig. 7.38. In

this picture, only the $t_{2\uparrow}(d_{yz})$ orbitals of the Mn^{3+} ion on the Ga site are expected to couple to the $sp^3{}_\uparrow$ hybrid orbitals of the ligand atoms, as the $d_\downarrow$-states (not shown in Fig. 7.38) are offset by the exchange energy at one Mn^{3+} site. The resulting levels can be understood qualitatively with the help of a defect molecule picture as shown in Fig. 7.38. The fivefold degenerate $3d_\uparrow$ orbitals of the Mn-ion are split into the two $e_\uparrow$-orbitals $(d_{x^2-y^2})$ and the three $t_{2\uparrow}$ orbitals (d_{yz}) by the tetrahedral crystal field of the surrounding nitrogen ligands. Their degeneracy is lifted furthermore by the trigonal crystal field of wurtzite GaN (not shown in Fig. 7.38). From linear combinations of the four $3sp^3{}_{\uparrow\downarrow}$ dangling bonds pointing towards the transition-metal impurity, an s-like $a_{1\uparrow\downarrow}$ orbital (not shown in Fig. 7.38) and three p-like $t_{2\uparrow\downarrow}$ orbitals are formed. Hybridization occurs between the impurity and the host $t_{2\uparrow}$ orbitals. According to Ref. 142, the host $a_{1\uparrow\downarrow}$ orbital and the transition-metal $4s_{\uparrow\downarrow}$ states form a doubly occupied bonding state deep in the semiconductor valence band, and an empty antibonding state high in the conduction band, which are also not included in Fig. 7.38. The $e_\uparrow$-orbitals of the transition-metal impurity cannot hybridize with the host orbitals and remain nonbonding. As the $d_\downarrow$-orbitals are offset into the conduction band by the exchange energy, their influence on the host $t_{2\downarrow}$ orbitals is small.

According to Fig. 7.38, the nature of the impurity gap states depends critically on the ordering of the non-interacting host $t_{2\uparrow\downarrow}$ (sp^3) dangling bond levels and the Mn^{3+} $t_{2\uparrow}(3d^4)$ atomic levels. The nature of the transition-metal induced gap state derived from the antibonding t_2 hybrid is dominantly p-like, if the hosts $t_{2\uparrow\downarrow}$ orbitals are initially located above the $3d_\uparrow$ levels like for Mn^{3+} in in GaAs:Mn.[142] The opposite ordering results in a dominantly d-like gap state, as for Mn^{3+} in GaN:Mn.[197] Because the influence of the ligands on this transition-metal state is very small, such a state is well approximated with standard crystal field theory. The observed splitting between the resulting t_2 and e gap states in GaN:Mn is much larger than the corresponding splitting for Cr^{2+} impurities in ZnS and GaP because of the level repulsion of the Mn^{3+} and the V_{Ga}^{3-} $t_{2\uparrow}$ orbitals.

More elaborate *ab initio* calculations based on the local-spin-density approximation (LSDA)[31, 117, 190, 196, 197, 206] obtain a similarly deep $Mn^{3+/2+}$ acceptor level in GaN and additionally predict a $Mn^{3+/4+}$ donor level about 1.4 eV below the $Mn^{3+/2+}$ acceptor level.[31] If this amphoteric character of deep Mn states in GaN is correct, high Mn concentrations would strongly hinder the presence of free electrons or holes in GaN, resulting in a semi-insulating film with the Fermi-level pinned around midgap by deep trap levels. This is consistent with the experimental observation of high resistivity, also reported in Ref. 128. In the codoped GaN:Mn:Mg samples of Ref. 138, a large number of PL transitions was observed around 1.1 eV, which could be interpreted as the spin-allowed ${}^4T_2 \rightarrow {}^4T_1$ internal transitions of the $3d^3$ system of ionized Mn^{4+} donors.[118] In Ref. 117, not only the electronic structure shown in Fig. 7.39, but also the magnetic moments inside the Mn spheres and the optical properties of GaN:Mn were calculated and discussed in the context of the known properties of GaAs:Mn. The gap states of GaN:Mn calculated

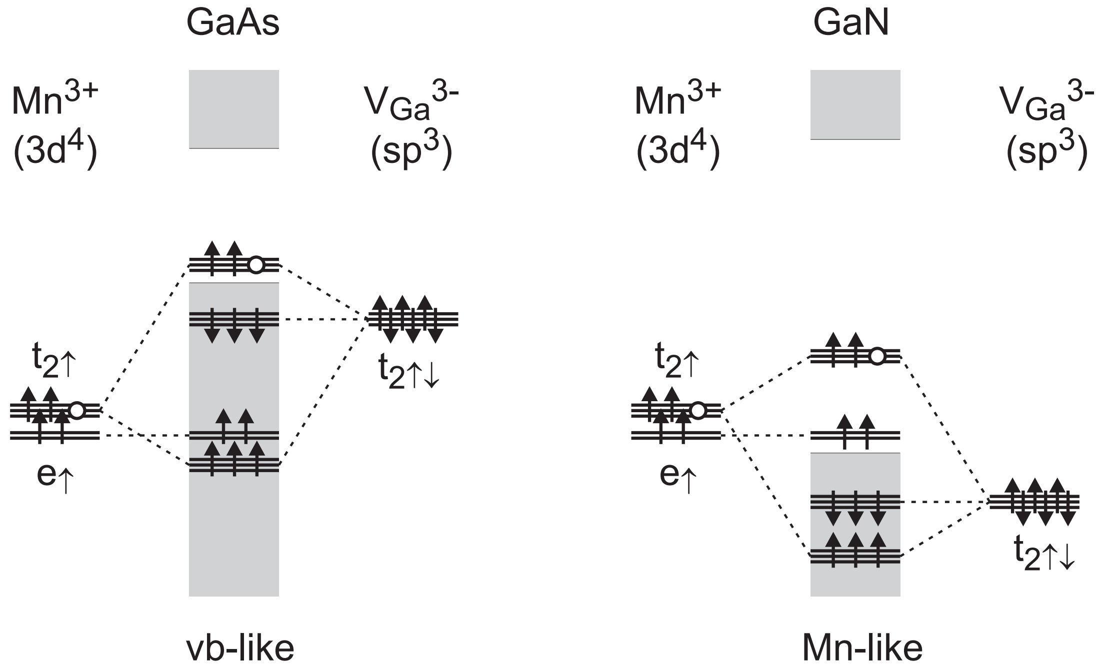

Figure 7.38: Defect molecule picture for transition-metal gap states of Mn^{3+} in narrow- and wide-bandgap semiconductors like GaAs and GaN. In this picture, the transition-metal induced gap states are derived from the antibonding $t_{2\uparrow}$ orbitals caused by the hybridization of the transition-metal $t_{2\uparrow}$ orbitals and the dangling bond $t_{2\uparrow}$ orbitals pointing towards the transition-metal ion from its ligands. These orbitals form the Ga vacancy defect states in the absence of substitutional Mn, in particular V_{Ga}^{3-} if no electrons or holes are transferred to the crystal. Note that according to the calculations of Refs. 203, 204, 205 the relaxed $V_{Ga}^{3-/4-}$ acceptor level is located at about 0.1 eV above the valence band maximum of GaN. The character of the Mn-related gap states depends of the relative energy position of the Mn^{3+} levels and the dangling bond $t_{2\uparrow\downarrow}$ orbitals. If the Mn^{3+} levels are above the dangling bond $t_{2\uparrow\downarrow}$ orbitals, the hybrid gap states are mostly d-like and localized, as in GaN:Mn. However, if the Mn^{3+} levels are below the dangling bond $t_{2\uparrow\downarrow}$ orbitals, the hybrid gap states are mostly p-like and delocalized, as in GaAs:Mn. In the case of Mn^{3+}, one of these $t_{2\uparrow}$ levels is occupied by a hole, which therefore either has valence-band (p-like) or ionic (d-like) character.

there agree well with the interpretation of our experiments. In particular, internal optical absorption around 1.3 eV is predicted between the e and t_2 orbitals, which agrees well with the zero-phonon line at 1.42 eV of Fig. 7.35 and of Ref. 128. The calculated acceptor wave functions are more strongly localized and less hybridized with the valence band in GaN:Mn compared to GaAs:Mn because of the different energy positions of Mn in the two materials.[117, 197]

According to the LSDA calculations[117, 196, 197] and to the optical experiments described above, d-like $t_{2\uparrow}$ and $e_{\uparrow}$-levels appear above the valence band of GaN, which are derived from the host $3sp^3{}_{\uparrow\downarrow}$ states. According to all theoretical calculations, the t_2-

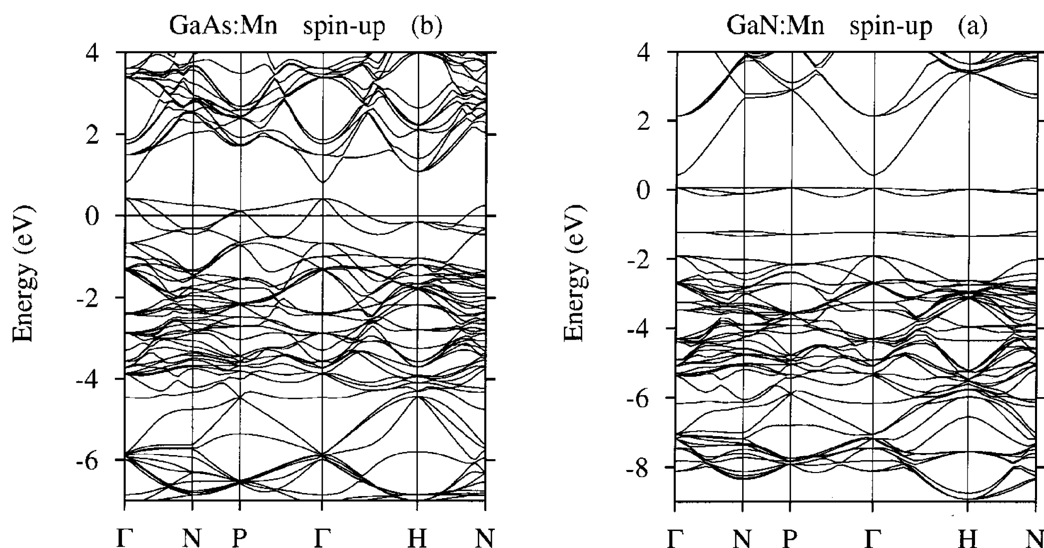

Figure 7.39: Energy bands of GaAs:Mn and GaN:Mn at [Mn]=3.125% according to LSDA Band structure calculations from Ref. 117. Whereas two localized Mn-related gap states occur in the band gap of GaN:Mn with an energy distance of 1.3 eV, the Mn-related states hybridize completely with the valence band in the case of GaAs:Mn.

level, which is occupied by a hole in the single-electron scheme of Fig. 7.38, is a very localized state whose properties are dominated by atomic d-orbitals. This is in contrast to GaAs:Mn, where an effective-mass like Mn^{2+}-h^{+} complex has been confirmed experimentally.(134) Here, the mostly p-like antibonding $t_{2\uparrow}$-level is very close to the valence-band edge derived from the GaAs $3sp^{3}{}_{\uparrow\downarrow}$ states. This explains the qualitatively different character of the calculated band structures of GaAs:Mn and GaN:Mn shown in Fig. 7.39 of Ref. 117, and agrees well with the different character calculated for the valence bands of the hypothetical compounds MnN and MnAs.(207)

Unfortunately, the statement that "Mn^{2+} introduces a hole on substitutional Ga^{3+}-sites" often found in the GaAs:Mn-related literature lacks a closer specification of the microscopic character of the type of hole. The discussion above shows that in the case of GaN this hole has mostly d-like character. Therefore, it is immobile and strongly localized, and not suitable for the mediation of ferromagnetism as proposed in Refs. 122, 208. In GaP:Mn, which lies between the cases of GaN:Mn and GaAs:Mn, it was possible to show by ESR that the neutral Mn acceptor is also in the Mn^{3+} state, which points to a similar interpretation as discussed for GaN:Mn.(172) However, some observations also suggest properties of a Mn^{2+}+h^{+}-like complex in GaP and still require interpretation.(23, 209)

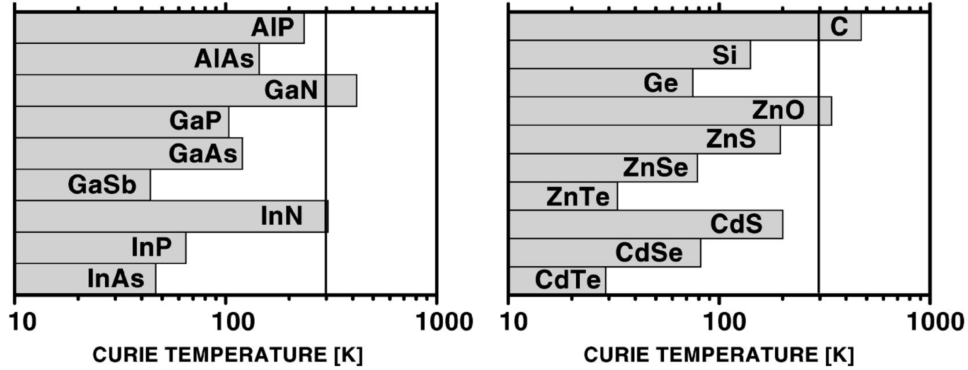

Figure 7.40: Curie Temperatures predicted for carrier-mediated ferromagnetism in various materials with $[Mn^{2+}] \approx 5\%$ and a hole concentration $p \approx 3.5 \times 10^{20}$ cm^{-3} (from Ref. 122).

7.5 Outlook: Ferromagnetism in GaN

According to the exchange mechanism proposed in Ref. 122, the magnetic ordering in dilute magnetic semiconductors results from the exchange interaction between localized magnetic spins and delocalized carriers. In particular, the extended wave functions of free or weakly bound holes enable long-range magnetic ordering, which should be adjustable by charge control, e.g. via external gates,[210, 211] even for low Mn concentrations up to high temperatures. The highest Curie temperatures with $T_c \geq 300$ K according to a mean-field Zener model are expected for a d^5 configuration (as found e.g. for Mn^{2+}) and valence-band holes as carriers mediating the magnetic coupling. In GaAs:Mn, the *pd* exchange energy $N_0\beta$ is typically about 1 eV, where N_0 is the concentration of cation sites and β the *pd* exchange integral between the mostly *p*-like valence-band states and the mostly *d*-like Mn^{2+} orbitals. It is assumed in Ref. 122 that the states involved and the exchange integrals β are similar for all tetrahedrally coordinated semiconductors, so that the exchange energy $N_0\beta$ is approximately proportional to the inverse unit cell volume a_0^{-3}. Because $T_c \propto N_0\beta^2 \propto a_0^{-3}$, compounds with small anions like nitrogen and oxygen are expected to lead to particularly high Curie temperatures. As an example, $T_c \approx 400$ K was calculated for GaN:Mn with a Mn^{2+} concentration $[Mn^{2+}] \approx 5\%$ and a hole concentration $p \approx 3.5 \times 10^{20}$ cm^{-3},[122] as shown in Fig. 7.40. The values for T_c can be scaled easily to different Mn^{2+} concentrations, as according to this model $T_c \propto [Mn^{2+}]$. Similarly, T_c can be scaled to different hole concentrations. For the simple assumption of a parabolic dispersion of the valence band, the magnetic susceptibility of itinerant holes is proportional to the kinetic energy of the holes, so that $T_c \propto k_F \propto \sqrt[3]{p}$, where k_F is the Fermi wave vector. However, due to the complicated shape of the valence band, the dependence on the hole concentration is not such a simple power law in GaAs, but depends even stronger on the hole concentration and scales roughly proportional to $\sqrt{p}$

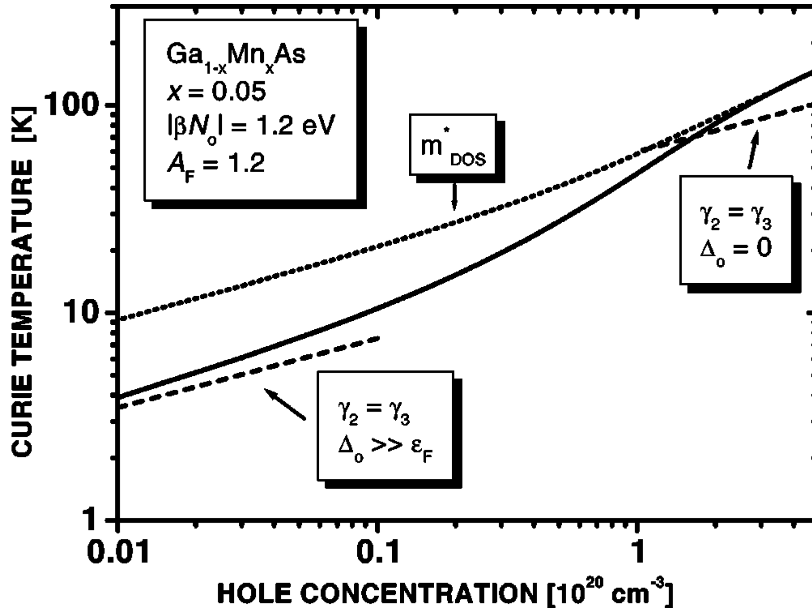

Figure 7.41: Scaling of the carrier-mediated ferromagnetic coupling with the hole concentration for GaAs:Mn with $[Mn^{2+}] \approx 5\%$ (from Ref. 122). The dashed line were calculated for valence bands with a parabolic dispersion.

as shown in Fig. 7.41 from Ref. 122. Obviously, high concentrations of both $[Mn^{2+}]$ and of holes p are required for a high Curie temperature, in addition to a small unit cell volume a_0^3, which is a principal advantage of GaN. Similar prerequisites are required for the polaronic and exchange-correlated interaction schemes of Refs. 212, 213, 214.

Obviously, large concentrations of valence band holes are only possible, if the Fermi level is located not too far above the valence band edge. As discussed in Ref. 215, valence band holes are required as carriers for strong ferromagnetic coupling because of the weakness of the *sd* exchange interaction. The transition-metal states, which are formed at such a Fermi level position according to the charge-transfer level schemes of Fig. 7.43 and 7.42 are listed in Tab. 7.7.

7.5.1 Charge-transfer levels of Cr, Mn, and Fe

From Fig. 7.2 and Tab. 7.1, it becomes immediately clear that the prerequisites for sufficiently large hole densities in the valence band must be discussed separately in III–V and II–VI semiconductors due to the different cation charge for these two classes of semiconductors. As in Mn-doped II–VI diluted magnetic semiconductors the isovalent Mn^{2+} ion does not introduce any charge-transfer levels in the band gap, the hole concentration can be controlled independently of the Mn doping. This makes Mn unique among the transition-metal impurities in II–VI semiconductors and particularly attractive for the individual control of spin and charge degrees of freedom in Mn-based dilute magnetic semiconductors.[211, 216, 217, 218, 219] In III–V semiconductors, this situation is more complex. Therefore, the energy position of the charge-transfer levels of Cr, Mn, and Fe in selected II–V and III–V semiconductor materials will be treated separately in detail in

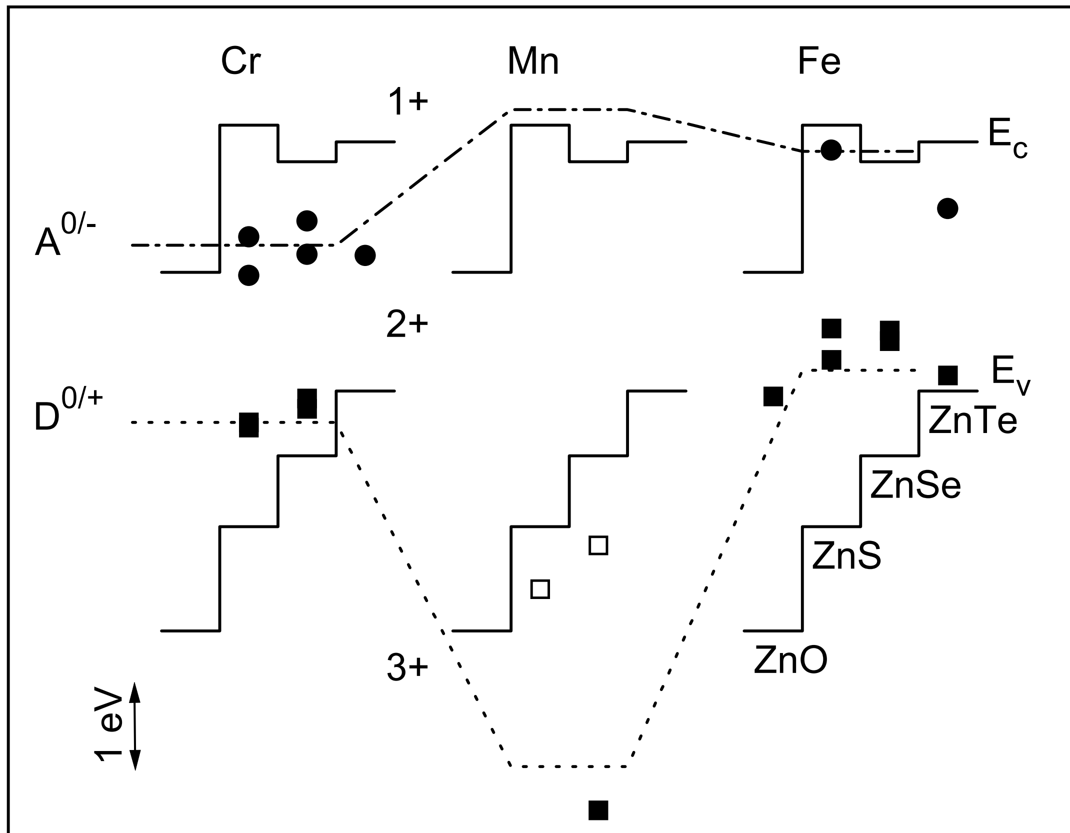

Figure 7.42: Charge-transfer levels $A^{0/-}$(circles) and $D^{0/+}$(squares) of the transition-metal impurities Cr, Mn, and Fe in Zn-based II–VI semiconductors with the band edges E_c and E_v aligned according to the internal reference rule.[118, 140, 142, 200] The band gaps and valence-band offsets were taken from Refs. 202, 220, and the experimentally observed charge-transfer levels (closed symbols) from Refs. 115, 118 and references therein. Theoretically predicted charge-transfer levels (open symbols) were taken from Refs. 31, 201. The lines separating the existence ranges of the transition-metal oxidation states are guides to the eye. See Fig. 7.43 for the charge-transfer levels in Ga-based III–V semiconductors.

the following. As discussed in the context of Fig. 7.37, charge-transfer levels of transition-metal impurities in various materials are aligned with respect to an internal reference energy, unlike the ionization energies of shallow hydrogenic donors and acceptors, which are defined with respect to the conduction-band minimum or valence-band maximum.

According to this so-called Langer-Heinrich rule, the energy distances between the charge-transfer levels of different transition-metal ions are similar in various host materials, which makes it possible to relate their energies to an internal reference level and to the experimentally observed band offsets,[142, 200, 201] as shown on a relative energy scale in Figs. 7.42 and 7.43. The acceptor levels of Cr, Mn, and Fe are located high above the valence-band edge in II–VI semiconductors, so that additional shallow doping is required to achieve the necessary hole concentrations. Unfortunately, such additional shallow ac-

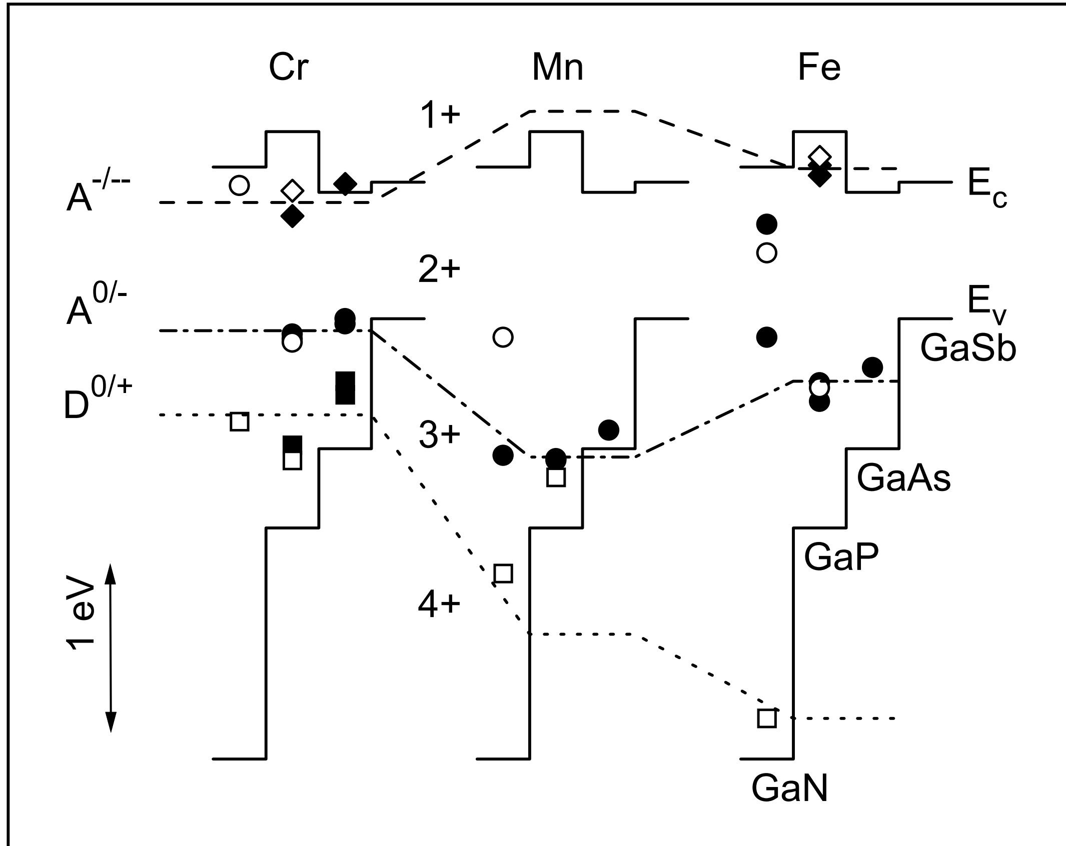

Figure 7.43: Charge-transfer levels similar to Fig. 7.42, but for Ga-based III–V semiconductors, for which hybridization and screening effects are more important than for the II–VI materials with a lower charge density of the valence electrons at the transition-metal site. However, as for the free ions, the most stable electronic configurations are observed for the d^5 configuration Cr^{1+}, Mn^{2+}, and Fe^{3+} with $S = 5/2$. In particular, the correlation energy of $Mn^{2+}(A^0)$ even exceeds the band gap in II–VI materials. For the same reason, the Mn-acceptor level $A^{0/-}$ is shifted towards the valence band in III–V materials, and the $Fe^{3+/2+}$ ($Cr^{2+/1+}$) charge-transfer levels are shifted up (down) in energy, respectively.

ceptors are compensated by transition-metal-induced donor levels in the cases of Cr and Fe doping. Only for the exceptionally stable d^5 configuration of the neutral Mn^{2+} ion is the correlation energy so high that the $Mn^{2+/3+}$ donor level is not located within the band gap, but shifted into the valence band.

Also in III–V compounds, Mn^{2+} is desirable for a high Curie temperature, because of its high spin $S = 5/2$ and the high exchange energy $N_0\beta$. However, here the Mn^{2+} oxidation state with the large correlation energy due to the half-filled d shell corresponds to the negatively charged acceptor state A^-. Therefore, both the $Mn^{2+/3+}$ acceptor level and the $Mn^{3+/4+}$ donor level are shifted towards the valence band, so that Mn becomes a shallow acceptor in GaAs:Mn.[118, 221] A consequence of the location of both charge-

transfer levels within the band gap of III–V materials is the reduction of free electrons and holes, unless the number of carriers exceeds the number of transition-metal centers

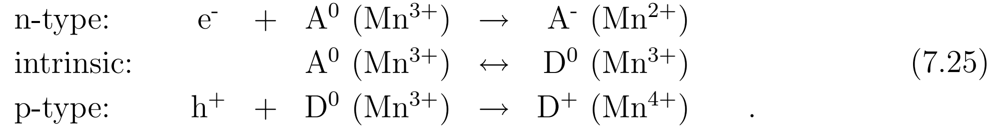

$$\begin{array}{llllll} \text{n-type:} & e^- & + & A^0\ (Mn^{3+}) & \rightarrow & A^-\ (Mn^{2+}) \\ \text{intrinsic:} & & & A^0\ (Mn^{3+}) & \leftrightarrow & D^0\ (Mn^{3+}) \\ \text{p-type:} & h^+ & + & D^0\ (Mn^{3+}) & \rightarrow & D^+\ (Mn^{4+}) \quad . \end{array} \tag{7.25}$$

Because of these reactions, the Fermi level is said to be pinned by the $Mn^{2+/3+}$ and $Mn^{3+/4+}$ charge-transfer levels in the band gap of the semiconductor material. A presence of carriers in the bands would require codoping in excess of the very high concentrations of transition-metal centers.

Without additional codoping, the presence of Mn^{2+} in III–V materials implies a position of the Fermi level at or above the $Mn^{3+/2+}$ charge-transfer level. Significant concentrations of free holes are only possible when the Fermi level resides within the valence band, or within a few k_BT above the valence-band maximum. Both conditions cannot be fulfilled at the same time if the $Mn^{3+/2+}$ charge-transfer level is located significantly above the valence-band edge. In GaAs:Mn, however, both conditions can be fulfilled because of the formation of a Mn^{2+}-h^+ complex with only 0.1 eV ionization energy. The valence-band like character of the Mn^{2+}-bound holes has been confirmed experimentally in this material.(134, 222) Therefore, GaAs:Mn becomes metallic at sufficiently high doping concentrations, and GaAs:Mn can be made ferromagnetic with $T_c = 110$ K at doping concentrations around 5%.(122)

For high concentrations of valence-band holes, also the $Mn^{3+/4+}$ donor level must be located below the valence-band edge. Otherwise, all introduced holes would be compensated by these donors, similar to the case of Cr and Fe in II–VI materials. References 221 and 218 claim that a configuration with the Mn donor and acceptor levels deep in the valence band is possible in most III–V semiconductors. In contrast, localized gap states with largely *d*-like character were predicted theoretically for Mn and other transition metals in GaN based on the local spin density approximation (LSDA) in the atomic-spheres approximation,(190) with the Green's function method,(31) with ab initio pseudopotentials and a plane-wave basis,(206) with the tight-binding linear-muffin-tin-orbital method,(117) with the Korringa-Kohn-Rostoker method, which additionally takes into account disorder,(196) and with fully relaxed calculations, including the generalized gradient approximation (GGA).(197, 223) Examples for the calculated charge-transfer levels from Ref. 31 are included in Fig. 7.43 with open symbols. Generally, LSDA seems to underestimate the correlation energies, which are predicted significantly smaller than observed experimentally from the charge-transfer levels. No significant difference besides broadening of the impurity bands appears between the most dilute and the most highly doped case according to the LSDA calculations.(117)

	GaN	GaP	GaAs	GaSb	ZnO	ZnS	ZnSe	ZnTe
Cr	D^+	D^+	D^+	A^-?	D^+	D^+	D^+	A^0?
Mn	D^+?	A^0	A^-	A^-	A^0?	A^0	A^0	A^0
Fe	D^+?	A^0	A^0	A^-	D^+	D^+	D^+	D^+

Table 7.7: Oxidation and charge states expected for Cr, Mn, and Fe impurities from Fig. 7.43 and 7.42 in the presence of large concentrations of valence-band holes, i.e. with the Fermi level located close to the valence-band edge. The question marks indicate that no experimental data concerning this oxidation state are available and that the extrapolation via the internal reference rule is uncertain.

7.5.2 Prospects for carrier-mediated ferromagnetism

Only small concentrations of valence-band holes can be generated in those materials with transition-metal centers acting as hole traps or compensating donors $D^{0/+}$ according to Eq. (7.25). In these materials, the number of holes will be strongly reduced because of the recombination $h^+ + D^0 \rightarrow D^+$. Consequently, materials with the $D^{0/+}$ state in the band gap cannot be used to generate hole-mediated ferromagnetism.

As shown in Tab. 7.7, codoping of transition metals with shallow acceptors is possible in materials like GaP:Mn, GaP:Fe, and GaAs:Fe, and in all Mn-doped II–VI materials, where the $D^{0/+}$ level is in the valence band, but the $A^{0/-}$ level is not. In these materials, the neutral transition-metal acceptor state A^0 is expected to be stable in the presence of valence-band holes. Indeed, ferromagnetism with $T_c < 3$ K has been achieved in ZnTe:Mn:N.[218, 224] As shown in Tab. 7.1, neutral Fe^{3+} acceptors would have the largest possible spin $S = 5/2$ and would therefore be preferred for carrier-mediated ferromagnetism rather than Mn^{3+} with $S = 2$, for which, furthermore, antiferromagnetic contributions to the spin-spin interaction are expected.[215] The prospects for GaN:Fe, which is a special case with a predicted $Fe^{3+/4+}$ donor level close to the valence-band edge, will be discussed separately in the following section.

From Fig. 7.43, the hole emission $A^0 \rightarrow h^+ + A^-$ is expected to occur spontaneously in GaAs:Mn, GaSb:Mn, and GaSb:Fe, where the $A^{0/-}$ level is also in the valence band or within a few kT of it. Therefore, transition-metal doping alone is expected to generate holes and localized spins at the same time in these materials, consistent with the metallic and ferromagnetic behavior of GaAs:Mn.[225] Because of the smaller lattice constant and higher exchange energy $N_0\beta \propto a_0^{-3}$ in GaAs, and because of the large spin $S = 5/2$ of Mn^{2+}, GaAs:Mn seems to be the optimum combination of properties to achieve both high concentrations of holes and localized spins at the same time.

The alignment of charge-transfer levels in related materials according to the Langer-Heinrich rule suggests that wide band gap semiconductors like AlN and GaN are rather unsuitable as candidates for carrier-mediated ferromagnetism. Similar to GaN, the valence

band of the narrow-gap material InN is mostly formed from nitrogen orbitals, so that the tight-binding picture of Fig. 7.38 probably also applies for InN:Mn. It is therefore unlikely that the $Mn^{3+/2+}$ acceptor level is much closer to the valence band of InN compared to GaN. Because of the narrow band gap of 0.7 eV of InN,[226] it could rather be located close to the conduction-band edge of InN, consistent with the calculated valence- and conduction-band offsets between InN and GaN of 0.8 eV and 1.8 eV, respectively.[227] Further studies on the strength of the *s-d* coupling are required to judge the prospects of InN for carrier-mediated ferromagnetism.

7.5.3 Other exchange mechanisms

Because of the intrinsic difficulties in preparing transition-metal-doped GaN with sufficient hole concentrations for the application of the Zener model of Ref. 122, it might be a more promising route to obtain ferromagnetic GaN by inspection of the predictions of other theoretical models, which can be applied to the transition-metal states found in GaN. Some important exchange mechanisms, which are believed to be responsible for ferromagnetism in other materials, are discussed in the following. *Ab initio* methods like those of Refs. 117, 196 can help to decide between the different possible mechanisms.

Bound magnetic polarons

A possible extension of carrier-mediated ferromagnetism based on strongly localized magnetic polarons for GaN is put forward for GaN in Ref. 221. The idea of bound magnetic polarons (BMPs) has been discussed many years ago for materials like EuO or CdMnTe,[228, 229, 230] where many localized spins interact with few weakly bound carriers of intermediate spatial extent. The spatial extend of these carriers is determined by the effective-mass radius $a^* = a_0\varepsilon^*(m_0/m^*)$ of hydrogenic effective-mass states with the Bohr radius $a_0 = 0.53$ Å of the hydrogen atom and the material's effective dielectric constant ε^* and the carrier mass m^*, and is typically of the order of 2 nm. At carrier densities above Mott's critical density $N_c \approx (0.25/a^*)^3 \approx 2 \times 10^{18}\text{cm}^{-3}$, their overlap eventually enables significant long-range interactions. Thus, in the presence of simultaneous overlap with the localized spins, a macroscopic spin polarization becomes favorable. As discussed in Ref. 231, the interaction mechanism of a BMP depends strongly on the configuration of the magnetic ions. The Brillouin-type permanent polarization of the isolated d^5 multiplets of Mn^{2+}- and Fe^{3+}-based BMP is determined either by fluctuations in the weak *sd* coupling regime, or saturates in the strong *pd* coupling regime. Note that *sd* exchange energies as small as $N_0\alpha \approx 14$ meV have been determined for Mn^{2+} in n-type GaN:Mn from measurements of the spin-relaxation times.[165] In contrast, the energy spectrum of Van-Vleck type ions like Fe^{2+} (d^6) consists of several states close to the ground state, which enable an nonzero spin-flip energy even in the absence of a permanent magnetic

field. Both contributions have to be taken into account for $Cr^{2+}(d^4)$- or $Mn^{3+}(d^4)$-based materials, as discussed in Ref. 231. However, the *sd* exchange energy $N_0\alpha \approx 0.2$ eV for CdS:Cr^{2+} is not high enough to enable room-temperature ferromagnetism in the d^4-based systems at realistic doping concentrations.

In GaAs:Mn, the localized spins would correspond to the Mn^{2+} states with S=5/2, whereas the weakly bound carriers would correspond to holes in the valence band or to weakly bound holes in the Mn^{2+}-h^+ complexes. The local coupling between both magnetic moments at the Mn sites is antiferromagnetic.[134, 232] Particularly for GaAs:Mn, the valence-band holes required for the carrier-mediated exchange can therefore be replaced by valence-band-like effective-mass-acceptor states with similar properties as real valence-band holes, supporting the validity of the Zener model of Ref. 122 for this material system. In GaN:Mn no such coexistence of localized and extended states is provided by the $Mn^{3+/2+}$-acceptors. Nevertheless, extended holes could be introduced independently by codoping the GaN:Mn crystal with shallow acceptors like Mg. Due to the high ionization energy of Mg acceptors in GaN,[233, 234] only a small fraction of these holes will be transferred to the valence band, so that the Zener model of Ref. 122 does not apply to this situation. Still, the polaronic picture of Ref. 221 does apply, as long as the holes remain in their extended effective-mass acceptor states. However, since $Cr^{3+/4+}$, $Mn^{3+/4+}$, and $Fe^{3+/4+}$ donor levels are predicted in the band gap of GaN according to the calculations of Ref. 31, the Fermi level will be pinned at these levels, and the extended holes will be captured in the charge-transfer process $(Cr/Mn/Fe)^{3+} + h^+ \rightarrow (Cr/Mn/Fe)^{4+}$, as discussed above. According to Fig. 7.43, the theoretical predictions for a $Cr^{3+/4+}$ donor level are supported from experimental data in GaP and GaAs and the internal reference rule. Therefore codoping most probably does not lead to the presence of free or weakly bound holes in GaN:Cr:Mg. The situation is similar in GaN:Mn:Mg, where crystals have been prepared and characterized in Ref. 138. The optical and electrical properties of these crystals are consistent with a Mn^{4+} oxidation state within the band gap of GaN, which would once more oppose carrier-mediated ferromagnetism in codoped GaN:Mn:Mg.

Considering the difficulties in predicting charge-transfer energies from theory, the location of the $Fe^{3+/4+}$ donor level in GaN is not sufficiently clear up to now to make a reasonable judgement on GaN:Fe:Mg. Similar to the unique role of Mn^{2+} in II–VI materials, the most stable neutral charge state in III–V materials is the d^5 configuration of neutral Fe^{3+} with a stable region covering almost 3 eV. Therefore, the BMP model could be very much appropriate for codoped GaN:Fe:Mg with localized Fe^{3+} spins and extended Mg-bound effective-mass acceptor holes, if the $Fe^{3+/4+}$ level is at lower energy than the Mg acceptor level in GaN. However, the doping efficiency of Mg in GaN has been reported to decrease at high Mg concentrations, with a maximum acceptor concentration of 10^{20} cm^{-3} achieved.[234, 235] Therefore, it is questionable whether high enough hole concentrations could be provided to overcome the inherent tendency of $3d^5$ transition-metal ions to form

a spin-glass phase,[122, 215] and whether the *pd* exchange integral $N_0\beta$ would indeed be as high as assumed, since it is known from ESR that the Fe^{3+} state is strongly distorted in the axial crystal field of GaN.[22, 164] The most important experimental parameter to be determined to judge the possibility of ferromagnetism in GaN:Fe:Mg is the exact energy position of the $Fe^{3+/4+}$ donor level in relation to the valence band of GaN.[236]

Virtual transitions

A rather universal exchange mechanism for the *pd* exchange of e.g. Mn in GaN has been pointed out in Ref. 237, based on virtual excitations from magnetic impurity levels to the valence band. In accordance to the *Bloemberg-Rowland* mechanism, the ferromagnetic Curie temperature was calculated from the energy gap for virtual excitations of about 0.1 eV in *p*-type GaAs:Mn. Assuming gap energies in the range of 0.2-0.3 eV for GaN:Mn, Curie temperatures around 200 K were predicted for a Mn concentration of 5%. However, regarding the experimental energy depth of 1.8 eV of the $Mn^{3+/2+}$ acceptor level in GaN, the Curie temperature predicted by this mechanism would be still far below 10 K at [Mn]$\approx$ 5%, so that the chances for ferromagnetism according to this mechanism are rather small in GaN:Mn.

Transition-metal ion states are coupled to the occupied valence bands via spin-dependent kinetic exchange due to the short-range *superexchange* interaction. In the standard atomic picture, this can be understood in terms of virtual transitions to the neighboring anion *p* orbitals. The superexchange interaction thus leads to antiferromagnetic spin orientation for most but some Cr- and V-based II–VI semiconductors,[238] and it is thought to be overcome by the ferromagnetic interaction in GaAs:Mn.[122] Also in Eu(S,O) and the Cr spinels, this competition between direct ferromagnetic and indirect antiferromagnetic superexchange is observed.[239] Antiferromagnetic or spin-glass interactions are of minor interest for spintronic devices, and will therefore not be discussed further for GaN:Mn here.

Double exchange

It is well established that the high Curie temperatures observed in the manganites are caused by a dynamical double exchange due to hopping between the $Mn^{3+}(d^4) \leftrightarrow M^{4+}(d^3)$ levels, e.g. $T_c \approx 350$ K in (La,Sr)MnO_3. The parallel orientation of the local moments is then favorable assuming the hopping process to be spin-conserving, so that the spin-up orientation of the itinerant electron is required because of Hund's coupling on each Mn site. Similarly, a short-range *dd* interaction could be strong enough for room-temperature ferromagnetism in highly transition-metal-doped (or alloyed) GaN. In Refs. 117, 196, the total energies were calculated for configurations of parallel, antiparallel, and unpolarized Cr, Mn, and Fe spins in GaN, which allowed the estimation of the stability of the ferro-

magnetic, antiferromagnetic and spin-glass phases. Without codoping, the ferromagnetic state was found to be very stable for Cr and Mn doping at concentrations around 10%. These results could be interpreted in terms of a *dd* double-exchange mechanism, suggesting that ferromagnetism in GaN might be possible via partly filled itinerant t_2 bands without free holes in the valence band. As *p* states are not involved directly in this mechanism, it is independent of the energy separation of the valence band and the transition-metal *d* states. However, without coupling to extended hole states, the long-range mediation of magnetic interactions is lost as well. At large doping concentrations, an impurity band of interacting *d* states is formed in the semiconductor band gap. Double exchange is energetically favorable, as the bottom of this impurity band stems from adjacent *d* states with parallel spin orientation. Therefore, the Curie temperature scales like the half-width of the impurity band, which according to the mean-field approximation is proportional to $\sqrt{[\mathrm{Mn}]}$.(240)

According to Ref. 196, this mechanism requires that the t_2 bands with a chance to become itinerant at high Mn concentrations should be partly filled for ferromagnetism in GaN. This is not the case for $Mn^{2+}(d^5)$ in *n*-type GaN, but it is for $Mn^{3+}(d^4)$ in intrinsic and $Mn^{4+}(d^3)$ in *p*-type GaN. As typically even nominally undoped GaN tends to be *n*-type due to residual donors, additional electrons are expected to compensate the $Mn^{3+/2+}$ acceptors, filling the t_2 band and lowering the Curie temperature, in agreement with the calculations of Ref. 240. Hole doping would stabilize the ferromagnetic phase, but a Fermi level in the middle of the t_2 band could be achieved more easily via Cr doping, in case of sufficiently high Cr solubility.(240) Both for $Cr^{2+}(d^4)$ in *n*-type GaN, as well as for $Cr^{3+}(d^3)$ in intrinsic GaN, partly filled t_2 bands would enhance the relevance of the ferromagnetic double-exchange mechanism. Because of the short-range nature of the double-exchange interaction, high doping concentrations are required to achieve ferromagnetism at room temperature via this approach. From the LSDA calculations of Ref. 240, Curie temperatures above room temperature were predicted for GaN:Cr and GaN:Mn with $[\mathrm{Cr}] > 2\%$. Experimentally, these predictions are supported by the observation of room-temperature ferromagnetism in GaN:Cr.(241) However, as free carriers are not involved in this *dd* double exchange any more, injection of spin polarization into nonmagnetic semiconductors and control of the magnetic properties via gates might be possible, but less promising for such materials.

Ferromagnetic clusters

Whereas the prospects for carrier-mediated ferromagnetism in GaN are found to be rather poor, significant experimental efforts have been triggered by the predictions of Ref. 122. These efforts led to the incorporation of very high concentrations of Mn into GaN.(125, 126, 127, 128, 157, 242, 243) Ferromagnetism with Curie temperatures as high as 940 K was reported for some of these GaN:Mn layers. However, high Curie temperatures have

been predicted[190, 244] and measured[153, 245, 246] also for various Mn_xN_y phases, so that the magnetization data alone are insufficient to verify the existence of carrier-mediated ferromagnetism in GaN:Mn films. Small magnetic Mn_xN_y clusters, as observed in Ref. 246 would be effectively invisible for macroscopic characterization techniques like x-ray diffraction or electron or ion scattering spectroscopy. Because of their strong magnetic moments, such clusters, or even small metallic droplets on the GaN:Mn surface[247] could dominate the magnetic properties of the investigated samples.[248] Similar considerations also apply for microscopic inclusions of Cr_xN_y and Fe_xN_y phases, some of which are known to be ferromagnetic at high temperatures.

The magnetic properties of such microscopic inclusions are probably difficult to investigate and to control, but could still enable efficient spin injection also in nitride semiconductors.[244] However, in this type of devices the external control of the magnetic material properties via illumination or electric fields is not possible any more, so that the major advantages of ferromagnetic semiconductors are lost. Depending on the type of device, microscopic ferromagnetic inclusions could as well be created in other well established semiconductors like Si and GaAs,[158] and would eventually provide little advantage compared to the deposition of a ferromagnetic metal contact on a semiconductor material.[249]

7.6 Conclusions

The incorporation of Mn^{2+} spins into GaN and AlN films at high concentrations has been confirmed unambiguously by ESR measurements. The observed ESR transitions are consistent with the spin Hamiltonian for isolated substitutional $^{55}Mn^{2+}$ centers close to the ideal Ga sites of the wurtzite lattice, and coordinated by four N atoms. Displacements from the ideal Ga and Al sites of a few percent of the ideal bond length were estimated from the axial distortion of the $^6A_1$ ground state observed in ESR. A correlation of the axial crystal field parameters and the macroscopic strain in GaN:Mn films was established, and found to agree with the predictions of the superposition theory of crystal fields. At the investigated Mn concentration of 10^{20} cm^{-3}, Mn^{2+} is present as isolated paramagnetic centers, and exchange effects are negligible.

It was concluded from the total Mn concentration observed in ERD measurements in comparison to the density of Mn^{2+} spins observed in ESR, that the majority of Mn ions in pure GaN:Mn samples with a low density of structural defects are not present in the Mn^{2+}, but in the Mn^{3+} state in GaN. Therefore, the assignment of the optical properties of GaN:Mn to Mn^{2+} has to be revised. A level scheme with the $Mn^{2+/3}$ charge-transfer levels located at 1.8 and 2.6 eV above the valence-band edge of GaN and AlN was established and compared to the expectations from the internal reference rule. In addition, an excited state of the neutral Mn^{3+} acceptors was observed at 1.4 eV above the Mn^{3+} ground state.

Trigonal crystal fields, biaxial strain, and Jahn-Teller distortions are probably responsible for the residual linewidth of 3 meV of this optical transitions. Further investigations will be required to determine the ground state fine structure of Mn^{3+} taking into account these orbital interactions. All observations suggest a strongly localized neutral Mn acceptor state in GaN, as compared to the effective-mass like acceptor state of Mn in GaAs. It is therefore questionable whether extrapolation of the Curie temperature in Ref. 122 is valid for materials with such different acceptor charge states as GaAs:Mn and GaN:Mn. The coexistence of Mn^{2+} and valence-band holes is not possible with the developed level scheme. One could argue that alternatively to Mn^{2+} also Mn^{3+} spins could provide local magnetic moments and that holes could be provided via codoping of GaN both with Mn and Mg. Concerning that scenario, however, one should keep in mind the predictions for a $Mn^{3+/4+}$ donor level, suggesting that Mn must be regarded as a deep trap for electrons and holes in GaN and seems *a priori* not suitable for possible applications in spintronics.

The prerequisites of free carrier-mediated ferromagnetism proposed by Ref. 122 seem to be unattainable in GaN:Mn. There is some chance of obtaining sufficiently high hole concentrations via codoping of GaN:Fe with Mg, if the $Fe^{3+/4+}$ donor level falls below the valence-band edge of GaN, or at least below the Mg acceptor level. GaN:Fe:Mg could then show ferromagnetism due to the overlap of the resulting bound magnetic polarons.(212) However, like for ZnO:Mn the stability of the spin-glass component due to the half-filled d-bands of GaN:Fe^{3+} is likely to suppress the carrier-mediated ferromagnetic interaction at the experimentally accessible hole concentrations around 10^{20} cm^{-3}.(234)

Alternatively, double exchange in GaN:Cr at [Cr] $> 2\%$ could lead to room-temperature ferromagnetism. As no host electronic states are directly involved in this exchange mechanism, the calculated Curie temperatures are similar for GaN:Cr and GaAs:Cr .(240) Here, the role of the semiconductor host is merely to provide a matrix that accommodates the Cr ions, and a dielectric background that helps to spread out the atomic d-orbitals. Their occupation and spin state could be manipulated indirectly via illumination, doping or gates in spintronic devices, which do not require spin transport. The solubility, which is typically low for deep defects and high for shallow dopants like GaAs:Mn, and the occurrence of Cr–Cr and Cr–N clustering(190) are important issues that have to be addressed experimentally in this respect. Curie temperatures up to 940 K have been reported for MBE-grown GaN:Mn films. It is most likely that these are related to microscopic magnetic inclusions. Their magnetization could eventually enable efficient spin injection in nitride semiconductors, although this interaction is not expected to respond to optical irradiation or to electric fields from gates.

8 Summary

Various examples of spin-spin interactions have been investigated in this work, and detailed discussions of results for the dangling bond wave function in amorphous germanium, the phosphorus donor state in diamond, and the Mn acceptor state in group III nitrides have been presented in the respective chapters. Also, outlooks concerning the desired properties of dopants and defects in these specific materials have been given at the end of each chapter. In particular, an extensive outlook concerning the prospects of ferromagnetism in GaN:Mn has been presented in Sec. 7.5.

Rather than to reiterate these discussions at this point, we want to stress here the magnitude and usefulness of the various spin-spin interactions for the characterization of this wide variety of defect states. Note, that the ionization energy of the midgap dangling bond state in amorphous germanium is not significantly larger than the phosphorus donor level at 0.6 eV below the conduction band of diamond and the Mn acceptor level at 1.8/2.6 eV above the valence band of Ga. In both latter cases, more extended and more shallow states would be desirable for the envisioned applications that require effective electronic and magnetic doping. However, the electronic and spin wave functions of both defect states were observed to be strongly localized and to undergo significant lattice relaxations.

Microwave energies in the range of $h\nu = 1.8 - 39$ μeV were used to measure spin-spin interactions in the energy range of 2 neV–8 μeV. These were observed as small offsets from the dominant *Zeeman interaction* of the electronic spins with the applied magnetic field. *Hyperfine interactions* of the electronic spins with the nuclear spins of the defect atoms provided the most important clues for the identification of the defect states under investigation. *Fermi contact interactions* of $|A_{\text{iso}}| = 0.20 - 4.6$ μeV were observed in the P-doped diamond film, and $|A_{\text{iso}}| = 0.33$ μeV and $A_{\text{iso}} = -0.80$ μeV in the a-Ge and GaN/AlN:Mn films, respectively. These were accompanied by *dipolar hyperfine* interactions with the defect nuclei of $|A_{\text{aniso}}| = 0.021 - 0.17$ μeV in the phosphorus-doped diamond crystals. From the viewpoint of these hyperfine interactions, the localization of the electron wave function at the central atom was smaller than expected. As no spin density at the nucleus is to be expected for pure d states at all, the observed Fermi-Contact interaction in GaN/AlN:Mn must be interpreted as a result of spin polarization. The magnitude of this effect was found to agree well with the chemical trend based on

the ligand electronegativity. The collective broadening of the spin resonance of dangling bond defects in amorphous germanium could be attributed to hyperfine interactions with more than $n = 100$ ^{73}Ge nuclei of the order of $|A_n| = 0.01$ μeV, indicating a localization radius $r_0 = 3.5$ Å of the defect wave function.

In the amorphous germanium films, these results could clearly be separated from *dipolar interactions* of the order of $|A_n| = 0.01$ μeV between the electronic spins, from *distant dipolar hyperfine interactions* with remote nuclear spins of $|A_{\text{eff}}| \leq 6$ neV, and from broadening due to fluctuations of the *spin-orbit interaction* of $0.02 - 0.5$ μeV. Zero-field splittings of $D = 3.7$ μeV were observed at an $S = 1$ high-spin state in diamond, and related to *dipolar interactions* between two adjacent electronic spins. The zero-field splittings of $D = 2.4 - 7.4$ μeV at Mn^{2+}-centers in GaN and AlN were related to an axial distortion of the spin states and successfully described by the weak-field scheme of *spin-orbit interactions* via excited configurations.

The method of electron spin resonance was not successful for the characterization of the Mn^{3+} ground states in the group III nitrides, most probably because of the strong *crystal field interaction* of its ground state wave function with tetrahedral and trigonal crystal fields of the wurtzite lattice. Strain broadening, which is probably causing the optical linewidth of the internal transition of Mn^{3+} of 3 meV in GaN:Mn is expected to strongly affect the spin-spin and spin-orbit interactions of the Mn^{3+} ground state, and therefore inhibit the investigation via X-band ESR. Therefore optical methods were employed to investigate the ground and excited states of GaN:Mn^{3+}. The conclusions of this study are based on the combination of electron spin resonance measurements of Mn^{2+}, and of optical measurement at the same samples with much larger energies. The results suggests that the theoretical prediction of room-temperature ferromagnetism due to *carrier-mediated exchange interactions* cannot be fulfilled in Mn-doped III nitrides.

This shows the significance of the measurement of spin-spin interactions even at very small energies for today's materials science and for the development of modern electronic device applications.

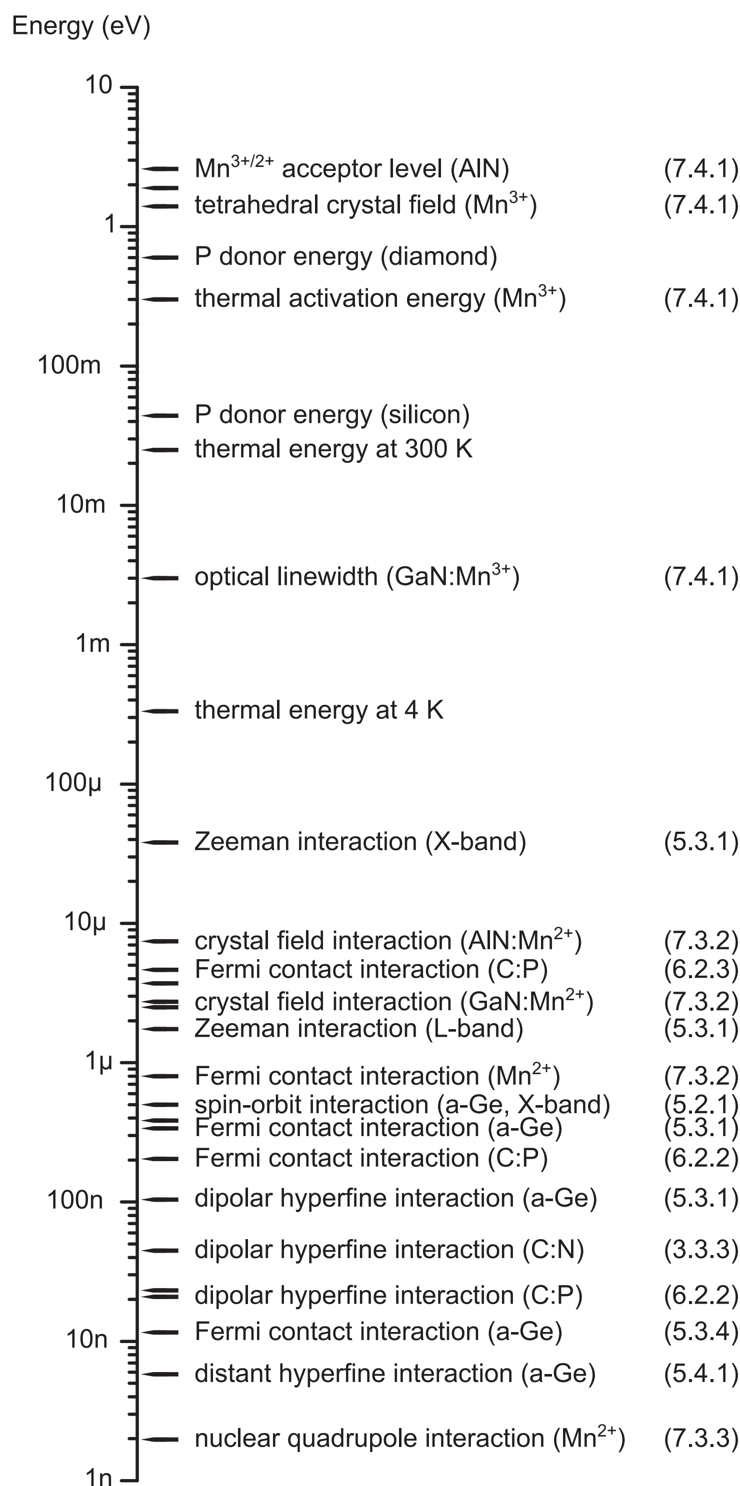

Figure 8.1: Energy scale of the interactions investigated in this work. Dipolar and Fermi contact hyperfine interactions were observed in the energy range from 0.01 to 5 μeV, and fine structure interactions from 0.01 to 5 μeV. The study of the Mn^{3+} states in GaN and AlN require much larger energies than the Zeeman energy with $S = 1/2$ in an X-band ESR spectrometer.

List of publications

1. C. E. Zybill, B. Li, F. Koch, and T. Graf, *Substrate influence on the domain structure of* (111) *PZT* $PbTi_{0.75}Zr_{0.25}O_3$ *films*, phys. stat. sol. (a) **177** (2000), 303.

2. M. W. Bayerl, M. S. Brandt, T. Graf, O. Ambacher, J. A. Majewski, and M. Stutzmann, *g-values of effective mass donors in* $Al_xGa_{1-x}N$ *alloys*, Phys. Rev. B **63** (2001), 165204.

3. T. Graf, M. S. Brandt, C. E. Nebel, M. Stutzmann, and S. Koizumi, *Electrically detected magnetic resonance studies of phosphorus doped diamond*, Physica B **308** (2001), 593.

4. A. Link, T. Graf, R. Dimitrov, O. Ambacher, M. Stutzmann, Y. Smorchkova, U. Mishra, and J. Speck, *Transport properties of two-dimensional electron gases induced by spontaneous and piezoelectric polarization in AlGaN/GaN heterostructures*, phys. stat. sol. (b) **228** (2001), 603.

5. T. Graf, M. S. Brandt, C. E. Nebel, M. Stutzmann, and S. Koizumi, *Electron spin resonance of phosphorus in n-type diamond* (invited), phys. stat. sol. (a) **193** (2002), 434.

6. A. Link, T. Graf, O. Ambacher, A. Jimenez, E. Calleja, Y. Smorchkova, J. Speck, U. Mishra, and M. Stutzmann, *Transport properties of 2DEGs in AlGaN/GaN heterostructures: Spin splitting and occupation of higher subbands*, phys. stat. sol. (b) **234** (2002), 805, and phys. stat. sol. (c) **1** (2002), 805.

7. A. Janotta, R. Janssen, M. Schmidt, T. Graf, L. Görgens, C. Hammerl, S. Schreiber, G. Dollinger, A. Bergmaier, B. Stritzker, and M. Stutzmann, *Dependence of the doping efficiency on material composition in n-type a-*SiO_x*:H*, J. Non-Cryst. Solids **299-302** (2002), 579.

8. T. Graf, M. Gjukic, M. S. Brandt, M. Stutzmann, and O. Ambacher, *The* $Mn^{3+/2+}$ *acceptor level in group III-nitrides*, Appl. Phys. Lett. **81** (2002), 5159.

9. A. Lehner, F. Kohl, S. A. Franzke, T. Graf, M. S. Brandt, and M. Stutzmann, *Photoconductivity and spin-dependent photoconductivity of hydrosilylated* (111) *silicon surfaces*, Appl. Phys. Lett. **82** (2003), 565.

10. S. T. B. Goennenwein, T. Graf, T. Wassner, M. S. Brandt, M. Stutzmann, J. B. Phillipp, R. Gross, M. Krieger, K. Zürn, P. Ziemann, A. Koeder, S. Frank, W. Schoch, and A. Waag, *Spin wave resonance in* $Ga_xMn_{1-x}As$, Appl. Phys. Lett. **82** (2003), 730.

11. A. Koeder, S. Frank, W. Schoch, V. Avrutin, W. Limmer, K. Thonke, S. Brotzmann, H. Bracht, S. T. B. Goennenwein, T. Graf, T. Wassner, M. Brandt, M. Stutzmann, M. Krieger, K. Zürn, P. Ziemann, and A. Waag, *Carrier concentration and lattice constant of GaMnAs*, extended abstract for the 12th Euro-MBE workshop, Bad Hofgastein, Austria (2003).

12. T. Graf, M. Gjucik, M. Hermann, M. S. Brandt, M. Stutzmann, and O. Ambacher, *Spin resonance investigations of* Mn^{2+} *in wurtzite GaN and AlN films*, Phys. Rev. B **67** (2003), 165215.

13. S. T. B. Goennenwein, T. Graf, T. Wassner, M. S. Brandt, M. Stutzmann, A. Koeder, S. Frank, W. Schoch, and A. Waag, *Ferromagnetic resonance in* $Ga_{1-x}Mn_xAs$, Journal of Superconductivity: Incorporating Novel Magnetism (JOSC) **16** (2003), 75.

14. T. Graf, M. Gjukic, L. Görgens, O. Ambacher, M. S. Brandt, and M. Stutzmann, *Charge transfer at the Mn acceptor level in GaN*, Journal of Superconductivity: Incorporating Novel Magnetism (JOSC) **16** (2003), 83.

15. T. Graf, M. Gjucik, L. Görgens, J. B. Philipp, M. Hermann, O. Ambacher, M. S. Brandt, and M. Stutzmann, *Growth and characterization of GaN:Mn epitaxial films*, J. Appl. Phys. **93** (2003), 9697.

16. T. Graf, M. S. Brandt, C. R. Miskys, J. A. Garrido, M. Hermann, O. Ambacher, M. Eickhoff, C. E. Nebel, S. Koizumi, and M. Stutzmann, *Electrically detected magnetic resonance and its application to diamond* (invited), extended abstract for the 54th DeBeers diamond conference, Cambridge, UK (2003).

17. S. Baldovino, S. Nokhrin, G. Scarel, M. Fanciulli, T. Graf, and M. S. Brandt, *Investigation of point defects at the high-k oxides*/(100)*Si interface by electrically detected magnetic resonance*, J. Non-Cryst. Solids **322** (2003), 168.

18. T. Graf, S. T. B. Goennenwein, and M. S. Brandt, *Prospects for carrier-mediated ferromagnetism in GaN*, phys. stat. sol.(b) **239** (2003), 277.

19. A. Janotta, R. Janssen, M. Schmidt, T. Graf, M. Stutzmann, L. Görgens, A. Bergmaier, G. Dollinger, C. Hammerl, S. Schreiber, and B. Stritzker, *The doping efficiency in a-SiO_x:H*, submitted to Phys. Rev. B.

20. T. Graf, T. Ishikawa, K. M. Itoh, E. E. Haller, M. Stutzmann, and M. S. Brandt, *Hyperfine interaction at dangling-bonds in amorphous germanium*, Phys. Rev. B **68** (2003), 205208.

21. J. B. Philipp, P. Majewski, L. Alff, A. Erb, R. Gross, T. Graf, M. S. Brandt, J. Simon, T. Walther, W. Mader, D. Topwal and D. D. Sarma, *Structural and doping effects in the half-metallic double perovskite A_2CrWO_6*, Phys. Rev. B **68** (2003), 144431.

22. S. T. B Goennenwein, T. Wassner, T. Graf, H. Huebl, J. B. Philipp, M. Opel, R. Gross, A. Koeder, W. Schoch, A. Waag, and M. S. Brandt, *Hydrogen control of ferromagnetism in a dilute magnetic semiconductor*, submitted to Phys. Rev. Lett.

23. M. S. Brandt, S. T. B. Goennenwein, T. A. Wassner, F. Kohl, A. Lehner, H. Huebl, T. Graf, M. Stutzmann, A. Koeder, W. Schoch, and A. Waag *Passivation of Mn acceptors in GaMnAs*, submitted to Appl. Phys. Lett.

24. S. T. B. Goennenwein, T. Graf, M. S. Brandt, and M. Stutzmann, *Verfahren zur Erzeugung und Charakterisierung von spinpolarisierten Ladungsträgersystemen und darauf beruhende Bauelemente*, Deutsche Patent-Offenlegungsschrift (2001), DE 10019697.

25. M. S. Brandt, S. T. B. Goennenwein, T. Graf, and H. Huebl, *Manipulation der magnetischen Eigenschaften von Halbleitern und magnetoelektronischen Bauelementen*, Deutscher Patentantrag (2003).

Acknowledgements

Finally, I would like to express thanks to all those people, who gave their important contributions to this work:

- **Prof. Dr. Martin Stutzmann**, who offered me the position as a PhD student at the WSI. He provided me with profound and up-to-date information and many innovative ideas that helped to keep my investigations focused on key topics of modern semiconductor physics.
- My great supervisor **Priv.-Doz. Dr. Martin S. Brandt**, who taught me not only the basic and advanced features of resonant spins. He supported my scientific work at all stages, and cared a lot about the personal needs of all of his students at the same time.
- **Tomomi Ishikawa**, **Prof. Dr. Kohei M. Itoh**, and **Prof. Dr. Eugene E. Haller**, who provided me with the very special isotope-engineered a-Ge samples.
- **Priv.-Doz. Dr. habil. Christoph E. Nebel** and **Prof. Dr. Satoshi Koizumi**, who gave me the opportunity to investigate state-of-the-art n-type diamond films.
- **Mario Gjukic**, **Martin Hermann**, **Dr. Alexandre P. Lima** and **Prof. Dr. Oliver Ambacher**, who managed the growth of pure and n-type GaN:Mn and AlN:Mn films and contributed significantly to their characterization.
- **Dr. Thomas Frank**, **Michael Weidner**, and **Akad. Dir. Dr. G. Pensl** for their interesting samples and the insights into DLTS and PL measurements of point defects in irradiated 4H-and 6H-SiC. I am sorry that our results did not make it into this thesis.
- **Angela Link** and **Claudio R. Miskys** for their quite challenging high-mobility 2DEGs in AlGaN and the ^{17}O-doped GaN samples, which also did not make it into this thesis.
- **Dr. Lutz Görgens** for the determination of the Mn concentrations of our GaN:Mn films via ERD.

- **Dr. J. Boris Philipp** and **Dr. Matthias Opel** for the magnetization measurements and their patience with the SQUID.
- **Dr. Martin Straßburg** and **Priv.-Doz. Dr. Axel Hoffmann** for their low-temperature optical transmission measurements.
- **Estelle Bauer** for her technical assistance with the 2.00 GHz spectrometer.
- **Dr. Sebastian T. B. Gönnenwein**, for the great discussions and brainstorming sessions. In the end, we almost managed to not get excited about the same physics at the same time.
- My former colleagues **Dr. Martin Bayerl**, **Dr. Günther Vogg**, **Dr. Andreas Janotta**, **Dr. Christopher Eisele**, and **Dr. Roland Zeisel**, who were the backbone of E25 during my PhD work.
- **Hans G. Hübl**, head of the ESR lab, **Sylvia Baldovino**, **Andrea Lehner**, **Thomas Wassner**, **Peter Huber** and **Florian Kohl**, who will definitely continue to keep the spinner subgroup as nice and active as always in the future.
- **Andrea Mitchell**, **Stephan Hofmann**, **Stefan Frantzke**, **Andreas Härtl**, **Olaf Weidemann**, **Barbara Baur**, **Stefan Stufler**, and **Dr. Bohuslav Rezek**, who let me participate in their interesting work at the AFM.
- **Veronika Enter** and **Liane Lindner**, who took care of my needs behind the curtains.
- **Heidi Büttner**, for the access to her apartment in case of need for concentration.
- My lovely family **Irene**, **Katrin**, and **Christina Graf**, who certainly needed to have a lot of patience with me, particularly in the final stages of this work, and my parents **Ingrid** and **Dr. Lothar Graf** for all their love and care.

This work was supported financially by the Deutsche Forschungsgemeinschaft (SFB 348).

Bibliography

[1] P. Y. Yu and M. Cardona, *Fundamentals of semiconductors* (Springer, Berlin, 2003), 3rd ed.

[2] J. M. Spaeth and H. Overhof, *Point defects in semiconductors and insulators, theoretical calculation of hyperfine interactions: Mapping of the impurity wave function*, vol. 51 (Springer, Heidelberg, 2003).

[3] C. Hermann and C. Weisbuch, *$\vec{k} \cdot \vec{p}$ perturbation theory in III-V compounds and alloys: A reexamination*, Phys. Rev. B **15**, 823 (1977).

[4] M. W. Bayerl, M. S. Brandt, T. Graf, O. Ambacher, J. A. Majewski, and M. Stutzmann, *g-values of effective mass donors in $Al_xGa_{1-x}N$ alloys*, Phys. Rev. B **63**, 165204 (2001).

[5] W. Kohn and J. M. Luttinger, *Hyperfine splitting of donor states in silicon*, Phys. Rev. **97**, 883 (1955).

[6] J. L. Ivey and R. L. Mieher, *Ground-state wave function for shallow-donor electrons in silicon. I. Isotropic electron-nuclear-double-resonance hyperfine interactions*, Phys. Rev. B **11**, 822 (1975).

[7] G. Feher, *Electron spin resonance experiments on donors in silicon I. Electronic structure of donors by the electron nuclear double resonance technique*, Phys. Rev. B **114**, 1219 (1959).

[8] K. Kopitzki, *Einführung in die Festkörperphysik* (B. G. Teubner Stuttgart, 1993).

[9] J. A. Weil, J. R. Bolton, and J. E. Wertz, *Electron paramagnetic resonance* (Wiley, New York, 1994).

[10] W. V. Smith, P. P. Sorokin, I. L. Gelles, and G. J. Lasher, *Electron spin resonance of nitrogen donors in diamond*, Phys. Rev. **115**, 1546 (1959).

[11] H. J. Bower and M. C. R. Symons, *Electron spin resonance spectra associated with nitrogen in diamonds*, Nature **210**, 1038 (1966).

[12] G. D. Watkins, *What we have learned about intrinsic defects in silicon: A help in understanding diamond?*, phys. stat. sol. (a) **186**, 167 (2001).

[13] A. Abragam and B. Bleaney, *Electron paramagnetic resonance of transitions ions* (Oxford University Press, Oxford, 1970).

[14] C. Rudowicz, *Concept of spin Hamiltonian, form of zero field splitting and electronic Zeeman Hamiltonians and relations between parameters used in EPR. A critical review*, Magnetic Resonance Review **13**, 1 (1987).

[15] C. A. Bates and K. W. H. Stevens, *Localised electron states in semiconductors*, Rep. Prog. Phys. **49**, 783 (1986).

[16] M. Cook and C. T. White, *Hyperfine interaction in cluster models of the P_b defect center*, Phys. Rev. B **38**, 9674 (1988).

[17] J. J. Sakurei, *Modern quantum mechanics* (Addison-Wesley, New York, 1994).

[18] J. W. Orton, *Electron paramagnetic resonance* (Iliffe Books, London, 1968).

[19] G. E. Pake and T. L. Estle, *The physical principles of electron paramagnetic resonance* (Benjamin, Reading, 1973).

[20] J. H. V. Vleck, *The theory of electric and magnetic susceptibilities* (Oxford, 1952).

[21] W. E. Carlos, J. A. F. Jr., M. A. Khan, D. T. Olson, and J. N. Kuznia, *Electron-spin-resonance studies of donors in wurtzite GaN*, Phys. Rev. B **48**, 17878 (1993).

[22] W. C. Zheng, S. Y. Wu, and J. Zi, *Defect structures for Fe^{3+}, Mn^{2+}, and Ni^{3+} impurities in wurtzite GaN crystals*, Z. Naturforsch. A **56**, 473 (2001).

[23] G. Hofmann, A. Keckes, and J. Weber, *Manganese-doped $GaAs_{1-x}P_x$ in the compositional range* $0.25 < x < 1$, Semicond. Sci. Technol. **8**, 1523 (1993).

[24] M. Stutzmann and D. K. Biegelsen, *Microscopic nature of coordination defects in amorphous silicon*, Phys. Rev. B **40**, 9834 (1989).

[25] J. H. N. Loubser and J. A. van Wyk, *Electron spin resonance in the study of diamond*, Rep. Prog. Phys. **41**, 1201 (1978).

[26] J. H. V. Vleck, *The dipolar broadening of magnetic resonance lines*, Phys. Rev. **74**, 1168 (1948).

[27] S. Blundell, *Magnetism in condensed matter* (Oxford University Press, Oxford, 2001).

[28] B. Pilawa, *New concepts for molecular magnets*, Ann. Phys. **8**, 191 (1999).

[29] S. Greulich-Weber, *EPR and ENDOR investigations of shallow impurities in SiC polytypes*, phys. stat. sol. (a) **162**, 95 (1997).

[30] P. W. Anderson and P. R. Weiss, *Exchange narrowing in paramagnetic resonance*, Rev. Mod. Phys. **25**, 269 (1953).

[31] U. Gerstmann, A. T. Blumenau, and H. Overhof, *Transition metal defects in group-III nitrides: An ab initio calculation of hyperfine interactions and optical transitions*, Phys. Rev. B **63**, 075204 (2001).

[32] P. W. Atkins and M. C. R. Symonis, *The structure of inorganic radicals* (Elsevier, Amsterdam, 1967).

[33] E. Fermi, *Über die magnetischen Momente der Atomkerne*, Z. Phys. **60**, 320 (1930).

[34] G. Breit, *Possible effect of nuclear spin on X-ray terms*, Phys. Rev. B **35**, 1447 (1930).

[35] C. P. Slichter, *Principles of magnetic resonance with examples from solid state physics* (Harper and Row, New York, 1963).

[36] S. A. Kajihara, A. Antonelli, J. Bernholc, and R. Car, *Nitrogen and potential n-type dopants in diamond*, Phys. Rev. Lett. **66**, 2010 (1991).

[37] M. S. Brandt, *Spinabhängiger Transport und Rekombination in Halbleitern*, Ph.D. thesis, Max-Planck-Institut für Festkörperforschung Stuttgart (1992).

[38] J. Wrachtrup, C. von Borczyskowski, J. Bernard, M. Orrit, and R. Brown, *Optical detection of magnetic resonance in a single molecule*, Nature **363**, 244 (1993).

[39] M. S. Brandt, R. T. Neuberger, and M. Stutzmann, *Spin-dependent capacitance of silicon field-effect transistors*, Appl. Phys. Lett. **76**, 1467 (2000).

[40] C. Boehme and K. Lips, *Spin-dependent recombination – an electronic readout mechanism for solid state quantum computers*, phys. stat. sol. (b) **233**, 427 (2002).

[41] D. J. Lepine, *Spin-dependent recombination on silicon surface*, Phys. Rev. B **6**, 1972 (436).

[42] D. Kaplan, I. Solomon, and N. F. Mott, *Explanation of the large spin-dependent recombination effect in semiconductors*, J. Phys. Lett. (France) **39**, L51 (1978).

[43] A. Lehner, F. Kohl, S. A. Franzke, T. Graf, M. S. Brandt, and M. Stutzmann, *Photoconductivity and spin-dependent photoconductivity of hydrosilylated (111) silicon surfaces*, Appl. Phys. Lett. **82**, 565 (2003).

[44] P. Kanschat, *ESR und spinabhängige Rekombination*, Ph.D. thesis, Philipps-Universität Marburg (2000).

[45] K. L. Brower, *^{29}Si hyperfine structure of unpaired spins at the Si/SiO_2 interface*, Appl. Phys. Lett. **43**, 1111 (1983).

[46] W. E. Carlos, *Paramagnetic centers at Si-SiO_2 interfaces in silicon-on-insulator films*, Appl. Phys. Lett. **50**, 1450 (1987).

[47] E. H. Poindexter, P. J. Caplan, B. E. Deal, and R. R. Razouk, *Interface states and electron spin resonance centers in thermally oxidized (111) and (100) silicon wafers*, J. Appl. Phys. **52**, 879 (1981).

[48] T. D. Mishima, P. M. Lenahan, and W. Weber, *Do P_{b1} centers have levels in the Si band gap? Spin-dependent recombination study of the P_{b1} "hyperfine spectrum"*, Appl. Phys. Lett. **76**, 3771 (2000).

[49] A. Stesmans and V. Afanas'ev, *Electrical activity of interfacial paramagnetic defects in thermal (100) Si/SiO_2*, Phys. Rev. B **57**, 10030 (1998).

[50] D. K. Biegelsen and M. Stutzmann, *Hyperfine studies of dangling bonds in amorphous silicon*, Phys. Rev. B **33**, 3006 (1986).

[51] T. Umeda, S. Yamasaki, J. Isoya, and K. Tanaka, *Electron-spin resonance center of dangling bonds in undoped a-Si:H*, Phys. Rev. B **59**, 4849 (1999).

[52] H. Yokomichi, I. Hirabayashi, and K. Morigaki, *Electron-nuclear double resonance of dangling-bond centers in a-Si:H*, Solid State Commun. **61**, 697 (1987).

[53] H. Yokomichi and K. Morigaki, *Observation of different types od dangling bonds and their photo-creation in a-Si:H, as elucidated by ENDOR measurements*, J. Non-Cryst. Solids **97-98**, 67 (1987).

[54] N. Ishii and T. Shimizu, *Origin of the ESR signal with* $g = 2.0055$ *in amorphous silicon*, Phys. Rev. B **42**, 9697 (1990).

[55] P. A. Fedders, D. A. Drabold, P. Ordejón, G. Fabricius, D. Sańchez-Portal, E. Artacho, and J. M. Soler, *Application of local-spin-density approximation to a-Si and tetrahedal a-C*, Phys. Rev. B **60**, 10594 (1999).

[56] M. Stutzmann and J. Stuke, *Paramagnetic states in doped amorphous silicon and germanium*, Solid State Comm. **47**, 635 (1983).

[57] F. C. Marques, M. M. de Lima Jr., and P. C. Taylor, *Optically excited paramagnetic centers in hydrogenated amorphous germanium*, J. Non-Crys. Solids **266-269**, 717 (2000).

[58] C. F. O. Graeff, M. Stutzmann, and M. S. Brandt, *Spin-dependent photoconductivity in hydrogenated amorphous germanium and silicon-germanium alloys*, Phys. Rev. B **49**, 11028 (1994).

[59] B. Movaghar, L. Schweitzer, and H. Overhof, *Electron spin resonance in amorphous Germanium and Silicon*, Phil. Mag. B **37**, 683 (1978).

[60] R. Vrijen, E. Yablonovitch, K. Wang, H. W. Jiang, A. Balandin, V. Roychowdhury, T. Mor, and D. DiVincenzo, *Electron-spin-resonance transistors for quantum computing in silicon-germanium heterostructures*, Phys. Rev. A **62**, 012306 (2000).

[61] K. Itoh, W. L. Hansen, E. E. Haller, J. W. Farmer, V. I. Ozhogin, A. Rudnev, and A. Tikhomirov, *High purity isotopically enriched* ^{70}Ge *and* ^{74}Ge *single crystals: isotope separation, purification and growth*, J. Mater. Res. **8**, 1341 (1993).

[62] M. Stutzmann and S. K. Biegelsen, *Electron-spin-lattice relaxation in amorphous silicon and germanium*, Phys. Rev. B **28**, 6256 (1983).

[63] N. Kishimoto, K. Morigaki, and K. Murakami, *Conductivity change due to electron spin resonance in amorphous Si-Au system*, J. Phys. Soc. Jap. **50**, 1970 (1981).

[64] M. S. Brandt and M. Stutzmann, *Spin-dependent conductivity in amorphous hydrogenated silicon*, Phys. Rev. B **43**, 5184 (1991).

[65] K. Lips, S. Schütte, and W. Fuhs, *Microwave-induced resonant changes in transport and recombination in hydrogenated amorphous silicon*, Phil. Mag. B **65**, 945 (1992).

[66] S. Hasegawa and S. Yazaki, *Connection between ESR and electrical conduction in amorphous Si films*, Phil. Mag. B **45**, 347 (1982).

[67] B. Movaghar and L. Schweitzer, *ESR and conductivity in amorphous germanium and silicon*, phys. stat. sol. (b) **80**, 491 (1977).

[68] N. F. Mott and E. A. Davis, *Electronic processes in non-crystalline materials* (Claredon Press, Oxford, 1971).

[69] R. G. Barnes and W. V. Smith, *Electric field gradients of atomic p electrons*, Phys. Rev. **93**, 95 (1954).

[70] G. A. N. Connell and J. R. Pawlik, *Use of hydrogenation in structural and electronic studies of gap states in amorphous germanium*, Phys. Rev. B **13**, 787 (1976).

[71] L. Kuebler, G. Gewinner, J. J. Koulmann, and A. Jaéglé, *EPR study on amorphous germanium*, phys. stat. sol. (b) **78**, 149 (1976).

[72] J. Stuke, *ESR in amorphous germanium and silicon*, Amorphous and liquid semiconductors **7**, 407 (1977).

[73] S. Lebib, M. Schoisswohl, J. L. Cantin, and H. J. von Bardeleben, *SiGe/SiGeO$_2$ interface defects*, Thin Solid Films **294**, 242 (1997).

[74] P. R. Cullis and J. R. Marko, *Electron paramagnetic resonance properties of n-type silicon in the intermediate impurity-concentration range*, Phys. Rev. B **11**, 4184 (1975).

[75] H. Dersch, L. Schweitzer, and J. Stuke, *Recombination processes in a-Si:H: Spin-dependent photoconductivity*, Phys. Rev. B **28**, 4678 (1983).

[76] M. S. Brandt, M. W. Bayerl, M. Stutzmann, and C. F. O. Graeff, *Electrically detected magnetic resonance of a-Si:H at low magnetic fields: the influence of hydrogen on the dangling bond resonance*, J. Non-Cryst. Solids **227-230**, 343 (1998).

[77] R. J. McEachern and J. A. Weil, *^{17}O hyperfine interaction for the $[GeO_4]^-_{I,II}$ and $[GeO_4/Li]^0_{A,C}$ centers in an enriched crystal of α-quarz*, Phys. Rev. B **49**, 6698 (1994).

[78] C. W. Myles, *Dynamics of a system of randomly distributed spins with multipolar interactions: Application to dipolar systems*, Phys. Rev. B **14**, 14 (1976).

[79] A. F. Kip, C. Kittel, R. A. Levy, and A. M. Portis, *Electronic structure of F centers: Hyperfine interactions in electron spin resonance*, Phys. Rev. **91**, 1066 (1953).

[80] C. Kittel and E. Abrahams, *Dipolar broadening of magnetic resonance lines in magnetically diluted crystals*, Phys. Rev. **90**, 238 (1953).

[81] M. H. Cohen and F. Reif, *Quadrupole effects in nuclear magnetic resonance studies of solids*, Solid State Physics **5**, 321 (1957).

[82] A. M. Stoneham, *Shapes of inhomogenously broadened resonance lines in solids*, Rev. Mod. Phys. **41**, 82 (1969).

[83] D. K. Wilson, *Electron spin resonance experiments on shallow donors in germanium*, Phys. Rev. **134**, A265 (1964).

[84] P. A. Fedders, *Static electric field gradients and associated magnetic-resonance line-shape changes due to a random distribution of point defects*, Phys. Rev. B **11**, 1020 (1975).

[85] D. Freude and H. Schmiedel, *NMR lineshapes of magnetic systems*, phys. stat. sol. (b) **54**, 631 (1972).

[86] M. Stutzmann, *Amorphous semiconductors*, vol. 3, p. 657 of *Handbook on Semiconductors, ed. by T. S. Moss* (Elsevier Science B.V., 1994).

[87] G. S. Jackel, J. J. Christiansen, and W. Gordy, *Structure and* ^{73}Ge *coupling of the* GeH_3 *radical*, J. Chem. Phys. **47**, 4274 (1967).

[88] G. S. Jackel and W. Gordy, *Electron spin resonance of free radicals formed from group-IV and group-V hydrides in inert matrices at low temperatures*, J. Chem. Phys. **47**, 4274 (1967).

[89] J. D. Cohen, J. P. Harbison, and K. W. Wecht, *Identification of the dangling-bond state within the mobility gap of a-Si:H by depletion-width-modulated ESR spectroscopy*, Phys. Rev. Lett. **48**, 109 (1982).

[90] S. Hasegawa and Y. Imai, *Annealing effects on relationships between ESR electrical and optical properties in a-Si:H*, Phil. Mag. B **45**, 347 (1982).

[91] L. G. Wang and A. Zunger, *Phosphorus and sulphur doping of diamond*, Phys. Rev. B **66**, R161202 (2002).

[92] S. Koizumi, M. Kamo, Y. Sato, H. Ozaki, and T. Inuzuka, *Growth and characterization of phosphorous doped (111) homoepitaxial diamond thin films*, Appl. Phys. Lett. **71**, 1065 (1997).

[93] A. Tajani, E. Gheeraert, N. Casanova, E. Bustarret, J. A. Garrido, G. Rumen, C. E. Nebel, M. E. Newton, and D. Evans, *Characterization of n-type doped homoepitaxial diamond thin films*, phys. stat. sol. (a) **193**, 541 (2002).

[94] K. Haenen, K. Meykens, M. Nesládek, G. Knuyt, C. Quaeyhaegens, L. M. Stals, S. Koizumi, and E. Gheeraert, *Low temperature photoconductivity detection of phosphorus in diamond*, phys. stat. sol (a) **174**, 53 (1999).

[95] H. Sternschulte, K. Thonke, R. Sauer, and S. Koizumi, *Optical evidence for 630-meV phosphorus donor in synthetic diamond*, Phys. Rev. B **59**, 12924 (1999).

[96] N. Teofilov, R. Sauer, K. Thonke, and S. Koizumi, *Donor phosphorus-related exciton luminescense in CVD diamond*, submitted to Phys. Rev. Lett.

[97] S. Koizumi, K. Watanabe, M. Hasegawa, and H. Kanda, *Ultraviolet emission from a diamond pn junction*, Science **292**, 1899 (2001).

[98] S. Koizumi, T. Teraji, and H. Kanda, *Phosphorus-doped chemical vapor deposition of diamond*, Diam. Rel. Mater. **9**, 935 (2000).

[99] E. Gheeraert, S. Koizumi, T. Teraji, H. Kanda, and M. Nesládek, *Electronic states of boron and phosphorus in diamond*, phys. stat. sol. (a) **174**, 39 (1999).

[100] M. Hasegawa, T. Teraji, and S. Koizumi, *Lattice location of phosphorus in n-type homoepitaxial diamond films grown by chemical-vapor deposition*, Appl. Phys. Lett. **79**, 3068 (2001).

[101] N. D. Samsonenko, V. V. Tokil, and S. V. Gorban, *Electron paramagnetic resonance of phosphorus in diamond*, Soviet Phys. Solid State **33**, 1409 (1991).

[102] J. Isoya, H. Kanda, M. Askaishi, Y. Morita, and T. Ohshima, *ESR studies of incorporation of phosphorus into high-pressure synthetic diamond*, Diamond and Rel. Mat. **6**, 356 (1997).

[103] M. E. Zvanut, W. E. Carlos, J. A. F. Jr., K. D. Jamison, and R. P. Hellmer, *Identification of phosphorus in diamond thin films using electron paramagnetic resonance spectroscopy*, Appl. Phys. Lett. **65**, 2287 (1994).

[104] N. Casanova, E. Gheeraert, A. Deneuville, C. Uzan-Saguy, and R. Kalish, *ESR study of phosphorus implanted type IIa diamond*, phys. stat. sol. (a) **181**, 5 (2000).

[105] R. Zeisel, *Optoelectronic properties of defects in diamond and AlGaN alloys*, Ph.D. thesis, Walter Schottky Institut (2000).

[106] R. C. Barklie, M. Collins, and S. R. P. Silva, *EPR linewidth variation, spin relaxation times, and exchange in amorphous hydrogenated carbon*, Phys. Rev. B **61**, 3546 (2000).

[107] X. Zhou, G. D. Watkins, K. M. M. Rutledge, R. P. Messmer, and S. Chawla, *Hydrogen-related defects in polycrystalline CVD diamond*, Phys. Rev. B **54**, 7881 (1996).

[108] C. F. O. Graeff, E. Rohrer, C. E. Nebel, M. Stutzmann, H. Güttler, and R. Zachai, *ESR and LESR studies in CVD diamond*, Mat. Res. Soc. Symp. Proceed. **423**, 495 (1996).

[109] R. Jones, J. E. Lowther, and J. Goss, *Limitations to n-type doping in diamond: The phosphorus-vacancy complex*, Appl. Phys. Lett. **69**, 2489 (1996).

[110] J. Goss, *Calculated electrical levels of point defects in CVD diamond*, presentation at the De Beer's Diamond Conference 2003, Cambridge.

[111] D. K. Wilson and G. Feher, *Electron spin resonance experiments on donors in silicon III. Investigation of excited states by the application of uniaxial stress and their importance in relaxation processes*, Phys. Rev. **124**, 1068 (1961).

[112] S. Sque and R. Jones, *Electrical activity of chalcogen and pnictogen hydrogen defects in diamond*, presentation at the De Beer's Diamond Conference 2003, Cambridge.

[113] R. Zeisel, M. W. Bayerl, S. T. B. Goennenwein, R. Dimitrov, O. Ambacher, M. S. Brandt, and M. Stutzmann, *DX behavior of Si in AlN*, Phys. Rev. B **61**, R16283 (2000).

[114] C. R. Miskys, J. A. Garrido, C. E. Nebel, M. Hermann, O. Ambacher, M. Eickhoff, and M. Stutzmann, *AlN/diamond heterojunction diode*, Appl. Phys. Lett. **82**, 290 (2003).

[115] O. Madelung, ed., *Landolt-Börnstein: Numerical data and functional relationships, condensed matter*, vol. 17, 22, and 41, Parts a and b (Springer-Verlag, Berlin, 1982).

[116] B. J. Coomer, J. P. Goss, R. Jones, S. Öberg, and P. R. Briddon, *Identification of the tetra-interstitial in silicon*, J. Phys.: Condens. Matter **13**, L1 (2001).

[117] E. Kulatov, H. Nakayama, H. Mariette, H. Ohta, and Y. A. Uspenskii, *Electronic structure, magnetic ordering, and optical properties of GaN and GaAs doped with Mn*, Phys. Rev. B **66**, 045203 (2002).

[118] A. Zunger, *Electronic structure of 3d transition-atom impurities in semiconductors*, Solid State Phys. **39**, 275 (1986).

[119] M. Oestreich, *Injecting spin into electronics*, Nature **402**, 735 (1999).

[120] S. A. Wolf, D. D. Awschalom, R. A. Buhrman, J. M. Daughton, S. von Molnár, M. L. Roukes, A. Y. Chtchelkanova, and S. M. Treger, *Spintronics: A spin-based electronics vision for the future*, Science **294**, 1488 (2001).

[121] Y. Ohno, D. K. Young, B. Beschoten, F. Matsukura, H. Ohno, and D. D. Awschalom, *Electrical spin injection in a ferromagnetic semiconductor heterostructure*, Nature (London) **402**, 790 (1999).

[122] T. Dietl, H. Ohno, and F. Matsukura, *Hole-mediated ferromagnetism in tetrahedrally coordinated semiconductors*, Phys. Rev. B **63**, 195205 (2001).

[123] T. Jungwirth, J. König, J. Sinova, J. Kučera, and A. H. MacDonald, *Curie temperature trends in (III,Mn)V ferromagnetic semiconductors*, Phys. Rev. B **66**, 012402 (2002).

[124] M. Zając, R. Doradziński, J. Gosk, J. Szczytko, M. Lefeld-Sosnowska, M. Kamińska, and A. Twardowski, *Magnetic and optical properties of GaMnN magnetic semiconductor*, Appl. Phys. Lett. **78**, 1276 (2001).

[125] T. Sasaki, S. Sonoda, Y. Yamamoto, K. Suga, S. Shimizu, K. Kindo, and H. Hori, *Magnetic and transport characteristics on high Curie temperature ferromagnet of Mn-doped GaN*, J. Appl. Phys. **91**, 7911 (2002).

[126] G. T. Thaler, M. E. Overberg, B. Gila, R. Frazier, C. R. Abernathy, S. J. Pearton, J. S. Lee, S. Y. Lee, Y. D. Park, Z. G. Khim, *et al.*, *Magnetic properties of n-GaMnN thin films*, Appl. Phys. Lett. **80**, 3964 (2002).

[127] M. L. Reed, N. A. El-Masry, H. H. Stadelmaier, M. K. Ritums, M. J. Reed, C. A. Parker, J. C. Roberts, and S. M. Bedair, *Room temperature ferromagnetic properties of (Ga, Mn)N*, Appl. Phys. Lett. **79**, 3473 (2001).

[128] R. Y. Korotkov, J. M. Gregie, and B. W. Wessels, *Optical properties of the deep Mn acceptor in GaN:Mn*, Appl. Phys. Lett. **80**, 1731 (2002).

[129] S. Kuwabara, T. Kondo, T. Chikyow, P. Ahmet, and H. Munekata, *Molecular beam epitaxy of wurtzite GaN-based magnetic alloy semiconductors*, Jpn. J. Appl. Phys. **40**, L724 (2001).

[130] S. J. Pearton, M. E. Ovenberg, G. Thaler, C. R. Abernathy, N. Theodoropoulou, A. F. Hebard, S. N. G. Chu, R. G. Wilson, J. M. Zavada, A. Y. Polyakov, *et al.*, *Characterization of high dose Mn, Fe, and Ni implantation into p-GaN*, J. Vac. Sci. Technol. A **20**, 721 (2002).

[131] S. J. Pearton, C. R. Abernathy, M. E. Ovenberg, G. T. Thaler, D. P. Norton, N. Theodoropoulou, A. F. Hebard, Y. D. Park, F. Ren, J. Kim, *et al.*, *Wide band gap ferromagnetic semiconductors and oxides*, J. Appl. Phys. **93**, 1 (2003).

[132] A. Y. Polyakov, A. V. Govorkov, N. B. Smirnov, N. Y. Pashkova, G. T. Thaler, M. E. Overberg, R. Frazier, C. R. Abernathy, S. J. Pearton, J. Kim, *et al.*, *Optical and electrical properties of GaMnN films grown by molecular-beam epitaxy*, J. Appl. Phys. **92**, 4989 (2002).

[133] J. Kim, F. Ren, G. T. Thaler, R. Frazier, C. R. Abernathy, S. J. Pearton, J. M. Zavada, and R. G. Wilson, *Vertical and lateral mobilities in n-(Ga,Mn)N*, Appl. Phys. Lett. **82**, 1565 (2003).

[134] J. Schneider, U. Kaufmann, W. Wilkening, M. Baeumler, and F. Köhl, *Electronic structure of the neutral manganese acceptor in Gallium Arsenide*, Phys. Rev. Lett. **59**, 240 (1987).

[135] P. G. Baranov, I. V. Ilyin, and E. N. Mokhov, *Identification of iron transition group trace impurities in GaN bulk crystals by electron paramagnetic resonance*, Mater. Sci. Forum **258-263**, 1167 (1997).

[136] P. G. Baranov, I. V. Ilyin, and E. N. Mokhov, *Identification of iron transition group trace impurities in GaN bulk crystals by electron paramagnetic resonance*, Solid State Commun. **101**, 611 (1997).

[137] P. G. Baranov, I. V. Ilyin, E. N. Mokhov, and A. D. Roenkov, *Identification of manganese trace impurity in GaN crystals by electron paramagnetic resonance*, Semicond. Sci. Technol. **11**, 1843 (1996).

[138] R. Y. Korotkov, J. M. Gregie, B. Han, and B. W. Wessels, *Optical study of GaN:Mn co-doped with Mg grown by metal organic vapor phase epitaxy*, Physica B **308**, 18 (2001).

[139] B. Clerjaud, *Transition-metal impurities in III-V compounds*, J. Phys. C **18**, 3615 (1985).

[140] P. Vogl, *Transition-metal impurities in semiconductors*, Festkörperprobleme **25**, 563 (1985).

[141] B. Clerjaud, C. Marti, and A. Billmann, *Forbidden transitions $\Delta m = 2$ induced by an axial crystal field in electron paramagnetic resonance of $3d^5$ ions in II-VI compounds*, phys. stat. sol. (b) **44**, 693 (1971).

[142] P. Vogl and J. Baranowski, *Theory of substitutional 3d-transition metal impurities in III-V and II-VI semiconductors*, acta physica polonica **A67**, 133 (1985).

[143] S. Uhlenbruck, *Transporteigenschaften von dotierten Manganaten*, Ph.D. thesis, Universität zu Köln (2000).

[144] C. E. Mortimer, *Chemie* (Georg Thieme Verlag, Stuttgart, 1987), 5th ed.

[145] F. A. Cotton, *Chemical applications of group theory* (Wiley, New York, 1990).

[146] Tanabe and Sugano, *On the absorption spectra of complex ions. (I)*, J. Phys. Soc. Jpn. **9**, 753 (1954).

[147] A. C. Hornmann, C. F. Shaw, and C. Frank, *A widespread error in the d^6 Tanabe-Sugano diagram (TF)*, J. Chem. Educ. **64**, 918 (1987).

[148] D. J. Newman and B. Ng, *The superposition model of crystal fields*, Rep. Prog. Phys. **52**, 699 (1989).

[149] M. Gjukic, *Mangan-Dotierung von Galliumnitrid* (Diplomarbeit, Walter Schottky Institut, TU München, 2002).

[150] O. Ambacher, *Growth and applications of group III-nitrides*, J. Phys. D Appl. Phys. **31**, 2653 (1998).

[151] C. Kisielowski, J. Krüger, S. Ruvimov, T. Suski, J. W. Ager, E. Jones, Z. Liliental-Weber, M. Rubin, E. R. Weber, M. D. Bremser, *et al.*, *Strain-related phenomena in GaN thin films*, Phys. Rev. B **54**, 17745 (1996).

[152] G. Dollinger, C. M. Frey, A. Bergmaier, and T. Faestermann, *Depth profile analysis with monolayer resolution using elastic recoil detection (ERD)*, Europhys. Lett. **42**, 25 (1998).

[153] M. Zając, J. Gosk, E. Grzanka, M. Kamińska, A. Twardowski, B. Strojek, T. Szyszko, and S. Podsiadło, *Possible origin of ferromagnetism in (Ga,Mn)N*, J. Appl. Phys. **93**, 4715 (2003).

[154] S. Dhar, O. Brandt, A. Trampert, K. J. Friedland, Y. J. Sun, and K. H. Ploog, *Observation of spin-glass behavior in homogeneous (Ga,Mn)N layers grown by reactive molecular-beam epitaxy*, Phys. Rev. B **67**, 165205 (2003).

[155] P. G. Baranov, E. N. Mokhov, A. O. Ostroumov, M. G. Ramm, M. S. Ramm, V. V. Ratnikov, A. D. Roenkov, Y. A. Vodakov, A. A. Wolfson, G. V. Saparin, *et al.*, *Current status of GaN crystal growth by sublimation sandwich technique*, MRS Internet J. Nitride Semicond. Res. **3**, 50 (1998).

[156] G. E. Archangelskii, F. Karel, J. Mareš, S. Pačesová, and J. Pastrňák, *The luminescence and EPR spectra of manganese activated AlN*, phys. stat. sol. (a) **69**, 173 (1982).

[157] S. Sonoda, H. Hori, Y. Yamamoto, T. Sasaki, M. Sato, S. Shimizu, K. Suga, and K. Kindo, *Properties of ferromagnetic $Ga_{1-x}Mn_xN$ films grown by ammonia MBE*, IEEE Trans. Magn. **38**, 2859 (2002).

[158] T. Hartmann, M. Lampalzer, P. J. Klar, W. Stolz, W. Heimbrodt, H. A. K. von Nidda, A. Loidl, and L. Svistov, *Ferromagnetic resonance studies of (Ga,Mn)As with MnAs clusters*, Physica E **13**, 572 (2002).

[159] J. Schneider, *Paramagnetische Resonanz von Fe^{+++}-Ionen in synthetischen ZnO-Kristallen*, Z. Naturforsch. A **17**, 189 (1962).

[160] J. Schneider and S. R. Sircar, *Paramagnetische Resonanz von Mn^{++}-Ionen in synthetischen und natürlichen ZnO-Kristallen (I) "Erlaubte" Übergänge $\Delta M = \pm 1, \Delta m = \pm 0$*, Z. Naturforsch. A **17**, 570 (1962).

[161] J. Schneider and S. R. Sircar, *Paramagnetische Resonanz von Mn^{++}-Ionen in synthetischen und natürlichen ZnO-Kristallen (II) Analyse der verbotenen Übergänge $\Delta M = \pm 1, \Delta m = \pm 1$*, Z. Naturforsch. A **17**, 651 (1962).

[162] I. Ilyin, *private communication.*

[163] R. R. Sharma, *Zero-field splitting of a ^6S ion in trigonal symmetry*, Phys. Rev. B **3**, 76 (1971).

[164] K. Maier, M. Kunzer, U. Kaufmann, J. Schneider, B. Monemar, I. Asaki, and H. Amano, *Iron acceptors in gallium nitride (GaN)*, Mat. Sci. Forum **143-147**, 93 (1994).

[165] A. Wołoś, M. Palczewska, Z. Wilamowski, M. Kamińska, A. Twardowski, M. Boćkowski, I. Grzegory, and S. Porowski, *s-d exchange interaction in GaN:Mn studied by electron paramagnetic resonance* (2003), submitted to Appl. Phys. Lett.

[166] Z. Wilamowski, A. Mycielski, W. Jantsch, and G. Hendorfer, *Spin dynamics in the mixed-valence compound HgSe:Fe*, Phys. Rev. B **38**, 3621 (1988).

[167] B. Bleaney and R. S. Rubins, *Explanation of some "forbidden" transitions in paramagnetic resonance*, Proc. Phys. Soc. **77**, 103 (1961), corrigendum Proc. Phys. Soc. **78**, 118 (1963).

[168] S. Wolfram, *Mathematica* (Addison-Wesley, Redwood City, 1991).

[169] A. Hausmann and H. Huppertz, *Paramagnetic resonance of ZnO:Mn^{++} single crystals*, J. Phys. Chem. Solids **29**, 1369 (1968).

[170] O. M. Fedorych, E. M. Hankiewicz, and Z. Wilamowski, *Single ion anisotropy of Mn-doped GaAs measured by electron paramagnetic resonance*, Phys. Rev. B **66**, 045201 (2002).

[171] S. J. C. H. M. van Gisbergen, M. Godlewski, T. Gregorkiewicz, and C. A. J. Ammerlaan, *Magnetic-resonance studies of interstitial Mn in GaP and GaAs*, Phys. Rev. B **44**, 3012 (1991).

[172] J. Kreissl, W. Ulrici, M. El-Metoui, A. M. Vasson, A. Vasson, and A. Gavaix, *Neutral manganese acceptor in GaP: An electron-paramagnetic-resonance study*, Phys. Rev. B **54**, 10508 (1996).

[173] J. T. Vallin and G. D. Watkins, *EPR of Cr^{2+} in II-VI lattices*, Phys. Rev. B **9**, 2051 (1974).

[174] T. Graf, M. Gjukic, M. S. Brandt, M. Stutzmann, and O. Ambacher, *The $Mn^{3+/2+}$ acceptor level in group III-nitrides*, Appl. Phys. Lett. **81**, 5159 (2002).

[175] W. L. Yu and M. G. Zhao, *Spin-hamiltonian parameters of ^6S-state ions*, Phys. Rev. B **37**, 9254 (1988).

[176] J. Kreissl, W. Gehlhoff, P. Omling, and P. Emanuelsson, *Electron-paramagnetic-resonance identification of a trigonal manganese-indium pair in silicon*, Phys. Rev. B **42**, 1731 (1990).

[177] W. Low and J. T. Suss, *Paramagnetic resonance spectrum of manganese in corundum*, Phys. Rev. **119**, 132 (1960).

[178] O. Ambacher, J. Majewski, C. Miskys, A. Link, M. Hermann, M. Eickhoff, M. Stutzmann, F. Bernardini, V. Fiorentini, V. Tilak, *et al.*, *Pyroelectric properties of Al(In)GaN/GaN hetero- and quantum well structures*, J. Phys.: Condens. Matter **14**, 3399 (2002).

[179] K. Wang and R. R. Reeber, *Thermal expansion of GaN and AlN*, Mater. Res. Soc. Symp. Proc. **482**, 863 (1998).

[180] M. Leszczynski, T. Suski, H. Teisseyre, P. Perlin, I. Grzegory, J. Jun, and S. P. T. D. Moustakas, *Thermal expansion of gallium nitride*, J. Appl. Phys. **76**, 4909 (1994).

[181] H. P. Maruska and J. J. Tietjen, *The preparation and properties of vapour-deposited single-crystal-line gan*, Appl. Phys. Lett. **15**, 327 (1969).

[182] C. Blanchard, R. Parrot, and D. Boulanger, *Spin-lattice coupling coefficients of a $3d^5$ ion in trigonal symmetry: Study of Mn^{2+} in zinc sulfide*, Phys. Rev. B **7**, 4072 (1973).

[183] A. Wołoś, M. Zając, J. Gosk, M. Palczewska, M. Kamińska, A. Twardowski, M. Boćkowski, and S. Porowski, *Mn impurity in GaN monocrystals* (2003), proceedings of ICPS 26, Edinburgh 2002.

[184] G. E. Barberis, G. B. Martins, and R. Calvo, *Spin-lattice interaction for ions in low-symmetry sites*, Phys. Rev. B **49**, 8583 (1994).

[185] N. Almeleh and B. Goldstein, *Electron paramagnetic resonance of manganese in gallium arsenide*, Phys. Rev **128**, 1568 (1962).

[186] S. P. Keller, I. L. Gelles, and W. Smith, *Paramagnetic resonance absorption in Mn-activated hexagonal ZnS*, Phys. Rev. **110**, 850 (1958).

[187] P. B. Dorain, *Electron paramagnetic resonance of manganese (II) in hexagonal zinc oxide and cadmium sulfide single crystals*, Phys. Rev. **112**, 1058 (1958).

[188] U. Kaufmann and T. A. Kennedy, *Quantitative ESR analysis of deep defects in LEC-grown GaP*, J. Electron. Mater. **10**, 347 (1981).

[189] X. Biquard, O. Proux, J. Cibert, D. Ferrand, H. Mariette, R. Giraud, and B. Barbara, *Local structure and valence state of Mn in $Ga_{1-x}Mn_xN$ epilayers*, J. Supercond.: Incorporating Novel Magnetism **16**, 127 (2003).

[190] M. van Schilfgaarde and O. N. Mryasov, *Anomalous exchange interactions in III-V dilute magnetic semiconductors*, Phys. Rev. B **63**, 233205 (2001).

[191] R. Y. Korotkov, J. M. Gregie, B. Han, and B. W. Wessels, *Mn-related absorption and PL bands in GaN grown by metal organic vapor phase epitaxy*, Physica B **308**, 30 (2001).

[192] J. J. Krebs and G. H. Stauss, *EPR of $Cr^{2+}(3d^4)$ in gallium arsenide: Jahn-Teller distortion and photoinduced charge conversion*, Phys. Rev. B **16**, 971 (1977).

[193] A. Wołoś, *private communication* (2003).

[194] T. Graf, M. Gjucik, M. Hermann, M. S. Brandt, M. Stutzmann, and O. Ambacher, *Spin resonance investigations of Mn^{2+} in wurtzite GaN and AlN films*, Phys. Rev. B **67**, 165215 (2003).

[195] D. Brunner, H. Angerer, E. Bustarret, F. Freudenberg, R. Höpler, R. Dimitrov, O. Ambacher, and M. Stutzmann, *Optical constants of epitaxial AlGaN films and their temperature dependence*, J. Appl. Phys. **82**, 5090 (1997).

[196] K. Sato and H. Katayama-Yoshida, *Material design of GaN-based ferromagnetic diluted magnetic semiconductors*, Jpn. J. Appl. Phys. **40**, L485 (2001).

[197] P. Mahadevan and A. Zunger, *Electronic structure and ferromagnetism of 3d transition metal impurities in GaAs*, unpublished.

[198] G. Grebe and H. J. Schulz, *Luminescence of Cr^{2+} centres and related optical interactions involving crystal field levels of chromium ions in zinc sulfide*, Z. Naturforsch. A **29**, 1803 (1974).

[199] F. Bantien and J. Weber, *Properties of the optical transitions within the Mn acceptor in $Al_xGa_{1-x}As$*, Phys. Rev. B **37**, 10111 (1988).

[200] J. M. Langer and H. Heinrich, *Deep-level impurities: A possible guide to prediction of band-edge discontinuities in semiconductor heterojunctions*, Phys. Rev. Lett. **55**, 1414 (1985).

[201] M. J. Caldas, A. Fazzio, and A. Zunger, *A universal trend in the binding energies of deep impurities in semiconductors*, Appl. Phys. Lett. **45**, 671 (1984).

[202] I. Vurgaftman, J. R. Meyer, and L. R. Ram-Mohan, *Band parameters for III-V compound semiconductors and their alloys*, J. Appl. Phys. **89**, 5815 (2001).

[203] J. Neugebauer and C. G. V. de Walle, *Atomic geometry and electronic structure of native defects in GaN*, Phys. Rev. B **50**, 8067 (1994).

[204] D. E. Boucher, G. G. DeLeo, and W. B. Fowler, *Simulations of GaN using an environment-dependent empirical tight-binding model*, Phys. Rev. B **59**, 10064 (1999).

[205] P. Bogusławski, E. L. Briggs, and J. Bernholc, *Native defects in gallium nitride*, Phys. Rev. B **51**, 17255 (1995).

[206] L. Kronik, M. Jain, and J. R. Chelikowsky, *Electronic structure and spin polarization of $Mn_xGa_{1-x}N$*, Phys. Rev. B **66**, 041203 (2002).

[207] A. Janotti and S.-H. Wei, *Electronic and magnetic properties of MnN versus MnAs*, Appl. Phys. Lett. **766**, 766 (2003).

[208] J. Blinowski and P. Kacman, *Kinetic exchange in diluted magnetic semiconductors*, Phys. Rev. B **46**, 12298 (1992).

[209] J. Okabayashi, A. Kimura, O. Rader, T. Mizokawa, A. Fujimori, T. Hayashi, and M. Tanaka, *Core-level photoemission study of $Ga_{1-x}Mn_xAs$*, Phys. Rev. B **58**, R4211 (1998).

[210] H. Ohno, D. Chiba, F. Matsukura, T. Omiya, E. Abe, T. Dietl, Y. Ohno, and K. Ohtani, *Electric-field control of ferromagnetism*, Nature **408**, 944 (2000).

[211] H. Boukari, P. Kossacki, M. Bertolini, D. Ferrand, J. Cibert, S. Tatarenko, A. Wasiela, J. A. Gaj, and T. Dietl, *Light and electric field control of ferromagnetism in magnetic quantum structures*, Phys. Rev. Lett. **88**, 207204 (2002).

[212] R. N. Bhatt and X. Wan, *Monte Carlo simulations of doped, diluted magnetic semiconductors — a system with two length scales*, Int. J. Mod. Phys. C **10**, 1459 (1999).

[213] J. König, T. Jungwirth, and A. H. MacDonald, *Theory of magnetic properties and spin-wave dispersion for ferromagnetic (Ga,Mn)As*, Phys. Rev. B **64**, 184423 (2001).

[214] J. König, J. Schliemann, T. Jungwirth, and A. H. MacDonald, *Ferromagnetism in (III,Mn)V semiconductors* (2001), http://arXiv.org/abs/cond-mat/0111314.

[215] P. Kacman, *Spin interactions in diluted magnetic semiconductors and magnetic semiconductor structures*, Semicond. Sci. Technol. **16**, R25 (2001).

[216] T. Dietl, *Diluted magnetic semiconductors*, vol. 25 of *Semiconductors and Semimetals* (Academic, Boston, 1988).

[217] A. C. Durst, R. N. Bhatt, and P. A. Wolff, *Bound magnetic polaron interactions in insulating doped diluted magnetic semiconductors* (2001), http://arXiv.org/abs/cond-mat/0111497.

[218] J. Blinowski, P. Kacman, and T. Dietl, *Kinetic exchange vs. room temperature ferromagnetism in diluted magnetic semiconductors* (2002), http://arXiv.org/abs/cond-mat/0201012.

[219] R. Fiederling, M. Keim, G. Rauscher, W. Ossau, G. Schmidt, A. Waag, and L. W. Molenkamp, *Injection and detection of a spin-polarized current in a light-emitting diode*, Nature **402**, 787 (1999).

[220] S. H. Wei and A. Zunger, *Calculated natural band offsets of all II-VI and III-V semiconductors: chemical trends and the role of cation d orbitals*, Appl. Phys. Lett. **72**, 2011 (1998).

[221] T. Dietl, F. Matsukura, and H. Ohno, *Ferromagnetism of magnetic semiconductors: Zhang-Rice limit*, Phys. Rev. B **66**, 033203 (2002).

[222] W. Schairer and M. Schmidt, *Strongly quenched deformation potentials of the Mn acceptor in GaAs*, Phys. Rev. B **10**, 2501 (1974).

[223] G. P. Das, B. K. Rao, and P. Jena, *Ferromagnetism in Mn-doped GaN: From clusters to crystals* (2002), http://arXiv.org/abs/cond-mat/0208257.

[224] D. Ferrand, J. Cibert, A. Wasiela, C. Bourgognon, S. Tatarenko, G. Fishman, T. Andrearczyk, J. Jaroszyński, S. Koleśnik, and T. Dietl, *Carrier-induced ferromagnetism in p-*$Zn_{1-x}Mn_xTe$, Phys. Rev. B **63**, 085201 (2001).

[225] H. Ohno, A. Shen, F. Matsukura, A. Oiwa, A. Endo, S. Katsumoto, and Y. Iye, *(Ga, Mn)As: A new diluted magnetic semiconductor based on GaAs*, Appl. Phys. Lett. **69**, 363 (1996).

[226] V. Y. Davydov, A. A. Klochikhin, V. V. Emtsev, S. V. Ivanov, V. V. Vekshin, F. Bechstedt, J. Furthmüller, H. Harima, A. V. Mudryi, A. Hashimoto, *et al.*, *Band gap of InN and In-rich* $In_xGa_{1-x}N$ *alloys* ($0.36 < x < 1$), phys. stat. sol. (b) **230**, R4 (2002).

[227] U. Grossner, J. Furthmüller, and F. Bechstedt, *Surface energies and surface dipoles at III-nitride(111) surfaces in dependence on stoichiometry*, phys. stat. sol. (b) **216**, 675 (1999).

[228] A. Mauger, *Magnetic polaron: Theory and experiment*, Phys. Rev. B **27**, 2308 (1983).

[229] T. Dietl, J. Spałek, and L. Świerkowski, *Theory of the bound magnetic polaron: A physical discussion and a comment*, Phys. Rev. B **33**, 7303 (1986).

[230] A. Mauger, *Reply to "Theory of the bound magnetic polaron: A physical discussion and a comment"*, Phys. Rev. B **33**, 7307 (1986).

[231] M. Herbich, A. Twardowski, D. Scalbert, and A. Petrou, *Bound magnetic polaron in Cr-based diluted magnetic semiconductors*, Phys. Rev. B **58**, 7024 (1998).

[232] V. F. Sapega, T. Ruf, and M. Cardona, *Spin-flip Raman scattering in Mn-doped GaAs: Exchange interaction and g factor renormalization*, Solid State Comm. **114**, 573 (2000).

[233] W. Götz, N. M. Johnson, J. Walker, D. P. Bour, and R. A. Street, *Activation of acceptors in Mg-doped GaN grown by metalorganic chemical vapor deposition*, Appl. Phys. Lett. **68**, 667 (1996).

[234] P. Kozodoy, H. Xing, S. P. DenBaars, U. K. Mishra, A. Saxler, R. Perrin, S. Elhamri, and W. C. Mitchel, *Heavy doping effects in Mg-doped GaN*, J. Appl. Phys. **87**, 1832 (2000).

[235] I. Akasaki and H. Amano, *Crystal growth of column III nitrides and their applications to short wavelength light emitters*, J. Cryst. Growth **146**, 455 (1995).

[236] R. Heitz, P. Maxim, L. Eckey, P. Thurian, A. Hoffmann, I. Broser, K. Pressel, and B. K. Meyer, *Excited states of Fe^{3+} in GaN*, Phys. Rev. B **55**, 4382 (1997).

[237] V. I. Litvinov and V. K. Dugaev, *Ferromagnetism in magnetically doped III-V semiconductors*, Phys. Rev. Lett. **86**, 5593 (2001).

[238] J. Blinowski, P. Kacman, and J. A. Majewski, *Ferromagnetic superexchange in Cr-based diluted magnetic semiconductors*, Phys. Rev. B **53**, 9524 (1996).

[239] P. Watcher, *Handbook on the physics and chemistry of rare earth*, vol. 1 (North-Holland, Amsterdam, 1979).

[240] K. Sato, P. H. Dederics, and H. Katayama-Yoshida, *Curie temperatures of III-V diluted magnetic semiconductors calculated from first-principles*, Europhys. Lett. **61**, 403 (2003).

[241] Y. K. Zhou, M. Hashimoto, M. Kanamura, and H. Asahi, *Room temperature ferromagnetism in IIIV-based diluted magnetic semiconductor GaCrN grown by ECR molecular-beam epitaxy*, J. Supercond.: Incorporating Novel Magnetism **16**, 37 (2003).

[242] M. Zając, J. Gosk, M. Kamińska, A. Twardowski, T. Szyszko, and S. Podsiadlo, *Paramagnetism and antiferromagnetic d-d coupling in GaMnN magnetic semiconductor*, Appl. Phys. Lett. **79**, 2432 (2001).

[243] C. A. Parker, J. C. Roberts, and S. M. Bedair, *Room temperature ferromagnetic properties of (Ga, Mn)N*, Appl. Phys. Lett. **79**, 3473 (2001).

[244] B. K. Rao and P. Jena, *Giant magnetic moments of nitrogen-doped Mn clusters and their relevance to ferromagnetism in Mn-doped GaN*, Phys. Rev. Lett. **89**, 185504 (2002).

[245] H. Yang, H. Al-Brithen, A. R. Smith, J. A. Borchers, R. L. Cappelletti, and M. D. Vaudin, *Structural and magnetic properties of η-phase manganese nitride films grown by molecular-beam epitaxy*, Appl. Phys. Lett. **78**, 3860 (2001).

[246] S. Dhar, O. Brandt, A. Trampert, L. Däweritz, K. J. Friedland, K. H. Ploog, J. Keller, B. Beschoten, and G. Güntherodt, *Origin of high-temperature ferromagnetism in (Ga,Mn)N layers grown on 4H-SiC* (0001) *by reactive molecular beam epitaxy*, Appl. Phys. Lett. **82**, 2077 (2003).

[247] T. Graf, M. Gjucik, M. S. Brandt, M. Stutzmann, L. Görgens, J. B. Philipp, M. Hermann, and O. Ambacher, *Growth and characterization of GaN:Mn epitaxial films*, J. Appl. Phys. **93**, 9697 (2003).

[248] K. Ando, *Magneto-optical studies of s,p-d exchange interactions in GaN:Mn with room-temperature ferromagnetism*, Appl. Phys. Lett. **82**, 100 (2003).

[249] H. J. Zhu, M. Ramsteiner, H. Kostial, M. Wassermeier, H. P. Schönherr, and K. H. Ploog, *Room-temperature spin injection from Fe into GaAs*, Phys. Rev. Lett. **87**, 016601 (2001).